The MESSENGER Ultraviolet and Visible Spectrometer: Calibration, Mercury Sodium Observation Strategies, and Analysis of In-flight Lunar Observations

by

Eric Todd Bradley

B.S., University of Alabama (Birmingham), 1997

M.S., University of Florida, 2001

A thesis submitted to the

Faculty of the Graduate School of the

University of Colorado in partial fulfillment

of the requirements for the degree of

Doctor of Philosophy

Department of Aerospace Engineering Sciences

2007

This thesis entitled:
The MESSENGER Ultraviolet and Visible Spectrometer: Calibration, Mercury Sodium Observation Strategies, and Analysis of In-flight Lunar Observations
written by Eric Todd Bradley
has been approved for the Department of Aerospace Engineering Sciences

_____
Prof. William Emery

_____
William McClintock

_____
Prof. Nick Schneider

_____
Prof. Larry Esposito

_____
Prof. Dan Baker

Date_____

The final copy of this thesis has been examined by the signatories, and we find that both the content and the form meet acceptable presentation standards of scholarly work in the above mentioned discipline.

Bradley, Eric Todd (Ph.D., Department of Aerospace Engineering Sciences)

The MESSENGER Ultraviolet and Visible Spectrometer: Calibration, Mercury Sodium Observation Strategies, and Analysis of In-flight Lunar Observations

Thesis directed by Dr. William McClintock

The MESSENGER Ultraviolet and Visible Spectrometer (UVVS) is one channel of the Mercury Atmospheric and Surface Composition Spectrometer (MASCS) that is presently on the MESSENGER spacecraft en-route to Mercury. The goal of this thesis is the calibration of the UVVS and development of observation strategies for Mercury's exosphere during the MESSENGER orbital phase. The calibration of the UVVS is crucial for the analysis of flight data. Both pre-launch laboratory and post-launch stellar calibration experiments that characterize the performance of the UVVS are described and results presented. Mercury has been shown to have a tenuous exosphere. Careful observation planning of the exosphere before orbit insertion is crucial in order to devise strategies to address key scientific questions concerning the nature of the Mercurian exosphere. A software planning tool has been developed that combines instrument performance, spacecraft orbital geometry, and predictions of sodium in Mercury's exosphere in order to develop observational strategies and set detection limits for sodium. Using the observation strategies, signal and SNR predictions based on a sodium exospheric model are made that characterize the ability of the UVVS to distinguish between sodium exospheric production processes. In 2005, MESSENGER flew by the Earth-Moon system and gave an opportunity to validate instrument detection limit predictions. A description of lunar limb

observations is given along with a comparison of detection limits based on real and model predicted data.

Dedication

This thesis is dedicated to my 2 sons
Hayden Walt Bradley and Heston Jacob Bradley

Acknowledgements

I would like to thank the members of my thesis committee, Bill McClintock, Bill Emery, Nick Schneider, Larry Esposito, and Dan Baker for the professional manner in which they contributed to my thesis as committee members. In particular, I thank my thesis advisor, Bill McClintock, for the opportunity and support to work on this project and for an extensive review of my thesis. I also give a special thanks to Nick Schneider for extremely helpful advice and guidance.

This project was supported by the National Aeronautics and Space Administration's Discovery program through a contract to the University of Colorado from the Carnegie Institution of Washington.

I thank Rosemary Killen for her Mercury sodium exospheric model that I used for my thesis research. I thank Greg Holsclaw for reviewing my defense presentation and for all the many conversations that we have had. I thank Dewey Anderson for his helpful insights concerning my defense presentation and for our lengthy discussions concerning scientific matters as well as many other subjects

I thank my parents, Roy and Shelby Bradley, for giving me a good childhood, for always being reliable, and for their many years of support. I especially thank my wife, Tara Bradley, who made as many sacrifices during the years that I worked on this thesis as I have made and who was always there to give me moral and emotional support.

Contents

Tables

Table

Figures

Figure

Chapter 1

Introduction

1.1 Thesis outline

The purpose of this thesis is to determine observation strategies for the exosphere of Mercury with the Ultra-Violet Visible Spectrometer (UVVS) channel of the Mercury Atmospheric and Surface Composition Spectrometer (MASCS) on the MErcury Surface, Space Environment, GEochemistry, and Ranging (MESSENGER) spacecraft. The bulk of this work emphasizes observations above the dayside of the planet because MASCS detects resonantly scattered sunlight from exospheric species (Section 1.4.2) and also because directly driven solar source processes operate primarily on the dayside. Also, on the nightside, tail sweeps will be used to observe exospheric species that are not in the shadow of the planet, but these observations consists of simply rotating the spacecraft about an axis that is normal to the sun line. A need exists to devise more complex observations of the dayside, hence the motivation for this thesis. Preparing to study Mercury's exosphere with MASCS requires several separate pieces of work and research. First, MASCS was subjected to a rigorous set of calibration experiments in order to characterize the performance of the instrument. Second, visualization software was developed in order to determine the temporal and spatial capability of MASCS to make observations while

MESSENGER is in orbit around Mercury. This second step led to the proposal of a systematic set of observations that map the exosphere of Mercury with the aim to produce the temporal and spatial coverage necessary to address key scientific questions concerning Mercury's exosphere. Third, the proposed set of observations was combined with results from calibration experiments in order to set detection limits for sodium in Mercury's exosphere. Fourth, the observation strategies were used to test a sodium exospheric model by characterizing the ability of MASCS to distinguish between variations in model predictions. The variation in model predictions were chosen to explore several key issues related to the sodium exosphere of Mercury. This was achieved by combining radiance predictions from the model with instrument performance in order to produce signal and uncertainty predictions.

This research is documented in the following chapters. Chapter 1 gives background information about Mercury, the MESSENGER mission, and the nature of the techniques employed in the observation of Mercury's exosphere. Chapter 2 records the calibration experiments and results for both ground based and post-launch calibrations. Chapter 3 is an overview of the exosphere of Mercury with emphasis on sodium. Chapter 4 describes the software that was developed for both the visualization of observations at Mercury as well as signal and uncertainty predictions. Chapter 5 lists the proposed set of observations throughout an Mercury year, the detection limits for the observations, and the signal and uncertainty predictions from testing the sodium exospheric model. Chapter 6 summarizes data taken during the lunar flyby that was used to gain further insight into the performance and operation of the instrument. Chapter 7 is the conclusion of the research.

The result of this thesis is to demonstrate systematic seasonal observation strategies of Mercury's exosphere that will provide a uniform dataset while at the same time answering key scientific questions concerning the exosphere of Mercury. Emphasis is placed on sodium, but the observation strategies are versatile enough to be used for the characterization of processes associated with other exospheric species. The specific science questions concerning Mercury's sodium exosphere that may be answered by the observation strategies developed in thesis are:

1) How much of the sodium exosphere consists of low energy solar driven production rate processes?
2) How much of the sodium exosphere consists of high energy isotropic production rate processes?
3) How much of the sodium exosphere is thermally desorbed from the surface?
4) What is the temporal and spatial variability of dawn side enhancements of sodium?
5) How does the surface density concentration of sodium vary with latitude?
6) What is the escape of neutral sodium from the system?

These specific questions are related more generally to question 6 from the list of key scientific questions (Solomon, et. al., 2001) that are also listed in Section 1.3.1.

1.2 Mercury overview

1.2.1 Mercury characteristics

Mercury is an end member planet in multiple physical parameters. Mercury is the closest planet to the Sun with the highest orbital eccentricity. Mercurys' orbit brings the planet to 0.307 AU from the Sun at perihelion and to 0.467 AU at aphelion, implying large variations in solar flux and surface temperature. Compositionally Mercury is the least massive (3.302×10^{23} kg) but yet most dense planet (5.3 g/cc uncompressed) which implies an iron-rich composition, Riner, et. al. (2007).

Mercury is the smallest planet with a diameter of 4880 km, which together with its mass implies the lowest gravitational escape speed.

Since Mercury is an end member planet in so many facets, this makes the study of Mercury particularly intriguing in terms of planetary formation processes. The key question concerning the formation of Mercury is how to explain the very high density of the planet. Based on cosmic abundances, the iron content of Mercury must be relatively large (Urey, 1952); however, as noted by Goettel, (1988), at present there is not a rigorous method to determine the composition of heavy elements that cause the high density of Mercury. Furthermore, observations and estimated compositions of Mercury imply a low concentration of FeO (Taylor and Scott., 2005). Formation models that seek to explain Mercury's high metal to silicate ratio include models in which giant impacts stripped away the silicate mantel from Mercury (Taylor and Scott, 2005; Wetherill, 1988), evaporation models in which Mercury formed very early in very hot solar nebula temperatures where most of the silicates vaporized (Cameron, 1985), and a 2 component model where refractory rich planetesimals close to the sun account for a fraction of the composition of the planet and earth-like planetesimals account for the remaining fraction (Taylor and Scott, 2005).

If exospheric species arise from the surface material, then the exosphere is inherently connected to the formation processes and planetary composition or to infalling material, i.e., meteoroid impact. For either case, volatile species such as sodium evaporate from the extreme surface layers very quickly (Leblanc and Johnson, 2003); however gardening of fresh regolith by micro-meteoritic impact or sputtering processes could replenish sodium if it is available beneath the extreme

surface (Killen et al., 2004b). Koehn and Sprague (2007) suggests that the solar wind may contain significant abundances of oxygen and calcium to supply the Mercurian exosphere of these species. However, Sprague (private communication, 2007) claims that insufficient quantities of sodium are available in the solar wind to account for the observed abundances of sodium in the exosphere.

The determination of the spatial and temporal variations of exospheric species will indirectly help to constrain some of the formation process models for Mercury. In order to ascertain if there is a solar wind component to the exosphere, other instruments such as the EPPS (Section 1.3) will need to be used in conjunction with exospheric mapping. If exospheric species such as sodium are found to be derived from the surface, then mapping the spatial and temporal variations will help constrain models for the various processes in which atoms are liberated from the surface. As will be discussed in Chapter 3, different source processes are characterized by unique signatures that should be detectable given a systematic observation campaign over a large range of spatial distributions as well as over seasonal cycles throughout the Mercury year.

1.2.2 3:2 spin-orbit resonance

Mercury spins on its axis every 58.646 earth days and rotates around the Sun every 88.969 earth days. This implies that Mercury has makes one complete revolution on its own axis during 2/3 of a Mercury year or that during the course of 2 Mercury

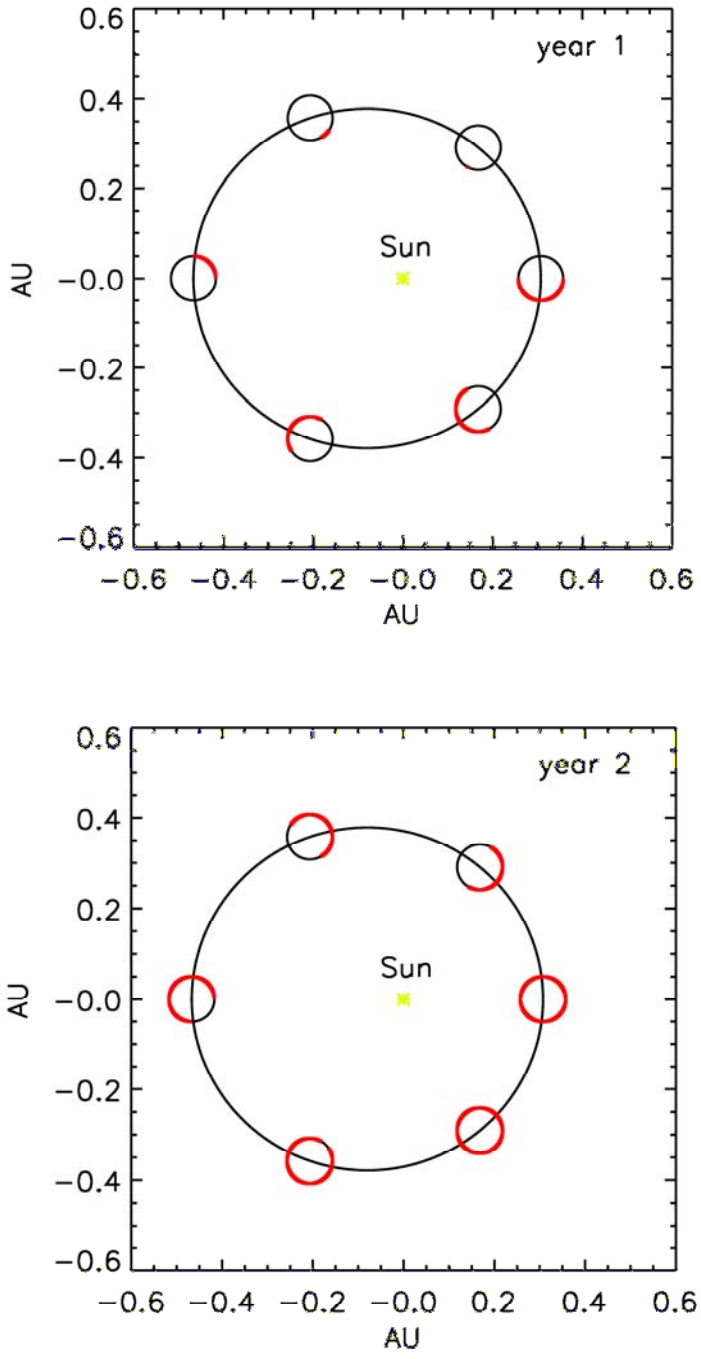

Figure 1.1. Mercury is shown for two successive years with the red curve representing the portion of the planet that has experienced a local noon. It takes 2 Mercury years for every location on the planet to have experienced noon-time.

years the planet rotates on its own axis 3 times. This has profound implications for the daily cycle of Mercury. Figure 1.1 illustrates how the regions of the planet that experience local noon progress throughout 2 Mercury years. At perihelion, where the planetary true anomaly = 0°, the sub-solar longitude is defined to be 0°. As the planet moves to aphelion, where where the planetary true anomaly = 180°, the sub-solar longitude is now at 90°, and only 25% of the planet has experienced a local noon. As the planet moves back to perihelion, the sub-solar longitude is now 180°, with 50% of the planet having now experienced a local noon. For the second year aphelion implies a sub-solar longitude of 270° with 75% of the planet having experienced a local noon, and when the planet arrives back at perihelion at the completion of 2 Mercury years, the sub-solar longitude is 0° and 100% of the planet has now experienced a local noon.

Due to the highly elliptical nature of Mercury's orbit, 0° and 180° longitude always experience the largest surface temperature, while 90° and 270° are the sub-solar regions that are always the coldest. These locations are known as hot poles and cold poles. Figure 1.2 shows how the temperature varies throughout the Mercury year. The temperature distribution is given by

$$T_{surface} = 50 + 450 * \cos(solzen)^{0.25} * \frac{0.465}{R} \qquad (1.1)$$

where solzen is the solar zenith angle for a point on the surface and R is the distance of Mercury from the Sun in AU (Killen, private communication, 2003).

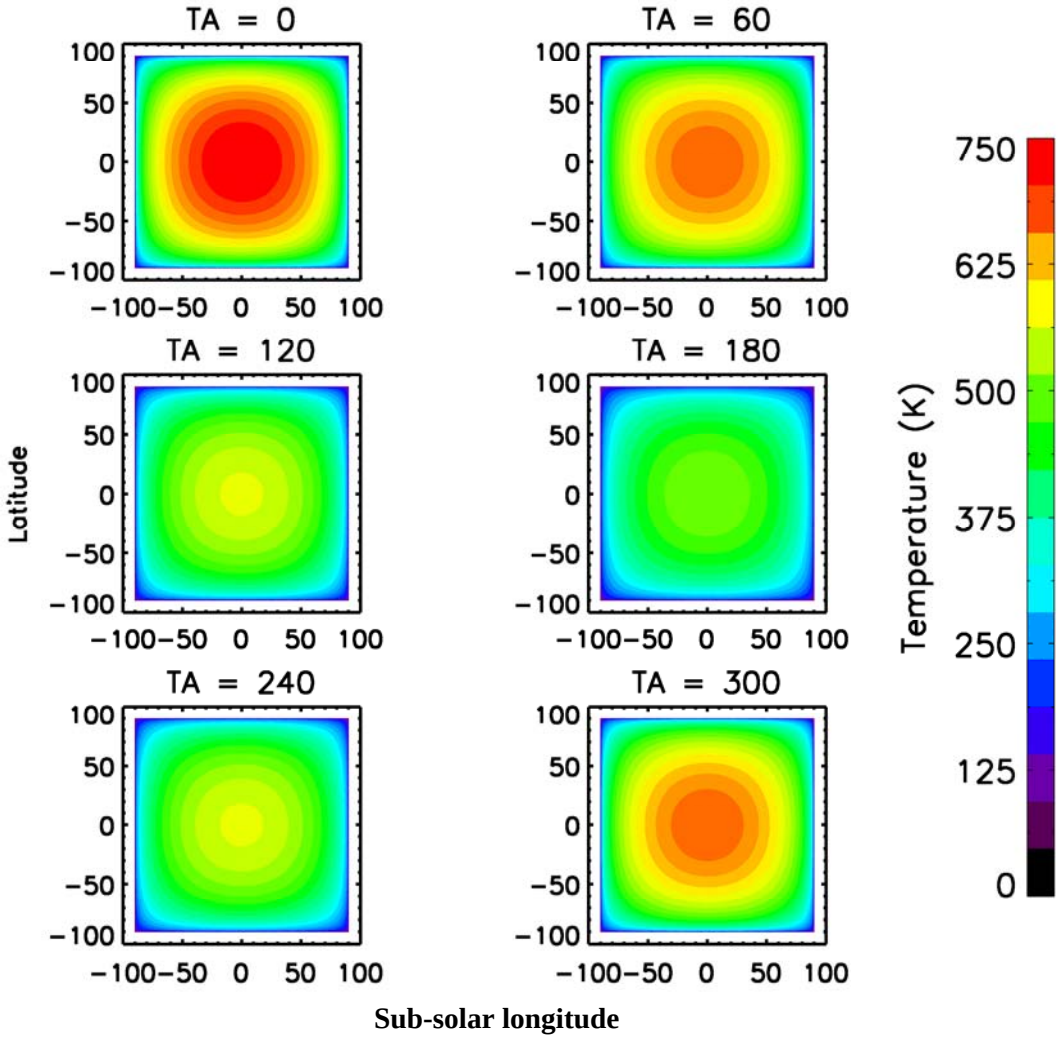

Figure 1.2. Temperature variations over the dayside surface throughout the Mercury year in true anomaly increments of 60°.

Equation 1.1 predicts a nightside temperature of 50 K, which is independent of planetary true anomaly. This implies that the temperature gradient from sub-solar to terminator much larger for perihelion than at aphelion. This has important implications for observing variations in thermally driven exospheric source processes, which will be discussed in Chapter 5.

1.3 The MESSENER mission

The problem with sending a spacecraft to orbit Mercury is due to the fact that Mercury is deep within the Sun's gravitational well, Stern and Vilas, 1988. Bepi Colombo was the first to propose that multiple flybys of Mercury separated by ~ 6 months were possible, which led to the flyby sequence of Mariner 10. The possibility of inserting a spacecraft into orbit around Mercury by means of presently available chemical rockets was first proposed by Yen in 1985, (Yen, 1989). This technique requires swingbys of Venus and Mercury in order to reduce the Mercury approach energy. The MESSENGER spacecraft relies on 2 flybys of Venus and 3 flybys of Mercury before going into orbit around Mercury. After launch in August 2004, MESSENGER was placed in a one year parking orbit around the earth, at the end of which MESSENGER flew by the earth-moon system. The two flybys of Venus occurred on October 24, 2006 and June 6, 2007. The three Mercury flybys will occur on January 14, 2008, October 6, 2008, and September 29, 2009 before orbit insertion on either March 18 or March 20, 2011.

1.3.1 MESSENGER instrumentation

MESSENGER carries a suite of 7 instruments to perform scientific investigations of Mercury's surface, exosphere, magnetosphere, and particle environment (Figure 1.3). The 7 instruments, listed in Table 1.1 with brief functionality descriptions, were chosen to address the following 6 key scientific questions (Solomon, et. al., 2001):

1) What planetary formational processes led to the high metal/silicate ratio in Mercury?
2) What is the geological history of Mercury?
3) What are the nature and origin of Mercury's magnetic field?
4) What are the structure and state of Mercury's core?
5) What are the radar-reflective materials at Mercury's poles?
6) What are the important volatile species and their sources and sinks on and near Mercury?

The goal of this thesis is to deal with question 6, although strong coupling between the exosphere, surface, solar wind, and magnetic field implies that addressing one question inadvertently leads to addressing other questions.

1.3.2 The MESSENGER orbit

Observation opportunities for the exosphere are closely linked to the orbit that MESSENGER is placed in around Mercury. MESSENGER will orbit Mercury once every 12 hours for 1 Earth year (or 4 Mercury years), giving a total of ~ 730 orbits. Figure 1.4 shows the orbital configuration. Every other orbit is almost exclusively reserved for down-linking of data, thus only 365 orbits will be available for

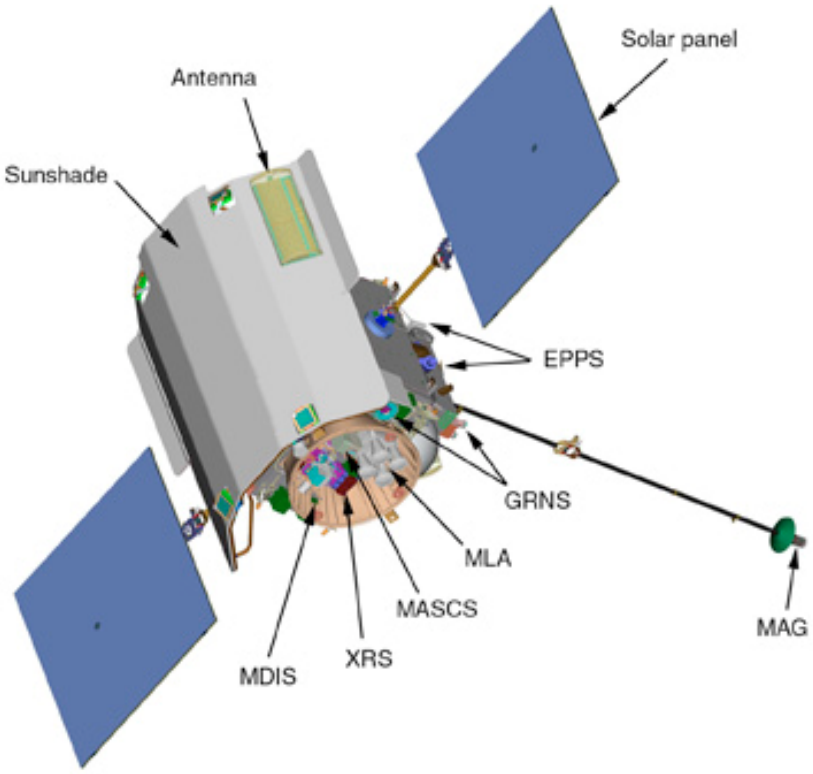

Figure 1.3. Diagram of MESSENGER spacecraft showing the instrument deck. This figure was taken from the MESSENGER website.

Instrument	Functionality
Mercury Dual Imaging System (MDIS)	This instrument consists of wide-angle and narrow-angle imagers that will map the surface.
Gamma-Ray and Neutron Spectrometer (GRNS)	This instrument will detect gamma rays and neutrons from the surface in order to map the relative abundances of different elements.
X-Ray Spectrometer (XRS)	This instrument will detect emitted X-rays from surface elements in order to determine relative abundances of elements.
Magnetometer (MAG)	This instrument will map Mercury's magnetic field.
Mercury laser Altimeter (MLA)	This instrument will characterize the topography of Mercury by use of a reflected laser beam.
Mercury Atmospheric and Surface Composition Spectrometer (MASCS)	This instrument will measure abundances from exospheric species as well as detect minerals on the surface.
Energetic Particle and Plasma Spectrometer (EPPS)	This instrument will measure the composition, distribution, and energy of charged particles in Mercury's magnetosphere.

Table 1.1. Instruments on the MESSENGER spacecraft that will perform scientific investigations of Mercury (paraphrased from the MESSENGER website http://messenger.jhuapl.edu/).

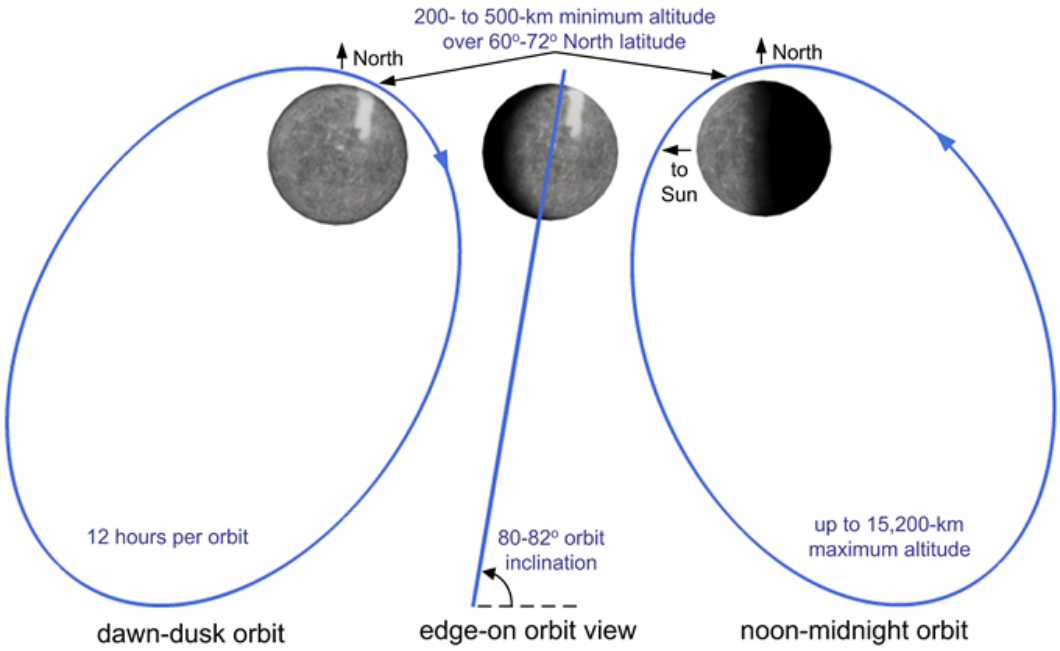

Figure 1.4. Orbit of MESSENGER around Mercury showing both the dawn-dusk and noon-midnight orbits. This figure was taken from the MESSENGER website.

observations. MESSENGER will be inserted in a highly eccentric orbit (e = 0.737) with a perihelion that will gradually rise from 200 km to 500km over a planetary latitude range from 60° to 72° North latitude throughout the course of the mission. The orbit will be inclined to ~ 80°, resulting in an orbit that is almost polar. Since MESSENGER's orbit makes such a small change over the course of the mission, the inertial observation strategies developed in this thesis throughout a Mercury year are valid over the course of the mission.

The MESSENGER orbit will be fixed in inertial space, which implies that as Mercury moves around the sun, there will be 2 times during the Mercury year that MESSENGER will pass directly above the sub-solar point. There will also be 2 times during the Mercury year that MESSENGER will pass directly above the terminator where it crosses the equator. The sets of orbits are called noon-midnight and dawn-dusk orbits, respectively. The noon-midnight orbits occur near planetary true anomalies of 97° and 276°, while the dawn dusk orbits occur near planetary true anomalies of 6° and 186°. This implies that the dawn-dusk orbits are almost coincident with perihelion and aphelion.

Due to the large eccentricity of MESSENGER's orbit, apoherm extends to ~ 15,000 km altitude, as shown in Figure 1.4. However, due to the orbit being fixed in space, apoherm at the noon-midnight orbit occurring at a planetary true anomaly of 97° will be on the dayside. Conversely, apoherm at the noon-midnight orbit occurring at a planetary true anomaly of 276° will be on the nightside. This has profound effects on the amount of time for observations of the dayside or nightside (or more importantly the tail region). The dichotomy in observations of the dayside

and tail regions of the planet implies that dayside observations are best at a true anomaly of 97° and tail observations are best at a true anomaly of 276°.

MESSENGER pointing control limits that ability to 1) plan for observations at a particular limb height and 2) know what limb height the observation occurred after completion. From Santo, et. al., (2001), the calculated attitude control is 500 μrad (1-σ) and the calculated knowledge is 250 μrad (1 σ). Furthermore, the calculated maneuverability is 0.006°/s^2 slew acceleration and 0.3°/s slew rate with a jitter of 15μrad in 0.1 s (1-σ). These values do not take into account the knowledge of the location of the spacecraft in its orbit.

1.3.3 MESSENGER orientation constraints

Due to the close proximity of Mercury to the Sun, MESSENGER was built with a sun shade that shields the instrument deck from direct solar illumination, Figure 1.3. The angle defined by a vector normal to the sun shade and the spacecraft-Sun vector may not exceed +/- 12°. Thus the spacecraft Z axis must always remain between 78° to 112° with respect to the spacecraft-Sun vector. The MASCS boresight is < 0.2° from the spacecraft Z axis, so to a reasonable approximation MASCS can only make observations within the same limits as for the spacecraft Z axis. Rotations about the spacecraft X and Z axes must obey the sun-shade constraint, while rotations of 360° about the spacecraft Y axis are permitted. A rotation about the spacecraft Z axis results in rotating the slit of the instrument, but since the maximum rotation is only +/- 12°, this achieves very little in terms of changing the spatial resolution of atmospheric profiles. A rotation about the spacecraft X axis within the +/-12° limit or

a rotation about the spacecraft Y axis results in pointing the boresight to different regions of the atmosphere; thus exospheric limb scans consists exclusively of combinations of spacecraft rotations around the X and Y axes. The sun-shade constraint limits pointing opportunities for MESSENGER and severely complicates the limb observing geometry. A result of this investigation is to produce software that helps visualize the non-intuitive nature of limb observing geometry.

1.4 Mercury observations

Mercury's small size and close proximity to the Sun make ground based observations difficult. The average angular diameter of Mercury seen from the earth is 6" with a maximum elongation of 28°. Thus astronomers are faced with observing Mercury during the daytime and subtracting off sky scattered light or observing Mercury for short periods before sunrise or after sunset while looking through a larger portion of the atmosphere. Also, Mercury exospheric observations from the earth are frequently pointed at the surface of the planet and thus the signal is inundated with reflected solar radiation. Furthermore, ground based observations below the short wavelength atmospheric cutoff at 330 nm or so are not possible so UV spectra of Mercury is unobtainable from the ground. So far, 3 exospheric species, Na, Ca, and K have been detected in Mercury's exosphere by ground-based observations.

Historically, space-based instrumentation has offered limited access to observing Mercury. Since Mariner 10 only made 3 flybys of Mercury, only ~ 45% of Mercury's surface was imaged by this mission (Strom, 1997). Mariner 10 detected 3

exospheric species, H, He, and O, with upper limits set for a variety of other species that were expected to be there. Other telescopes, such as Hubble, have not been used to observe Mercury due to the close proximity of the planet to the Sun. In contrast, with the 3 MESSENGER flybys, 1 Earth year in orbit, and the suite of instruments on board, the surface, exosphere, magnetosphere, and solar wind environment of Mercury will be systematically mapped both spatially and temporally. The fact that data will be returned from multiple instruments studying different aspects of Mercury at the same time will lead to a combined dataset unprecedented for Mercury observations of the past. Chapter 5 will describe the spatial and temporal coverage as well as possible sodium detection limits for the observations of the exosphere with MASCS.

1.4.1 The Rayleigh

Exospheric emissions that fill the field of view of the instrument are considered extended sources of radiation, as opposed to point sources that under-fill the field of view such as the observation of a star. Furthermore, since the observation of an atmosphere generally measures emissions along the line of sight into the atmosphere, a unit needed to be defined that accounted for emissions arising from both the lateral extent and along the direction of the observation. Figure 1.5 shows the geometry associated with this type of observation with a description that follows from Chamberlain, 1961.

Every unit volume within the atmosphere is emitting radiation, from which only a portion of the radiation falls within the field of view of the instrument, shown in red.

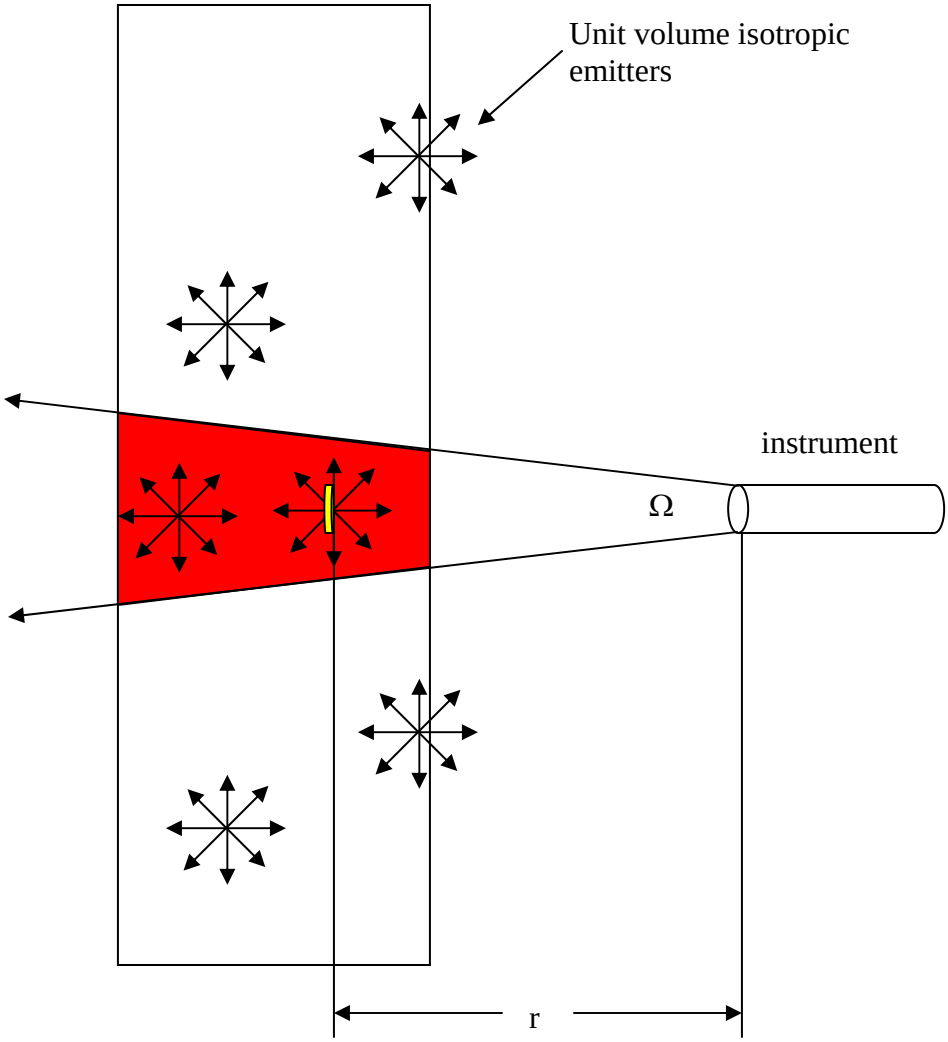

Figure 1.5. Schematic of light intercepted by an instrument from an extended source. The nature of the angular extent over which light enters the instrument is fundamental to the definition for the Rayleigh.

Imagine a volume of length dr, an area = 1 cm^2, and a distance r from the detector, shown in yellow. If the volume is emitting photons isotropically at a rate F(r) photons/cm^3/sec, then the photons intercepted by the aperture of the instrument per second are $A/4\pi r^2$ F(r) *1 cm^2 dr, where A is the area of the entrance pupil. If the volume of emitters is then increased to completely encompass the solid angle subtended by the instrument field of view, then the photons falling within by the field of view per second will be $A/4\pi r^2$ F(r) dr r^2 Ω.

If now the depth of the atmosphere is taken into account by integrating all contributions encompassed by the solid angle, the photons intercepted by the detector per second are

$$N\left(\frac{photons}{\sec ond}\right) = \frac{A\Omega}{4\pi}\int_0^\infty F(r)dr \tag{1.2}$$

where the approximation has been made that the cross-sectional area of atmosphere subtended by Ω does not vary significantly. If Equation 1.2 is multiplied by $(4\pi / A\Omega)$, then the equation may be written as

$$4\pi * I\left(\frac{photons}{\sec * cm^2}\right) = \int_0^\infty F(r)dr \tag{1.3}$$

where *I* is in units of photons/second/cm^2/sr and may be considered the surface brightness. The Rayleigh is then defined as

$$1R = \frac{10^6}{4\pi} \frac{photons}{\sec * cm^2 * ster} \tag{1.4}$$

This definition of the Rayleigh follows the generalized photon radiance definition proposed by Baker and Romick, 1976. Therefore if a surface brightness, *I*, is measured by counting photons over an extended source, then the number of Rayleighs is obtained by

$$\#R = \frac{\#\, photons * 4\pi}{10^6} \tag{1.5}$$

Historically, since the Rayleigh was first used as a unit to deal with column emission from the atmosphere, the definition according to Equation 1.5 did not contain 4π, and thus the Rayleigh was defined in units of photons/sec/cm^2. However, for this work the Rayleigh adheres to the definition of Equation 1.5.

1.4.2 Resonance scattering

Exospheric observations consist of MASCS detecting solar radiation that has been resonantly scattered from exospheric species. For sodium this consists of incident solar radiation exciting sodium atoms from the ground state, $3s^2S_{1/2}$, to the first excited state. The first excited state is split by spin-orbit coupling into 2 fine structure components, $3p^2P_{1/2}$ and $3p^2P_{3/2,}$ which are further split into 4 and 6 hyper-fine

components, respectively, by coupling between the nuclear spin and total electronic angular momentum (Brown and Yung, 1976). The center wavelengths of the two fine structure components are derived from the centroids of the respective hyperfine components, which are weighted by their oscillator strengths. The results are known as the sodium D lines, with the centroid wavelength of the D1 line at 5895.92 Å and the centroid wavelength of the D2 line at 5889.95 Å

1.4.3 g-values

The number of solar photons resonantly scattered per second by an atom is called the g-value. This value depends in part on the quantum mechanical nature of the atom and also on the number of available solar photons in the vicinity of the atom. The g-value at Mercury is given by

$$g(\lambda) = \frac{\pi F(\lambda)}{R^2} * \frac{\lambda^2}{c} * \frac{\pi * e^2}{mc} * f$$
$$F(\lambda) = \gamma * F_{cont} \qquad (1.6)$$

where $F(\lambda)$ is the solar flux at 1 AU, R^2 is the distance from the sun to Mercury in AU, λ is the centroid wavelength of the line after accounting for any Doppler shifting effects, c is the speed of light, e is the charge of an electron, m is the mass of an electron, f is the oscillator strength, γ is the fraction of the solar continuum "seen" by the atom after accounting for any Doppler shifting effects, and F_{cont} is the solar continuum near the spectral line. The term $\frac{\lambda^2}{c}$ converts flux/wavelength to flux/Hz

and the term $\frac{\pi * e^2}{mc}$ is the integrated scattering cross section for a classically driven harmonic oscillator with units $cm^2 Hz$. The classical scattering cross section arises from treating the electron as a harmonically bound particle (Rybicki and Lightman).

Figure 1.6 is a high resolution spectrum in the vicinity of the sodium D lines that shows the Fraunhofer absorption lines. The lines are formed because of the presence of sodium in the solar photosphere. In the case of a sodium atom in the Mercurian exosphere that has no radial component of velocity with respect to the Sun, the atom will "see" solar photons at the minima of each Fraunhofer line. If the atom has a radial velocity component with respect to the Sun, the atom will resonate with solar radiation that is Doppler shifted from the minima for each line. The motion of sodium atoms with respect to Mercury covers a wide range of velocities with radial components towards and away from the Sun. These motions result in broadening each spectral line, typically on the order of milli-angstroms. However, as Mercury moves around the Sun, the radial component of the velocity of the planet with respect to the Sun varies; so the exosphere collectively has a radial component of velocity with respect to the Sun due to the motion of the planet. This velocity is responsible for Doppler shifting the broadened spectral lines away from the centroid of the Fraunhofer absorption lines and results in varying fractions of the solar continuum "seen" by the atom.

The solar continuum in the region near the Fraunhofer lines varies inversely with the square of the distance of Mercury from the Sun. Since Mercury is in a highly elliptical orbit by planetary standards, the distance of Mercury from the Sun is 0.307

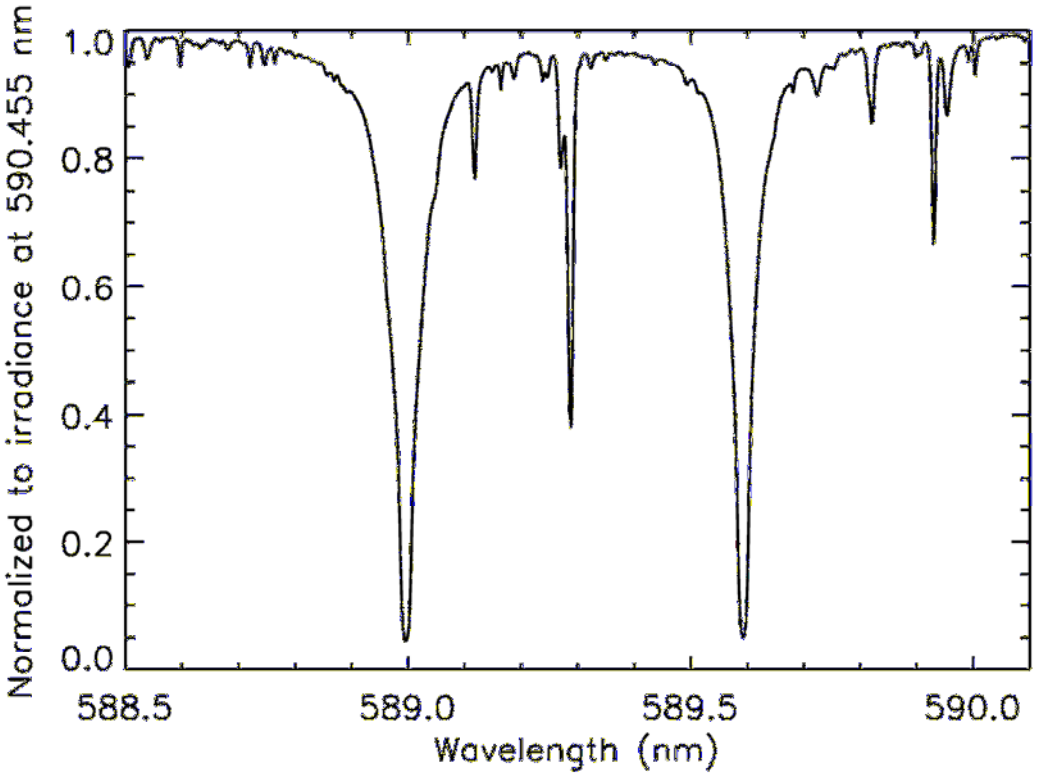

Figure 1.6. High resolution solar spectrum showing the sodium fraunhofer absorption lines. Data from Delbouille and Roland, 1981.

AU at perihelion and 0.467 AU at aphelion, resulting in ~ 57% more solar photons in the continuum at perihelion than at aphelion. Figure 1.7 shows the Mercury-Sun distance, Mercury radial velocity with respect to the Sun, and Doppler shift of the sodium D_2 line, all as a function of planetary true anomaly.

Both the Doppler shifting of the spectral lines away from the Fraunhofer minima and the variation in continuum levels due to the proximity of Mercury from the Sun act collectively to modulate the g-value for sodium at Mercury. Figure 1.8 (top panel) shows the variation of the g-values throughout the Mercury year. The minimum g-values occur at a planetary true anomaly of 180° and the maximum at a true anomaly of 64°, with values for each line ranging from 1.4 photons/second and 2.5 photons/second at a minimum to 23.8 photons/second and 39.7 photons/second at maximum for the D_1 and D_2 lines, respectively.

1.4.4 Radiation pressure

A solar photon that resonantly scatters from a sodium atom imparts momentum to the atom with the momentum having a direction the same as the incident photon. Therefore the acceleration experienced by an atom due to resonant scattering of solar photons is proportional to the g-values. The acceleration experienced by an atom due to solar radiation is given by

$$a_{rad} = \left(\frac{h}{\lambda m} \right) * g \tag{1.7}$$

where h is Planck's constant, λ is the wavelength, m is the mass of a sodium atom, and g is the g-value derived in Section 1.4.3.

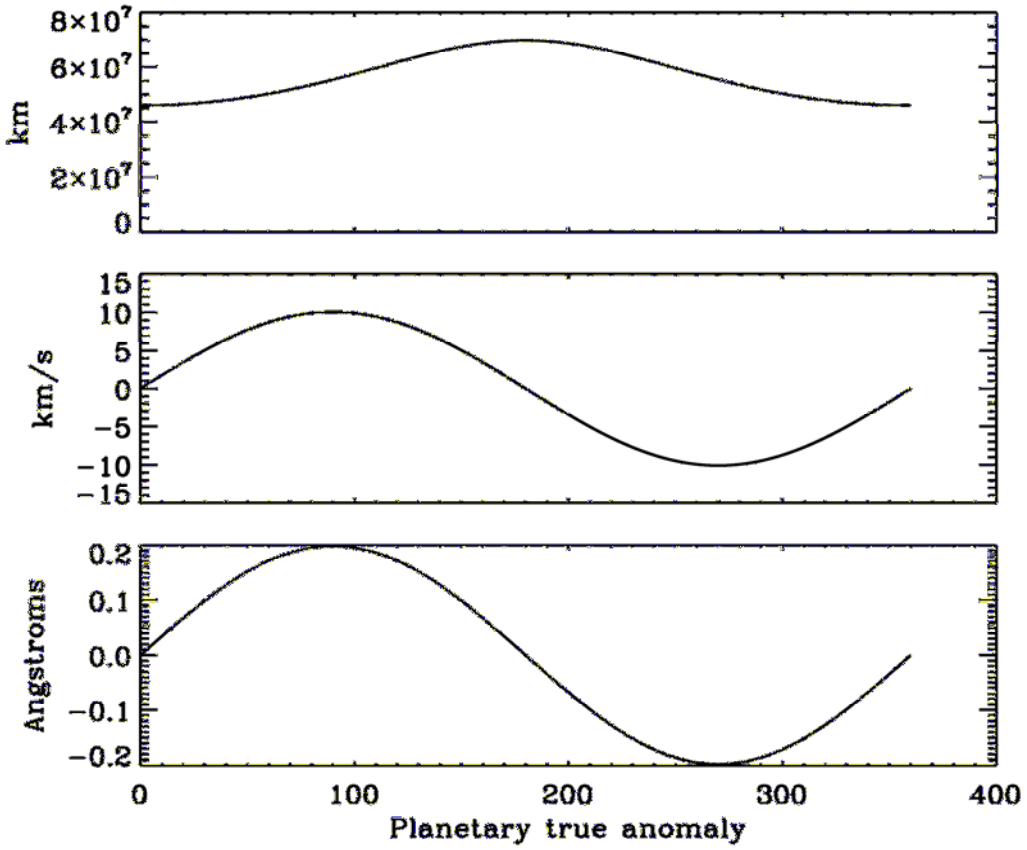

Figure 1.7. Plots of Mercury-Sun distance (top panel), Mercury radial velocity with respect to the Sun (middle panel), and Doppler shift of the sodium D_2 line (bottom panel), all as a function of planetary true anomaly. The Doppler shift of the D_1 line is similar to the Doppler shift of the D_2 line and is indistinguishable for the scale of this plot, so only the D_2 line Doppler shift is shown.

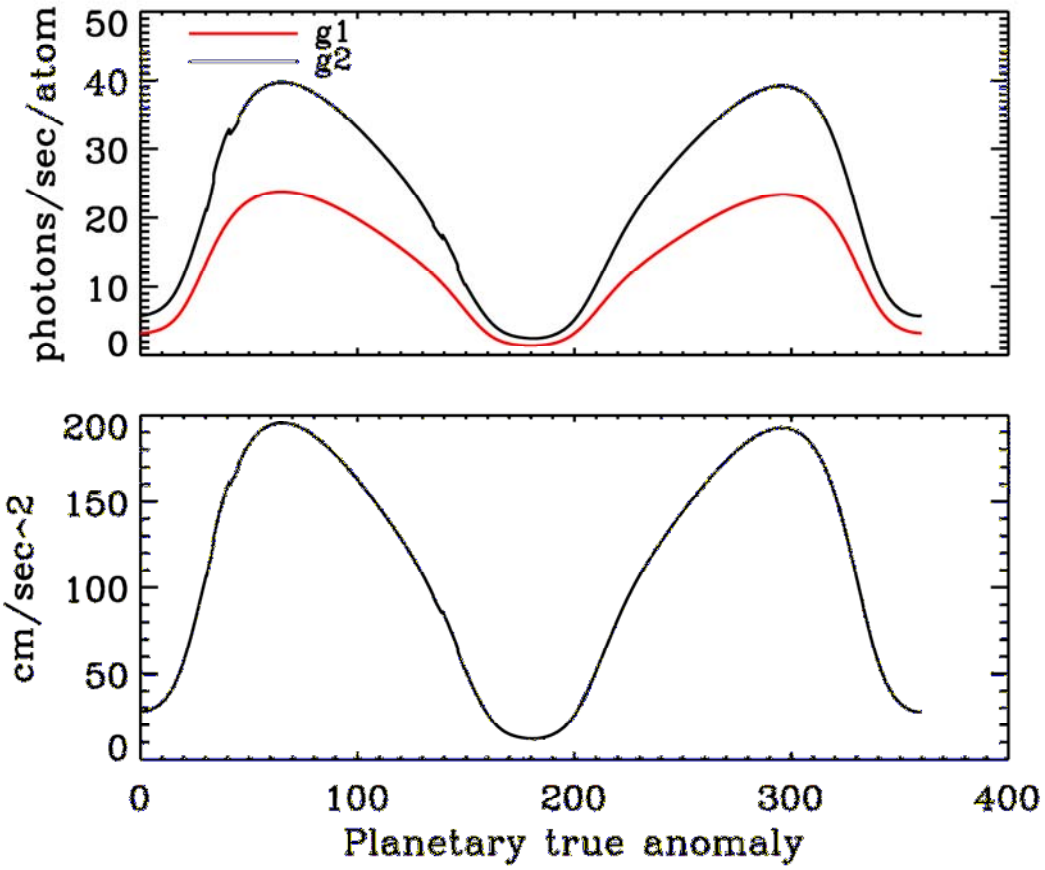

Figure 1.8. G-values (upper panel) of sodium throughout the Mercury year. The peaks result from the combined effects of proximity to the Sun and radial velocity of the planet with respect to the Sun. Acceleration due to radiation pressure for both D lines (lower panel)

The collective effect of radiation pressure on the sodium exosphere is to impart a force that drives the atoms anti-sunward, and is responsible to the observed sodium tail (Potter et. al., 2001). Derivations from Smyth and Marconi (1995) show that the acceleration on a sodium atom at maximum radiation pressure is 54% of surface gravity and at minimum radiation pressure is 3% of surface gravity, with surface gravity ~ 3.8 cm/sec^2. Figure 1.8 (lower panel) shows the variation of radiation pressure with planetary true anomaly.

1.4.5 D_2 to D_1 line ratio

The optical depth of the sodium D1 and D2 lines differ in that the optical depth of the D2 line is ~ 2X the optical depth of the D1 line, with optical depth being the number of absorbing atoms multiplied by the absorption coefficient at each of the D lines along an integrated line of sight. As long as the column abundance is small enough so that the optical depth of both lines may be considered optically thin, i.e., the optical depth of each line is < 1, the ratio of the radiance of the D2 line to the D1 line is a constant and is given by the ratio of the respective g-values. This is because the radiance of each line is linearly proportional to the g-value multiplied by the column abundance; so the radiance of each line increases by the same factor for increasing column abundance. However, as the column abundance increases to the point that the lines become optically thick, i.e., the optical depth is > 1, there is no longer a linear relationship between the increase in column abundance and the radiance. It is in this non-linear regime that the ratio of the D2 line to the D1 line may be a measure of the column abundance. Figure 1.9 serves to illustrate this effect

for a planetary true anomaly of ~ 6 degrees. In the linear regime the D2 radiance is consistently higher than the D1 radiance by the same amount, thus the D2/D1 ratio is independent of the column abundance. However, in the non-linear region, the D2/D1 ratio varies with column abundance, and measuring it uniquely determines the column density. It should be noted that the D2/D1 ratio also varies with planetary true anomaly. The optical depth for the D1 line where the gas is sufficiently hot to ignore hyperfine structure is given by Brown and Yung, 1976, as

$$\tau_{D1} = 1.1*10^{-10} T^{-\frac{1}{2}} N \tag{1.8}$$

where T is the temperature and N is the column density in Na/cm^{-2}. This implies that for a temperature of 1000 K, $\tau_{D1} = 1$ for $N = 2.87*10^{11}$ Na/cm^{-2}. Since the optical depth of the D2 line is ~ 2X the D1 optical depth, $\tau_{D2} = 1$ for $N = 1.44*10^{11}$ Na/cm^{-2}.

The spectral resolution of the UVVS is such that the sodium doublet may be resolved into both the D1 and D2 lines. The D2/D1 line ratio may be used as a measure for the column abundance. However, Killen (personal communication, 2003) predicts that sodium column abundances at Mercury may be too small to occupy the non-linear regime for most measurements. Therefore this method may only find use for rare occasions when the column abundance is sufficiently large. Alternatively, if column abundances are such that the D lines are optically thin, then the absolute sensitivity of the instrument along with measured radiance from the D lines can be used to determine the abundance.

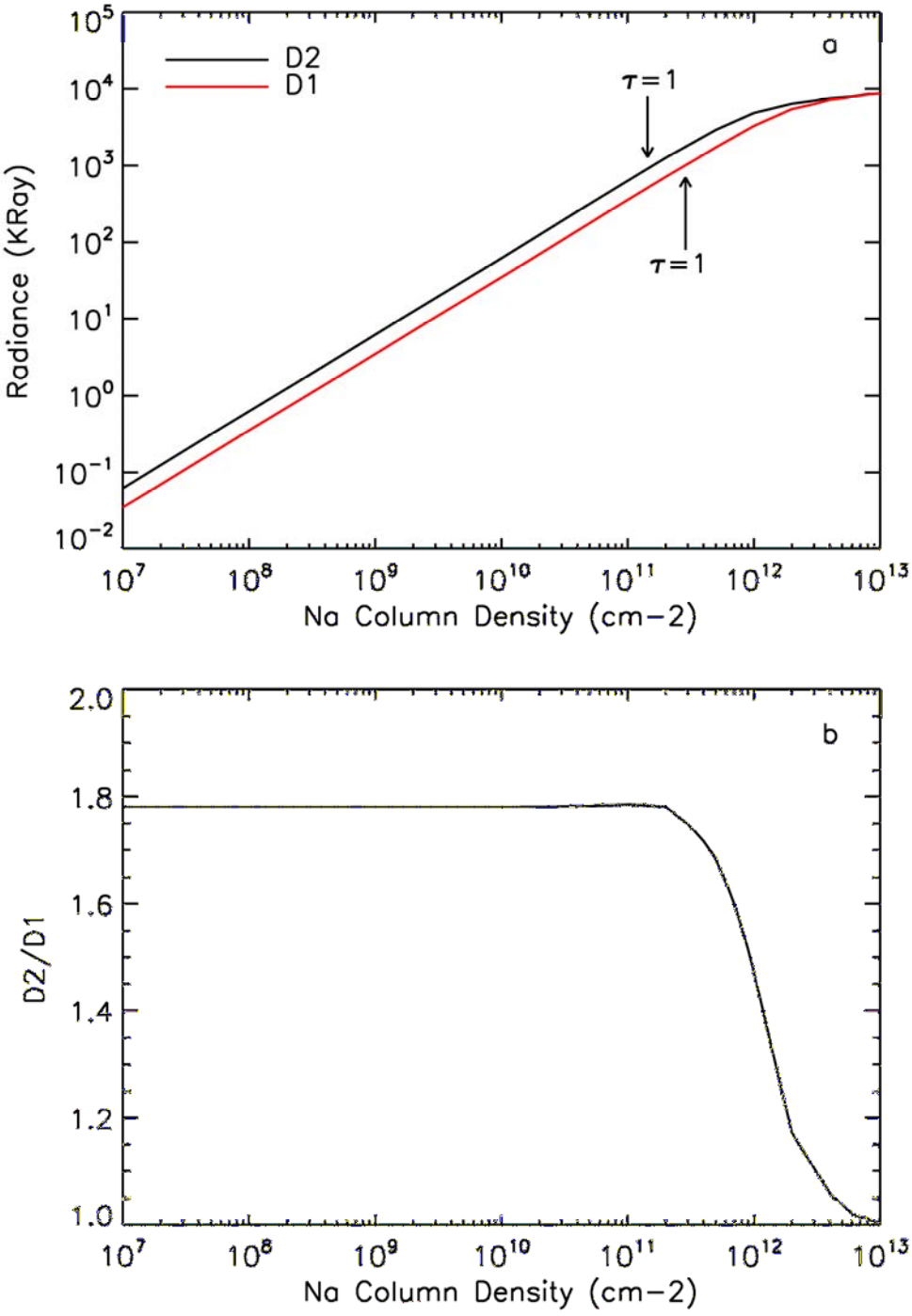

Figure 1.9. Sodium D_1 and D_2 curves of growth (a) and corresponding D_2/D_1 line ratio (b) for a temperature of 1000 K and for a planetary true anomaly of 6°. The column abundances for optical depth equal to unity are shown by the arrows in figure (a) for both of the D lines.

1.5 Observation of Mercury's exosphere by MESSENGER

MASCS will observe the Mercurian exosphere by taking spectra of resonantly scattered solar radiation from exospheric species. Furthermore, exospheric observations will be made with the boresight of the instrument pointed tangentially across the limb of the exosphere, as opposed to pointing towards the surface, Figure 1.10.

1.5.1 Tangentially integrated column abundances

Chamberlain, 1978, derives the tangentially integrated column abundance for an isotropic, barometric exosphere, which is given by

$$N_{\tan}(r) = \int_{-\infty}^{+\infty} N(r')ds \tag{1.9}$$

where r' is the distance from planet center up to some point along the tangential line representing an observation and r is the distance from planet center to the closest approach of the tangential observation vector. Chamberlain's solution is

$$N_{\tan}(r) \approx N(r)(2*\pi*r*H)^{1/2} * (1+\tfrac{3}{8}*H/r+\cdots) \tag{1.10}$$

where H is the scale height, and N(r) is the density at height r from the planet center. This result implies that the height of the closest approach to the surface is used to express tangentially integrated column abundances. This is because the point closest

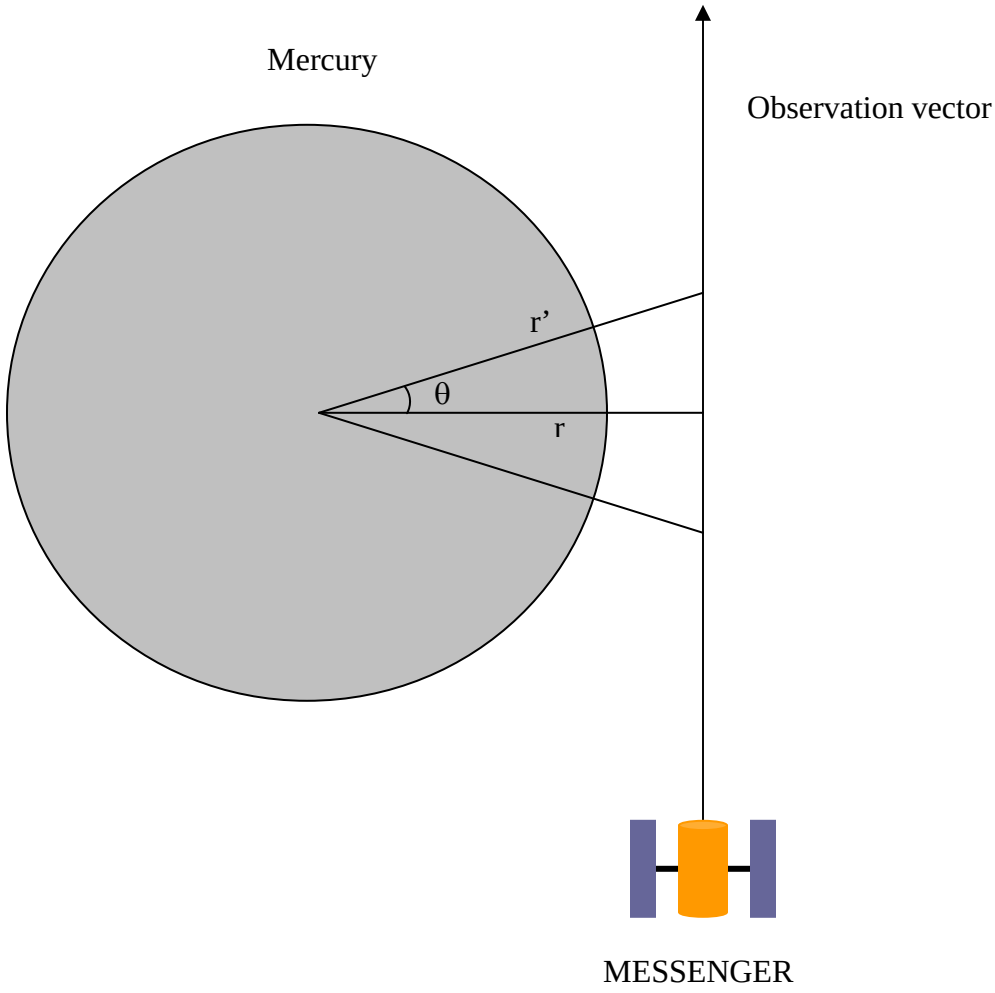

Figure 1.10. Schematic of the geometry associated with MESSENGER making a limb observation.

to the surface is also where the atmospheric density is greatest and thus is the largest value contributing to the integrated density along the tangential line of sight.

Equation 1.9 has been numerically solved for angular values less than $\pi/2$ and greater than $-\pi/2$ in order to determine over what angles the greatest contribution to the tangential column abundance arises from. For scale heights of sodium at Mercury equal to 50 km and 250 km, ~ 90% of the tangentially integrated column abundance falls within θ = +/- 15° and θ = +/- 30°, respectively. Therefore, in this thesis the tangent height will be referenced extensively to mean the point of closest approach for an observation line of sight, but integrated column abundances includes contributions from the exosphere along the line of sight within θ = +/- 30°.

1.5.2 Attitude control capabilities

In anticipation of exospheric profile observations, guidance and control at APL developed generic pointing strategies termed radial scans (Figure 1.11). The concept is that the spacecraft points above the limb and thus establishes a radial vector extending from the planet center out to the tangent point. The spacecraft then slews in order to make observations somewhere along this radial vector, such that the vector extending from the instrument in the direction of the boresight always intersects the radial vector at some height above the surface. This height does not have to remain fixed, but may move up and down the radial vector. There are constraints as to how much the spacecraft can slew both in terms of slew rate and solar illumination keep-out pointing constraints (Section 1.3). This capability of MESSENGER will be used extensively for observation strategies to map the exosphere of Mercury (Chapter 5).

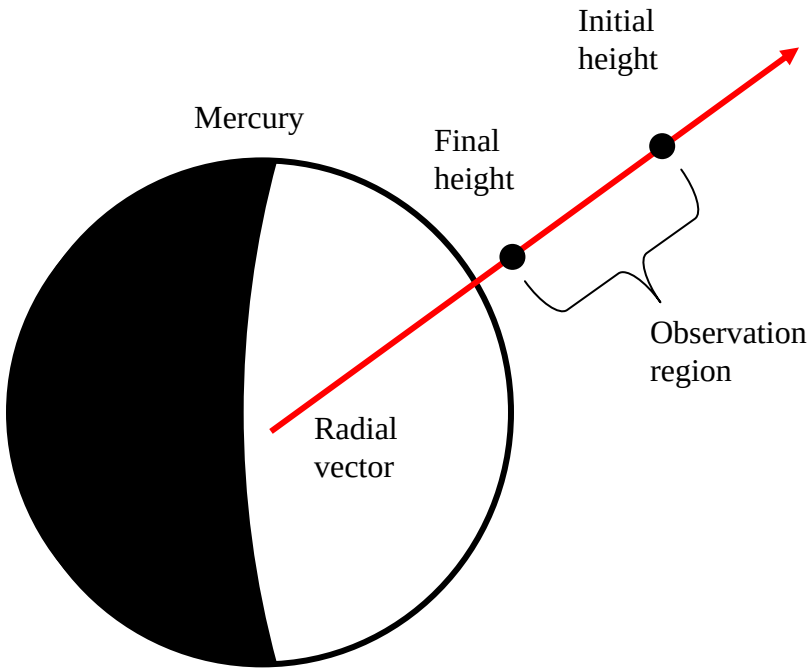

Figure 1.11. View from the spacecraft along the boresight of the instrument for observations along a radial vector. The vector is established from the initial observation that extends from the center of the planet to the initial height above the limb. Successive observations follow along this vector down towards the surface of the planet.

1.6 Summary

This chapter has described the background material needed to support this thesis. An outline of the thesis has been given with a list of scientific questions that are addressed in developing observation strategies. A general overview of Mercury has been given. Since it is beyond the scope of this thesis to write a comprehensive review about Mercury, emphasis has been placed on the physical processes that most directly affect observations of the exosphere. References are given for more in-depth reviews of Mercury. An overview of the MESSENER mission has been given; with brief descriptions of each instrument as well as spacecraft orbit and pointing capabilities. An overview of the physics associated with the observation of sodium in the exosphere is given; which includes a description of the Rayleigh, g-values, radiation pressure, and line ratios. A general description of making exospheric observations was given. This included the nature of limb observations and how the tangentially integrated column abundance is related to the zenith column abundance. Furthermore, a description was given concerning spacecraft attitude control capabilities that will be used to make exospheric observations.

Chapter 2

MASCS UVVS Pre-launch and Post-launch Calibration

2.1 Introduction

2.1.1 Overview of instrument calibration

The goal of the calibration experiments is to characterize the performance of the instrument in preparation for data reduction of observational data. The uncertainty in the science data product arises from both uncertainties in observations as well as uncertainties in instrument performance. The instrument must be shown to perform within acceptable limits to achieve the science goals of the mission, see Chapter 1. In light of the importance of characterizing instrument performance, the instrument has been subjected to a rigorous calibration campaign.

Calibrations have consisted of both pre-launch and post-launch measurements. Pre-launch calibrations were performed in the black lab, clean room, and MOBI facility, all at the Laboratory for Atmospheric and Space Physics (LASP) at the University of Colorado, as well as in a large clean room at the Johns Hopkins Applied Physics Laboratory (JHU/APL). Pre-launch calibration experiments are given in Table 2.1.

Post-launch calibrations have consisted of periodic stellar calibrations and lunar observations during the Earth flyby in August, 2004. Calibration products from

Parameter	Value	Accuracy	Ground Measurement
Telescope Boresight		0.025°	0.025°
Detector Dark Counts	0.1-300 c/second		
Wavelength Scale	115-600 nm	1 nm	0.1 nm
Spectrometer PSF	~1nm FWHM	10 %	5 %
Spectrometer FOV	0.05° X 01.0°	10 %	5 %
Spectrometer Scatter	10^{-5} @ 50 NM	20 %	10 %
Spectrometer Stray light			
Polarization	< 50 %	5 %	2 %
Telescope Off-axis response	10^{-6} at 5°	10 %	5 %
Window Transmission			
Absolute Sensitivity	100-500 c/sec/kRay	15-20%	10-15%
PMT Linearity	90 % @ 50 kHz	10 %	5 %

Table 2.1. List of pre-launch calibration experiments.

stellar observations include instrument pointing determination and refinement, sensitivity, and detector dark counts. Calibration products from the lunar flyby include detector dark counts and off-axis light response.

2.1.2 Calibration facilities

The pre-flight calibrations were performed in either the black lab, MOBI vacuum facility, or the clean room. The black lab calibration facility was used to perform the majority of non-vacuum and non-thermal calibrations on the MASCS ultraviolet-visible spectrometer (UVVS). The facility consisted of a Newport 4 X 14 feet vibration dampened optical table sitting in a lab with blackened walls, floor, and ceiling in order to minimize laboratory stray light. On the table was an optical

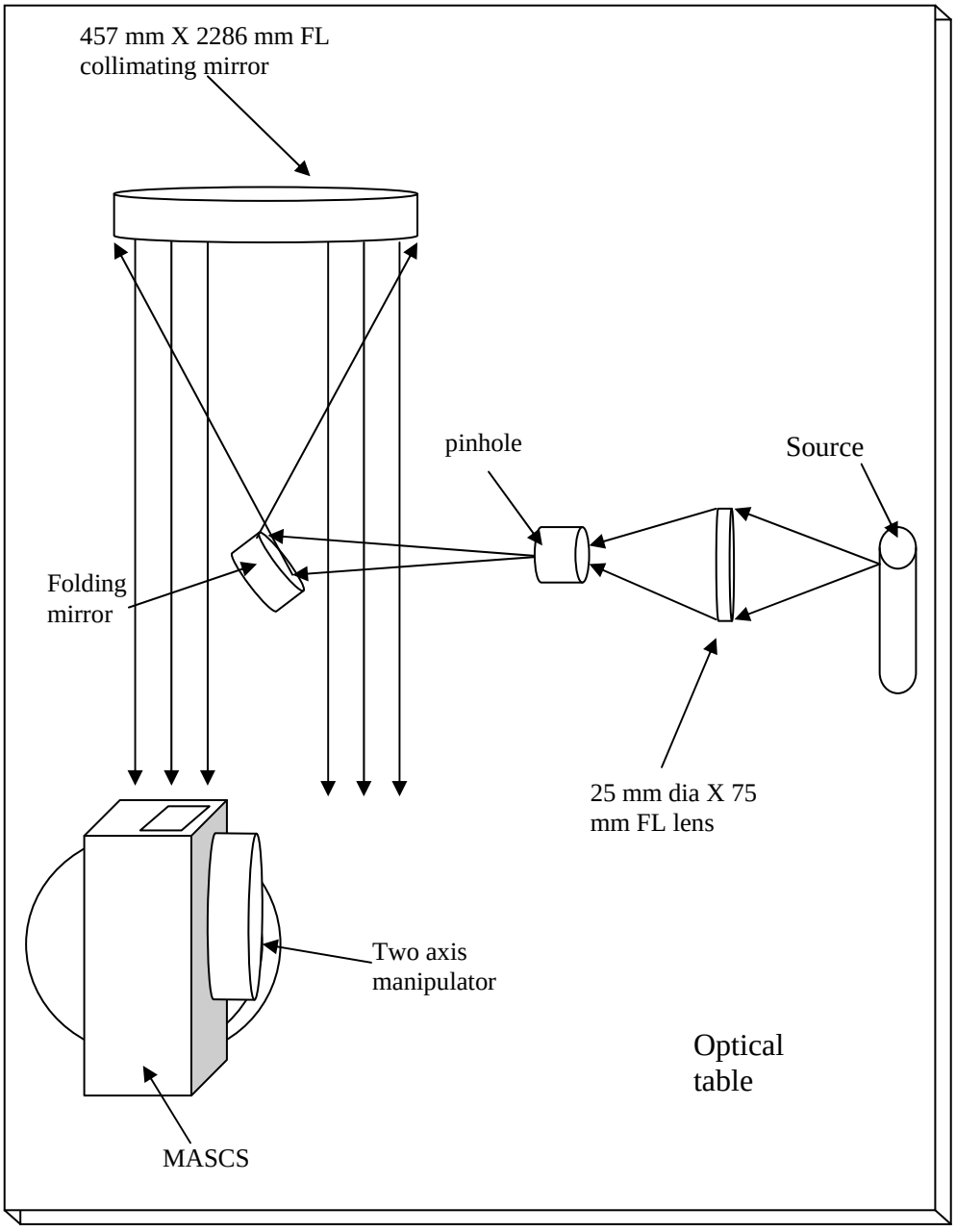

Figure 2.1. Black lab UVVS calibration optical setup

arrangement that was common to all of the black lab UVVS calibration experiments with minor variations (Figure 2.1). The optical setup consisted of a lamp source that was situated on a linear positioning stage with two degrees of freedom. The lamp source could be changed at will from a range of available pen-ray lamps to a deuterium lamp. Light from the lamp

passed through a 25 mm diameter X 75 mm FL silica lens that was also attached to a translation stage; and with proper positioning of the lamp and lens, an optical configuration with an F/# = 5 was created. The light was imaged from the lens down to a pinhole. The pinhole consisted of a pinhole positioning mount in which any of a range of pinholes could be inserted. The pinhole was positioned at the focal point of a 457 mm diameter X 2286 mm FL (F/# = 5) spherical concave collimating mirror via a 45 degree oriented folding mirror. The collimating mirror was completely filled yielding a beam of collimated light 457 mm in diameter. The MASCS instrument was positioned on a 2-rotation axis manipulator consisting of two Newport rotation stages fastened together. The centers of rotation of the manipulator were placed at the telescope limiting aperture and the telescope was placed in the path of collimated light. This allowed for the aperture of the telescope to be completely filled.

The MOBI UVVS calibration facility was used to perform all vacuum and thermal calibrations on the MASCS ultraviolet-visible spectrometer (UVVS). The vacuum requirement is needed to reach wavelengths of light that would be absorbed by air as well as allow thermal cycling without concern for condensation. The thermal tests are needed to characterize the performance of the instrument given the relatively large temperature swings that will be encountered in flight. The facility, shown in Figure

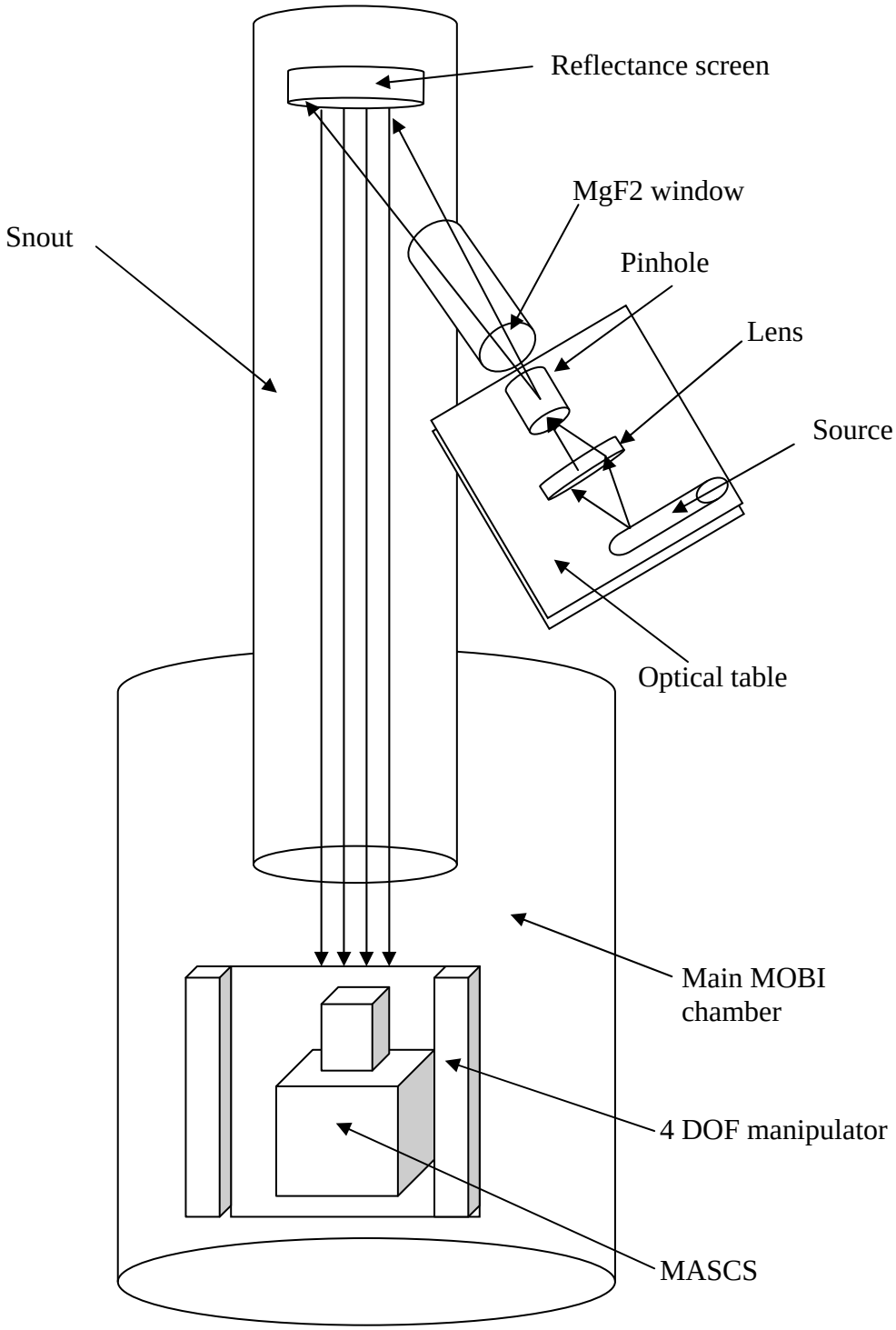

Figure 2.2. MOBY UVVS Calibration setup

2.2, consisted of a large vacuum chamber with a long snout extruding from one end that contained an off-axis parabolic mirror at the end of the snout. A smaller snout that angled off to the side allowed a lamp source external to the tank to irradiate the parabolic mirror and produce a collimated beam of light in the main chamber of the MOBI tank. The lamp source optical arrangement consisted of two configurations. One consisted of a small optical table with an optical configuration that consisted of a lamp source that could be changed at will from a range of available pen-ray lamps to a deuterium lamp. The light from the lamp was imaged down to a pinhole via a silica lens. The pinhole consisted of a pinhole positioning mount in which any of a range of pinholes could be inserted. Light from the pinhole traveled to the white reflectance screen and was dispersed to give a flat-field. Behind the reflectance screen was a 90" focal length off-axis parabolic mirror that was used for the radiometric calibrations. The instrument was pointed at the screen with both the field of view and aperture is filled. The second optical configuration consisted of using a monochromator that was designed to mount onto the outside of the smaller snout. The monochromator consisted of an internal lamp source and a diffraction grating whose angle could be selected to produce a narrow spectral band of light. There was also a pinhole internal to the monochromator that was positioned so that the emerging light covered the reflectance screen and allowed for the same instrument viewing conditions as with the previous lamp source. For either of the optical arrangements, the instrument was mounted on a 4 degree of freedom manipulator in the path of the collimated light. The 4 degrees of freedom consisted of translation from side to side, vertical translation, rotation in the elevation direction, and rotation in the right ascension

direction. The centers of rotation were placed at the telescope aperture stop. Beside the instrument and in line with the aperture stop of the telescope were NIST calibrated detectors for radiometric measurements. The translation of the manipulator was enough to allow the NIST detectors to be moved into the same spatial position as the instrument telescope.

Clean rooms at LASP and JHU/APL were used with a class rating of 10,000 that contained an optical table along with other optical hardware. There was not a fixed setup as for the black lab and MOBI, but instead optical testing equipment and hardware were positioned as needed. The clean rooms provided a low particulate environment in order to minimize debris from contaminating the instrument.

2.1.3 Stellar observation summary

Stellar observations of low-variability stars allows for tracking instrument degradation throughout the mission by re-calibrating the radiometric sensitivity. This relies on comparing the detected signal to known fluxes from the star. During the course of the stellar calibrations performed to date, many sources of stellar fluxes have been used and compared, including data from SOURCE/SOLSTICE, IUE, STIS, ground based telescopes, and stellar flux models. Typically, for a single stellar observation, the sensitivity is derived using multiple reference datasets in order to compare results.

Instrument boresight was also determined from stellar calibrations. The spacecraft was moved in a rastering motion that allows for the instrument field of view to pass over the star several times. The pointing of the spacecraft was referenced to the +Z

axis with grating scans timed such that 2-3 complete grating scans occur while the image of the star was in the entrance slit. The centroid of the stellar image was located within the slit along with interpolated spacecraft orientation. In this manner the boresight of the spacecraft with respect to the spacecraft +Z axis was found.

Table 2.2 shows the stellar observations through January, 2007. Stars are selected based on low-variability, i.e., fluxes that vary by much less than 1 % over thousands of years (Mihalas, 1978) and suitable signal for spectral coverage. Thus, for the 7 year flight to Mercury, the flux from the stars may be considered constant. Typically type O and A stars are chosen since the spectral range of MASCS UVVS is from 115 nm to 600 nm and the spectra of theses stars peak within this spectral region.

2.2 Instrument description

The Mercury Atmospheric and Surface Composition Spectrometer (MASCS) contains two channels, a Ultra-Violet Visible Spectrometer (UVVS) and a Visible Infra-Red Spectrograph (VIRS). The UVVS side of MASCS is shown in Figure 2.3. The UVVS is an Ebert-Fastie scanning grating monochrometer that covers a spectral range from 115 to 600 nm. The spectral range is divided into 3 channels (visible, mid-uv, and far-uv) with a separate photo-multiplier tube serving as a detector for each channel (summarized in Table 2.3). Light is first collected by an F/5 cassagrain telescope that is shared between the UVVS and VIRS. The light is focused to the entrance slit of the UVVS that is 4.54 mm X 0.178 mm in size. The focal length of the telescope is 257.6 mm, and in conjunction with the size of the entrance slit, gives

Star	Name	Date	S/C flip	Detector	Comments
Alpha Leo	Regulus	12/8/2004	Flipped	MUV FUV	Contamination cover was closed; got stray solar spectrum
Alpha Lyra	Vega	4/19/2005	Not-flipped	MUV FUV	Contamination cover was closed
Alpha Gru	Alnair	6/14/2005		MUV FUV	
Alpha Lyra	Vega	10/4/2005	Not-flipped	MUV FUV	Contamination cover was open
Alpha Psa	Formahault	2/23/2006		VIS MUV FUV	Missed the star due to pointing error
Alpha Canis Majoris	Sirius	7/11/2006		VIS MUV FUV	Did first successful VIS channel calibration
Alpha Psa	Formahault	8/25/2006		VIS MUV FUV	Very low count rates
Alpha Virgo	Spica	1/09/2007		VIS MUV FUV	
Alpha Canis Majoris	Sirius	3/20/2007		VIS MUV FUV	Did first successful boresight along the length of both slits

Table 2.2. Stellar observation summary

Star	**Spectral Class**	**Visual Magnitude**
Alpha Leo	B7V	+ 1.35
Alpha Lyra	A0V	+ 0.04
Alpha Gru	B7IV	+ 1.74
Alpha Lyra	A0V	+ 0.04
Alpha Psa	A3V	+ 1.19
Alpha Canis Majoris	A1V	- 1.46
Alpha Psa	A3V	+ 1.19
Alpha Virgo	B1V	+ 0.19
Alpha Canis Majoris	A1V	- 1.46

Table2.2(continued)

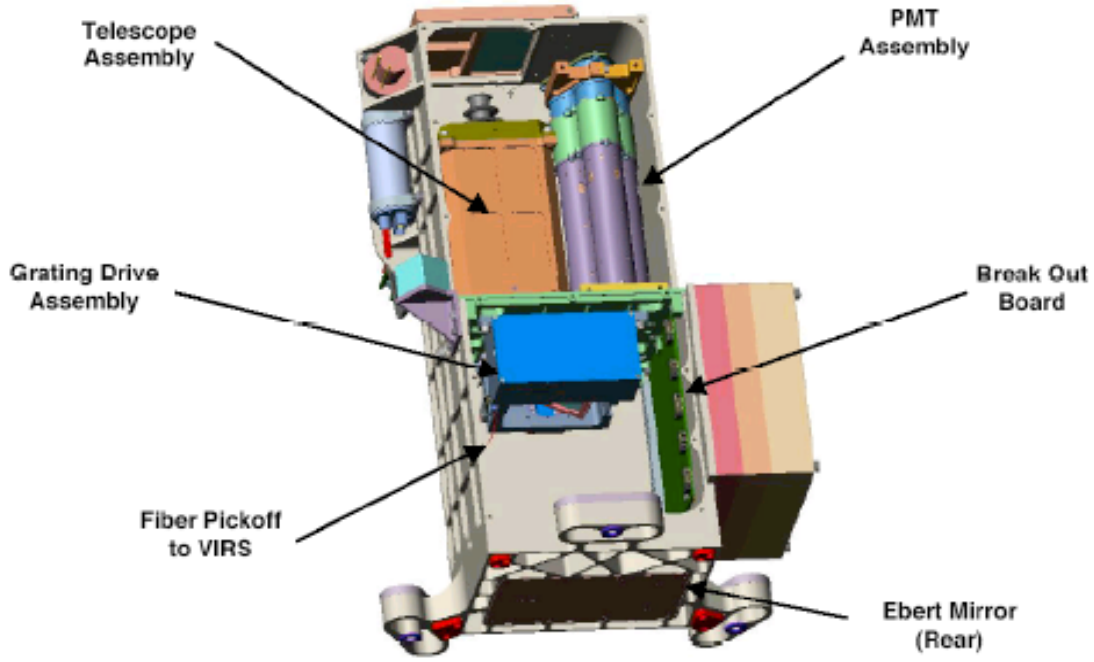

Figure 2.3. UVVS side of MASCS showing the telescope, internal spectrometer optics, and pmt assembly.

Channel	**Spectral range (NM)**	**Grating scan angle (degrees)**	**Photo-multiplier tube photo-cathode/ window material**
Far U.V.	115 – 192.01	13.48 – 25.32	CsI/MgF_2
Mid U.V.	160 – 320	10.61 – 22.39	CsTe/Fused Silica
Visible	280 – 600	21.55 – 48.5	Bialkali/Fused Silica

Table 2.3. Characteristics of the 3 UVVS spectral channels

a field of view of 1.01 X 0.040 degrees. The focal length of the spectrometer is 125 mm. The light emerging from the entrance slit strikes one side of a concave Ebert mirror, which is then reflected towards a scanning reflection grating. The grating has a ruling of 2400 lines/mm and serves to spatially disperse the light according to wavelength. The spectrum of light is directed back to the other side of the Ebert mirror where it gets reflected once more towards the exit slit plane of the instrument. There are three exit slits, one for each channel. For a given channel, the scanning of the grating directs light of varying wavelength at the output of the respective exit slit and into the detector. Note that because of the finite size of the exit slits, a spectral interval of light passes through the exit slit for a given position of the grating; so there is some spread in the spectral output. The three channels are divided according to wavelength and are listed below along with grating scan angles and the respective photo-multiplier tubes for each channel. The grating scan angle is measured with respect to the optical axis of the spectrometer.

The UVVS contains a slit mask mechanism that may be used to reduce the amount of light that enters the spectrometer. This is achieved by a mask covering all but a small square of the center of the entrance slit; which results in a field of view of approximately 0.05° X 0.040°. This is used to allow the UVVS to view the surface of the planet (surface mode), which would otherwise saturate the instrument. The fully open slit is used for limb viewing of the atmosphere (atmospheric mode) because the radiation that enters the instrument from the atmosphere is much less than that reflected from the surface. Based on the measurement requirements given in the

introduction, a list of the design performance criteria is given by McClintock and Lankton, (2006).

2.3 Telescope boresight

The pre-launch telescope boresight was measured by using the 2 axis manipulator to position the image of a star source from the alignment mirror back onto itself. The point source consisted of a halogen lamp illuminating a pinhole that was at the focus of the collimator. The star source reflected off of the alignment cube and the manipulator was oriented such that the star image was visually placed on top of the pinhole. The star source was then scanned across the entrance slit in both the spectral and spatial directions. In the spatial direction both the atmospheric and surface slits were measured.

The telescope boresight was determined before and after shake. The experiment consisted of determining the centroid of the entrance slit in both atmospheric and surface mode with respect to the alignment cube. The values are given in Table 2.4. Note that +/- values are with respect to rotation about the respective spacecraft axis following the right-hand rule.

Post-launch stellar calibrations have allowed for the determination of the atmospheric and surface slit boresights with respect to the spacecraft body frame. An example of the raster scan for the α-CMa, 7/11/2006, observation is shown in Figure 2.4. For this example, the spacecraft rotated about the X and Y axes to cause the instrument field of view to cross the star in the spectral direction while working its way up along the spatial direction of the field of view. This type of raster scan is

Slit and direction	Pre-Shake	Post-Shake
Atmospheric Slit (Spectral Direction) Rotation about y axis	+0.076	+0.098
Atmospheric Slit (Spatial Direction) Rotation about x axis	+0.026	-0.021
Surface Slit (Spatial Direction) Rotation about x axis	+0.016	-0.031

Table 2.4. Relation of UVVS atmospheric and surface slit boresights to the alignment cube.

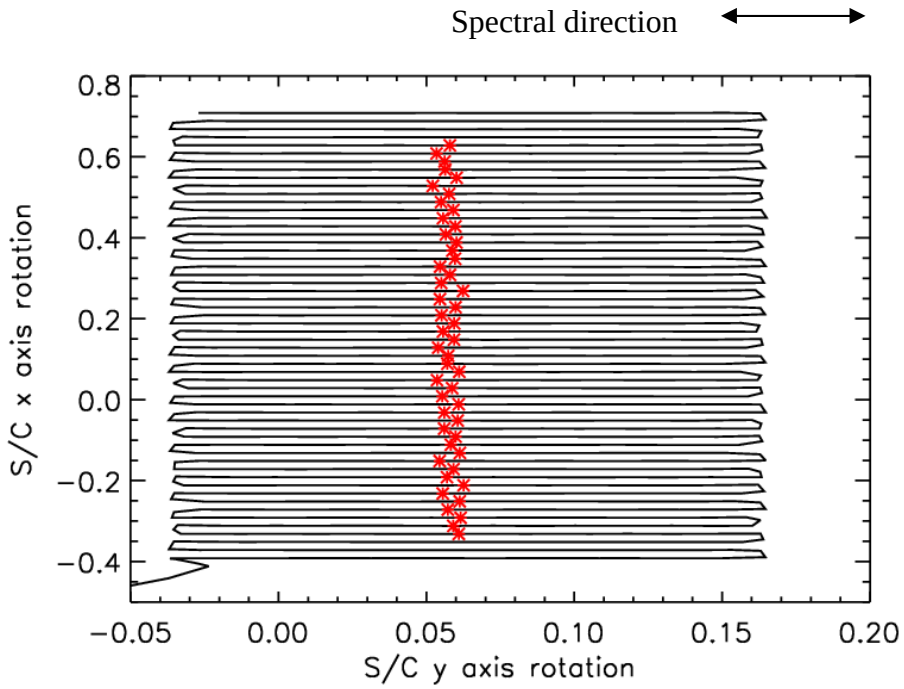

Figure 2.4. Raster scan for α-CMa using the atmospheric slit. The red stars are the locations of the image of the star while near the center of the slit in the spectral direction.

typically better suited for determining the boresight in the spectral direction. Alternatively, the raster scan for other stellar calibrations has crossed the spatial direction of the slit while working its way along the spectral direction; which is better suited for determining the boresight in the spatial direction. For either raster scan, the grating is in ziz-zag mode with an integration time that allows for multiple grating scans while the image of the star is in the field of view for a single sweep. The red stars shown in Figure 2.4 represent the centroid of the stellar image in the spectral direction for each sweep.

The direction cosines of the star in the spacecraft body frame are determined by transforming the coordinates of the star in RA and DEC to the spacecraft body frame by using quaternions that are returned in 1 second increments. As the field of view of the UVVS sweeps across the star, the direction cosines of the star in the spacecraft body frame are interpolated to correspond with the peaks in signal output. For multiple peaks that occur along the length of the slit, the mean of the direction cosines are determined to locate the centroid of the slit. The boresight lies closest to the spacecraft + Z axis, thus the direction cosines of the boresight are also expressed by $\tan^{-1}\left(\frac{x}{z}\right)$ and $\tan^{-1}\left(\frac{y}{z}\right)$ in the XZ and YZ planes, respectively.

Table 2.5 gives X-Z and Y-Z plane angles as well as direction cosines for the atmospheric and surface slit boresights determined from stellar calibrations. The surface slit has only been used for stellar calibrations since July, 2006. The X-Z plane and Y-Z plane values are only determined for raster scans in the spectral and

spatial directions, respectively. Note that the center of the surface slit is displaced from the center of the atmospheric slit in the Y-Z plane, with the center of the surface slit 0.01° closer to the origin. The data of Table 2.5 show a small displacement of the surface slit from the atmospheric slit in the X-Z plane; however from the knowledge of the mechanical nature of the surface slit, there should be no displacement in this direction. The discrepancy is most likely due to low rastering resolution, typically 0.02° along the length of the 0.05 degree surface slit, which results in only two data points with the stellar image fully in the slit. With increased resolution from future raster scans, the displacement of the surface slit from the atmospheric slit in both planes will probably be slightly different.

Figure 2.5 shows the location of the slits looking out from the spacecraft along the +Z axis. Note that the center of the surface slit is 0.01° closer to the origin of the spacecraft coordinate system in the Y-Z plane than the atmospheric slit center. The slit centers in the Y-Z plane were determined by taking the mean of the values in Table 2.5, while the centers for both slits in the X-Z plane were determined by taking the mean of the values for the atmospheric slit in the Y-Z plane.

The raster scan down the length of the slit gave an opportunity to assess the rotation of the instrument with respect to the spacecraft X and Y axes. Figure 2.6 shows 4 scans made down the length of the slit. The image of the star remained in the field of view for both of the two middle rows. The raster rows were 0.01° apart and since the width of the slit is ~ 0.04°, the slit is well aligned with the spacecraft y axis.

Atmospheric slit boresight values

Star	Date	Raster direction	Boresight		Direction cosines		
			x-z plane	y-z plane	X	Y	Z
α-lyre	10/4/2005	Spectral	0.061922470	----------	0.0010807326	----------	0.99998199
α-CMa	7/11/2006	Spectral	0.057793958	----------	0.0010086792	----------	0.99998394
α-Psa	8/25/2006	Spectral	0.056047345	----------	0.00097819550	----------	0.99998399
α-Virgo	1/09/2007	Spectral	0.058651440	----------	0.0010236447	----------	0.99998389
α-CMa	3/20/2007	spatial	----------	0.14271483	----------	0.0024908088	0.99998428

Surface slit boresight values

Star	Date	Raster direction	Boresight		Direction cosines		
			x-z plane	y-z plane	X	Y	Z
α-CMa	7/11/2006	Spectral	0.052878021	----------	0.00092289291	----------	0.99999681
α-Psa	8/25/2006	Spectral	0.051770867	----------	0.00090356924	----------	0.99999655
α-Virgo	1/09/2007	Spectral	0.055590162	----------	0.00097022857	----------	0.99999679
α-CMa	3/20/2007	Spatial	----------	0.13418560	----------	0.0023419775	0.99999684

Table 2.5. Boresight results from stellar calibrations.

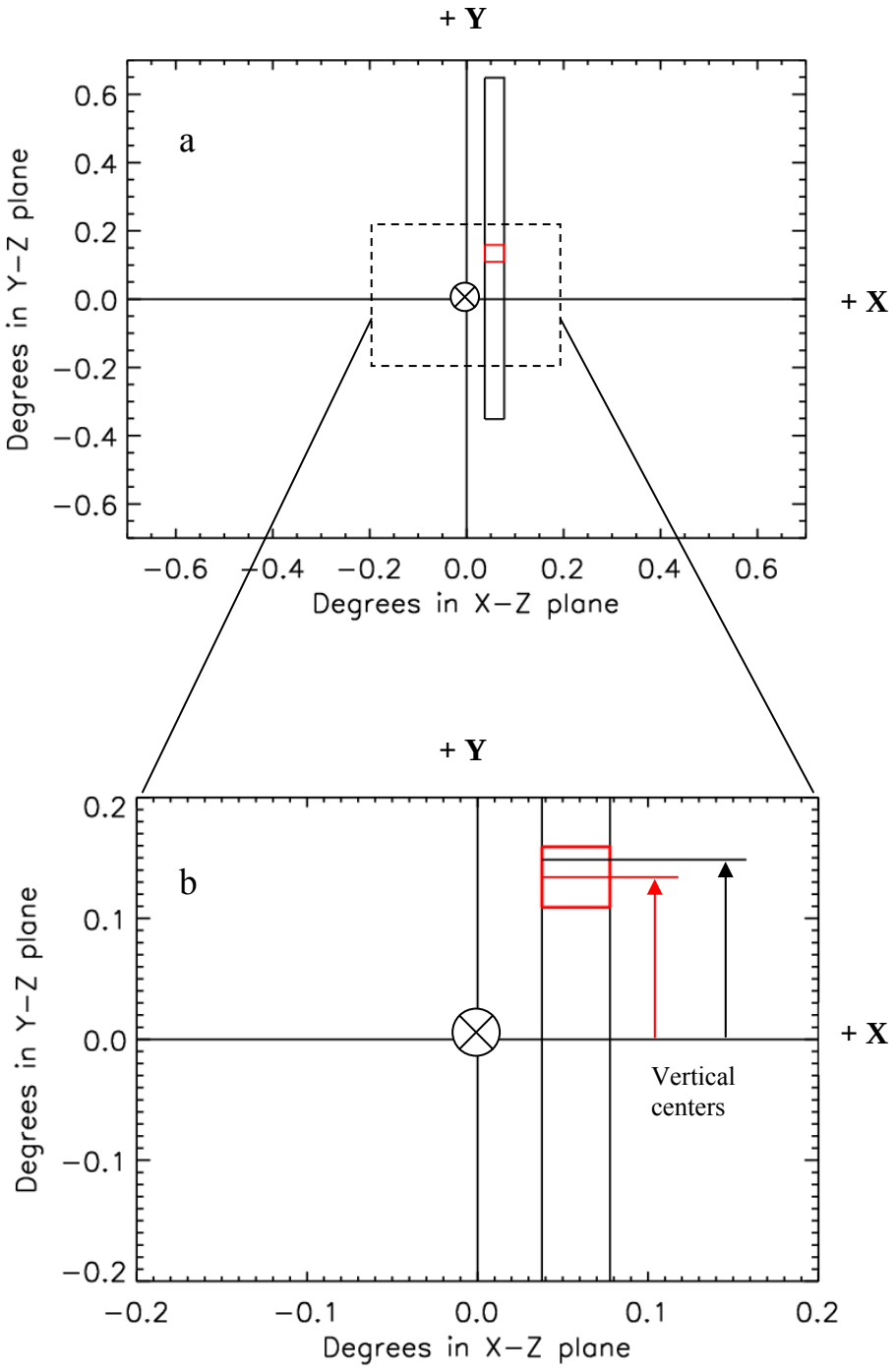

Figure 2.5. Plot "a" shows the location of the atmospheric slit in black and the surface slit in red with respect to the spacecraft X and Y axes, drawn to scale. The magnified plot, "b", shows the vertical center of each slit with respect to the spacecraft Y axis. The slit centers are the mean of the values given in Table 2.5.

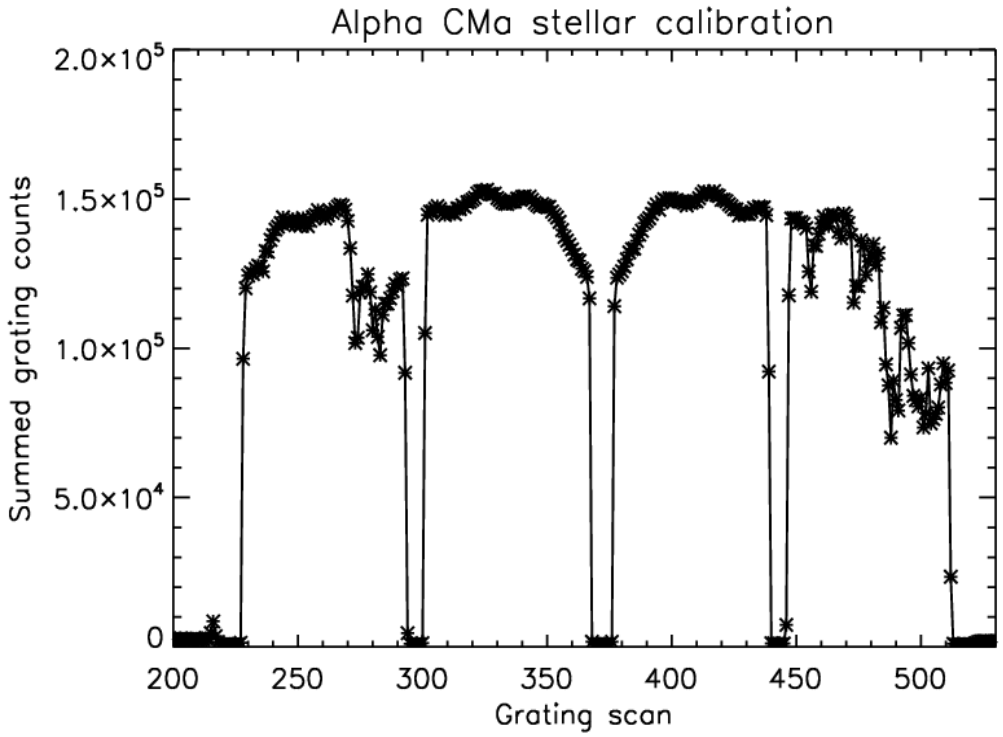

Figure 2.6. Sum of individual grating scans for the α CMa, 3/20/2007 stellar observation. The two middle rows show that the stellar image remained in the slit over the entire slit length

2.4 Dark counts

The photomultiplier detectors are subject to thermionic emission, which is a function of the photocathode work function and temperature. Studies of photomultiplier detectors have indicated that the thermionic emission varies exponentially with temperature (Hamamatsu Photonics, 1994). A series of dark scans were performed in vacuum over a range of temperatures from approximately -23° to +45° C. The inside of the vacuum chamber was kept dark while the grating was scanned with both the VIS and MUV channels turned on. During each grating scan, the temperature of each channel was sampled periodically and recorded in the data housekeeping packet. The time for a complete grating scan was much less than the variation in temperature of the vacuum chamber; so for a given scan, the mean of the recorded temperatures was calculated as the temperature of each channel. The mean of the counts/second was calculated for each channel and for each scan, giving the thermionic emission as a function of temperature. The plot of this data is shown in Figure 2.7. The FUV channel showed negligible dark counts and is therefore not included.

IDL was used to fit an exponential function to each set of data and the results are also shown in the figure as the solid lines. The exponential functions for both the VIS and MUV channels are given by

$$\frac{\text{Counts}}{\text{second}}(\text{VIS}) = 0.9580 * \exp^{0.1294*T} + 0.8853$$
$$\frac{\text{Counts}}{\text{second}}(\text{MUV}) = 0.01888 * \exp^{0.0778*T} + 0.2263 \qquad (2.1)$$

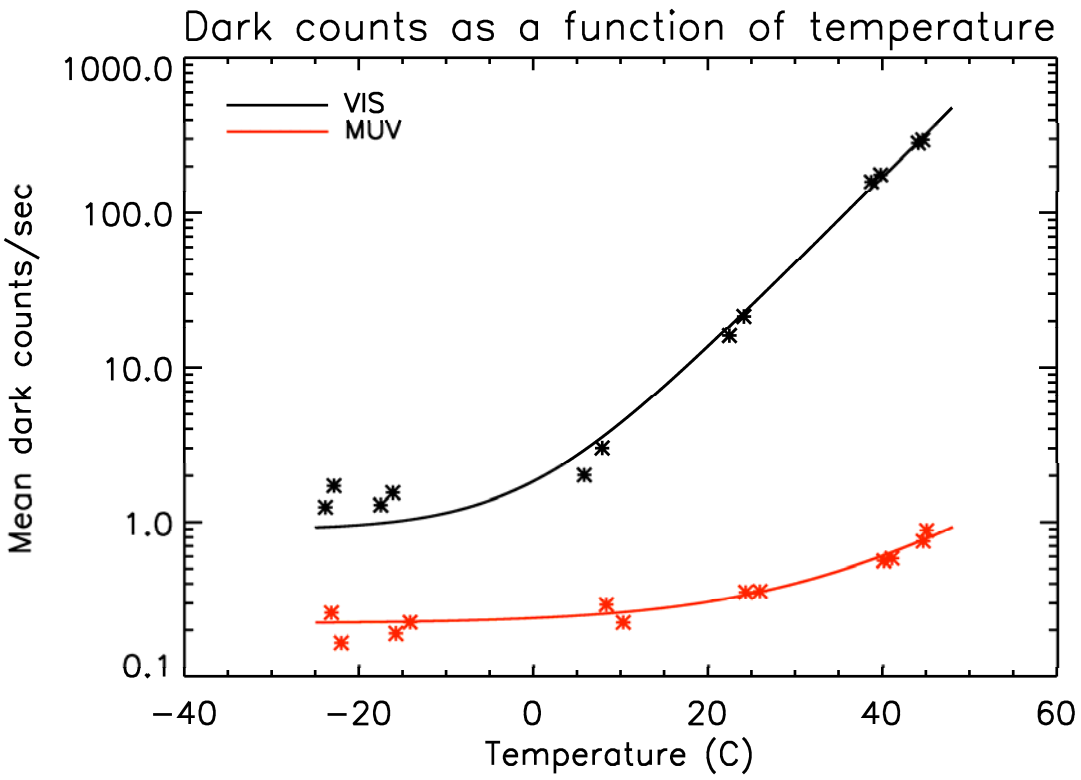

Figure 2.7. Dark counts as a function of temperature for the VIS and MUV detectors.

All subsequent analysis of calibration data used Equation 2.1 to determine the thermionic emission at the temperature of each experiment, which was then subtracted off from the experimental data.

Variations of the Mercury-Sun distance throughout the Mercury year will induce detector temperature variations. Figure 2.8 shows the predicted dark count rate for the VIS detector over the course of the Mercury year.

2.5 Wavelength scale

The UVVS wavescale is determined by the equation for an Ebert-Fastie spectrometer according to

$$
\begin{aligned}
&m\lambda = 2d\sin(\theta)\cos(\phi) \\
&m = \text{order number of diffraction} \\
&\lambda = \text{wavelength in Angstroms} \\
&d = \text{grating groove spacing} \\
&\theta = \frac{(\beta + \alpha)}{2} \\
&\phi = \frac{(\beta - \alpha)}{2}
\end{aligned}
\qquad (2.2)
$$

where α is the angle of incidence and β is the angle of diffraction for the grating. ϕ is the half angle difference, which is fixed by the geometry of the spectrometer for each channel. $\theta = \alpha + \phi$, where $\alpha = (A + n*\Delta)$. A is a constant determined by experiment, Δ is the grating step size, and n is the grating step number. The grating drive was

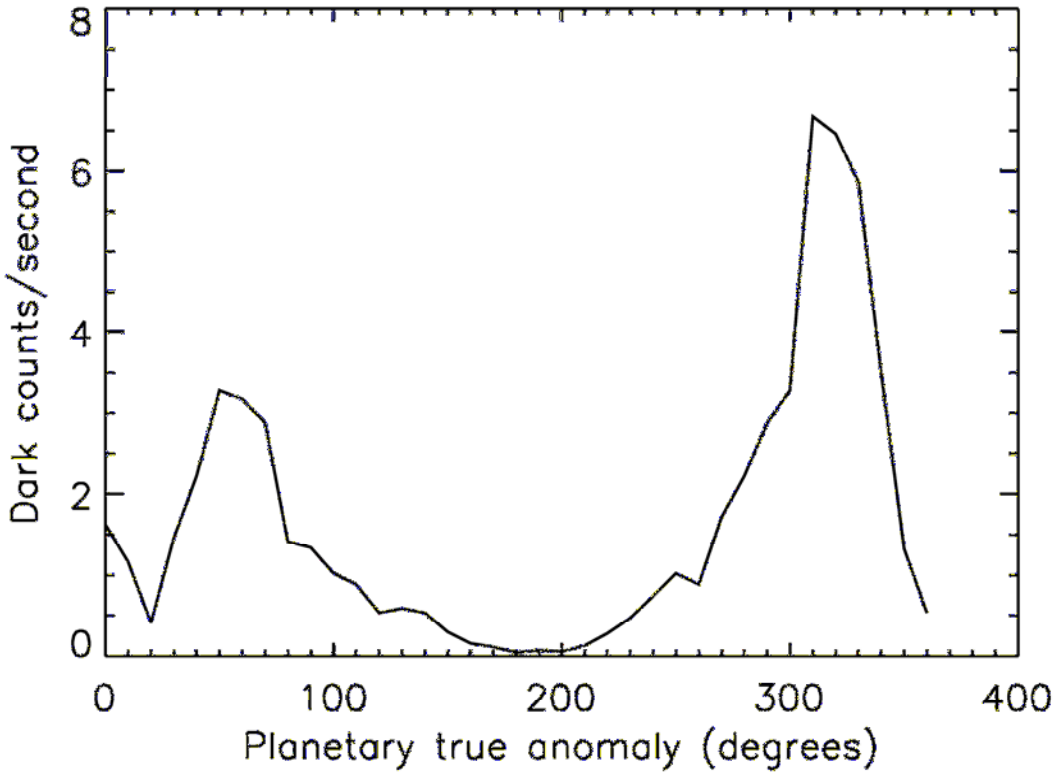

Figure 2.8. Variation of VIS channel dark count rate as a function of planetary true anomaly derived from pre-launch thermal measurements.

designed for a minimum grating step size of 0.0167°. The VIS channel was used at ambient room temperature to scan the spectrum of a mercury lamp, from which 6 spectral lines were chosen covering the operational range of the VIS channel. IDL was used to fit a gaussian to each of the 6 spectral lines, which yields the center of the line as a function of grating step position. This data, along with the wavelength of each line obtained from NIST, was used with IDL to perform a non-linear least squares curve fit in order to determine A, Δ, and ϕ from the above listed grating equation. The MUV and FUV values of ϕ were then determined by taking data over one spectral line and adjusting the respective value of ϕ until the gaussian determined wavelength of the line corresponded with NIST standards. The values for ϕ, Δ, and A were found to be ϕ = 9.997633, 12.331906, and 14.67254 degrees for the VIS, MUV, and FUV channels respectively, Δ = 0.016664671 degrees, and A = -2.0203037 degrees. The standard deviation of the difference between the wavelength of the spectral lines calculated with the above parameters in the grating equation and the spectral line values obtained from NIST is 0.20891829. Inserting the parameter values into the equation for and Ebert-Fastie spectrometer and recalling that the VIS and MUV are first order while the FUV is second order gives:

$$\begin{aligned} \text{VIS}: \ \lambda(\text{nm}) &= 820.679 * \sin(7.977 + 0.016664650 * \text{n}) \\ \text{MUV}: \ \lambda(\text{nm}) &= 814.106 * \sin(10.312 + 0.016664650 * \text{n}) \\ \text{FUV}: \ \lambda(\text{nm}) &= 403.079 * \sin(12.652 + 0.016664650 * \text{n}) \end{aligned} \tag{2.3}$$

A plot of grating step position vs. wavelength is given in Figure 2.9 for each channel.

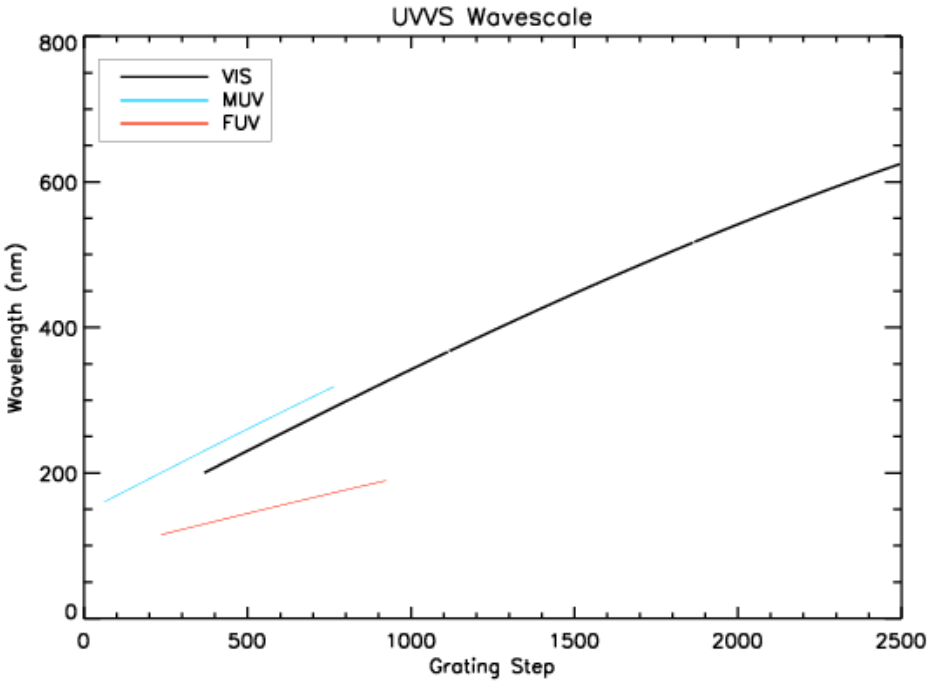

Figure 2.9. Plot of grating step position vs. wavelength for each channel. For each channel, the plot is only given over the spectral sensitivity range of each channel.

The temperature dependence of the wavelength scale was determined by observing a spectral line with each channel while thermal cycling MASCS in MOBI. For each channel the grating was scanned over a single spectral line over a range of temperatures from $-27^{\circ}\mathrm{C}$ to $+36^{\circ}\mathrm{C}$ and the gaussian center of the grating step position was determined by IDL. The mean step position for each channel over the temperature range is determined and the difference between step position at each temperature and the mean for each channel is plotted in Figure 2.10. The standard deviation of the grating step position at the center of the spectral line over the temperature range for each channel is 0.285886, 0.207281, and 0.212572 for the VIS, MUV, and FUV channels, respectively.

The center wavelength for several spectral lines was computed using the wavelength equation with the experimentally determined parameters. These results were compared to NIST center wavelength values for the spectral sources in order to access the accuracy of the wavelength scale. The results in Figure 2.11 show that the residual errors associated with using the wavelength equation are less than 0.05 nm

2.6 Point spread function

As the grating is scanned, the image of the entrance slit is convolved with the exit slit as shown in Figure 2.12. For a given spectral line, the line is not infinitely narrow due to the natural broadening of the line as well as pressure and Doppler broadening. However, the broadening due to the convolution of the image of the entrance slit with the exit slit of the spectrometer is the most dominant effect on the spread of the line compared to the other broadening mechanisms.

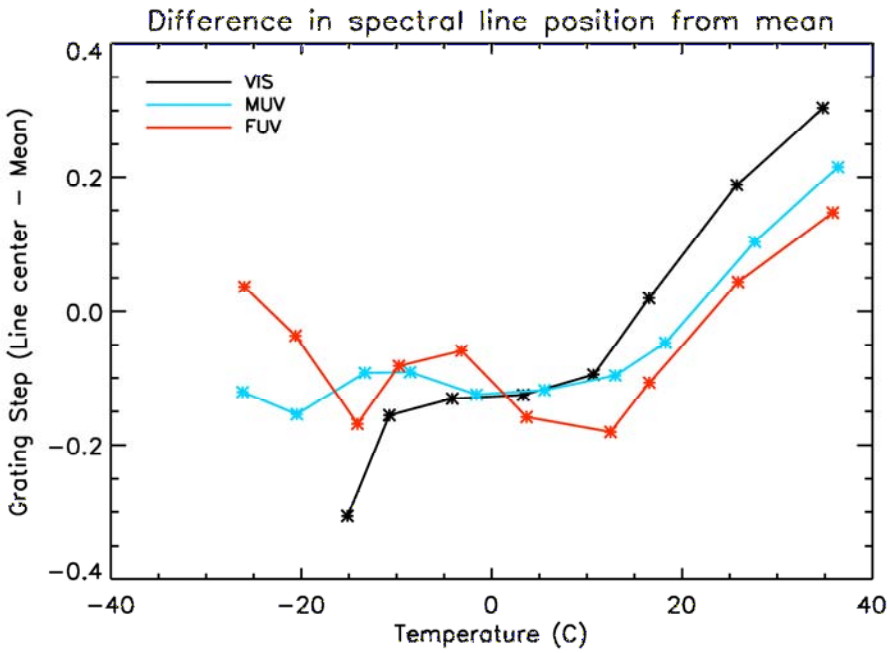

Figure 2.10. UVVS wavelength scale shift as a function of temperature.

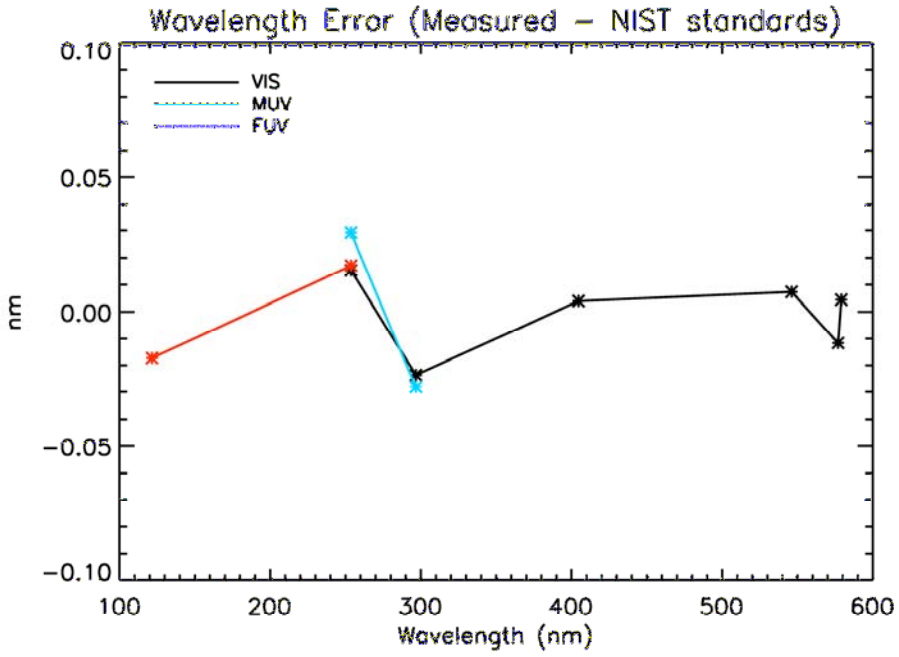

Figure 2.11. Residual errors in the UVVS wavelength scale.

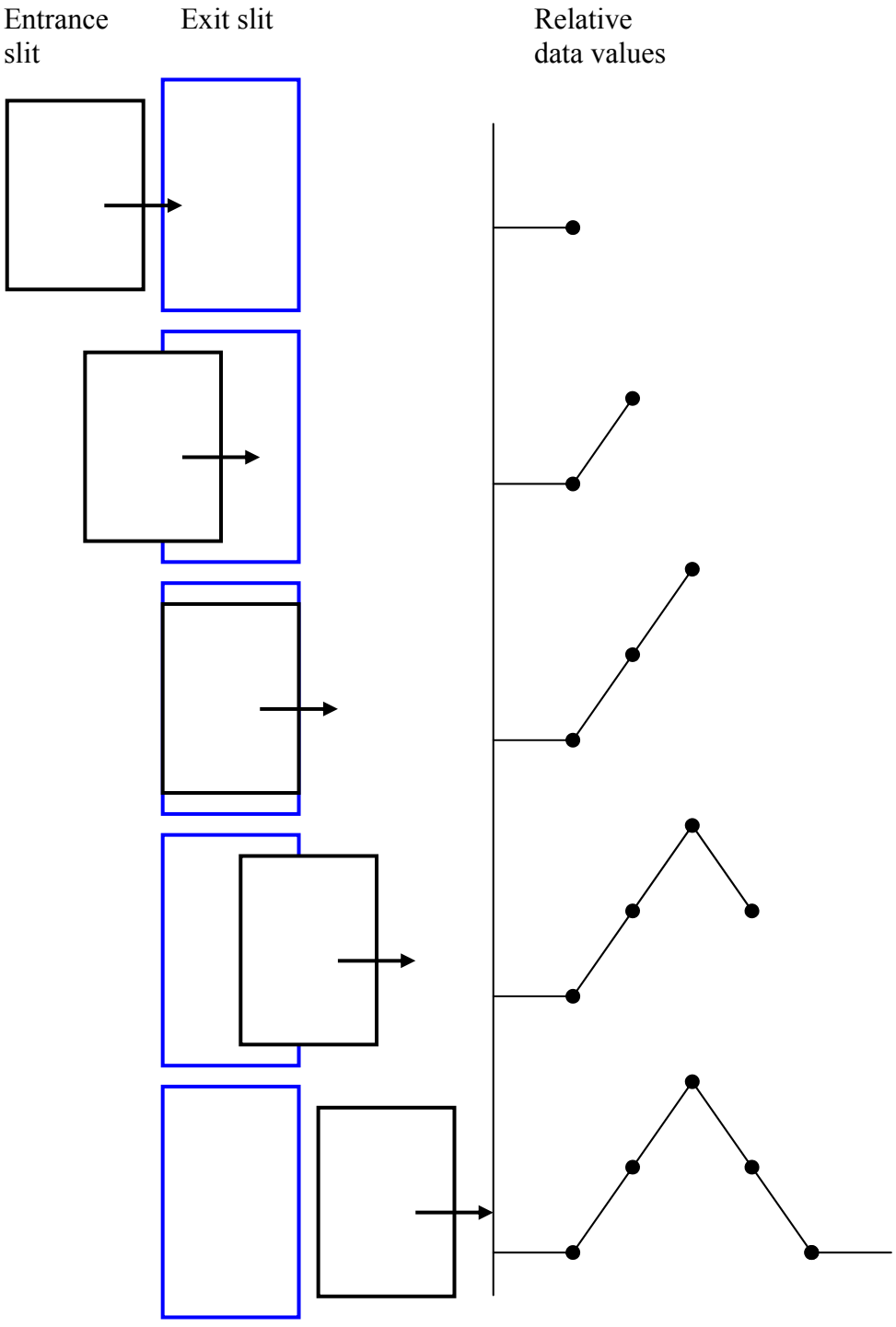

Figure 2.12. Scanning of image of entrance slit across the exit slit. The data points on the right demonstrate that the signal is proportional to the overlap of the entrance slit image and the exit slit.

The resulting count rate for scanning the grating over a spectral line is a trapezoidal function. To get the corrected count rate at line center, the area under the trapezoidal curve must be integrated and divided by the bandpass. Numerically, this is done by summing the counts generated by scanning a spectral line and dividing by the ratio of bandpass/grating step size. The image of the entrance slit is given by

$$W'_{en} = W_{en} * \left(\frac{\cos(\alpha)}{\cos(\beta)} \right) \tag{2.4}$$

where W_{en} is the width of the entrance slit, α is the incidence angle of light on the grating, and β is the diffraction angle from the grating. The bandpass of the instrument can be determined by differentiating the grating equation, with the result

$$\begin{aligned} \Delta\lambda &= \frac{d}{m * F} * \cos(\beta) * W_{ex} \text{ if } \cos(\beta) * W_{ex} > W_{en} * \cos(\alpha) \\ \Delta\lambda &= \frac{d}{m * F} * \cos(\beta) * W_{en} \text{ if } \cos(\alpha) * W_{en} > W_{ex} * \cos(\beta) \end{aligned} \tag{2.5}$$

where d is the grating ruling spacing, m is the diffraction order, and F is the spectrometer focal length. Figure 2.13 shows plots of the bandpass and grating step size as a function of wavelength for each channel.

Spectral lines were used to characterize the point spread function of all 3 channels of the spectrometer. A mercury 2536.5 angstrom line and a 5320 angstrom laser line

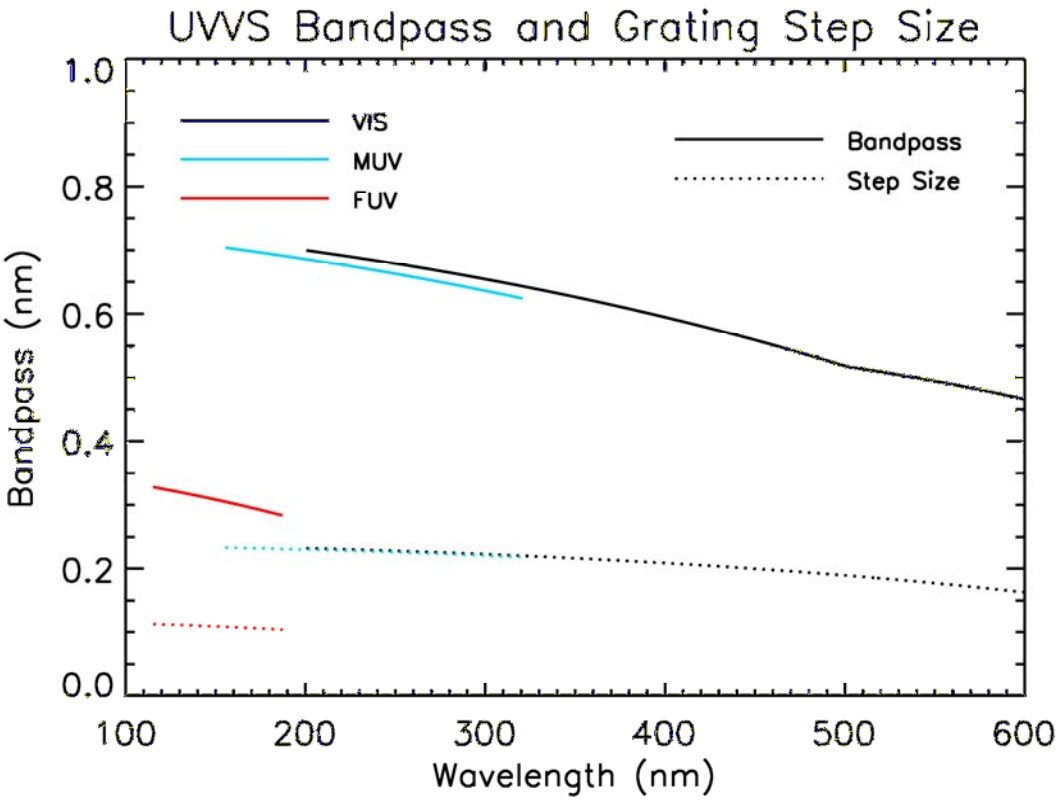

Figure 2.13. Plot of bandpass and grating step size verses wavelength for each of the 3 channels.

were used to characterize the VIS channel point spread function. A mercury 2536.5 angstrom line and hydrogen lyman alpha were used to characterize the FUV channel point spread function. A mercury 2536.5 angstrom line was used to characterize the MUV channel point spread function. For each data set, a gaussian was fit to the data using the gaussfit function of IDL. This function returns a set of 6 constants for a given set of data that are used in the gaussian function as:

$$f(x) = A_0 \exp^{\frac{-z^2}{2}} + A_3 + A_4 x + A_5 x^2$$
$$\text{where } z = \frac{x - A_1}{A_2} \tag{2.6}$$

The FWHM of the gaussian fit to the data is computed and given in both grating steps and Angstroms. The 5 plots are shown in Figures 2.14 through 2.17.

Figure 2.18 is a spectrum of a low pressure sodium lamp showing the point spread of the sodium doublet. Since the two lines are only 6 Å apart, there is overlap in the signal near the spectral center of the two lines. An idl routine using the instrument profiles is used in order to de-convolve the spectra into separate lines.

The change in the FWHM of a spectral line as a function of temperature was measured in the MOBI vacuum chamber for each channel. A single spectral line was scanned over a range of temperatures and IDL was used to fit a gaussian to the spectral line. From this information, the FWHM was calculated at each temperature and for each channel. The temperature range was -27 C to +36 C. For a given

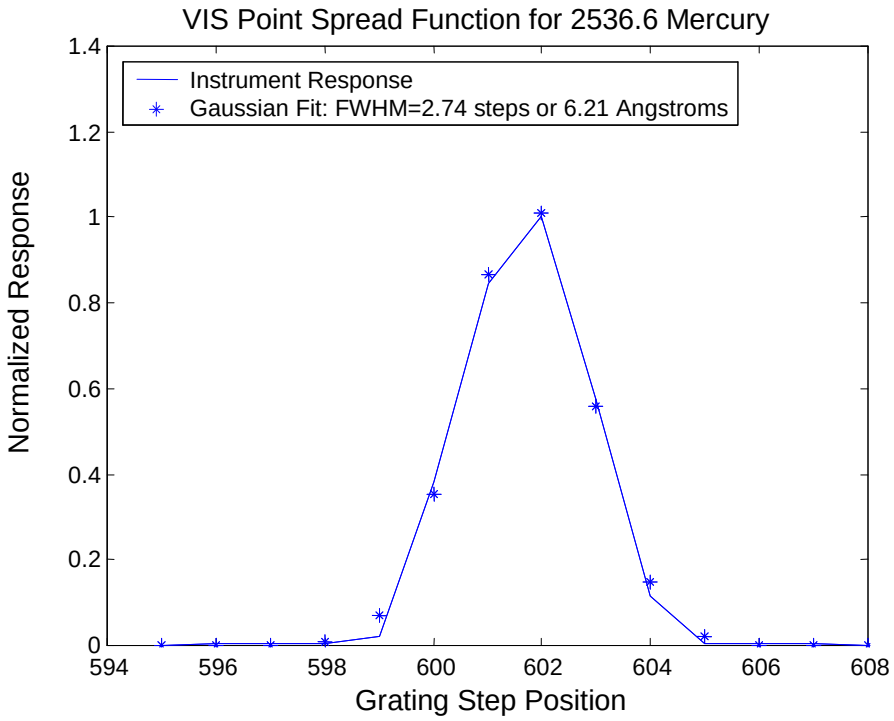

Figure 2.14. VIS channel point spread function for the 253.65 nm mercury line.

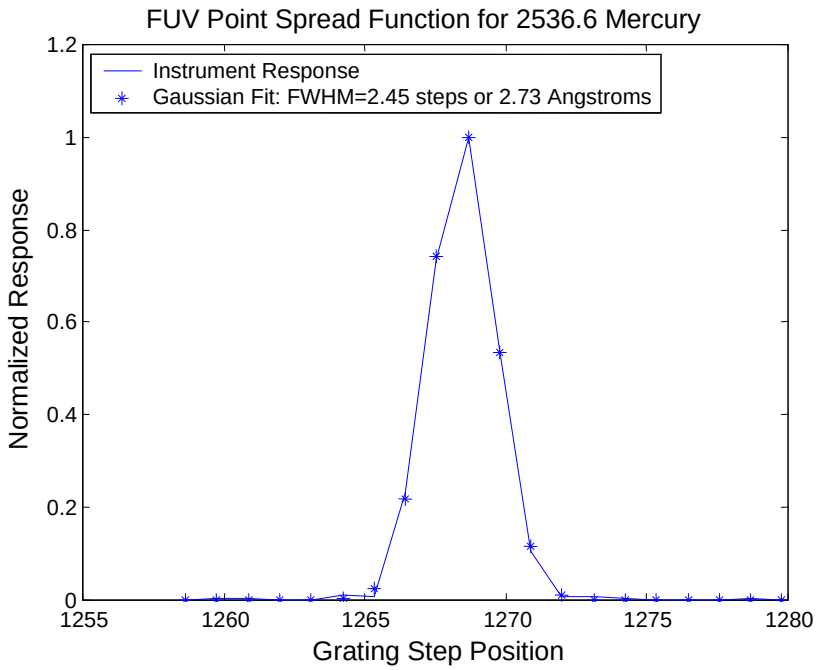

Figure 2.15. FUV channel point spread function for the 253.65 nm mercury line.

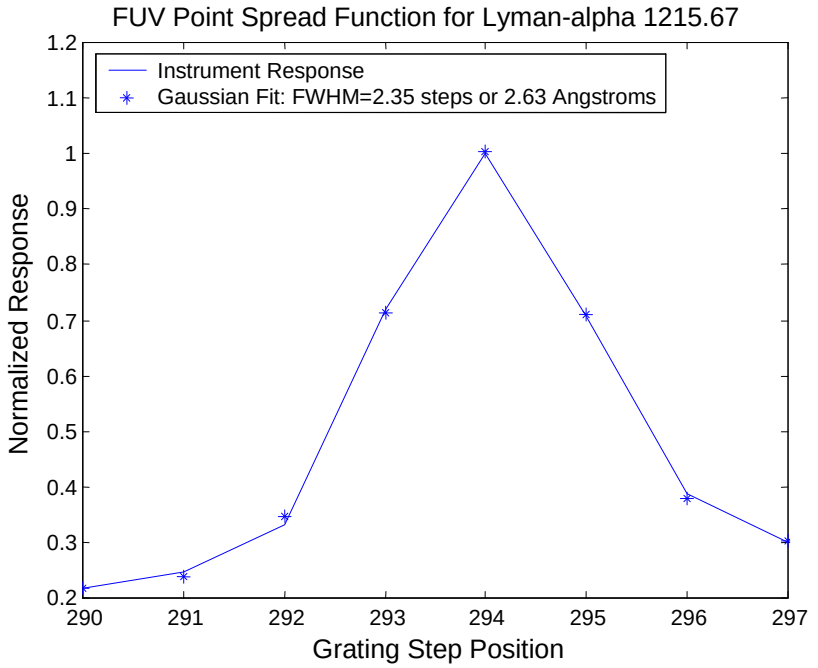

Figure 2.16. FUV channel point spread function for the 121.567 nm lyman alpha line.

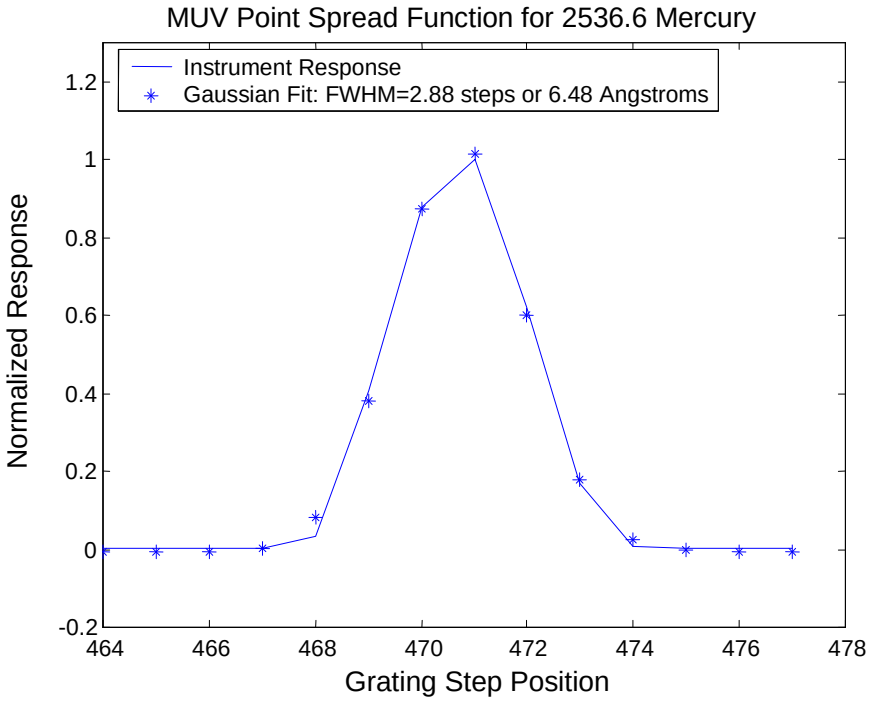

Figure 2.17. MUV channel point spread function for the 253.65 nm mercury line.

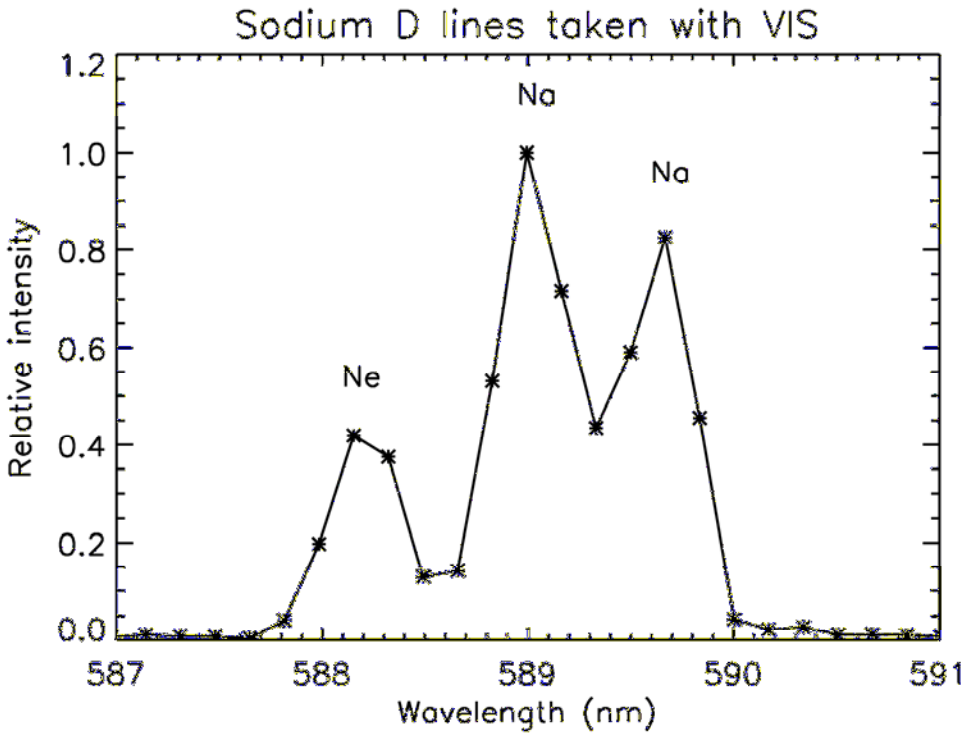

Figure 2.18. Spectrum of the sodium doublet demonstrating the overlap of spectral lines due to the point spread function. The lamp that was used was a sodium lamp with neon as the inert gas, hence the neon line as well.

channel, the mean of the FWHM values was determined and the fractional change of the FWHM at a specific temperature from the mean FWHM was calculated and plotted as a function of temperature for each channel in Figure 2.19. The standard deviation of the FWHM for each channel over the temperature range is 0.0713398, 0.0410318, and 0.101247 for the VIS, MUV and FUV channels respectively.

The grating step dependence of the point spread function was determined by observing several spectral lines sources that span the spectral range of the instrument. Figure 2.20 shows that the FWHM of the point spread function increases ~ 25 % from the shortest wavelength to the longest.

2.7 Field of view

The field of view was characterized for each channel in both the spectral and spatial directions. In addition, the spatial direction was characterized for both the atmospheric and surface slit. The VIS and MUV channels were measured using the two-axis manipulator in the black lab to scan a point source across the field of view in the spectral and spatial directions. A mercury pencil lamp was used and the 2537 angstrom line was scanned over for each channel. The FUV channel was measured in vacuum with a two-axis manipulator that scanned a point source over the field of view in the spectral and spatial directions. A deuterium lamp was used with the monochrometer set to zero order and the grating was scanned over the lyman alpha line. The point source was not as small as for the VIS and MUV experiments, and the manipulator was more unstable than the black lab manipulator; which is the reason that the sides of the FUV plots for angular changes on the order of 0.01° in both the

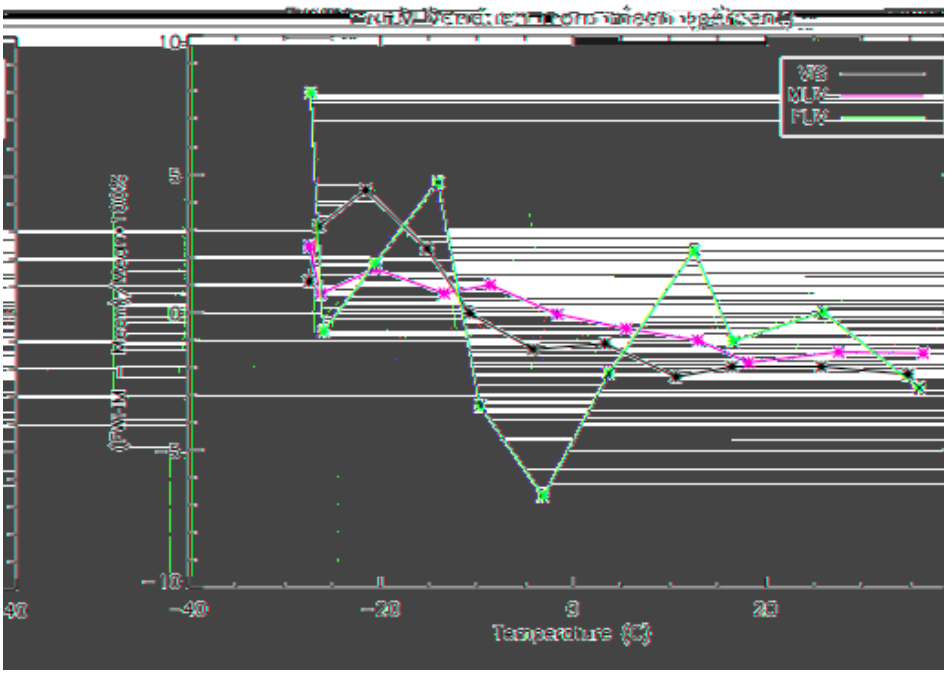

Figure 2.19. Variation of point spread function with temperature.

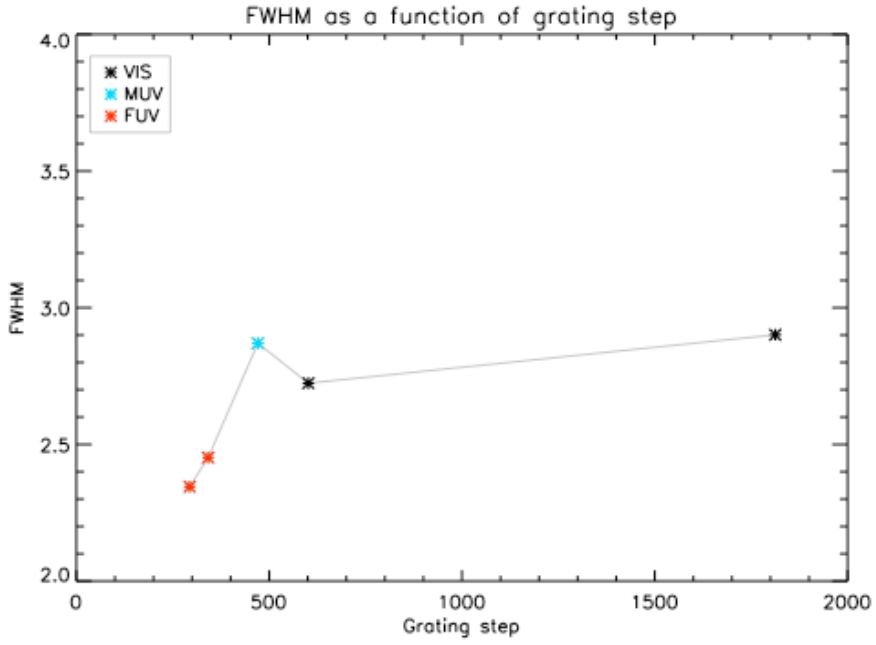

Figure 2.20. Variation of point spread function with grating step.

spectral and spatial direction do not fall off sharply.

The results are given in Figures 2.21 through 2.23. When the spectrometer is placed in surface slit mode, a shutter that has an opening near the center is actuated to cover the entrance slit, providing an opening that is almost square in size. However, this shutter is displaced from the entrance slit, and thus from the telescope focal plane, in the direction towards the Ebert mirror. This causes the light that enters the spectrometer through the surface slit to be out of focus and is the reason why the surface slit field of view plots do not have a sharp fall-off.

2.8 Spectrometer scattered light

The spectrometer scattered light was measured using a 532 nm laser. The output of the laser was diffused and then directed to the collimator, giving a beam of light that both filled the aperture and the field of view of the instrument. Data were taken in multiple grating scans. In order to extend the dynamic range for low signal levels, a neutral density filter was inserted in the optical path in the 532 nm region and then removed for wavelengths spectrally far away from 532 nm. An overlap region between the neutral density set of data and the non-neutral density set of data was compared to determine a multiplying factor for the central wavelength data.

The results of the scattered light experiment are given in Figure 2.24. The amount of light is 10^{-5} at 50 nm from the 532 nm line. The large lobe that is present at around 525 nm motivated the need for further investigation. An experiment consisting of the summation of a series of scans of a Mercury 2536.5 was done to observe the behavior of the lobe at a shorter wavelength. This data is shown in

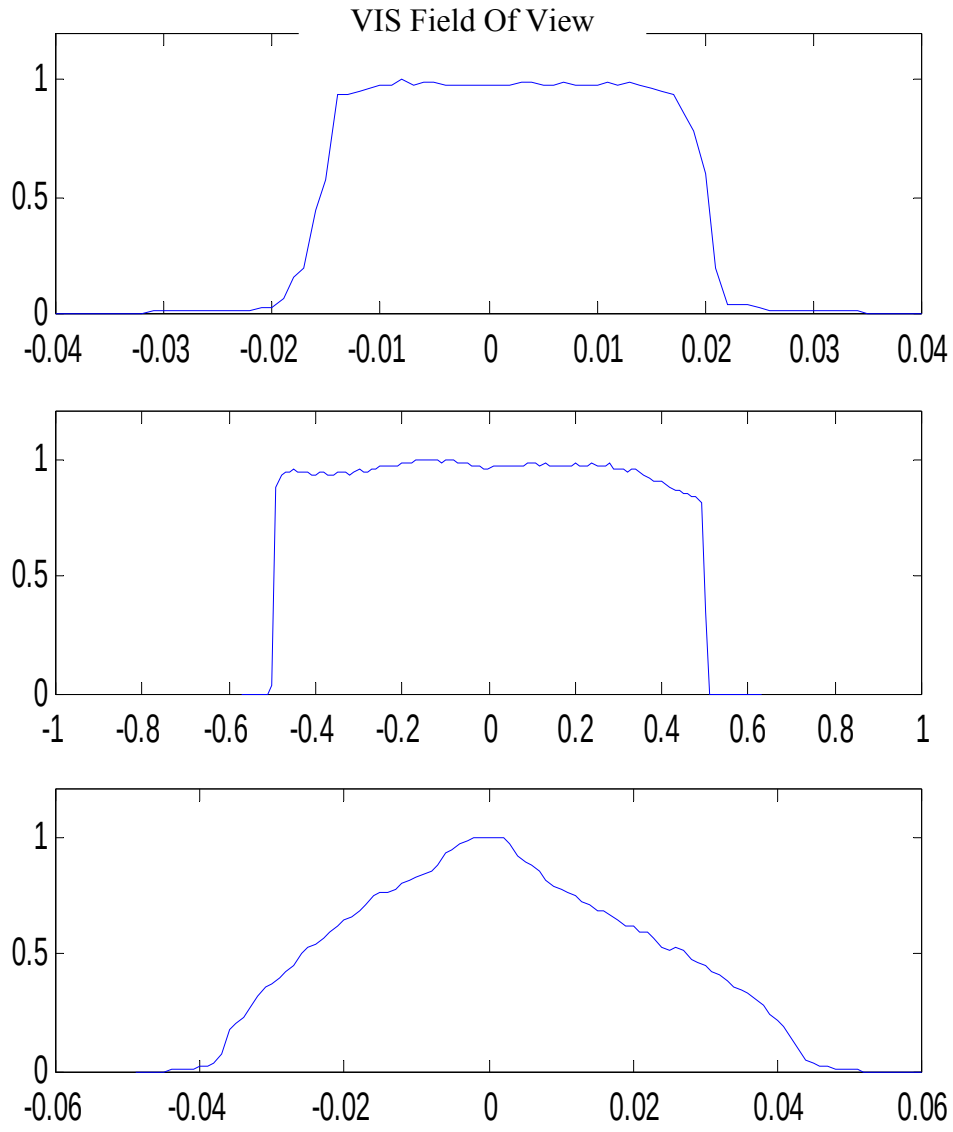

Figure 2.21. VIS channel field of view with angle from for the atmospheric slit in both the spectral and spatial directions and the surface slit in the spatial direction.

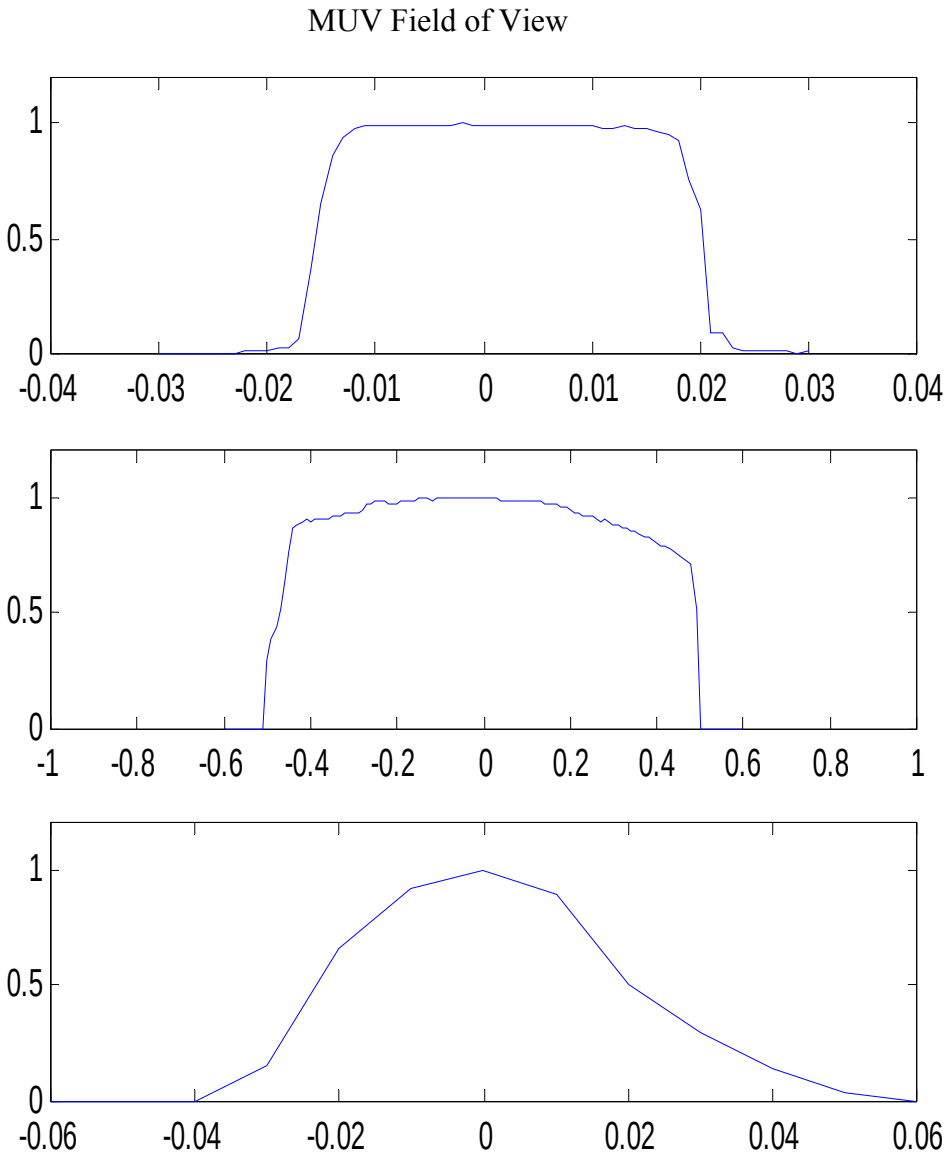

Figure 2.22. MUV channel field of view with angle from for the atmospheric slit in both the spectral and spatial directions and the surface slit in the spatial direction.

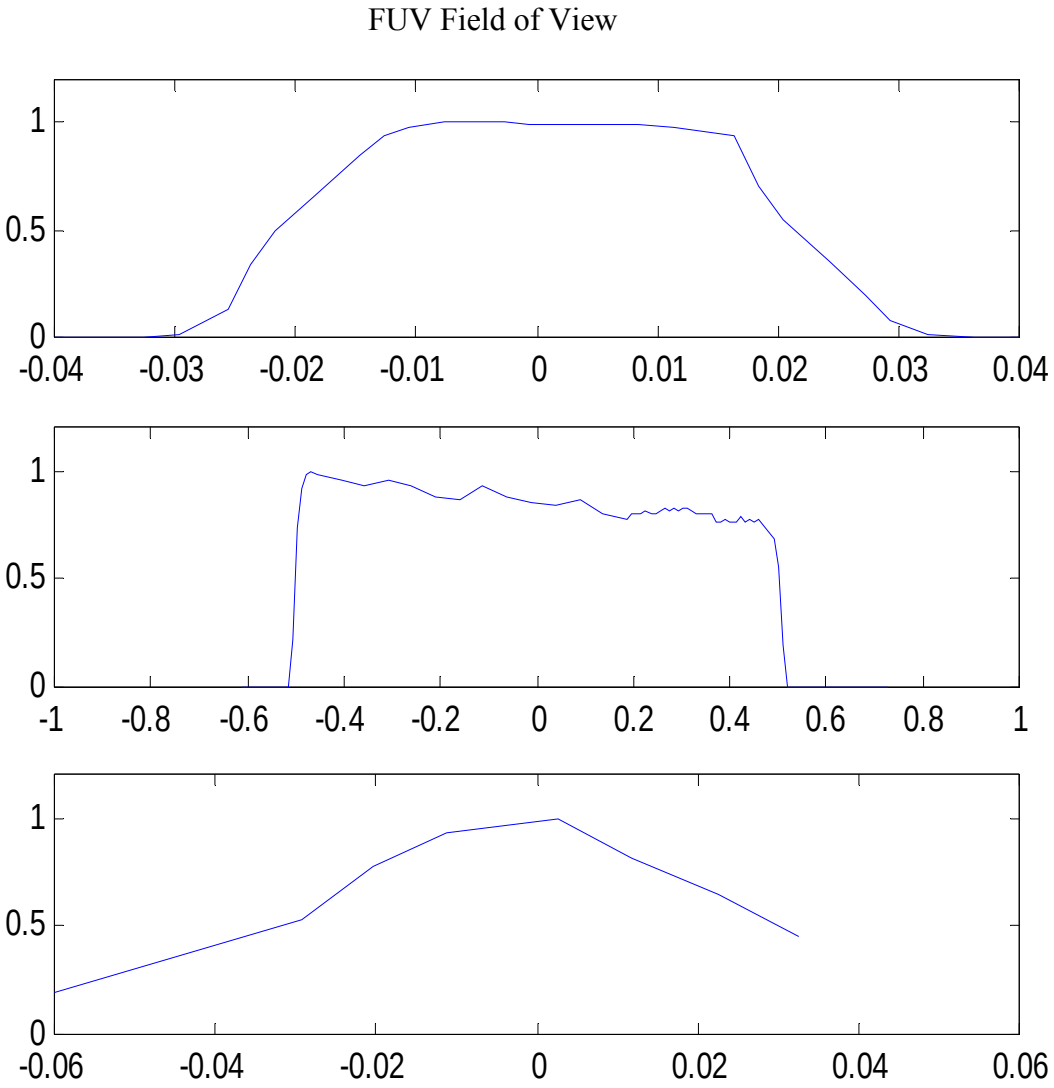

Figure 2.23. FUV channel field of view with angle from for the atmospheric slit in both the spectral and spatial directions and the surface slit in the spatial direction.

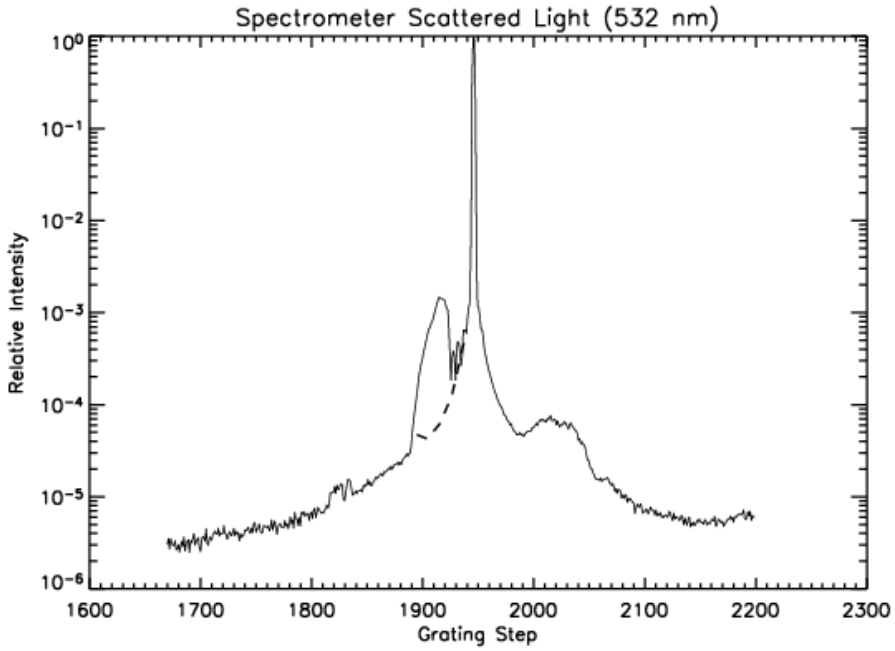

Figure 2.24. Grating scatter of a 532 nm laser. The lobe to the left of the peak is presently unexplained.

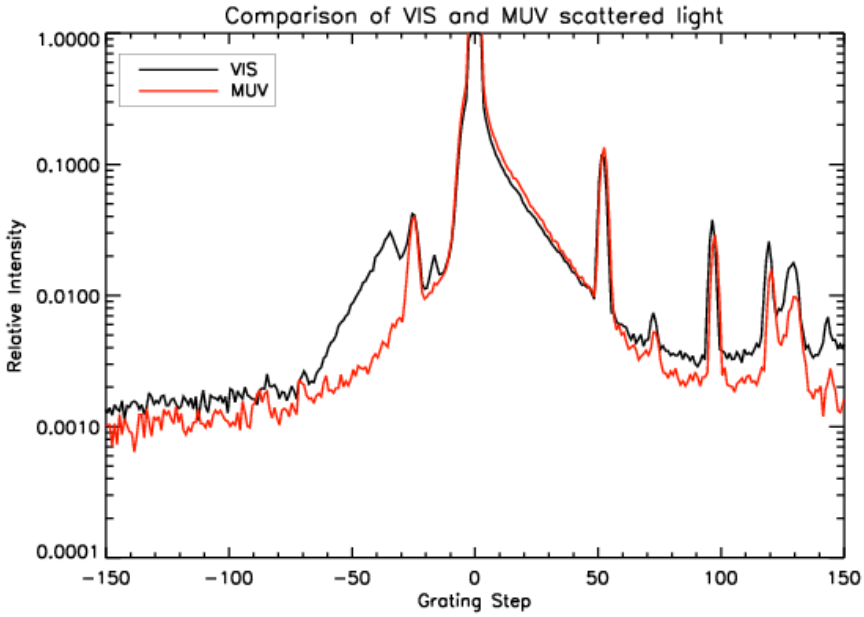

Figure 2.25. Grating scatter of the mercury 253.65 nm line showing the same lobe as for the 532 nm line.

Figure 2.25. Although the cause of the lobe is the subject of debate, it is a characteristic of the spectrometer.

2.9 Spectrometer stray light

Spectrometer stray light arises from light reflected off of structures within the instrument. The spectrometer stray light was characterized for a broad spectrum by using data taken from an FEL lamp at APL, Figure 2.26. Both the telescope aperture and the field of view were filled. The flat region from 140 nm to 210 nm is light scattered from the more dominant FEL continuum at the longer wavelengths. Dark counts were measured by blocking the telescope and subtracting from the FEL spectrum in order to address the issue of spectrometer stray light independently. The fraction of stray light was obtained by taking the mean of the counts at shorter wavelengths (the blue portion of the curve) and dividing by the mean of the counts centered around the peak of the curve (the red portion of the curve) and found to be 0.1 % of the mean peak counts.

2.10 Spectrometer polarization

The polarization was measured in the black lab using a deuterium lamp for a wavelength range of approximately 210 nm to 500 nm and a halogen lamp for a wavelength range of approximately 500 nm to 620 nm. The output of the lamp was followed by a collimating lens. A Glan-Taylor prism polarizer immediately followed the lens so that the collimated beam of light passed through the polarizer. The

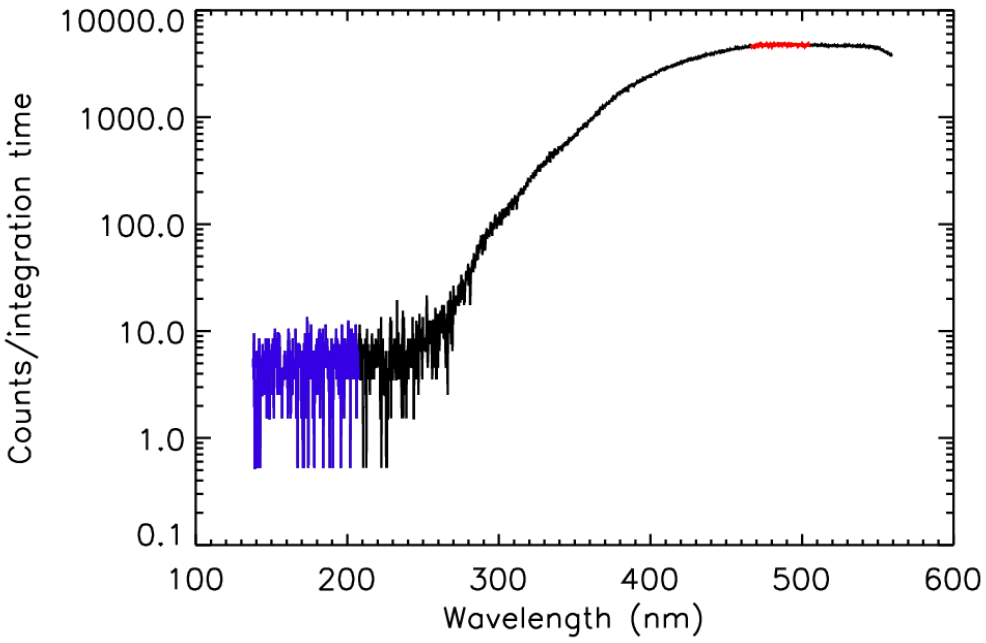

Figure 2.26. FEL spectrum obtained with the VIS channel showing scattered light in the region below 220 nm. The dark counts have been subtracted.

polarizer was then followed by another lens that imaged the light down to a pinhole. The pinhole was at the focal point of the large collimating mirror. The instrument was pointed at the mirror and oriented such that an image of the pinhole was formed in the entrance slit of the UVVS. At the same time, light completely filled the aperture. The instrument was mounted on a rotation stage so that the entrance slit could be rotated around the optical axis of the instrument. Several data sets were taken at different orientations until the signal was maximized, indicating light polarized perpendicular to the grating grooves. Data was then taken at this orientation and at 90 degrees to this orientation. Both the VIS and MUV channels were tested with this configuration. The lower limit of the measurable wavelength was determined by the cutoff of the polarizer, which began to roll off sharply at approximately 210 nm.

Figure 2.27 shows the polarization response of the UVVS plotted as the ratio of $(l_{\text{perp}} - l_{\text{para}})/(l_{\text{perp}} + l_{\text{para}})$, where $l_{\text{perp}}(l_{\text{para}})$ are the instrument response to light polarized with its electric vector perpendicular (parallel) to the grating grooves. The blue curve is the polarization response taken with the MUV channel using the deuterium lamp. The red curve is the polarization response taken with the VIS channel using the deuterium lamp. The green curve is a longer wavelength polarization response taken with the VIS channel and the halogen lamp. The reason for using the halogen lamp at longer wavelengths is because the deuterium lamp begins to cut-off around 500 nm and causes the statistical error of the photon counting to become large. The statistical error for the MUV at a wavelength of 210 nm is 5.5 %.

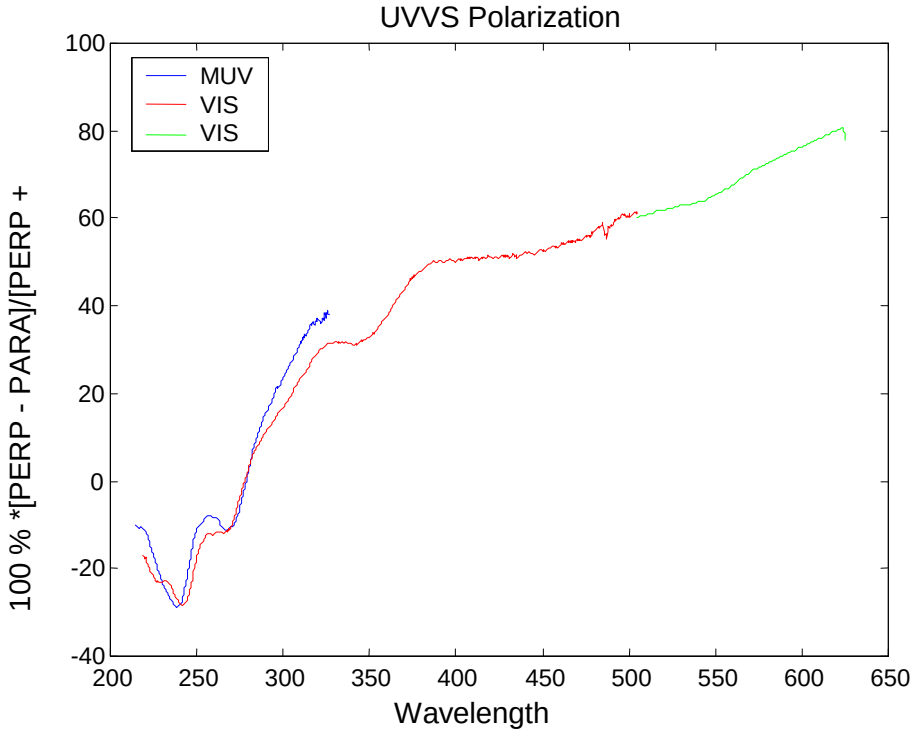

Figure 2.27. The percent polarization for the UVVS. The black curve is the polarization taken with the MUV channel using the deuterium lamp, the red curve is the polarization taken with the VIS channel using the deuterium lamp, and the green curve is the polarization taken with the VIS channel using a halogen lamp

2.11 Telescope off axis response

The telescope off-axis response was measured in the laboratory by using the 2 axis manipulator to scan a star source in both the spectral and spatial directions. The star source was a mercury pencil lamp imaged onto a pinhole at the focal point of the collimator. The size of the pinhole in conjunction with the focal lengths of both the collimator and the telescope made the image of the pinhole under-fill the entrance slit of the instrument, however the telescope aperture was completely filled. The MUV channel was used to scan over the Mercury 2537 angstrom line. The reason for the MUV channel was to minimize laboratory scattered light effects.

The data for both the spectral and spatial directions were taken in 5 different sets. A neutral density filter was inserted for the data sets in which the star source moved across the entrance slit. The filter was removed for the other scan ranges. Some overlap between the central data set and the adjacent data sets was purposely done in order to characterize the neutral density filter. This method allowed for a pinhole size to be used that gave enough light to accurately determine the off-axis response out to an angle of approximately 5°. The manipulator was stepped at a high angular resolution as the star source moved across the entrance slit, and then in the interest of time the angular step resolution was decreased for the other data sets. The results are shown in Figures 2.28 and 2.29. Figure 2.28 shows the relative response in the spectral direction. At 0.5° from the center of the slit the signal has decreased by 4 orders of magnitude. The error at 0.5° due to photon counting statistics is 0.756%; however, the error at 5° is approximately 6%. Figure 2.29 shows the relative response in the spatial direction. At 1° from the center of the slit the signal has

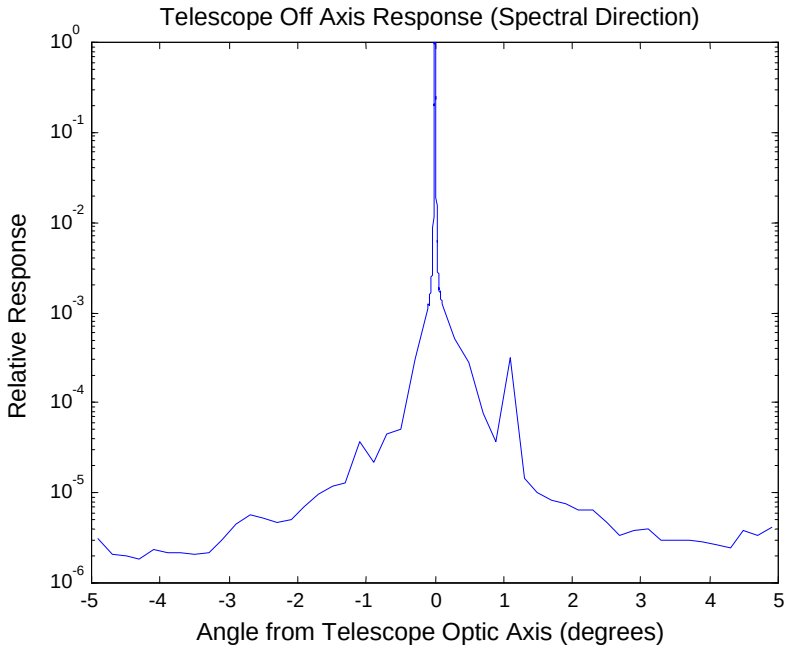

Figure 2.28. Off axis response for a point source in the spectral direction.

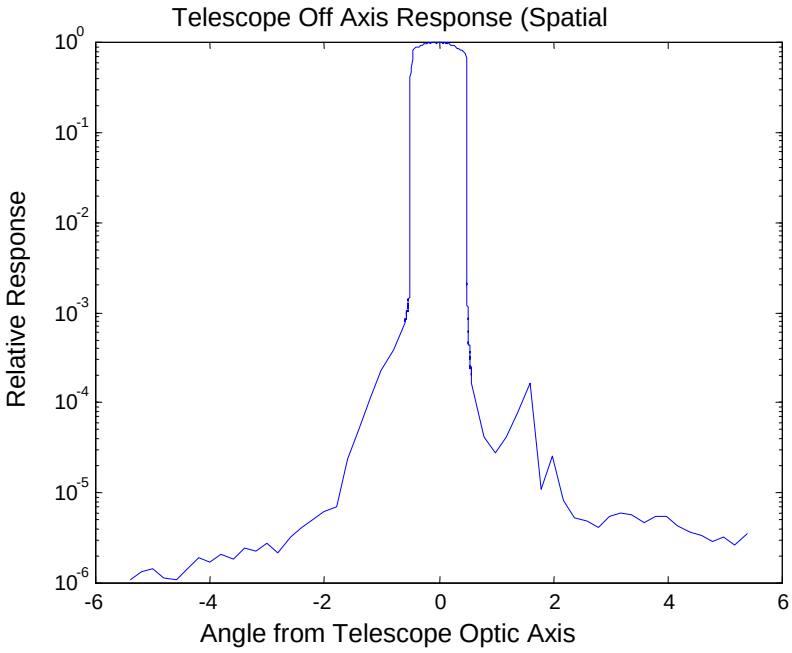

Figure 2.29. Off-axis response for a point source in the spatial direction with the atmospheric slit.

decreased by approximately 4 orders of magnitude. The photon counting error at 1° is 3.65% while the error at 5° is approximately 10%.

After orbit insertion, the angular size of Mercury as seen from the spacecraft will vary from 17° to 60° during atmospheric observations, depending on the orbital position of MESSENGER. Thus the point source response is not an adequate representation of the off-axis light that will enter the instrument. Furthermore, the laboratory calibration for the point source was only done for the across slit and along slit directions. During an observation of Venus when the diameter of the planet was 0.012° as seen from the telescope, a small 2-dimensional map was generated using the surface slit (Figure 2.30). These results show that the off-axis response is not rotationally symmetric; which is consistent with theory because the optics in the telescope are square. Two factors must be included in order to make off-axis light predictions at Mercury: 1) a 2-diminsional map of the off-axis response that extends over a larger angular range than that shown in Figure 2.29 and 2) the convolution of the 2-diminsional off-axis response with an extended source that simulates Mercury. An off-axis model was developed that incorporated these 2 factors with provisions described as follows. The point source response taken in the lab was extrapolated from ~ +/- 5° to +/- 10° degrees in order to sum data points over a larger area for an extended source. The values of the point source off-axis response for angles greater than |5°| are considered conservative in the sense that they may over-estimate the off-axis light contribution to the signal (McClintock, private communication, 2007). Based on the results shown in Figure 2.30, the 2-dimensional off-axis field was assumed to not be rotationally symmetric, but to resemble a sinc function. Therefore,

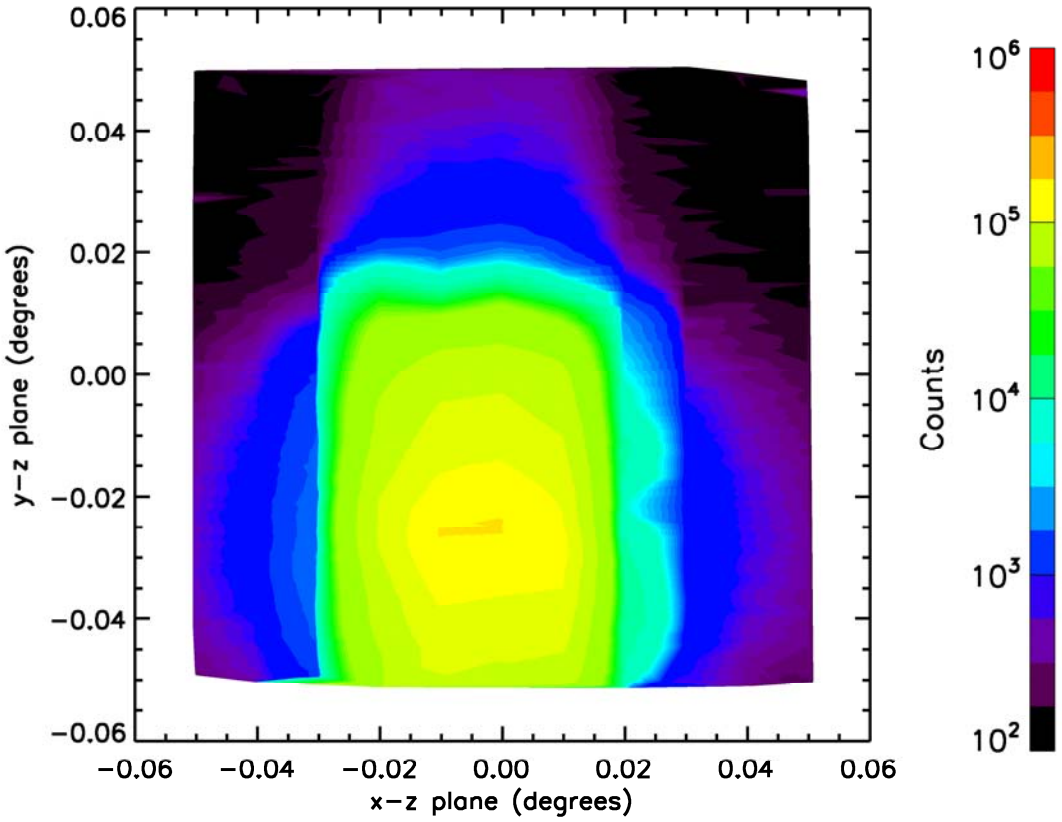

Figure 2.30. Two dimensional off-axis response to observations made of Venus using the surface slit when the planetary angular diameter was 0.012°. The results indicate that the response is not rotationally symmetric; which is expected since all optical components in the telescope are square.

the point source off-axis response in the spatial direction was multiplied by the point source response in the spectral direction at every value along the extent of the spatial direction off-axis response. This created a 2 dimensional off-axis response array that ranges from +/- 10° in both directions. All points from the surface of the extended body outside of the 10° square off-axis light model are not counted and thus do not contribute to the off-axis light estimate. This does not compromise the off-axis light estimate since light from angles > 10° are assumed to not make a significant contribution to the total off-axis light. The 2 dimensional point source off-axis response is shown in Figure 2.31. The resulting 2-dimensional off-axis response of the instrument was then convolved with an extended source representing Mercury.

The convolution of the 2-diminsional off-axis response with an extended source is dealt with by making use of a lunar image taken by MDIS during the MESSENGER lunar flyby (Figure 2.32). Multiple angular sizes of the lunar image were convolved with the 2 dimensional point source response and found that variations in angular size from 20° to 60° do not produce significantly different off-axis light results.

During the MESSENGER flyby of Venus, the VIRS channel of MASCS measured the off-axis response. The angular size of Venus was ~ 60°, which gave the first opportunity to measure the extended source off-axis response of the instrument since the UVVS and VIRS channels share a common telescope. The VIRS off-axis curve along with the model surface slit and atmospheric slit off-axis curves are shown in Figure 2.33. Reasonable agreement between the two sets of curves validates the off-axis model for extended sources. Note that the model surface slit off-axis response

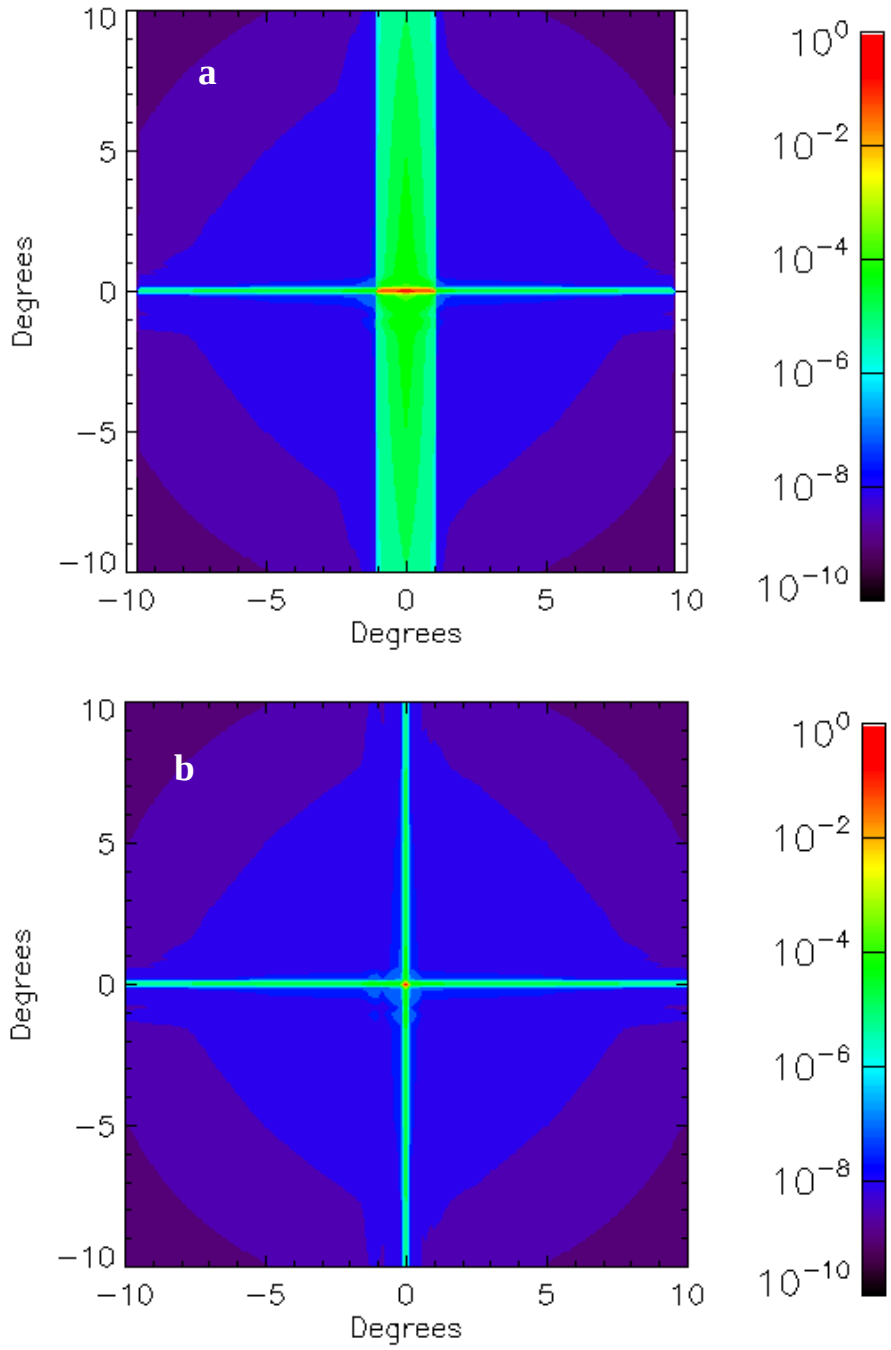

Figure 2.31. The 2-dimensional off-axis response for both the atmospheric (a) and surface slit (b) constructed from using the laboratory point source response in both the spatial and spectral directions.

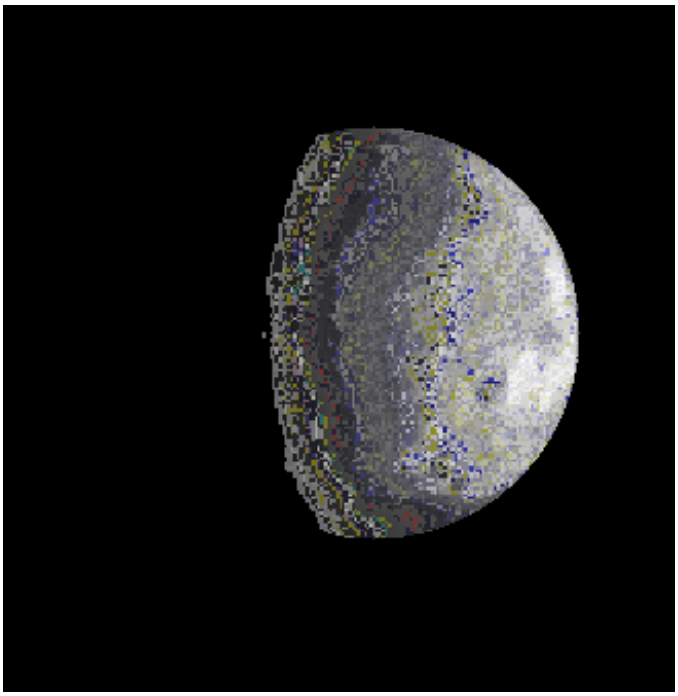

Figure 2.32. Image of the Moon taken by MDIS during the MESSENGER flyby of 2005. This image is expanded to the correct angular size of Mercury as seen by the instrument after orbit insertion and used to represent Mercury for off-axis light derivations.

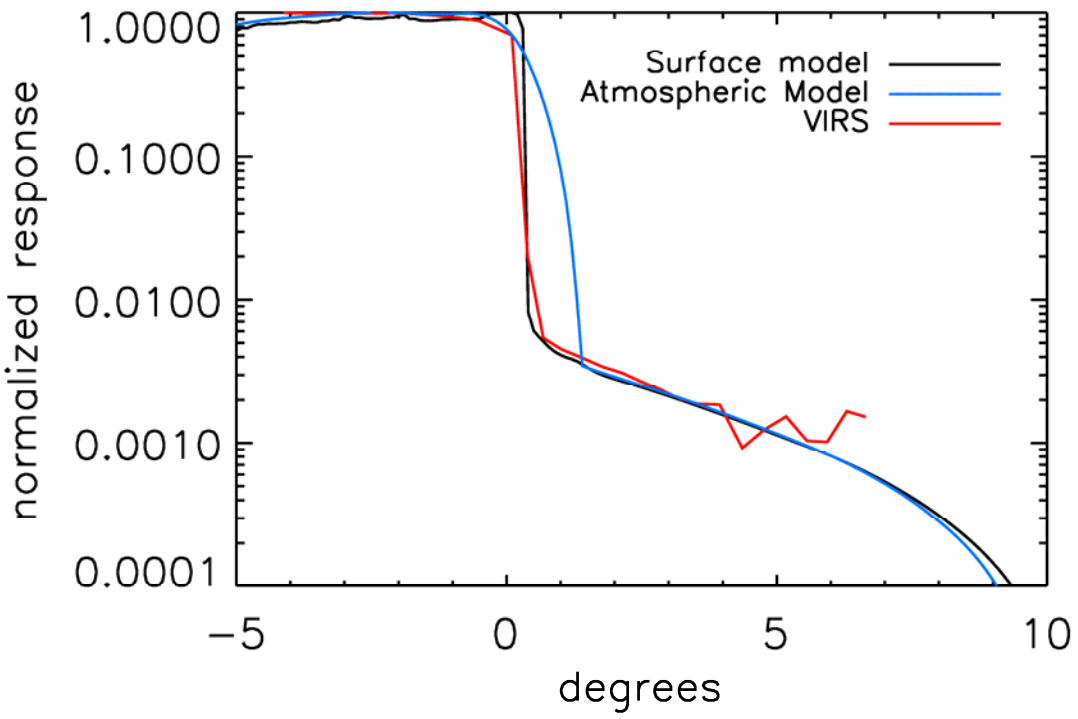

Figure 2.33. Off-axis response for a vertical angle of 0° for both the surface and atmospheric slits convolved with a 60° extended source. Also shown is the off-axis curve derived from VIRS observations during the Venus flyby.

more closely matches the VIRS measured off-axis response. This is expected since the UVVS surface slit is closer in size to the VIRS entrance aperture than the atmospheric slit is to the VIRS entrance aperture.

The normalized result for the convolution of the 2-dimensional off axis response with the lunar image expanded to an angular size of 20° is shown in Figure 2.34 for both the atmospheric and surface slits. The atmospheric slit shows an extended falloff as a function of angle on the sub-solar edge of the planet. The reason for this is that the angle shown for either slit is at the center. Since the length of the atmospheric slit is 1°, then a portion of the slit overlaps the surface for angles up to 0.5°.

2.12 Window transmission

The telescope window transmission was measured for a wavelength range of approximately 2000 angstroms to 6250 angstroms with the VIS channel in ambient conditions and for a wavelength range of 1169 angstroms to 1723 angstroms with the FUV channel in vacuum conditions. For the VIS channel, a deuterium lamp was used to irradiate a reflection screen. The instrument was pointed towards the center of the screen so that the telescope aperture and spectrometer entrance slit were completely filled. Data was taken by scanning the grating over the VIS wavelength range first with the contamination cover open and then with the contamination cover closed. The window transmission was determined as a function of wavelength by taking the ratio of data with cover closed to data with cover open.

The FUV window transmission was measured using a deuterium lamp as the

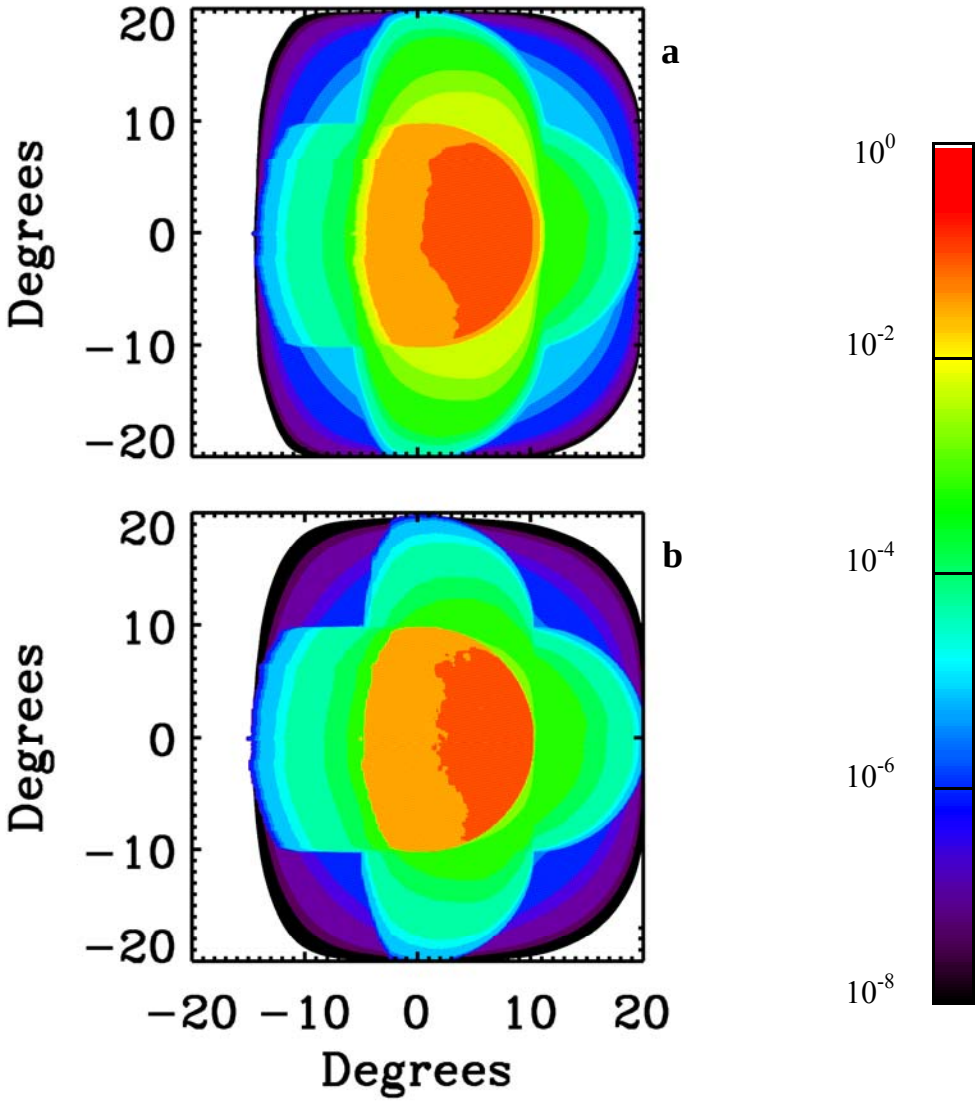

Figure 2.34. Result of convolving the extended off-axis response for both slits (Figure 2.31) with the simulated image of Mercury in Figure 2.32. The black circle represents the disk of Mercury, which is 20° in diameter for this example. 2.34a is for the atmospheric slit and 2.34b is for the surface slit.

source for a monochrometer mounted on the vacuum chamber. The exit slit of the monochrometer was large enough to allow the entrance slit of the UVVS to be completely filled. The monochrometer exit slit was also placed at the focus of the off- axis paraboloid mirror in the vacuum chamber allowing for a beam of collimated light that completely filled the UVVS telescope aperture. Data was taken at discrete wavelength bands of the deuterium lamp by varying the spectral output of the monochrometer. At each spectral band, the UVVS grating was scanned over the wavelength range. This method was conducted first with the contamination cover open and then with the contamination cover closed. The window transmission was determined by the same ratio method as for the VIS channel. The results are given in Figure 2.35.

2.13 Radiometric sensitivity

2.13.1 Overview

The radiance is given by

$$\mathrm{L}(\lambda_{\mathrm{j}}) = \frac{\left[\mathrm{C}(\lambda_{\mathrm{j}}) * N(C) - \mathrm{D(j)} - \mathrm{Sc}'(\lambda_{\mathrm{j}}) - Stray(\lambda_{\mathrm{j}})\right]/\Delta t}{A * \Delta\lambda * R_c(\lambda_{\mathrm{j}}) * \overline{\Omega} * (1 - Sc)} = \frac{C_{corr}(\lambda_{\mathrm{j}})/\Delta t}{A * \Delta\lambda * R_c(\lambda_{\mathrm{j}}) * \overline{\Omega}} \qquad (2.7)$$

where C is the counts at grating step j, N is the non-linearity correction, D is the dark counts, Sc' is the grating scattered light from all other grating positions into position j, Stray is the light that scatters from structures within the instrument, A is the telescope effective aperture, $\Delta\lambda$ is the spectral bandpass, R_c is the instrument

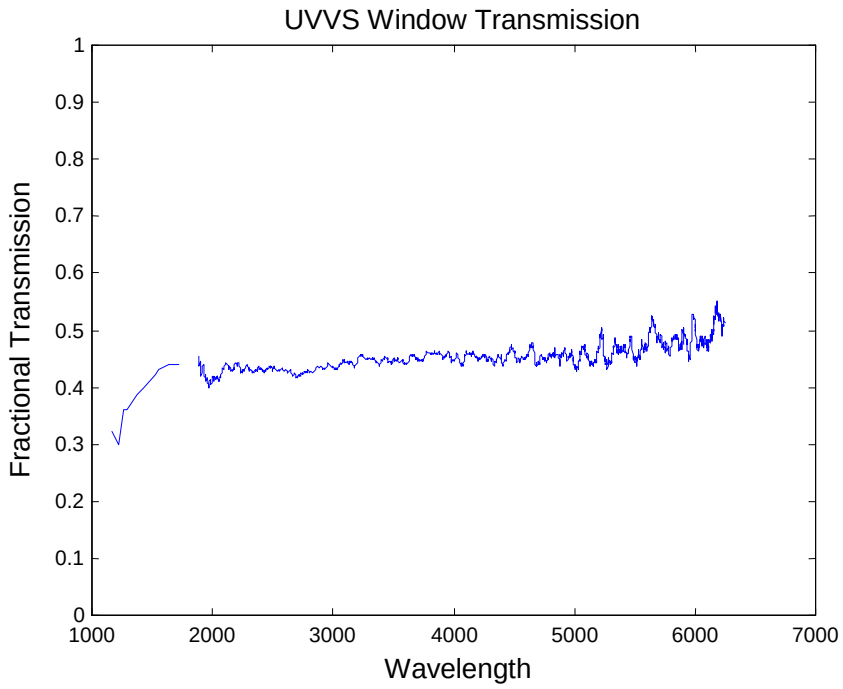

Figure 2.35. Transmission of light through the window compared to the transmission with the door in the open configuration. Note that the door is now open and will be for the remainder of the mission.

responsivity, $\overline{\Omega}$ is the effective field of view, and Sc is the grating scattered light that scatters out of the bandpass at position j into all of the other grating positions.

For an extended continuous source, the radiometric calibration determines $A * \Delta\lambda * R_c(\lambda_j) * \overline{\Omega}$, thus the sensitivity may be expressed as

$$Sen(\lambda_j) = \frac{C_{corr}(\lambda_j)/\Delta t}{L(\lambda_j)} \tag{2.8}$$

The light that is scattered into position j is determined by subtracting the convolution of the grating scatter function from Figure 2.24 with the count rate from the count rate. The light that is scattered out of position j is determined by integrating the curve of Figure 2.24 for all grating steps other than step j with the curve centered on step j.

For a point continuous source, where the telescope aperture is filled but the field of view is not, the radiometric calibration measures $A * \Delta\lambda * R_c(\lambda_j)$. The sensitivity is then given by

$$Sen(\lambda_j) = \frac{C_{corr}(\lambda_j)/\Delta t * \overline{\Omega}}{L(\lambda_j)} \tag{2.9}$$

where the effective field of view is determined from Section 2.7. Note that a single point source measurement only characterizes the sensitivity of one region of the photo-cathode active area, which typically varies from point to point. It is advantageous to take several point source measurements at different photo-cathode regions and then average the counts from the total number of measurements.

From Section 2.6, the measurement of a spectral line requires that in addition to the count rate being corrected for non-linearity, dark counts, scattered light, and stray light, the count rate must also be corrected for grating sampling. This is done numerically by dividing the sum of the count rate by the ratio of bandpass to grating step size.

2.13.2 Pre-launch calibration

Pre-launch radiometric sensitivity calibrations were performed both in vacuum and in the ambient environment. The vacuum calibrations consisted of a monochromatic point source at the focus of an off-axis parabolic mirror. This produced a collimated beam that filled the aperture but not the field of view, thus producing an irradiance at the instrument. Figure 2.2 shows the optical layout of the MOBI experiments. The beam was scanned by a NIST calibrated photo-detector at the same location as the instrument. The FUV and MUV channels were calibrated using this method.

The ambient atmosphere calibration was performed in a large clean room at Johns Hopkins Applied Physics Laboratory for both the VIS and MUV channels using NIST calibrated spectral lamps to irradiate a scattering screen. The scattering screen consisted of an aluminum plate coated in-house with Munsell 6080 barium-sulfate paint. Two lamps were used, an FEL F-540 and a deuterium RB-398, located at 198 cm and 99 cm normal to the screen, respectively. Each lamp had accompanying data sheets with tabulated irradiance values as a function of wavelength for a distance of 50 cm. The irradiance of the lamp was converted to a radiance according to

$$L = \frac{E * Refl}{\pi} * \left(\frac{50}{distance} \right)^2 \quad (2.10)$$

where E is the lamp irradiance, Refl is the screen reflectivity, π accounts for the light emitted from the screen per steradian and distance is the distance of the lamp from the screen. The instrument was placed at $\sim 20^{\circ}$ from the normal to the screen, close enough such that the projected field of view on the screen was small enough for light to completely fill both the telescope aperture and the field of view. Data from the deuterium lamp was used for sensitivity over the entire MUV spectral range and from 200 nm to 372 nm for the VIS channel. Data from the FEL lamp was used for the VIS channel sensitivity from 372 nm to 625 nm.

Atmospheric absorption was accounted for by placing the FEL lamp 393 cm from the screen and compared to spectra taken with the lamp at 198 cm. Furthermore, tabulated atmospheric absorption values as function of wavelength were provided by McClintock and interpolated to the relevant wavelengths of the sensitivity calibration.

The screen reflectivity was published in data sheets accompanying the barium-sulfate material and typically had values from 0.92 to 0.98. However, the reflectance was also a function of the roughness of the painted scattering screen. In addition, the lower wavelength of the data sheets was 225 nm.

The stray light in the laboratory that entered the instrument was measured by placing an occultation surface between the screen and lamp and then repeating the same experiments. The count rates from the occulted screen measurements were subtracted from the non-occulted measurements. Note that this also accounts for

subtracting off detector dark counts, thus the detector dark counts were not explicitly subtracted from the data.

Stray light from within the spectrometer, which is different from the laboratory stray light described above, is considered insignificant for the region of the spectra where count rates are high, but is included as a correction for the benefit of the lower count rate regions of the spectrum. Using the spectrometer stray light assessment from Section 2.9, the peak count rate was multiplied by 0.001, with the result subtracted from the count rate associated with each grating step.

The grating scattered light was accounted for by convolving the curve in Figure 2.24 with the count rate and then subtracting from the count rate at each grating step. The light scattered out of a grating step was accounted for by integrating the curve of Figure 2.24 and adding the result back to the data at that grating step. The sensitivity was determined by using Equation 2.8 with the radiance given by Equation 2.10.

2.13.3 Post-launch stellar calibration

Post-launch calibrations have been performed using known stellar sources in which the instrument field of view is raster-scanned across the star. This gives an opportunity to compare sensitivity curves with laboratory data as well as to monitor the degradation of the instrument sensitivity throughout the mission. Table 2.2 summarizes the stellar calibrations performed from launch to the present. The best signal for the VIS and MUV channel stellar calibrations was obtained from the α-CMa observation while the best signal for the FUV channel was obtained from the α-

Lyre observation. An example of the α-Cma data taken with the VIS channel is shown in Figure 2.36

The sum of the counts from each grating scan is shown in Figure 2.37, with the red stars representing the peak of each sweep. Note that the sensitivity of the VIS channel varies in the direction along the length of the slit. In order to compare with scattering screen experiments where the instrument observes an extended source, the grating scans corresponding to the peak values of Figure 2.37 were averaged together. This amounted to averaging 49 grating scans to produce an average point source response of the instrument as well as to increase the SNR due to using more counts. The SNR was increased further by binning the data to an effective bandpass of 10 nm. Similarly, for the MUV and FUV stellar calibrations, 10 and 11 grating scans were averaged, respectively, with binning to produce an effective 5 nm bandpass for both channels.

Since the star is a point source and does not fill the field of view, the sensitivity for a point source follows from Equation 2.9 but is shown here in order to demonstrate the conversion to units of kiloRayleighs.

$$\mathrm{Sen} = \frac{\dot{C}_{\mathrm{corr}} * 0.04^{\circ} * 1^{\circ} * \left(\frac{\pi}{180^{\circ}}\right)^{2}}{\mathrm{E}_{\mathrm{star}} * \frac{4\pi}{10^{9}}} \tag{2.11}$$

where $\dot{C}_{\mathrm{Corr}}$ are the counts/second measured by the detector, $\mathrm{E}_{\mathrm{star}}$ is the irradiance of

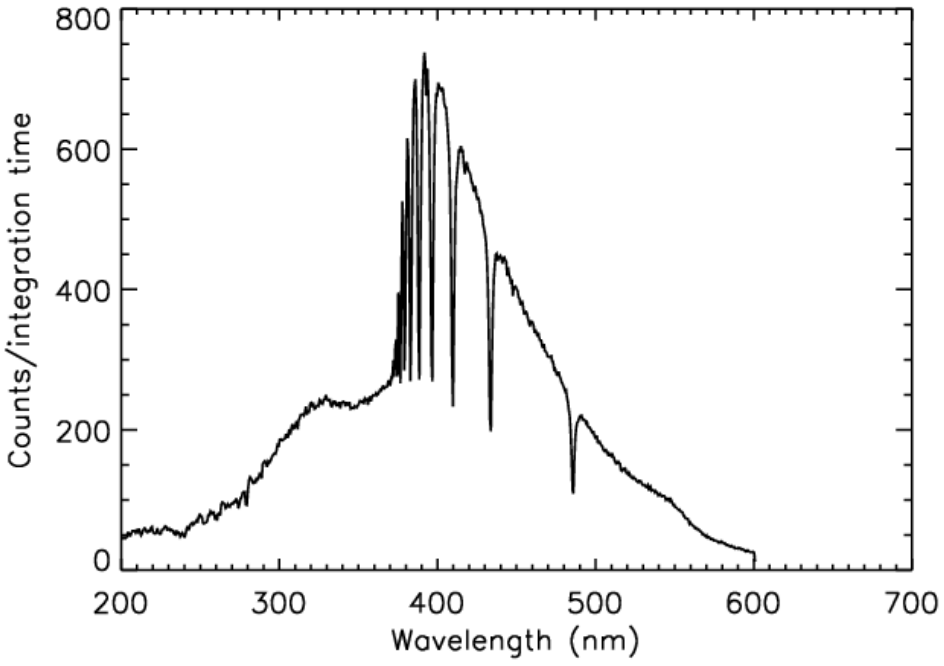

Figure 2.36. VIS channel spectra of α-Cma used to derive the sensitivity of the VIS channel after launch.

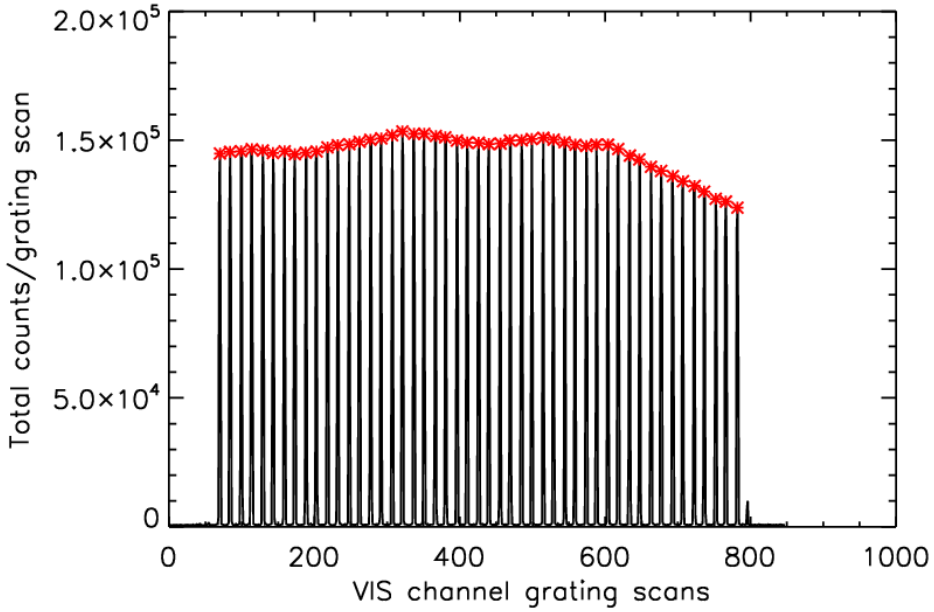

Figure 2.37. The sum of the counts in each grating scan of 660 grating steps while the instrument was being rastered across the star. The peak of each line, represented as a star, corresponds to the locations of the red stars in Figure 2.4.

the star in $\frac{\text{photons}}{\text{second} * \text{cm}^2}$, 0.04° is the slit width, 1° is the slit length, $\left(\frac{\pi}{180^\circ}\right)^2$ converts both angles to radians, and $\frac{4\pi}{10^9}$ is a conversion factor that allows for the sensitivity to be expressed as count rate per kilo-Rayleigh.

The dark counts were determined by taking the mean of the count rates associated with grating scans at the edge of the spacecraft raster scan, i.e., when the star was at the maximum off-axis angle from the field of view. This value was then subtracted from the stellar signal data. The scattered light was determined by multiplying 0.001 by the maximum count rate and subtracting the result from each grating step.

Figure 2.38 shows the radiometric sensitivity for continuous sources for all 3 channels of the UVVS and Figure 2.39 shows the spectral line sensitivity for all 3 spectral channels, which is the continuum sensitivity divided by the bandpass. Figures 2.40 – 2.42 show the continuum and spectral line sensitivities for each channel separately plotted on a linear scale. The results represent measurements performed in the laboratory as well as in flight. The FUV channel sensitivity was done in the laboratory in MOBI, whereas the MUV and VIS channel sensitivities from the laboratory were done using the scattering screen. All sensitivity for all 3 channels has been determined in flight using stellar sources.

The MOBI sensitivity curves agree with the stellar observation sensitivity curves to within a few percent for the FUV and MUV channels. However, larger discrepancies are noticed between the stellar observation sensitivity curves and the scattering screen sensitivity curves from the MUV and VIS channels. The discrepancy may be due in part to the explanation in Section 2.13.2. The reflectance

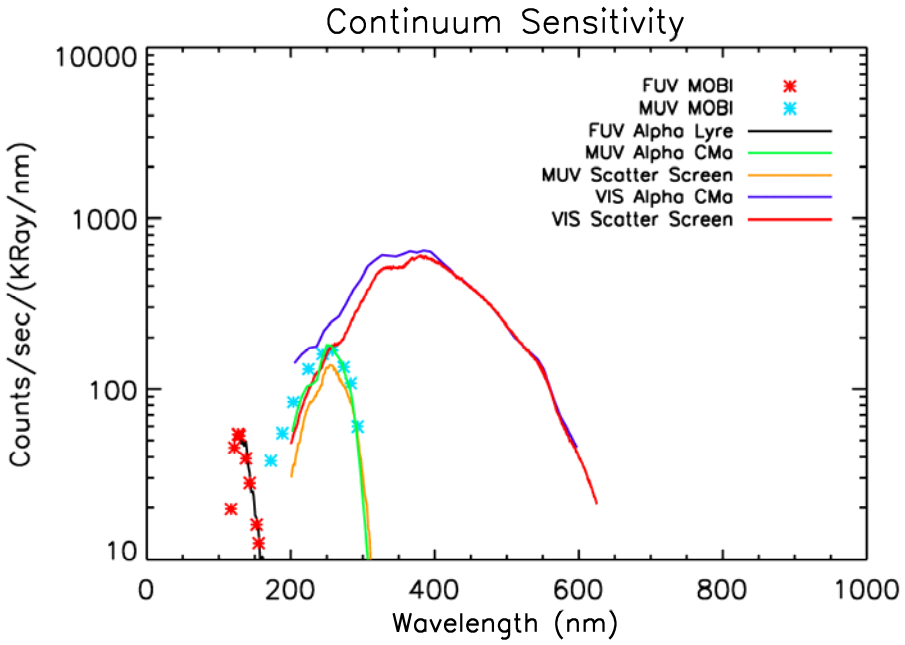

Figure 2.38. Radiometric sensitivity of a continuous source for the FUV, MUV, and VIS channels. The FUV sensitivity was determined by both MOBI and stellar calibration measurements.

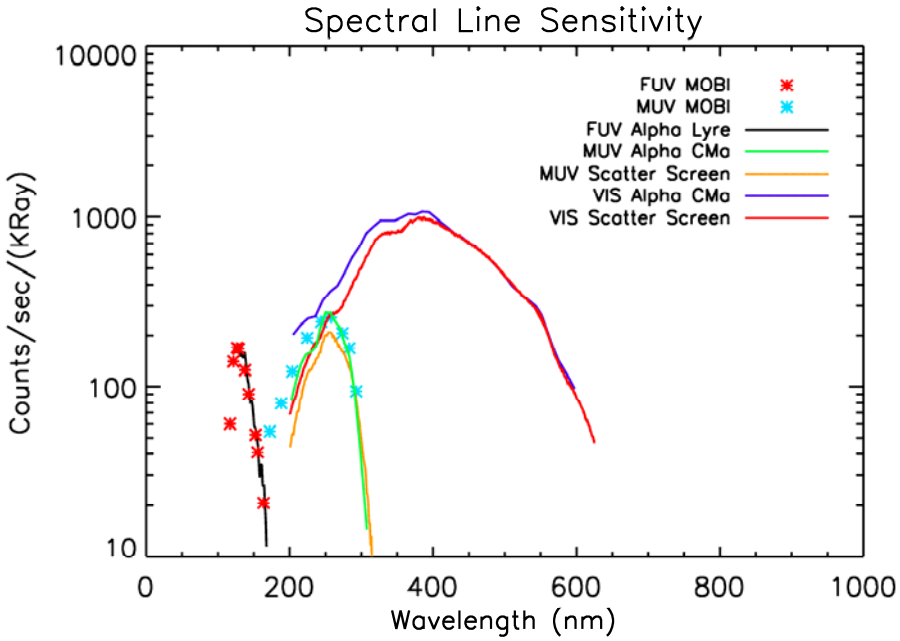

Figure 2.39. Spectral line radiometric sensitivity of FUV, MUV, and VIS channels. These curves are the continuum sensitivity curves divided by the bandpass of each channel, respectively.

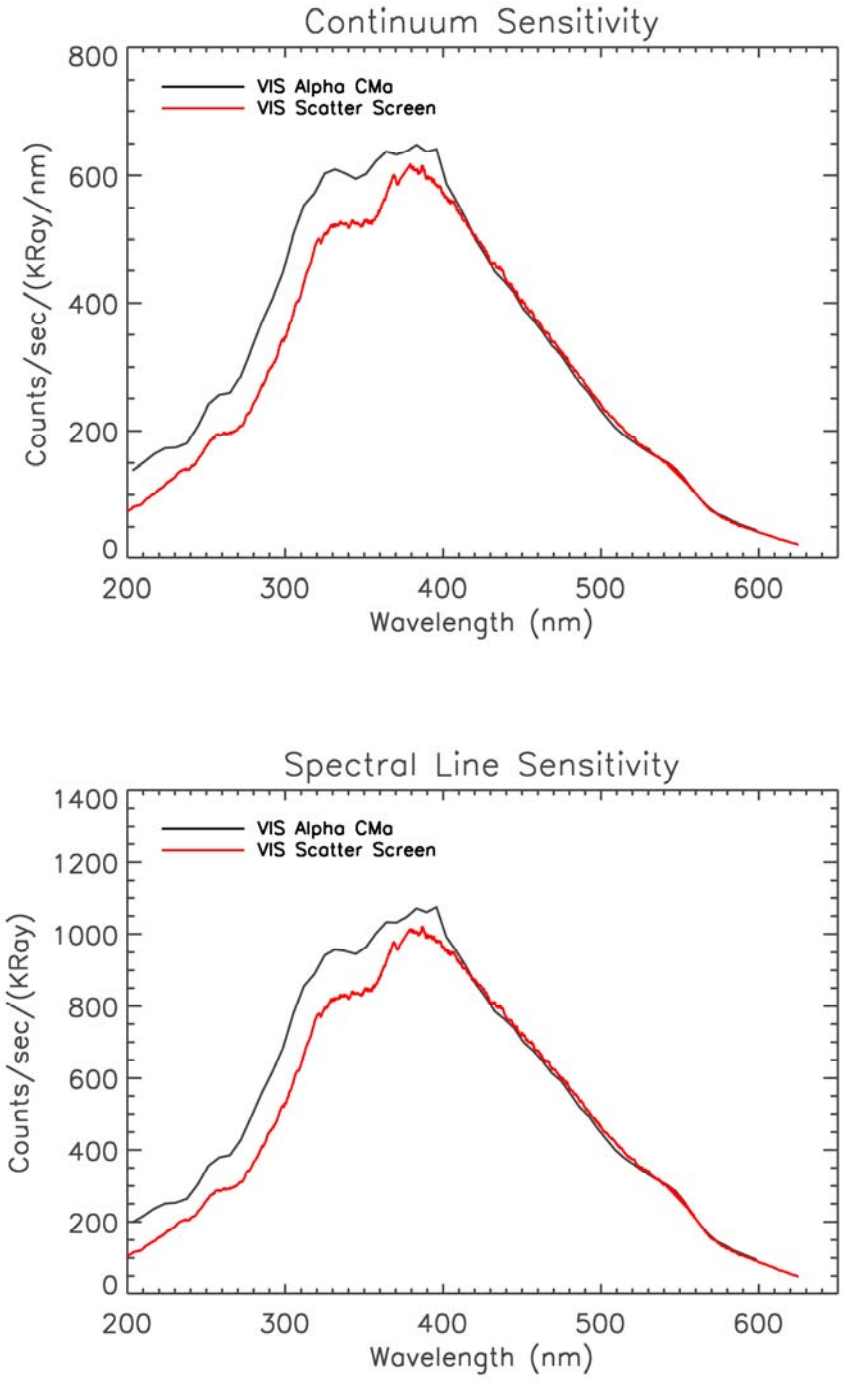

Figure 2.40. Continuum and spectral line sensitivity for the VIS channel plotted on a linear scale.

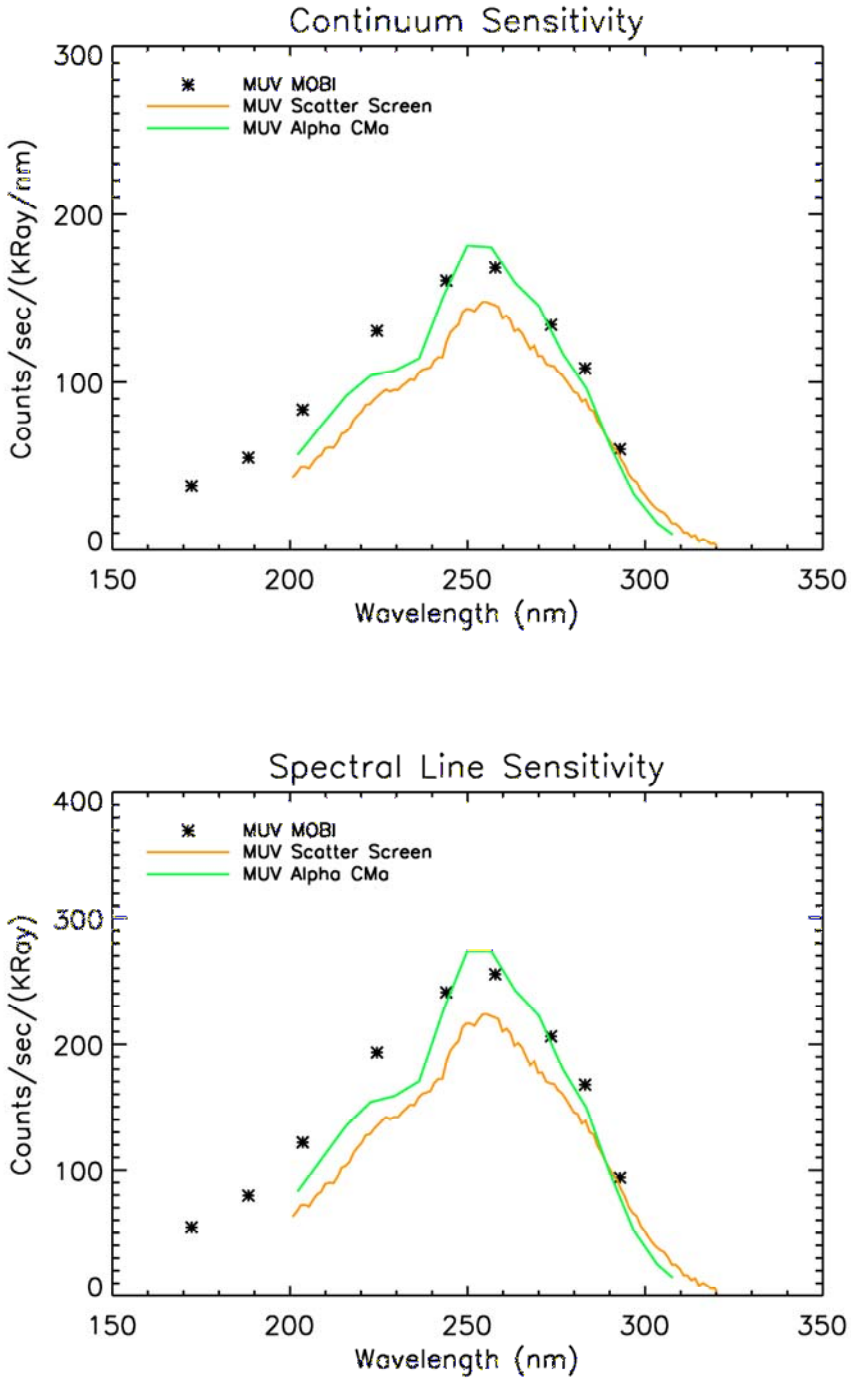

Figure 2.41. Continuum and spectral line sensitivity for the MUV channel plotted on a linear scale.

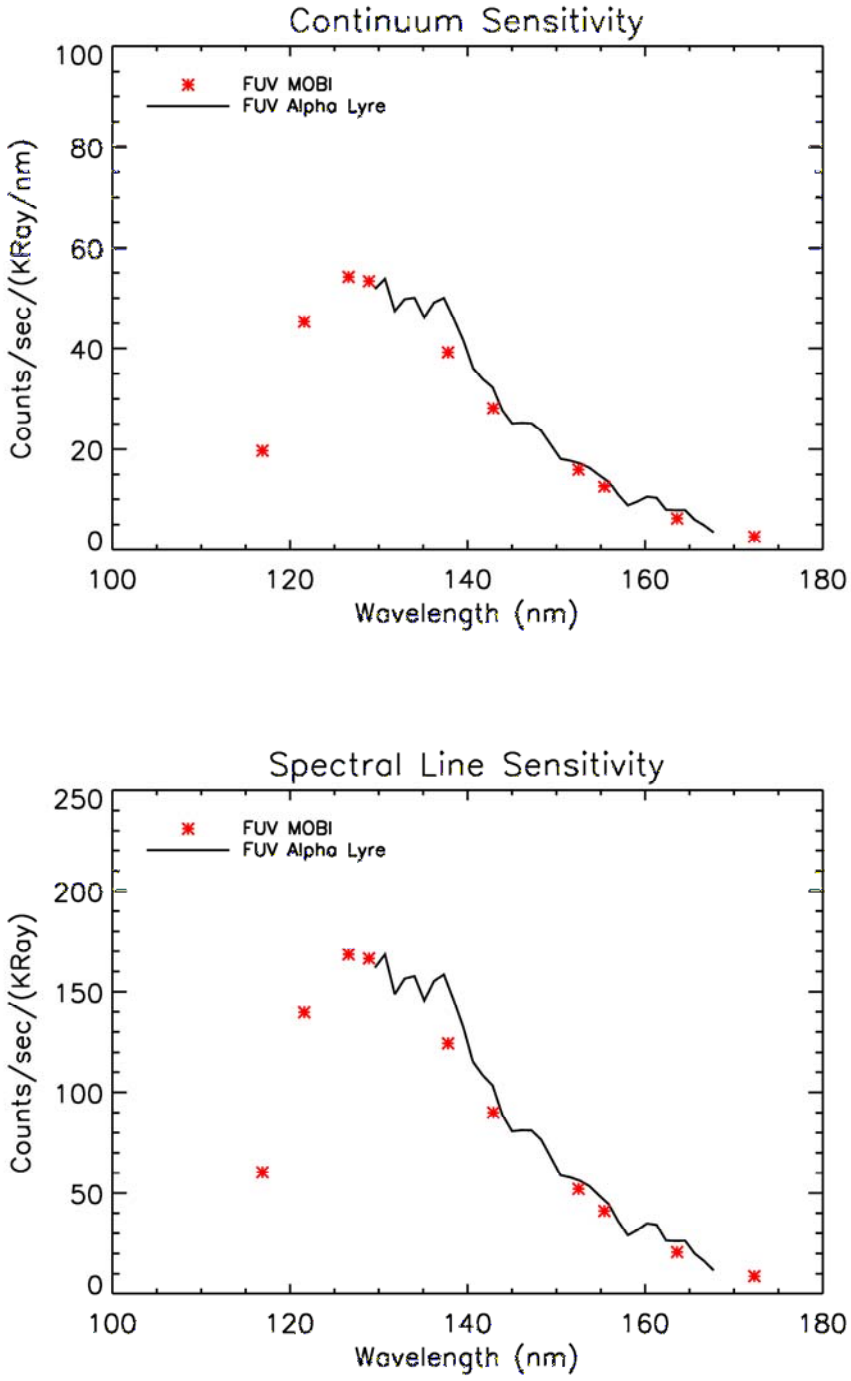

Figure 2.42. Continuum and spectral line sensitivity for the FUV channel plotted on a linear scale.

values for the barium sulfate paint used for the scattering screen may not represent the overall reflectance of the screen and thus may be misleading

2.14 Dead time correction

As photons arrive at a pmt, pulses are generated and fed to an AMPTEK A-111 charge sensitive preamplifier-discriminator. The A-111 produces an output with pulse width determined by the bias on the amplifier. If a second input pulse arrives at the A-111 before the output pulse has finished, then this second pulse is not counted.

Assume a photon arrival rate of R. Figure 2.43 shows two pulses from the PMT arriving at the A-111. If τ_1 is longer than τ_2, the second pulse will not be counted. Due to the statistical nature of photon arrival rates, a photon arrival rate less than the pulse width duration may still lead to the temporal difference in consecutive input pulses being smaller than the output pulse width duration, resulting in missed counts. The probability of missed counts increases as the arrival rate increases. The corrected count rate is given by

$$C_{corr} = \frac{C}{(1 - C * \tau)} \tag{2.12}$$

When the average arrival rate becomes as short as the pulse width, a saturation effect is reached where the correction factor does not accurately correct for photon arrival rate. The dead-time correction was measured to be 620 ns, 519 ns, and 498 ns for the VIS, MUV, and FUV channels, respectively.

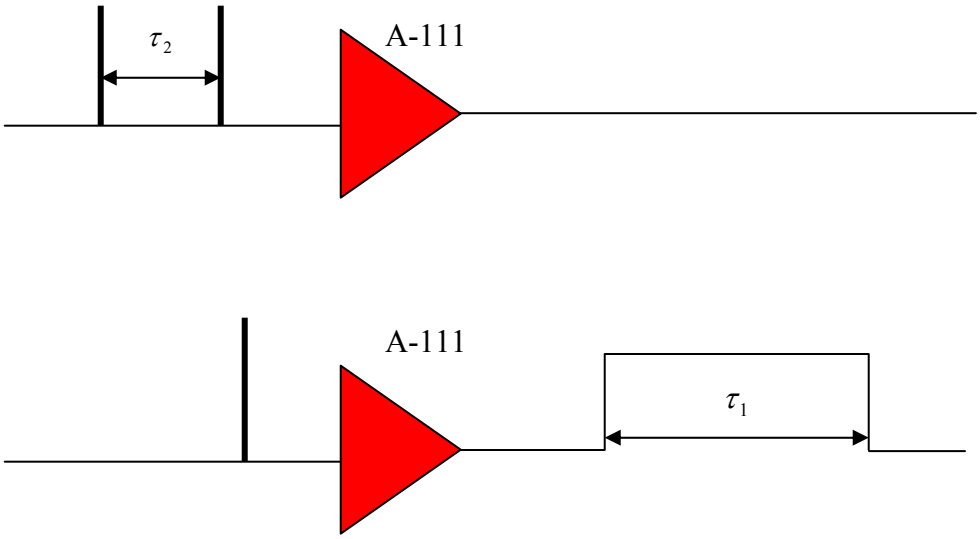

Figure 2.43. Schematic of two pulses arriving at the input of the A-111 preamplifier-discriminator.

2.15 Summary

The relation of the atmospheric and surface slit boresights to one another was measured in ground based calibrations and found that the center of the surface slit was 0.01° offset from the center of the atmospheric slit in the Y-Z plane. Post-launch stellar calibrations confirmed this and also allowed for the determination of the boresights of both slits with respect to the spacecraft axes. The mean of the direction cosines of the mean boresight of the atmospheric and surface slits in the spacecraft body frame are [0.00102281, 0.0024908088, 0.999984] and [0.000932230, 0.0023419775, 0.999997], respectively. The length of the atmospheric slit is closely aligned with the spacecraft Y axis.

The dark counts show an exponential dependence with increasing temperature as predicted from the data sheets of the photomultiplier tubes. Preliminary post-launch calibrations indicate that detector dark counts may be ~ 10X the ground value for lower temperatures.

Wavelength scale measurements are consistent with calculated values to within ~ 0.05 nm. All three channels show nearly the same dependence of wavelength scale on temperature, with a maximum deviation < 0.4 grating steps for the highest temperatures.

The point spread function behaves in a manner consistent with calculated values given the physical parameters of the spectrometer. Thermal tests show that the point spread function typically varies by less than 5% of the mean for each of the three channels over the expected operational temperatures for the mission and also shows a small dependence on grating step.

The measured field of view is consistent with the predicted values based on telescope focal length and entrance slit width. The surface slit is out of focus in the spatial direction and is demonstrated by the non-sharp roll-off of the signal from the peak value.

Spectrometer scattered light drops by several orders of magnitude over a small grating step range. A large lobe exists at ~ 50 grating steps shortward of the central grating step position.

Spectrometer stray light is ~ 0.1% of the peak value for observing a broad spectrum such as the reflected solar spectrum from the lunar surface. This is typically only significant in spectral regions where very low signal is expected.

The absolute value of the polarization ranges from 0% at short wavelengths to 80% at long wavelengths. Results are similar to the Galileo UVS (Hord, et. al., 1992) that covered a spectral range from ~ 220nm to ~ 420 nm.

The telescope off-axis response to a point source dropped by several orders of magnitude over 1° for both the spectral and spatial directions. Note that for the spatial direction, the width of the slit is significant enough that it must be accounted for. A 2 dimensional extended source off-axis model was developed based on pre-launch and post-launch point source measurements. The point source measurements were used to create a 2-dimensional point-source off-axis response that was convolved with an extended source comparable in size to Mercury during exospheric observations. The model shows reasonable agreement to off-axis light measurements taken during the Venus flyby where the angular diameter of the planet was 60°. In lieu of a uniform data set of extended source off-axis measurements covering a full

range of angles, assumptions were made concerning the off-axis response and are listed in Section 2.11. The off-axis model is subject to updates pending further off-axis calibration measurements that may be made during the mission.

The window transmission was typical for the transmission properties of MgFl. However, since the contamination cover is now open and will remain open for the duration of the mission, the window transmission does not need to be factored into the data. For future reference, the contamination cover was still closed for the first 3 stellar calibrations (Table 2.2).

The radiometric sensitivity was best determined from MOBI experiments and from stellar calibrations. The stellar calibrations give similar results to the MOBI results and should therefore be well suited for tracking future instrument degradation. Note that FUV stellar calibration is difficult around the lyman alpha absorption feature due to interstellar absorption of starlight by hydrogen.

The non-linearity has been demonstrated to be significant for count rates exceeding 10^5 for the VIS channel. The correction made a significant difference in the lunar surface observations and will certainly be required for Mercury surface observations.

Chapter 3

Mercury's Surface Bounded Exosphere

3.1 Introduction

3.1.1 General description of the exosphere

The Mercurian atmosphere is characterized by a tenuous collection of atoms and possibly some molecules, each of which are on ballistic orbits, satellite orbits, or escaping trajectories. For each species, the collective source and loss rates are such that a thick atmosphere never accumulates; thus collisions among air-borne atoms are rare, allowing the mean free path of an atom to be at least as large as a typical scale height. Furthermore, since atom-atom collisions are rare, the only collision an atom typically may experience is a collision with the surface. This implies that the correct definition of Mercury's atmosphere is that of a surface-bounded exosphere where each species of atom may be considered to act independently of other species and the exobase is the surface of the planet. To date, only hydrogen, helium, oxygen (Broadfoot, 1976), sodium (Potter and Morgan, 1985), potassium (Potter and Morgan,1986), and calcium (Bida et al., 2000) have been observed at Mercury. Table 3.1 gives information about abundances of each species (Hunten et al., 1988). Other

Known species	**Number density cm^{-3}**
H	23, 230 (hot and cold components)
He	6.0×10^{3}
O	4.4×10^{4}
Na	$1.7 - 3.8 \times 10^{4}$
K	5×10^{2}
Ca	~ 10^{-1} (Mangano et al., 2007)

Table 3.1. Known exospheric species. All values but Ca are taken from Hunten (1988).

species that are expected to be observed at Mercury are magnesium, silicon, argon, iron, OH, aluminum, and sulfur.

The strong coupling between exospheric atoms, Mercury's weak magnetic field and the IMF, and the surface has profound consequences for Mercury's exosphere. The interaction between Mercury's magnetic field and the IMF affect the exosphere by 1) creating cusp regions where solar wind ions, which would otherwise be deflected under quiet sun conditions, may be funneled down to impinge on the surface and 2) by transporting recently ionized exospheric atoms either out of the exosphere or back to the surface. Modeling of sodium ions within Mercury's magnetosphere (Killen et al., 2004a) suggests that 60 % of sodium ions are recycled back to the surface of the planet, while the other 40 % are lost to the solar wind.

Since the exobase is the surface of the planet, gas-surface interactions are important but poorly constrained. An atom that encounters the surface may be either physically adsorbed or chemically absorbed. Hunten et al. (1988) describes physical absorption as physical-scale bonding of an atom to the surface with bonding energies < 0.5 eV and chemical-scale bonding of an atom to the surface with bonding energies > 0.5 eV. The amount of energy that an atom exchanges with the surface is described by the energy accommodation coefficient, and following the convention by Hunten et al. is given by

$$\alpha = (E2 - E0)/(E1 - E0) \tag{3.1}$$

where E2 is the final energy, E1 is the mean energy of thermally accommodated atoms with the local surface temperature, and E0 is the initial energy.

Hunten et al. (1988) defines source atoms as those atoms that have been released from the surface but have not come back and interacted with the surface, while ambient atoms are those that have had at least one encounter with the surface after the initial release process. With these definitions, a significant component of the exosphere consists of ambient atoms making ballistic hops on the surface, especially the heavier atoms, where the atoms eventually either stick to the surface and await ejection back into the exosphere by a source process or become photoionized. A smaller fraction of the heavy atoms as well as most of the hydrogen and helium probably do very little hopping but escape to the interplanetary medium.

3.2 Overview of the sodium exosphere

Since the discovery of sodium in Mercury's exosphere in 1985 by Potter and Morgan, observations have shown sodium to be highly variable both temporally on timescales of days (Killen et al., 2001) and spatially in terms of dawn-dusk asymmetries (Sprague et al., 1997), high latitude enhancements typically with north-south asymmetries (Potter et al., 1999; Sprague et al., 1997), and an extended sodium tail in the anti-sunward direction driven by radiation pressure (Potter et al., 2002).

3.2.1 High latitude enhancements

Potter et al. (1999) observed over a 6 day period and noted initially that sodium emission was relatively uniform over the dayside, then a high latitude enhancement of sodium appeared in the southern hemisphere, moved to the northern hemisphere, and then back to the southern hemisphere. Over the six days the total amount of visible sodium in the exosphere increased from 1.39×10^{28} atoms to 4.23×10^{28} atoms, or about a factor of 3. Sprague et al. (1997) show high latitude enhancements from observations in 1987 and then in 1988. The observations from 1987 show that northern and southern abundances exceeded equatorial values by a factor of 2 and then a day later abundances were similar at all latitudes. Observations in 1988 also showed higher abundances in the northern and southern hemispheres compared to the equatorial regions. In addition, the northern enhancement abundance was about 4 times larger than the southern enhancement abundance.

An explanation based on IMF-magnetic field considerations suggests that high latitude enhancements may be present due to solar wind sputtering (Killen et al.,

2001, Killen et al., 2004a, Sarantos et al., 2001), which could be modulated by fluxuations in the IMF and solar wind. Modeling by Sarantos (2001) shows that open cusp regions that arise due to the interconnection of the IMF with Mercury's magnetic field could allow considerable numbers of solar wind ions to impact onto localized regions of the planet, thereby sputtering sodium from the surface. Depending upon the orientation of the IMF, the cusp regions could favor either the northern or southern hemisphere. Potter et al. (1999) note that there were a number of CME events that occurred during their observations, some of which were directed in the vicinity of Mercury. Alternatively, it has been proposed that spatially localized sodium bright regions in either the northern or southern hemisphere could be associated with regions of enhanced sodium surface concentrations. As the planet rotates and brings the enhanced region to small enough solar incidence angles, the region would become hot enough so that an observable increase in the flux of vaporized sodium would occur (Sprague et al., 1998). This explanation is based on radar bright spots that have been observed on Mercury's surface as well as the Caloris Basin region, above which sodium emission line enhancements were observed. Killen et al. (2001) present observations above the Caloris basin and noted that no enhancements of sodium emission seemed to be correlated with the Caloris basin.

3.2.2 Dawn dusk asymmetries

Sprague et. al (1997) conducted observations of 5 sectors spanning Mercury's dayside at equatorial and mid-latitude regions. Their results showed that morning and midday column abundances were 3 times larger than the afternoon sectors. Potter et

al. (2006) present observations over 94 separate days from 1997 to 2003 and were able to capture sodium images over a wide range of Mercury true anomaly angles. The results show dawn side enhancements that are modulated by radiation pressure variations, with peak dawn side enhancements ~ 2.5 greater than non-dawn side regions during peak radiation pressure. During minimum radiation pressure, the dawn side to non-dawn side ratio dropped to ~ unity. The dusk side to non-dusk side ratio was typically less than unity and did not seem to vary with true anomaly angle; implying a deficit of sodium in the dusk terminator hemisphere.

Hunten and Sprague (2002) offer an explanation that sodium ions are implanted on the nightside from the magnetotail, where they are then available to be released at sunrise. Further enhancements could be due to dayside sodium atoms accommodated to the surface temperature that have a tendency to become cold trapped near the terminator or on the night-side of the planet. Radiation pressure could also act to push some of the dayside sodium to the nightside (Ip, 1990; Sprague et al., 1997; Leblanc and Johnson, 2003, Potter et al., 2006). This explanation could account for the radiation pressure dependence observed by Potter et al (2006). Killen has offered an alternative explanation that dawn dusk asymmetries could be the result of the tendency of the magnetic field to transport exospheric sodium ions towards the dawn terminator (Killen et al., 2004b), where they stick to the surface and neutralize, and thus collect to form an enhanced surface concentration of sodium.

3.2.3 Extended Sodium Tail

Models have predicted the existence of a radiation pressure driven extended sodium tail (Ip, 1986, Smyth and Marconi, 1995, Leblanc and Johnson, 2003), where radiation pressure would push sodium atoms in the anti-sunward direction. Radiation pressure on a sodium atom at velocity = 0 with respect to the planet varies by a factor of ~ 16 from its minimum value at aphelion to its maximum value at a true anomaly of ~ 64 degrees. Potter et al. (2002) have published observational results that seem to confirm this relationship and are presently still performing ground-based observations at other planetary true anomalies (Killen, private communication, 2005). Figure 3.1 shows a simple model of sodium atoms ejected from discrete locations on the dayside surface with their trajectories terminating either after impact with the surface or after a 10,000 second photoioization time. The atoms are ejected over a range of initial velocities with two figures showing the lower and higher ejection velocities, respectively. The planet was at a true anomaly of 64°, thus the sodium atoms experienced maximum radiation pressure. For ejection velocities from 274-1738 m/s, the time of flight before impacting the surface is short enough that radiation pressure never has time to transport the atoms away from the planet into the tail region; although for the ejection energies near 1738 m/s the atoms launched from the terminator migrate to the nightside. For ejection velocities from 1943-4759 m/s the times of flight of the atoms are large enough that radiation has time to transport the atoms to the tail region. An interesting phenomena is that for velocities from ~ 1943 m/s to ~ 2600 m/s, the relative influence of radiation pressure and planet gravity is such that atoms ejected from one hemisphere of the planet are transported to the tail

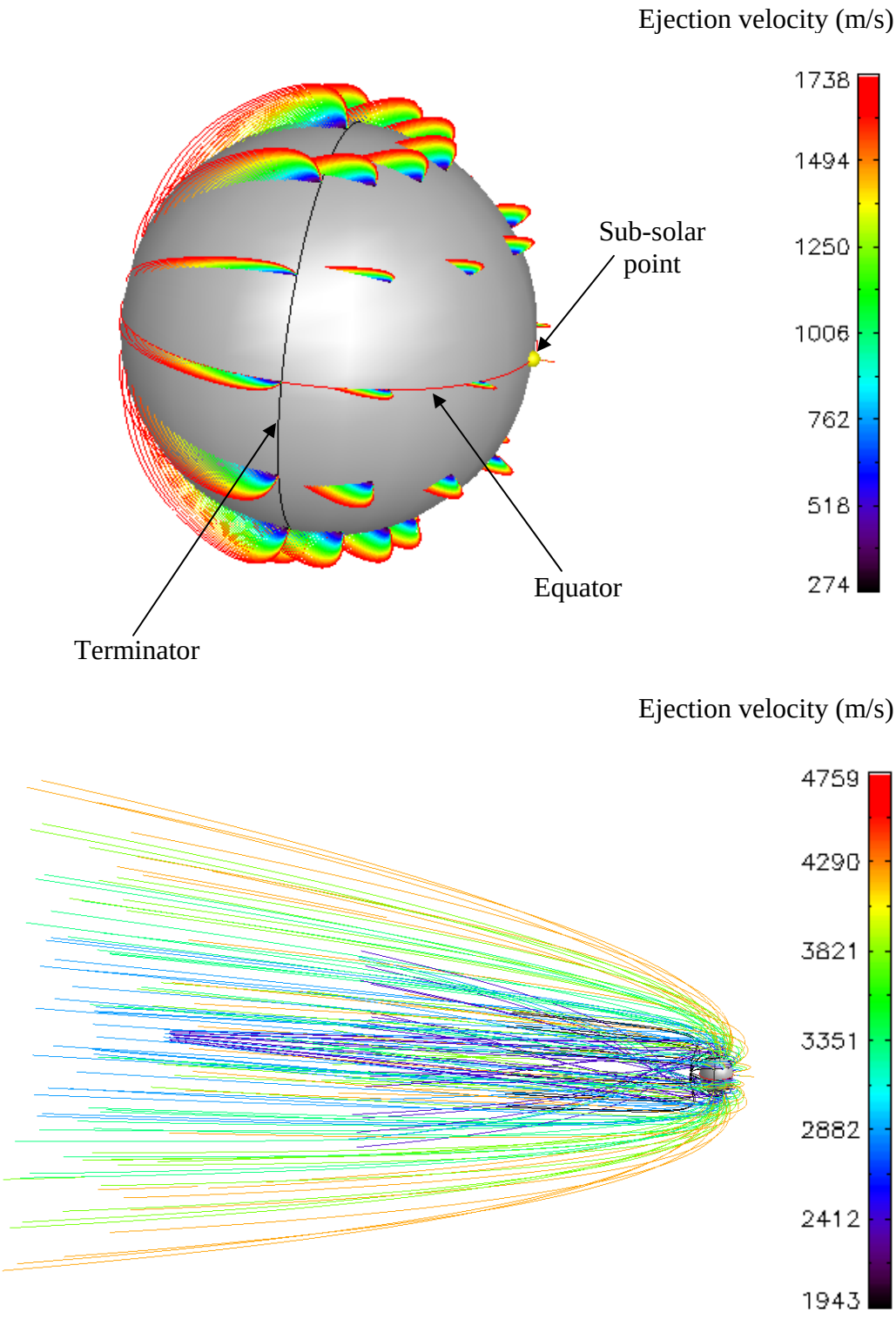

Figure 3.1 Two energy regimes of the sodium tail at a planetary true anomaly of 64 degrees. All atoms are ejected normal to the local surface.

region corresponding to the opposite hemisphere; whereas atoms with initial velocities greater that ~ 2600 m/s remain on the side of the planet from which they started. The above values are only approximate since the transport of atoms also depends on cosine of the zenith angle of the ejection point, i.e., atoms ejected near the sub-solar point are driven back down near the sub-solar point since radiation pressure is acting normal to the surface at that location. Furthermore, the simple model depicted in Figure 3.1 does not account for the relative probability of atoms ejected at a specific velocity for a source process nor does the simple model account for the dependence of source rates on surface location, i.e., for most source processes, there is a lower probability for atoms to be ejected from the terminator region. Also, in this simple model each atom is ejected normal to the local surface, but in reality most atoms are ejected at a non-zero angle with respect to the surface normal. However, the model does give a general sense of how atoms that are found in the tail must have initially had large ejection velocites. Table 3.2 gives the most probable ejection velocity for a source process, which implies that atoms found in the tail region must have originally had ejection velocities in the high energy tail of a given source process. The physics that governs radiation pressure is described in Section 3.4.1.

3.2.4 Smoothly varying sodium component

The key source processes for sodium include photon stimulated desorption, thermal vaporization, meteoritic vaporization, and solar wind sputtering (Table 3.2). The key loss processes that remove neutral sodium from the exosphere include photo-ionization followed by transport along the IMF, dayside surface capture, gravitational

Source/Loss Process	**Spatial Variability (assuming isotropic surface density)**	**Temporal Variability of column abundance**	**Typical Scale Height (km)**	**Typical time of flight (s)**	**Most probable ejection speed (m/s)**
Photon Stimulated Desorption	Azimuthal symmetry about sub-solar point, weakly dependent on local time	Weak seasonal dependence	~ 100 (sub-solar)	~ 330	~ 870 to ~ 1060
Thermal Vaporization	Azimuthal symmetry about sub-solar point, strongly dependent on local time	Strong seasonal dependence	~ 50 (sub-solar)	~ 230	~ 550 to ~ 730
Meteoritic Vaporization	Homogenous around planet or possible leading edge enhancement	Weak seasonal dependence	~ 230	~ 500	~ 1500
Solar Wind Sputtering	Localized regions at mid to high latitudes	Highly variable on timescales of days	~ 150	~ 400	~ 1060

Table 3.2. Four major sodium source processes with corresponding characteristics.

escape, and lateral transport to the nightside, Smyth and Marconi (1995). It is possible that there may be an orderly varying component to the sodium exosphere where a steady state condition exists between slowly varying source and loss processes and is modulated by radiation pressure (Killen, 1990). This would serve to maintain a sodium exosphere that varies temporally on timescales comparable to seasonal changes and spatially in a manner that coincides with predictable physical source processes. The plausibility of this hypothesis is based on the fact that in the absence of enhanced surface regions of sodium concentration or ion sputtering regions the majority of the key source processes are temporally smoothly varying functions of planetary true anomaly and spatially smoothly varying functions of geometry. Since Mercury's eccentricity is ~ 0.206, variations in the planetary true anomaly implies large variations in Mercury-Sun distance (Chapter 1). Thus the solar photon flux varies by ~ 57 % from perihelion to aphelion, assuming constant solar output over a 44 day period. Photon stimulated desorption and thermal vaporization source rates as well as photo-ionization are proportionally affected; meteoritic vaporization is also affected by solar distance but follows a different power law variation with solar distance (Section 3.3.3). Regardless of the source process, the ambient component of sodium may become partially or fully accommodated to the surface temperature; thus the Mercury-Sun distance also affects the ambient component through surface temperature variations. Geometrically, photon stimulated desorption and thermal vaporization source rates are symmetric about the sub-solar point due to azimuthal symmetry of photon flux and surface temperature. Meteoritic

vaporization may be homogeneous or show a leading edge enhancement; however the source rate should still follow a predictable geometry.

3.3 Source process physics

3.3.1 Ion Sputtering

Ion sputtering is a process where solar wind ions impact the surface of the planet and sputter atoms from the surface. Ion sputtering has been studied both experimentally with lunar samples as the target surface (McDonnell and Flavill, 1974) and with Monte-Carlo models (Flavill et al., 1980). Sputtering is described as occurring when ions or atoms of at least a few electron volts impact a solid surface and a recoil from the incident particles momentum is transferred to an atom near the surface in the target surface. This can lead to near-surface atoms acquiring energy greater than the binding energy of the lattice and being ejected. Typical binding energies for Mercury are in the range of 1.2 to 2.65 eV. The number of atoms released from the target surface per the number of incident particles is defined at the yield, Y. Results from experiments indicate that impacting solar wind ions composed of H^+, He^{2+}, and heavier ions traveling at 400 km/s produces a yield of 1/24, 0.3, and 10 respectively. Killen (2001) computes a total yield by weighting each of the above yields by their respective number density in the solar wind and summing the result. Using number densities of 95%, 4%, and 1% for H^+, He^{2+},and heavier ions, respectively gives

$$Y_{ion} = \frac{1}{24} * 0.95 + 0.3 * 0.04 + 10 * 0.01 \approx 0.15 \ \frac{\text{atoms}}{\text{ion}} \qquad (3.2)$$

The issue of how ions get from the solar wind to the surface of Mercury has been the subject of debate. Since Mercury is known to possess a weak magnetic field, a magnetopause should be in place and therefore deflect the solar wind from most of the planet. Using an analogy with the Earth-magnetosphere-solar wind system, ions should only enter the magnetosphere in the cusp regions close to either pole. Sarantos et. al. (2001) conducted magnetospheric-IMF modeling studies to show that the size and location of open cusp regions are modulated by the relative sizes of the IMF spatial components. As the IMF turns more southward with respect to Mercury, interconnection with Mercury's magnetic field opens up a larger cusp region that is shifted closer to the equator and allows solar wind ions to penetrate into the magnetopause and impact the surface. Since the IMF and solar wind are temporally variable, the size and location of the open cusp regions are somewhat chaotic. Thus the amount of ion sputtering is a temporally and spatially highly variable source process.

For a given cusp region, the rate of sodium ejected from the surface due to ion sputtering is given by

$$\text{Rate}_{\text{ion}}\left(\frac{\text{Na}}{\text{cm}^2\text{s}}\right) = \text{Y}_{\text{ion}} * \text{f}_{\text{na}} * \text{v}_{\text{wnd}} * \rho_{wnd} * \text{f} \qquad (3.3)$$

where Y_{ion} is the yield defined earlier, f_{na} is the fraction of sodium in the surface, v_{wnd} is the velocity of the solar wind, ρ_{wnda} is the density of the solar wind at Mercury, and f is the ratio of the cross-sectional area of the solar wind that gets funneled into the cusp region to the area of the cusp region at the surface. Using

v_{wnd} = 3.22 km/s, $\rho_{wnda} = 169 \frac{ion}{cm^3}$, Y=0.15, f_{na}=0.005, and f = 2 gives a sputtered flux of sodium of $8.16 * 10^6 \frac{na}{cm^2 s}$.

Recycling of photoions back to the surface and secondary sputtering has been studied by Killen et al. (2004a) as well as Ip (1993). After a sodium atom is sputtered from the surface by any process, it is subject to photoionization, and consequently experiences transport in addition to gravitational attraction due to the magnetic field of Mercury. Killen and Sarantos followed the trajectories of sodium ions ejected from the dayside of the planet. The results indicate that about 60% of the photoions reimpact the surface with about 40% impacting the dayside. However, typical energies of the dayside re-impacting ions are on the order of 10 to 100 eV. As a comparison, the mean weighted energy of the solar wind ions based on the values of the proportion of the species given above as well as a velocity of 400 km/s and using sodium as representative of the heavier ions

$$\begin{aligned} \overline{E} &= \frac{1}{2} m_{H^+} v^2 * 0.95 + \frac{1}{2} m_{He^{2+}} v^2 * 0.04 + \frac{1}{2} m_{Na^+} v^2 * 0.01 \\ &\approx 1117 \text{ eV} \end{aligned} \tag{3.4}$$

Recall that for these solar wind conditions the yield was only 0.15. This comparison serves to illustrate that re-impacting photoions do not have enough energy to produce significant secondary sputtering. Ip studied the energy and trajectories of sodium ions that were on the night-side. Although these ions may acquire large amounts of

energy in the night-side region of the magnetosphere, the high energy ions impact on the night-side, which probably causes sputtering but is beyond the scope of this work.

Both theoretical and experimental research has been done on the sputtered energy distributions. Sigmund (1981), through theoretical arguments, determined that the energy distribution of sputtered particles is given by

$$f(v) \propto \frac{E_e}{(E_e + E_b)^{3-2*m}} \tag{3.5}$$

where E_e is the energy of the ejected atom, E_b is the binding energy, and m is a value that depends on the characteristics of the material being sputtered. The peak of the energy distribution was shown to be given by $E_{max} = \frac{E_b}{2}$. Weins et al., (1997) performed experiments on powdered Na_2SO_4 cold-welded together in a KBr press. Impacting ions were provided by a 200 μm beam of Ar+ ions that were normally incident on the target. The velocity distribution for sodium was fit with the distribution of Equation 3.5 with m = 0, a value appropriate for sputtered metals, and is shown in Figure 3.2. Wurtz and Lammer (2003) gave an expression for the sputtered energy distribution that also accounts for the incident ion energy:

$$f(E_e) \propto \frac{E_e}{(E_e + E_b)^3}\left\{1 - \left[\frac{(E_e + E_b)}{E_i}\right]^{1/2}\right\} \tag{3.6}$$

This is the distribution that is used for this work with a binding energy that ranges from 1.2~2.65 eV and a peak energy equal to half this range. Using $E = \frac{1}{2}mv^2$ gives velocities corresponding to the peak energy range of 2244 m/s to 3334 m/s.

3.3.2 Photon stimulated desorption

Photon stimulated desorption is a process where solar photons strike the surface of the planet and liberate atoms. Experimental studies of the desorption of sodium from various oxides have been done by Madey et al., (1998) and Yakshinskiy and Madey (1999) as well as desorption of sodium from a lunar basalt sample (Yakshinskiy and Madey, 2004). Yakshinskiy and Madey describe photon stimulated desorption as occurring via two processes. One, an electron is freed from the substrate and attaches to a Na+. This places the now neutralized Na atom in a repulsive configuration with the surface and consequently causes the Na to desorb (Yakshinskiy and Madey, 1999). Two, photons excite neutral sodium so that the atom is placed in an excited state and desorbs (Madey et al., 1998). Experimental values of the cross section for photon stimulated desorption of sodium for ambient substrate temperatures, i.e., 300 K, have been determined by Yakshinskiy and Madey (1999) to be to be $Q_{photon}(300K) \approx (3 \pm 1) * 10^{-20} cm^2$ for photon energies > 4 eV. For photon energies < 4 eV little or no desorption occurs. Values of Q_{photon} specific for Mercury are debatable due to lack of knowledge about the surface characteristics, i.e., porosity, composition, etc. This model uses $Q_{photon}(300K) = 1 * 10^{-20} cm^2$.

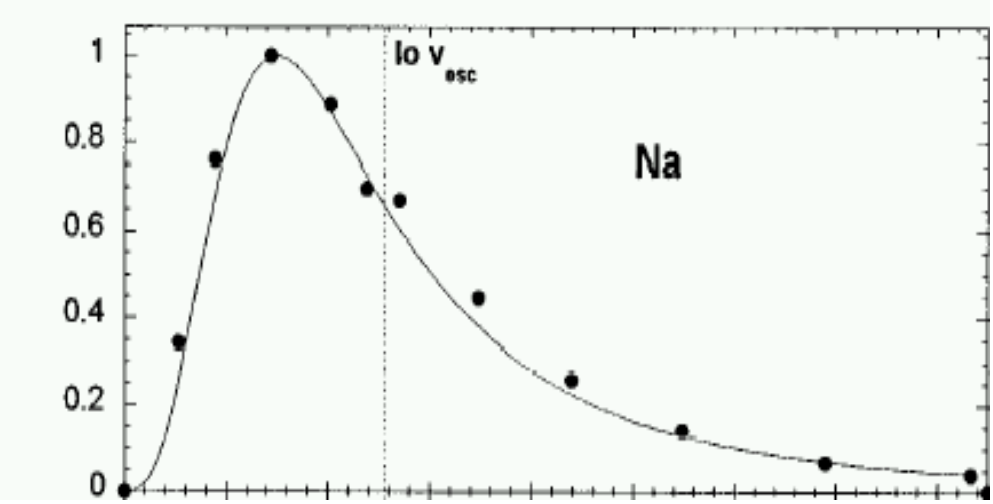

Figure 3.2. Ion sputtered velocity distribution determined experimentally by Weins (1997).

Yakshinskiy and Madey (2004) demonstrated that the cross sections are dependent on variations in substrate temperature. Experimental studies of photon stimulated desorption from a lunar sample were conducted over a temperature range from 100 to 600 K, Figure 3.3. The desorption of sodium from the sample was found to be 10X greater at a temperature of 470 K than at 100 K. Using the desorption cross section for 300 K that Yakshinskiy determined in 1999, Killen fit a function to Yakshinskiy's temperature dependence results and obtained

$$\mathrm{Q}_{\mathrm{photon}}(T) = \mathrm{Q}_{\mathrm{photon}}(300K) * \left[1.395 - 0.0235 * \left(\frac{5040}{T_{surf}} \right) \right] \tag{3.7}$$

where $\mathrm{T}_{\mathrm{surf}}$, the temperature of the surface of the planet, varies according with solar zenith angle, θ, according to

$$T_{surf} = 450 * (\cos\theta)^{0.25} * \frac{0.465}{R} + 50 \tag{3.8}$$

where R is the distance of Mercury from the Sun in AU.

The rate of sodium photon sputtered from the surface is given by:

$$\mathrm{Rate}_{\mathrm{photon}} \left(\frac{\mathrm{Na}}{\mathrm{cm}^2 \mathrm{s}} \right) = \mathrm{Q}_{\mathrm{photon}}(T) * \mathrm{F}_{\mathrm{sun}} \frac{\cos\theta}{R^2} * \mathrm{f}_{\mathrm{na}} * \sigma * \mathrm{scalef} \tag{3.9}$$

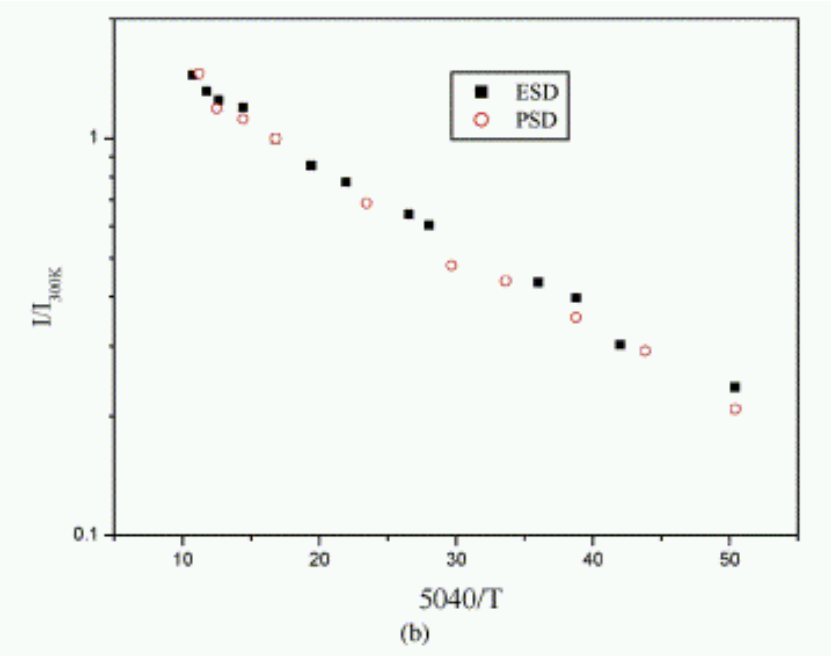

Figure 3.3. Temperature dependence of photon stimulated desorption determined experimentally by Yakshinskiy (2004).

where $Q_{photon}(T)$ is described above, F_{sun} is the wavelength integrated solar photon flux with energy > 4 eV at 1 AU, cosθ is the solar zenith angle, R is the distance of Mercury from the Sun in AU, f_{na} is the fraction of sodium in the surface, σ is the surface density of the surface regolith, and scalef is a factor that accounts for the solar cycle.

For R = 0.3788 AU and zenith angles of 0 and 80 degrees, the surface temperatures are 602.4 and 407.6 K respectively. Using $Q_{photon}(300K) = 1*10^{-20} cm^2$ gives photon desorption cross sections of

$$\begin{aligned} Q_{photon}(602.4K) &= 1.198*10^{-20} cm^2 \\ Q_{photon}(407.6K) &= 1.104*10^{-20} cm^2 \end{aligned} \tag{3.10}$$

Using $F_{sun} = 10^{14} \frac{photons}{cm^2 s}$, f_{na}=0.005, $\sigma = \frac{7.5*10^{14}}{\mathrm{cm}^2}$, and scalef = 1.77 gives photon desorption rates of

$$\begin{aligned} \mathrm{Rate}_{photon}\left(\frac{\mathrm{Na}}{\mathrm{cm}^2\mathrm{s}}\right) &= 5.54*10^7 \\ \mathrm{Rate}_{photon}\left(\frac{\mathrm{Na}}{\mathrm{cm}^2\mathrm{s}}\right) &= 8.87*10^6 \end{aligned} \tag{3.11}$$

for zenith angles of 0 and 80 degrees respectively.

Studies by Yakshinskiy and Madey (1999) show that photon desorbed sodium atoms are “hot", meaning that the freed atoms have kinetic energies considerably higher (> 1 eV) than thermal energies. For this reason, photon stimulated desorption

energies are usually much higher than the surface temperature of Mercury. Yakshinskiy and Madey (2001) gives a most probable velocity of desorbed Na of ~1000 m/s as shown in Figure 3.4.

Leblanc and Johnson (2003) fit a Maxwell-Boltzman distribution to Yakshinskiy and Madey's results and obtained close results using a temperature given by $T = \frac{V^2 * m}{2 * k}$, where V is the peak of the velocity distribution, m is the mass of a sodium atom, and k is Boltzman's constant. Using the peak velocity of 1000 m/s gives T = 1384 K. Following Leblanc and Johnson, this same approach is adopted for the treatment of the energy distribution of photon stimulated desorption in this body of work. It should be noted that due to lack of knowledge of porosity and composition, the peak velocity of 1000 m/s corresponding to T = 1384 K from Yakshinskiy and Madey's laboratory measurements serves only as a starting point. Values ranging from 1000 K to 1500 K, corresponding to peak velocities of 850 m/s to 1041 m/s, have been proposed by Killen (private communication) and Leblanc and Johnson (2003).

3.3.3 Meteroitic vaporization

Meteroitic vaporization occurs when micro-meteors strike the surface of the planet and vaporize sodium from both the surface and from within the meteor. Vaporization occurs as a result of pressure due to impact reaching a critical value such that material within the surface and impactor are converted to vapor. The critical pressure corresponds to a shock front that moves radially from the point of impact and

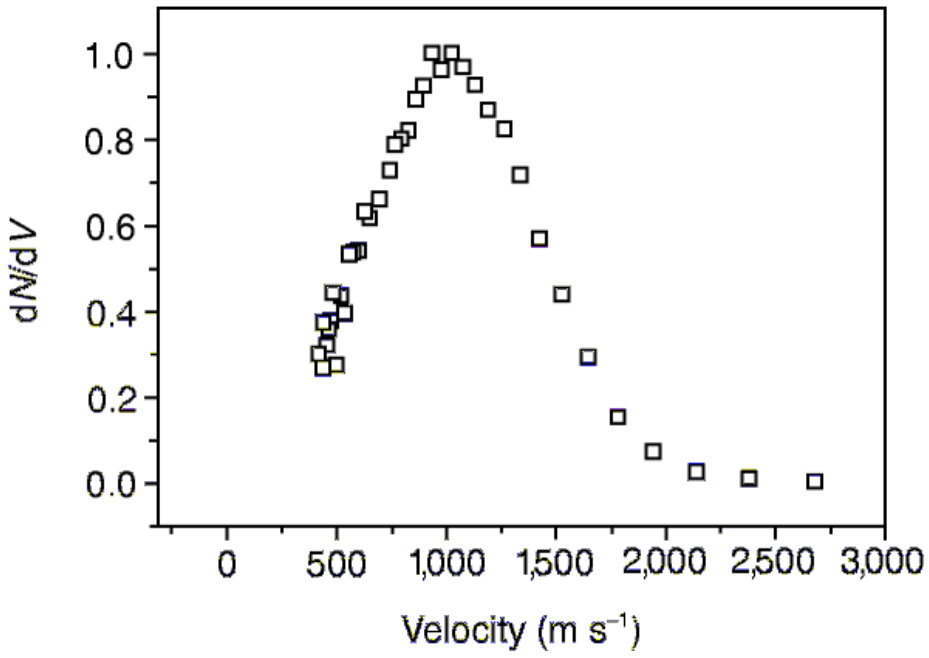

Figure 3.4. Photon desorption velocity distribution determined from experiments by Yakshinskiy and Madey (2001).

consequently diminishes in magnitude with distance. The distance where the pressure drops below the critical pressure defines the extent of vaporization and hence the volume of vaporized material. The vapor production is dependent on the physical properties of both the projectile and the target material, the impact momentum, and impact angle (Morgan and Killen, 1998). From Morgan and Killen,

$$\frac{\Delta V_{vap}}{\Delta V_{proj}} = \frac{1}{2}\left(\frac{r_{vap}}{r_{proj}}\right)^3 \tag{3.12}$$

where ΔV_{vap} is the volume of vapor, ΔV_{proj} is the volume of the projectile, r_{vap} is the radius inside which the pressure is larger than the critical pressure, and r_{proj} the radius of the projectile. Using the relation $density = \frac{mass}{volume}$ for both the vaporized volume and projectile gives

$$\frac{\Delta m_{vap}}{\Delta m_{proj}} = \frac{1}{2}\frac{\rho_{reg}}{\rho_{proj}}\left(\frac{r_{vap}}{r_{proj}}\right)^3 \tag{3.13}$$

where ρ_{reg} is the mass density of the regoith.

The ratio $\frac{r_{vap}}{r_{proj}}$ has a functional dependence on the velocity of the impactor given by Killen as

$$\frac{r_{vap}}{r_{proj}}(v) = \left[0.29 * \frac{26GPa}{P_p(v)}\right]^{av+b} - c\,, \tag{3.14}$$

where a, b, and c have values of 52 s/m, 1.18, and 2 respectively (Lange and Ahrens, 1982) and $P_p(v)$ is the peak pressure given by Melosh (1989) as

$$P_p = \frac{1}{4}\rho v_{proj}^2 \left(\frac{2C}{v_{proj}} + S \right) \tag{3.15}$$

where C is a constant close to the bulk speed of sound in the medium, and S is an empirical constant related to the material properties such as volume coefficient of expansion, bulk modulus, and specific heat (Morgan and Killen, 1998). The projectiles follow a velocity distribution given by Cintala (1992) as

$$f\left(v_{proj}\right) = kr^2 \left(\frac{v_{proj}}{u} \right)^3 \exp^{-\gamma u} \tag{3.16}$$

where k is a normalization constant, r is the distance of the projectile from the sun, $u = \left(rv_{proj}^2 + v_E^2\right)$, and γ = 0.247.

Since the velocity of the projectiles follows the above distribution, the equation giving the ratio of the mass of vapor to the mass of the projectile must be integrated over the distribution. This gives

$$\frac{\Delta m_{vap}}{\Delta m_{proj}} = \frac{1}{2}\frac{\rho_{reg}}{\rho_{proj}} \int \left(\frac{r_{vap}}{r_{proj}} \right)^3 f(v_{proj}) dv_{proj} \tag{3.17}$$

where $\int\left(\frac{r_{vap}}{r_{proj}}\right)^3 f(v_{proj})dv_{proj}$ is the total volume of vapor per total volume of projectiles.

Rearranging Equation 3.17 and replacing the mass of projectiles with the mass flux of incoming projectiles gives

$$\frac{d\sigma_{vap}}{dt} = \frac{1}{2}\frac{\rho_{reg}}{\rho_{proj}}\frac{d\sigma_{proj}}{dt}\int\left(\frac{r_{vap}}{r_{proj}}\right)^3 f(v_{proj})dv_{proj} \tag{3.18}$$

which is now an expression for the mass flux of vapor $\left(\frac{kg}{cm\,s}\right)$ leaving the surface of the planet. In terms of the number of sodium atoms, the final expression for meteoritic vaporization is

$$\text{Rate}_{\text{meteor}}\left(\frac{Na}{cm^2 s}\right) = \frac{0.023}{6.022 * 10^{23}}\frac{1}{2}\frac{\rho_{reg}}{\rho_{proj}}\frac{d\sigma_{proj}}{dt}\int\left(\frac{r_{vap}}{r_{proj}}\right)^3 f(v_{proj})dv_{proj} \tag{3.19}$$

The final quantity to be determined is the mass flux of projectiles $\left(\frac{d\sigma_{proj}}{dt}\right)$, which is given by Killen as

$$\frac{d\sigma_{proj}}{dt} = \rho_{proj}(1\,\text{AU}) * r^{-1.4} * v_{ave} \tag{3.20}$$

where ρ_{proj} is the density of the interplanetary medium at 1 AU, r is the distance of the projectile from the Sun in AU, and v_{ave} is the average intersection velocity. Figure 3.5 shows a schematic of the geometry associated with a meteor impact.

Laboratory experiments to determine the energy of vaporized material from impacts have been conducted by Eichhorn (1977a, 1977b). A variety of projectile and target materials was sampled, i.e., carbon impacting tungsten, iron impacting gold, etc. Results indicated that the energy of ejected material was dependent on both projectile/target material as well as projectile velocity. For projectile velocities in the range of 5 to 20 km/s, energy values for various combinations of projectile/target materials ranged from 2500 to 5000 K. Leblanc and Johnson (2003) assumed the energy distribution of impact ejected atoms is Maxwellian. Adopting this same idea gives a peak velocity range of 1344 m/s to 1901 m/s according to $v = \sqrt{\frac{2kT}{m}}$.

3.3.4 Thermal Vaporization

Thermal vaporization is due to the heating of the surface followed by the evaporation of atoms on the extreme surface into the exosphere. Madey et al. (1998) explains this process as occurring when an alkali ion picks up an electron from the surface and becomes a neutral. This places the atom in a higher energy state than the ionic state causing the atom to desorb. Killen (2004a) gives the rate of thermal vaporization of sodium as

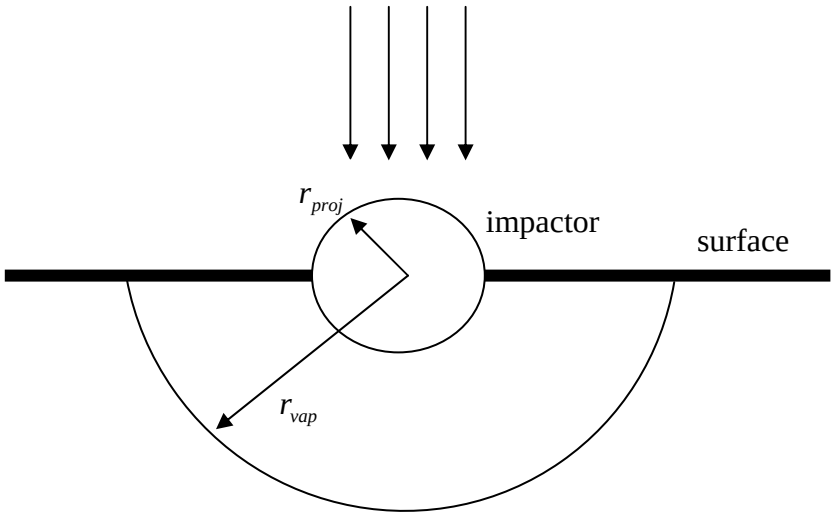

Figure 3.5. Schematic diagram showing the radii of the projectile and vaporization region

$$R_{vap}\left(\frac{Na}{cm^2 s}\right) = \upsilon\,\sigma\, f_{Na} \exp\left(\frac{-U}{kT}\right) \tag{3.21}$$

where ν is the vibrational frequency for the van der Waals potential of sodium atoms on the surface, σ is the surface number density, f_{Na} is the fraction of sodium atoms on the extreme surface, U is the binding energy, k is Boltzman's constant, and T is the surface temperature. Yakshinskiy et. al. (2000) conducted thermal desorption experiments of sodium from silicon di-oxide. Results indicate that the binding energy, U, ranges from ~1.4 eV/atom to ~2.7 eV/atom with $\nu = 10^{13}\,s^{-1}$. The rate of thermal vaporization is a strong function of U, thus the range given above causes a large variation in the vaporization rate. Model simulations by Killen showed that values of U much less than 2.7 eV/atom produces values of thermal vaporization rate too large to be consistent with observed data. Killen recommends U = 2.7 eV/atom be used (private communication).

Using Equation 3.8 for the surface temperature, with R = 0.3788 AU and zenith angles of 0 and 80 degrees, the surface temperatures are 602.4 and 407.6 K respectively. Using $\sigma = \frac{7.5*10^{14}}{\mathrm{cm}^2}$, and f_{na} =0.005, gives thermal vaporization rates of

$$R_{vap}\left(T = 602.4K\right) = 949\frac{Na}{cm^2 s}$$
$$R_{vap}\left(T = 407.6K\right) = 1.5*10^{-8}\,\frac{Na}{cm^2 s} \tag{3.22}$$

The energy distribution of thermally vaporized sodium atoms follows a Maxwell-Boltzman distribution (Leblanc and Johnson, 2003), with the peak energy accommodated to the surface temperature. For the temperature variation in the example above, 602.4 K to 407.6 K, the most probable velocities calculated according to $v_{prob} = \sqrt{\frac{2kT}{m}}$ gives $v_{prob} \approx 660 \text{ to } 543 \ {}^{m}/_{s}$ respectively.

3.4 Loss process physics

A distinction should be made between a loss from the exosphere and a loss from the Mercurian system. A neutral sodium atom may be removed from the exosphere but not from the Mercurian system by photoionization followed by surface impact and implantation to the surface or by a neutral sodium atom impacting the surface followed by adsorption. Surface implantation or adsorption may be divided into either dayside surface sticking or nightside cold trapping. Alternatively, a sodium atom may be lost from the Mercurian system by photoionization followed by transport along the IMF along an escape trajectory from the planet or by gravitational escape due to the atom initially having a velocity > the escape velocity or acquiring velocity > the escape velocity by radiation pressure (Smyth and Marconi, 1995). Thus Smyth and Marconi (1995) outline 4 major source processes, photo-ionization followed by transport along the IMF, dayside surface capture, gravitational escape, and lateral transport to the nightside, as previously mentioned in Section 3.2.4

Mercury's mass, size, and close proximity to the Sun lead to relatively large loss rates for air-borne sodium atoms. Typical photoionization timescales for sodium at

Mercury are 1.4 to 3.3 hours, depending on the Mercury-Sun distance (Smyth and Marconi, 1995). Surface sticking timescales are more difficult to qualitatively define due to the largely unconstrained properties of accommodation and surface sticking coefficients. However, since typical source processes have characteristic energies much less than those needed to gravitationally escape from the planet even in the presence of maximum radiation pressure (Table 3.2 and Figure 3.1), photoionization or neutral adsorption to the surface are probably the dominant loss process for most airborne sodium atoms. Thus most sodium atoms generally make several ballistic hops before being adsorbed to the surface or before being photoionized. Only the small fraction of sodium atoms occupying the higher energy regime of the velocity distribution is likely to escape from the gravitational influence of the planet. Ion sputtered atoms that follow a Sigmund-Thompson distribution will generally have a high energy tail that does not fall off as rapidly as for a Maxwellian distribution, thus ion sputtered atoms may be responsible for supplying part of the sodium atoms observed in the extended regions of the exosphere that are on escaping trajectories. Also, since the characteristic temperature of meteoritic vaporization is ~ 3000 K, there may be enough atoms left in the high energy tail of this process to supply part of the extended exosphere.

3.4.1 Photoionization

Photoionization occurs when an atom absorbs a photon with enough energy to free an electron. The threshold ionization energy for sodium occurs as a wavelength of 2412.57 Angstrons (Huebner et al., 1992). Theoretical cross-sections for sodium

ionization has been given by Chang and Kelly (1975) and is shown in Figure 3.6. Chang and Kelly explain the non-zero minimum that occurs near 200 nm as being due to spin-orbit effects. Also, experimental cross sections have been determined by Hudson and Carter (1967) with a larger cross section at longer wavelengths than the theoretical value (Huebner et al., 1992). The rate coefficient over a differential wavelength interval is obtained by integrating the cross section over the solar photon flux and is given by Huebner et al., (1992) as

$$k_i(\tau_i) = \int_{\lambda_i}^{\lambda_i+\Delta\lambda} \sigma(\lambda)\Phi(\lambda)\exp^{-\tau(\lambda)}\, d\lambda \qquad (3.23)$$

where $\sigma(\lambda)$ is the photoionization cross section, $\Phi(\lambda)$ is the unattenuated solar photon flux at wavelength λ, and $\tau(\lambda)$ is the optical depth. The overall rate coefficient is determined by integrating over all wavelengths up to the threshold wavelength. Hubner made calculations for the rate coefficient of sodium at 1 A.U. assuming $\tau(\lambda) = 0$ (above the atmosphere). Huebner gives sodium rate coefficient values for both the theoretical and experimental cross sections. For theoretical cross sections the rate coefficients are $5.92 * 10^{-6} s^{-1}$ for quiet sun conditions and $6.52 * 10^{-6} s^{-1}$ for active sun conditions. Quiet Sun conditions is defined by Huebner as the non-flaring Sun at medium activity and active Sun conditions as the Sun near solar maximum. For experimental cross sections, Huebner obtained rate coefficients of $1.62 * 10^{-5} s^{-1}$ and $1.72 * 10^{-5} s^{-1}$ for quiet and active Sun conditions respectively.

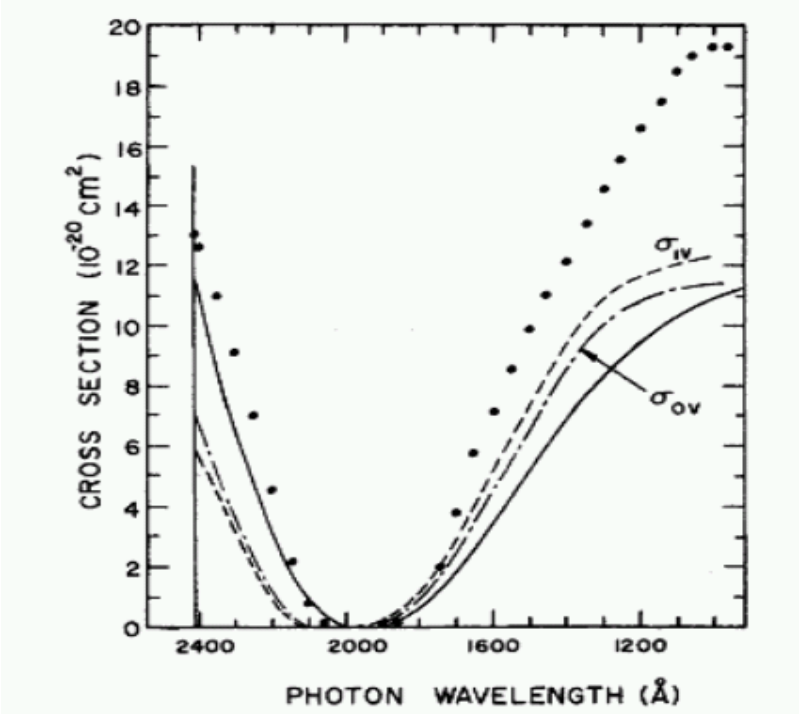

Figure 3.6. Theoretically derived photoionization cross section of sodium as a function of wavelength by Chang and Kelly (1975). The minimum photoionization energy occurs near 2400 angstroms. The dip in the curve near 1900 angstroms can be explained by spin-orbit effects.

Killen uses the rate determined from the experimental cross section values and will thus be adopted for this body of work. The photoionization lifetime is the inverse of these values and is proportional the square of the distance from the Sun in A.U., thus the photoionization of sodium at Mercury for R = 0.3788 A.U. and for quiet Sun conditions is 8857 seconds.

3.4.2 Dayside Surface Capture

When a sodium atom collides with the surface, the atom exits the surface after a residence time that is typically short for physical adsorption ($3.6*10^{-7}$ seconds for a surface temperature of 200 K) and even shorter times for higher temperatures (Hunten et al., 1988). Based on energy accommodation coefficients derived from laboratory experiments of sodium onto α-quartz, Hunten et al. (1988) gives an energy accommodation coefficient of 0.62 and predicts that ambient sodium should be thermally accommodated to the surface temperature. Chemical adsorption is typically more complex than physical adsorption with longer residence times. The effect of long residence times due to both physical adsorption for cold temperatures as well as chemical desorption is described collectively by the surface sticking coefficient (Smyth and Marconi, 1995). This coefficient is the probability that an atom encountering the surface will stick to it. This process represents a loss to the exosphere when the sodium atom completely sticks to the surface and awaits some source process to release the atom from the surface again. Smyth and Marconi distinguish between an atom that either sticks or partially sticks, with the latter not necessarily representing a loss to the exosphere.

3.4.3 Gravitational escape

Gravitational escape occurs when an atom has enough energy to escape from the gravitational influence of the planet. In the absence of any other forces acting on the atom, the escape velocity can be derived by setting the kinetic energy equal to the potential energy

$$\text{K. E.} = \text{P.E.}$$

$$\frac{1}{2}mv^2 = \frac{mMG}{r} \tag{3.24}$$

$$v_{esc} = \sqrt{\frac{2MG}{r}}$$

Where M is the mass of the planet, G is the gravitational constant, and r is the distance from the center of the planet to the starting point of the atom. If the atom is ejected from the surface, then the escape velocity is

$$v_{esc} = \sqrt{2g_o r_o} \tag{3.25}$$

where g_o is the gravity at the surface and r_o is the radius of the planet. For Mercury, $g_o = 3.7\,\mathrm{m/s^2}$ and $r_o = 2440\,\mathrm{km}$; thus the escape velocity is ~ 4.3 km/s. Note that the escape velocity is independent of ejection angle, so it does not matter if the atom is ejected normal to the surface or at an angle.

There is not an analytical solution to the escape velocity if radiation pressure is also included as a force on the atom. Part of this is due to the fact that the tangential

component of radiation acceleration acting on an atom varies according to where on the planet the atom was ejected, as explained in Section 3.2.3. Furthermore, as radiation pressure accelerates the atom, the velocity of the atom with respect to the Sun continually changes and Doppler shifts the atom further away from the center of the sodium Fraunhofer line; thus the acceleration due to radiation pressure is time varying.

3.4.4 Cold trapping

Cold trapping pertains to atoms that begin on the dayside and migrate towards the terminator or nightside and stick in the colder regions of the planet. This phenomenon has two causes, 1) the random walk of atoms is skewed towards the colder regions of the planet and 2) radiation pressure forces atoms towards the terminator. The first cause can be explained by considering that atoms ejected from a point on the surface are randomly ejected over all angles with respect to the local surface normal. Atoms ejected towards warmer surface regions will, after bouncing off of the surface, retain more energy than atoms ejected towards the colder surface regions. Atoms bouncing towards the colder region will lose energy faster and then become cold trapped. The net effect is that atoms will randomly walk around the surface and tend to accumulate on the colder regions, i.e., the terminator or nightside. The second cause, radiation pressure, is azimuthally symmetric around the sub-solar point with increasing tangential acceleration for larger solar zenith angles. Radiation pressure is explained in more detail in Section 3.5.1. Both processes act to push

atoms towards the terminator; and in the absence of surface density replenishment would deplete the sub-solar surface region of sodium.

Lateral transport of ambient atoms is affected by surface accommodation and partial sticking, Section 3.4.2, and thus represents another method of loss governed in part by the surface accommodation coefficient and surface sticking coefficient. Ultimately, both dayside surface capture and lateral transport consist of sodium atoms sticking to the surface, but with lateral transport the atoms remain a part of the ambient exosphere long enough to migrate to the nightside. Modeling by Smyth and Marconi (1995) shows that migration times of atoms ejected with velocity = 1km/s from the sub-solar point to the terminator with maximum radiation pressure takes 11.7 to 2.8 hours for energy accommodation coefficients from 1 to 0, respectively.

3.5 Dynamics

3.5.1 Radiation pressure

Radiation pressure pushes atoms in an anti-sunward direction resulting in atoms either being transported away from the sub-solar region towards the terminator or completely swept away from the planet. The difference is primarily due to the time of flight an atom has without consideration of radiation pressure, the angle at which the atom was ejected, and the location from which the atom originated. An atom that is ejected normal to the surface at the sub-solar point experiences a force from radiation pressure parallel to the surface normal. Alternatively, an atom that is ejected normal to the surface at the terminator experiences a force from radiation pressure tangent to the surface normal. Atoms that acquire enough velocity from

radiation pressure to reach escape velocity and that are on a trajectory that leads away from the planet are considered to be completely lost from the system; however atoms that are simply displaced towards the terminator may become cold trapped and are lost from the exosphere but are not completely lost from the planet. The governing equations for radiation pressure are given in Chapter 1.

3.5.2 Magnetospheric transport of ions

Magnetospheric modeling (Killen et al., 2004) has shown that the transport of ions within Mercury's magnetosphere is the result of coupling between Mercury's magnetic field as well as the IMF. Killen, 2004, showed ~ 60 % of Na^+ being recycled back to the surface, with ~ 2/3 of the 60 % impacting the dayside and the other 1/3 impacting the nightside. The ions that impacted the dayside showed a tendency towards the dawn side of the planet. Assuming that Na^+ is neutralized after impacting the surface, magnetospheric transport of Na^+ is responsible for the redistribution of sodium and may explain localized enhancements. The remaining 40 % of Na^+ escaped to the solar wind and were lost from the system.

3.6 Unresolved issues with the sodium exosphere

One of the unanswered questions is whether an atom, upon encountering the surface, accommodates to the surface temperature or remains at a higher temperature. Hunten et al. (1988) predicted that ambient sodium should accommodate quickly to the surface temperature. In contrast, Killen et al. (1999) observed sodium at locations

ranging from the equatorial region to the poles and found that line profiles were consistent with temperatures ~ 700 K hotter than surface temperatures.

Presently it is unknown if species in Mercury's exosphere arise from internal sources or are supplied by external means, i.e., meteoritic vaporization or the solar wind. Most of the community agrees that hydrogen and helium are most likely supplied by the solar wind, but heavier atoms that are less abundant in solar composition are more difficult to account for. Given the low vaporization temperature of sodium coupled with high sub-solar surface temperatures of ~700 K, sodium should have vaporized away from the planet long ago. One possible explanation by Killen and Morgan (1993) is that sodium may be higher in abundance in the crust than terrestrial values by 1 – 2 %. Gardening processes such as ion sputtering and meteoritic impact may then serve to bring sodium up from below the extreme surface and then be available for ejection into the exosphere. Alternatively, sodium may be supplied by micro-meteors or cometary impact where the composition of either of the two contains significant amounts of sodium (Rietmeijer, 2004). Also, it is possible that the solar wind could contain enough sodium ions to act as a supply of sodium to the Mecurian system, but presently little is known about the fractional composition of sodium in the solar wind. This process would also require that the IMF and Mercury magnetic field couple in such a way as to allow sodium ions to impact the surface.

The dominant source process for maintaining the sodium exosphere is the subject of much debate. Modeling by Leblanc and Johnson (2003) shows that thermal vaporization is responsible for most of the sodium in the exosphere. In this model,

the majority of sodium is quickly vaporized from the central region (< 50° solar zenith angle) of the dayside, and consequently leaves little exospheric column abundance in the same region. Killen (2004b) proposes that the overturning of surface grains by energetic processes combined with diffusion of sodium through freshly overturned grains maintains a fresh supply of sodium in the sub-solar regions. Calculations show that this process allows sodium to be brought to the extreme surface at a rate of ~ 10^7 Na/cm^2/s. Killen proposes that photon stimulated desorption may actually be energetic enough to act on the sodium and thereby be the dominant source process.

It is unknown at present what fractions of the sodium exosphere are low energy and high energy. Given that the maximum scale height of sodium thermally vaporized from the surface is ~ 60 km and the typical scale height for photon stimulated desorption is ~ 100 km, any sodium observed in the extended sodium corona most likely does no arise from these sources but from more energetic processes such as meteoritic vaporization.

3.7 Summary

This chapter has given a brief overview of Mercury's exosphere, with emphasis on sodium. Rather than be an exhaustive review on the exosphere, the characteristics that are relevant to this investigation have been presented. The morphology of sodium has been presented, with emphasis on enhancements as well as smoothly varying components to the exosphere. The governing physics behind the 4 major source processes (ion sputtering, photon stimulated desorption, meteoritic

vaporization, and thermal vaporization) has been given. Loss processes (photoionization, dayside surface capture, gravitational escape, and cold trapping) are discussed with the distinction made between atoms that are lost from the exosphere but remain a part of the Mercurian system and atoms that are completely swept away and are lost from the system. The dynamics of sodium, both by radiation pressure and magnetospheric transport, have been discussed; with emphasis on how atoms are merely relocated on the planet or lost from the system. Unanswered questions pertaining to the sodium exosphere have been presented and serve to motivate the investigations of this thesis as well as to motivate the range of exospheric experiments that needs to be performed by MASCS.

Chapter 4

Observation Planning Software Tool

4.1 Introduction

Developing observation strategies to answer key scientific questions about Mercury and its exosphere requires making predictions for the results from simulated observations. These predictions rely broadly on two parameters: 1) geometrical pointing capabilities and 2) predicted signal and SNR for a simulated observation. Software has been developed that combine spacecraft orbital and pointing geometry, sodium exospheric emissions, and instrument performance into a tool for the purpose of generating and evaluating simulated observations. Spacecraft orbital and pointing geometry is obtained from the MESSENGER Trajectory Database, maintained by KinetX, Inc. and the Johns Hopkins University Applied Physics Laboratory (JHU/APL). Sodium exospheric emissions are determined by a dayside sodium exospheric model developed by Killen (unpublished) in conjunction with exospheric profile and radiance modeling (Section 4.3). The instrument performance relies on calibration results, which is discussed in Chapter 2.

The end products of the software tool are visual aids for observational opportunities and signal/SNR predictions for simulated observations. The flow chart of Figure 4.1 outlines the algorithm of the software tool. The tool is typically run in

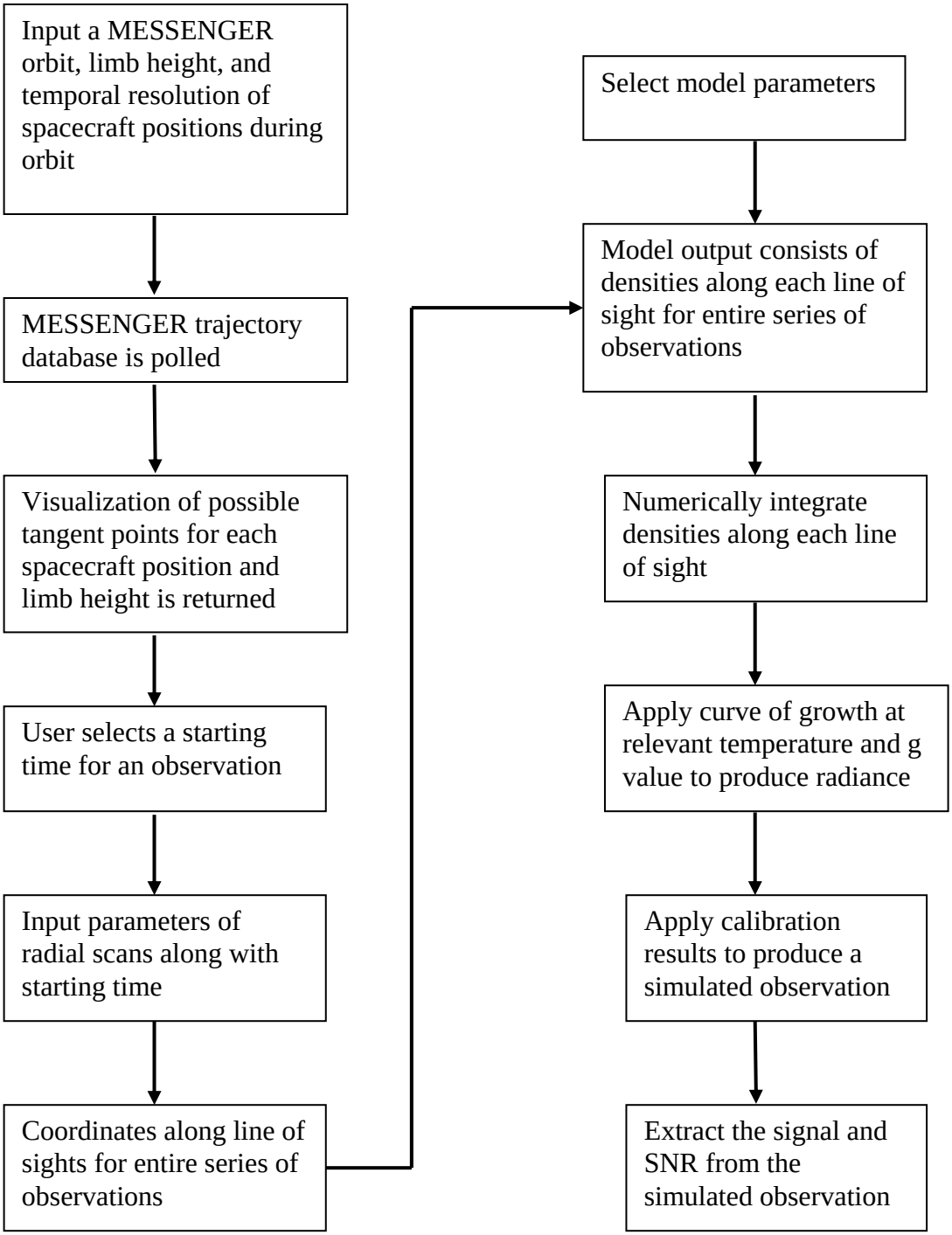

Figure 4.1. Flowchart of software tool that begins with user specified inputs for orbital and observational parameters and ends with signal and SNR predictions.

two stages, thus the flowchart is divided into two columns.

4.2 MESSENGER trajectory database

The orbital database consists of the current best predicted trajectory that will be subject to updates throughout the life of the mission. The database is interactive in the sense that the user first inputs the date during the mission that data is needed as well as the duration in time of the returned data. Data may be returned in time increments of seconds, minutes, hours, or days. Next the user inputs the parameters needed, i.e., spacecraft position and velocity relative to Mercury, the position of Mercury relative to the Sun, orbital elements of the spacecraft or Mercury, etc. The parameters may also be returned using a variety of coordinate systems such as Earth Mean Ecliptic & Equinox of J2000, Mercury Equator & Prime Meridian, etc. Additional parameters are available on the web site http://messenger.jhuapl.edu/MD/servlet/Trajdb?state=0 . The database is used here to determine the position and velocity of the spacecraft with respect to Mercury and the true anomaly of Mercury with respect to the Sun.

Visualization software has been developed that utilizes the trajectory data in order to show where the spacecraft can point at any time in an orbit. For a given time during an orbit, possible tangent points are plotted at some preset height above the limb, resulting in a curve above the planet surface. The curve is limited only by sun-shade constraint violations. This is done for multiple spacecraft positions, which results in a family of curves that represent possible pointing options during the course of an orbit. Results are given in Chapter 5.

After a spacecraft position has been selected, parameters are input to the tool in order to produce a series of radial scans, described in Chapter 1. Input parameters to the tool for the purpose of generating radial scans are the starting and ending altitudes of each radial scan, the range over the planet that the radial scans cover, the duration of each radial scan, and the number of radial scans during a sequence of observations.

4.3 Sodium exospheric emissions

The predicted radiance from the sodium exosphere begins by making sodium exospheric density predictions for a given set of parameters by using a sodium exospheric model. The densities are determined at discrete locations along the line of sight for a simulated observation. The densities are then numerically integrated along the line of sight in order to produce a tangentially integrated column abundance. A curve of growth for sodium radiance as a function of column abundance is then used to calculate a radiance value that enters the instrument from the observed column.

4.3.1 Sodium exospheric model

The sodium model of Mercury's exosphere was developed by Rosemary Killen (unpublished). The model is an analytic, constant gravity model that consists of a 220 X 220 grid over the dayside surface that is regularly spaced in latitude and longitude. Both the latitude and longitude range from -89.1818° to +89.1818°, with the grid centered at the sub-solar point. The angular change in latitude or longitude between two adjacent grid points is ~ 0.818 degrees, i.e., equal angles between adjacent grid points but non-constant distance between grid points. The model is steady state in the

sense that parameters such as the true anomaly of the planet, solar photon flux, and micro-meteoroid bombardment are all given preset values at the beginning of each model run and do not vary with time. Source processes (photon stimulated desorption, meteoroid vaporization, and thermal vaporization), each of which has its on input parameters, are determined for each grid point resulting in source rates in units of $\frac{Na}{cm^2 s}$. The source processes follow the governing equations given in Chapter 3. Three loss processes (photo-ionization, surface sticking, and radiation pressure transport), each of which are described in detail in Chapter 3, are included in this model. The loss processes are used to determine a characteristic loss time for each source rate. Thus the source rate multiplied by the characteristic loss time gives a column abundance. The outputs of the model for each source process and at each grid point are source rate, column abundance, and scale height.

4.3.2 Distribution of density with height

The sodium exospheric model does not produce density distributions with height, but instead produces source rates, column densities, and scale heights; all based on the constant gravity assumption. Laboratory tests of meteoritic vaporization and thermal vaporization demonstrate that the energy distribution of ejected sodium atoms may be closely approximated by a Maxwell-Boltzman energy distribution (see Chapter 3). Madey et al., (1998), concluded that atoms ejected by photon stimulated desorption do not follow a Maxwellian distribution. However, close examination of Figure 12 from Madey et al., (1998), for the case of the moon shows that for heights above the surface out to 1 lunar radii the difference between densities associated with

the laboratory determined energy distribution does not differ significantly from a Maxwellian distribution. Furthermore, Leblanc and Johnson, (2003) were able to fit a Maxwellian curve to the photon stimulated desorption data of Madey for a temperature of 1500 K. Killen (personal communication) recommended a characteristic temperature equal to 1100 K for photon stimulated desorption. Thus, the energy distributions of all 3 processes are treated as Maxwellian, with characteristic temperatures of 3000 K, 1100 K, and the surface temperature for meteoritic vaporization, photon stimulated desorption, and thermal vaporization, respectively. Furthermore, since the model assumes constant gravity with column abundances, scale heights, and radiation pressure all calculated under this assumption, the distribution of density with height also relies on a constant gravity assumption.

For a Maxwellian distribution of velocities and a constant gravity assumption, the density profile above a model grid point is calculated from the barometric formula as

$$\rho(z) = \rho_o \exp\left(\frac{-z}{H}\right) \tag{4.1}$$

where ρ_o is the density at the surface associated with a grid point and source process, z is the height extending radially outward from the planet above the grid point, and H is the scale height for the source process. For a Maxwellian energy distribution, the scale height is the height an atom travels to in the absence of all forces other than gravity when the ejection velocity is equal to the most probable speed from the Maxwellian energy distribution and the ejection angle is normal to the surface.

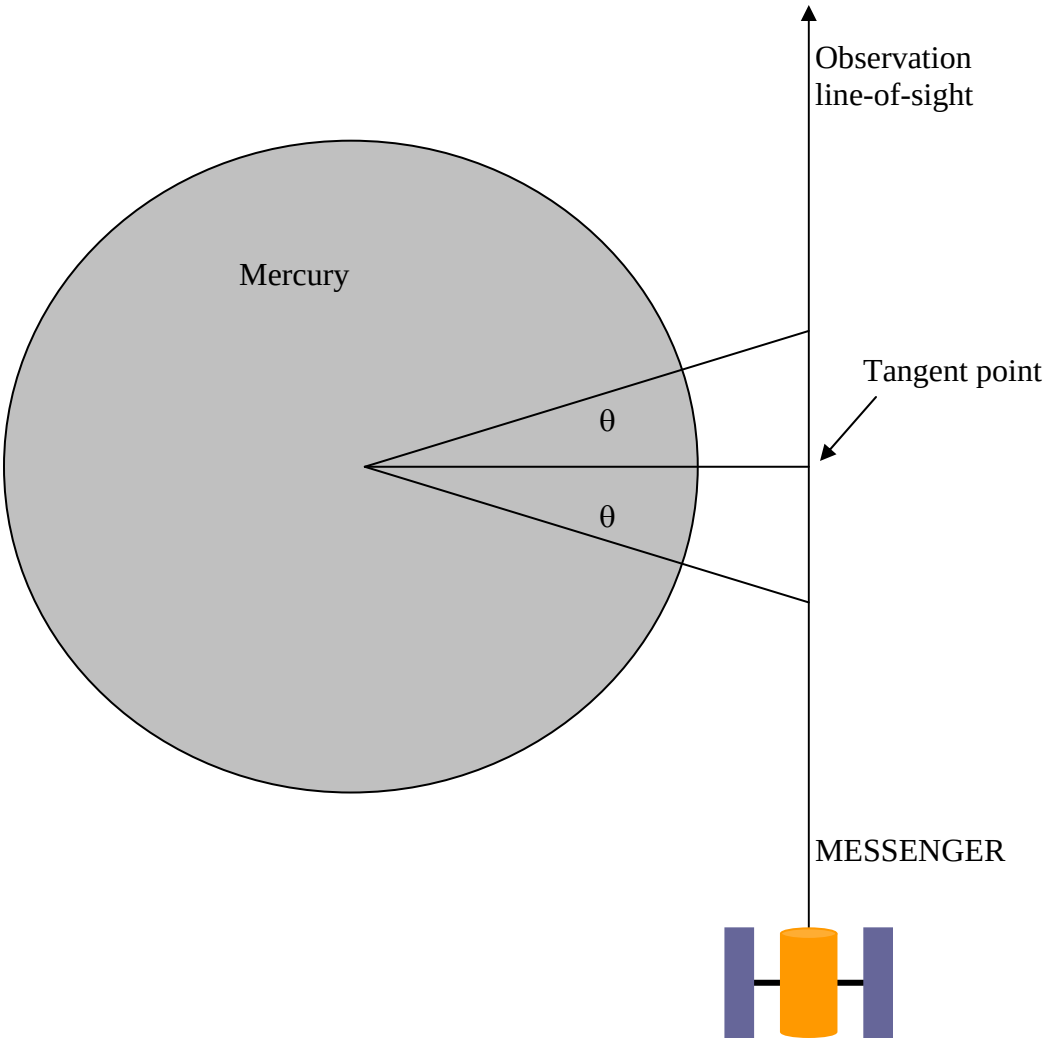

Figure 4.2. Typical limb scan showing the tangent point and angles from the tangent point to emphasize the variation of density along the line of sight.

Furthermore, the density at the surface, ρ_o, for a grid point is determined by dividing the zenith column density by the scale height. Density distributions as a function of height above the planet are determined for each source process separately.

4.3.3 Tangentially integrated column densities

Tangentially integrated column densities are determined by interpolating density values above model grid points to values along the line of sight and numerically integrating along the line of sight. The contribution to the integrated density is largest at the tangent point and then decreases with increasing angle, θ, from the tangent point. (Figure 4.2). A comparison was made with the analytical solution (Chamberlain, 1978) to validate that the numerical integration gives accurate tangential column abundances. In order to use the analytical solution, the column densities and scale heights of all of the model grid points are set to the same value, making the exosphere isotropic. Three radial scans, near the dawn terminator, dusk terminator, and sub-solar point, that range from ~ 50 – 1000 km in altitude are performed. Within each radial scan, columns at 8 equally spaced altitude positions are calculated, as denoted by the stars in Figure 4.3. The results from the numerically integrated tangential column abundance are divided by the results from the analytically determined column abundance for each altitude point and for each radial scan. The three curves are plotted in Figure 4.3 and coincide at each point in altitude; this shows that the numerical integration technique is consistent for radial scans that span the dayside hemisphere. For each radial scan, the numerical method agrees with the analytical method within 3 – 4 % over the altitude range tested.

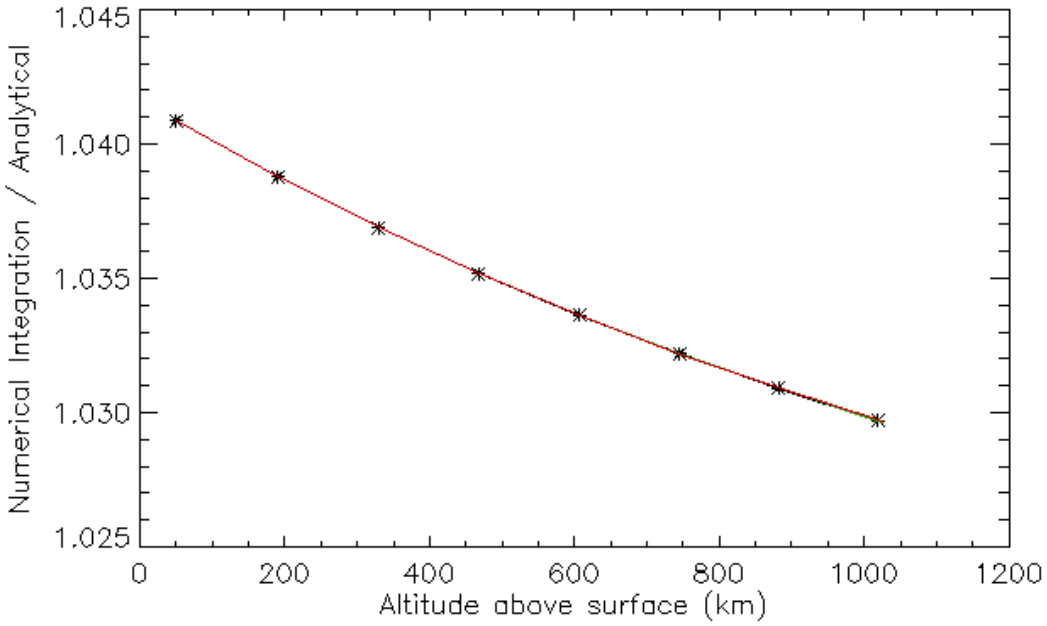

Figure 4.3. Ratio of numerically integrated column abundance from the software planning tool to the analytically derived tangential column abundance for an isotropic exosphere.

The reason the numerical integration method is used instead of the analytical method of Chamberlain is because the exosphere is generally not isotropic, and thus the analytical solution is no longer valid.

4.3.4 Limitations of the constant gravity assumption

The inaccuracy associated with treating density profiles with constant gravity increases with increasing height above the planet. The acceleration of gravity above the planet surface varies according to

$$g(r) = \frac{MG}{r^2} \tag{4.2}$$

where M is the mass of the planet, G is the gravitational constant, and r is the distance from the center of the planet. The constant gravity assumption assumes r is the planetary radius and does not vary, thus the value of gravity at the surface of the planet. Figure 4.4 shows the ratio of true gravity to the surface gravity up to a height of 1000 km above the planet surface. The assumption of constant gravity is ~ 30% in error at ~500 km above the surface, thus plots of all predicted signal values above 500 km will be denoted as dashed lines.

Table 3.2 shows that the largest scale height for the 3 source processes is meteoritic vaporization, which is ~ 230 km, so an altitude of 500 km is more than 2 scale heights for the most energetic process. This serves to illustrate that although observations will be made for heights greater than 500 km, the majority of the sodium exosphere is beneath this height and the constant gravity approximation is reasonable.

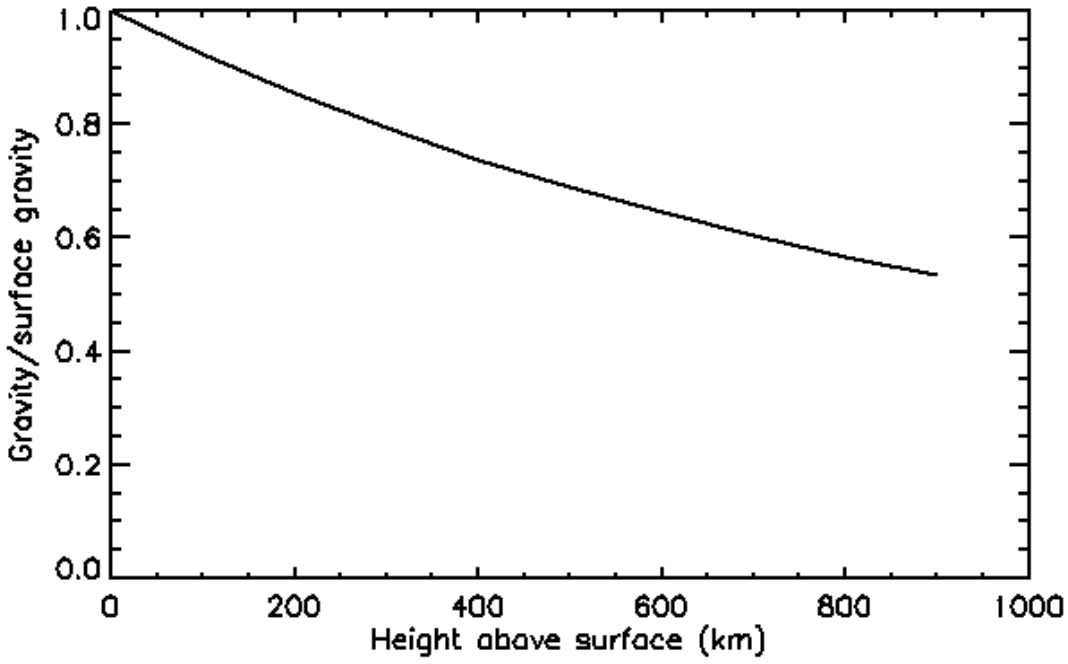

Figure 4.4 Plot of gravity above the surface divided by gravity at the surface. The agreement is ~ 70% at ~ 500 km above the planet surface. This altitude serves as a cutoff point for the results of the tangentially integrated column abundance.

4.3.5 Conversion of tangentially integrated column abundances to radiances

Chapter 1 describes the physics behind resonant scattering. The approach adopted here to predict radiance values for the sodium D lines from the integrated column abundance is to use a sodium curve of growth. After determining the tangentially integrated column abundance, a curve of growth (Figure 4.5) is used to calculate radiance values for both of the sodium D lines for the column density. The curve of growth varies according to the g-values and characteristic temperature of the source process. Figure 4.5 shows the curve of growth for g-values associated with a planetary true anomaly = 96° and for a temperature of 1100 K. This temperature lies in the range of expected characteristic temperatures for photon stimulated desorption. For other source processes and g-values, the curve of growth is modified for characteristic temperatures associated with each source process as well as for variation in g-values with true anomaly.

Figure 4.6 shows the radiance values for the numerically integrated tangential column abundance from photon stimulated desorption above the sub-solar point at a planetary true anomaly of 96°. The red vertical line denotes 500 km above the surface, at which the constant gravity assumption is 30% in error from gravity determined by the $1/r^2$ law.

4.4 Predicted count rate and uncertainty

The photons that enter the instrument are the sum of solar photons resonantly scattered from exospheric sodium and solar photons reflected from the planet surface that enter the instrument off-axis from the telescope boresight, known as the solar

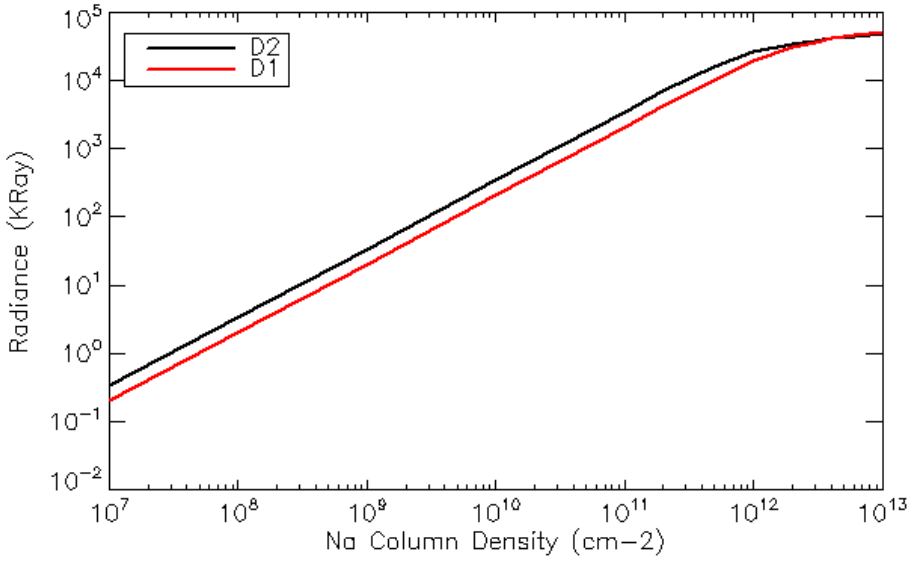

Figure 4.5. Curve of growth for both of the sodium D lines at Mercury for a planetary true anomaly = 96° and for a temperature of 1100 K.

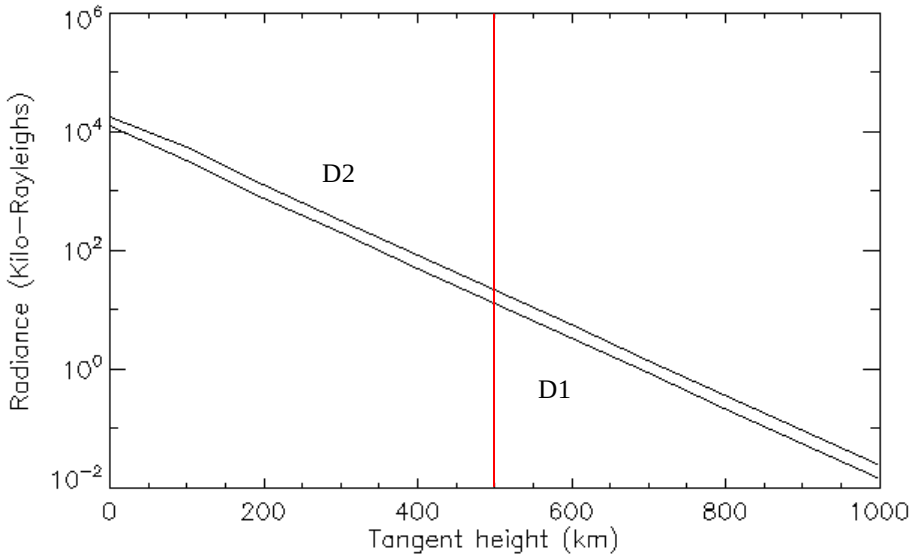

Figure 4.6. Radiance of both the sodium D1 and D2 lines as a function of tangent height.

continuum background. The count rate output from the instrument results from these photons as well as detector dark counts arising from themionic emission in the photomultiplier tube detector. The count rates from each of these 3 processes are predicted separately and then added to give the predicted count rate for an observation.

The density for photon stimulated desorption was numerically integrated along the line of sight and then the curve of growth of Figure 4.5 was used to determine the radiance for each line. The red vertical line at 500 km denotes where the constant gravity assumption is in error by ~ 30%.

4.4.1 Count rates from sodium exospheric emission

The total count rate corrected for grating sampling arising from exospheric sodium is given by

$$\dot{C}_{corr} = L_{line} * S_{line} \tag{4.3}$$

with L_{line} the radiance of one of the sodium D lines and S_{line} the sensitivity of the instrument at that line. The sensitivity of the UVVS VIS channel for spectral lines is shown in Chapter 2, Figure 2.38.

The counts are then distributed in wavelength by the instrument point spread function at each grating step in the vicinity of the sodium D lines by convolving the corrected count rate with the instrument profile function. The instrument profile

function was determined experimentally by scanning the grating over a spectral line and fitting a Gaussian to the data point, as described in Chapter 2.

The convolution of the total count rate corrected for grating sampling for both of the sodium D lines with the instrument profile function is shown graphically in Figure 4.7. Although the spectral lines are not purely delta functions, they are on the order of 10's to 100's of mÅ wide. Thus, in comparison to the width of the instrument profile function, the lines are approximated as delta functions.

Thus predicted radiances from the sodium exospheric model are used in Equation 4.3 to produce delta functions for corrected count rates for both sodium D lines; which are then convolved with the instrument profile function to produce count rates at each grating step. Figure 4.8 shows the predicted count rate spectrum without background for photon stimulated desorption for an observation 100 km above the sub-solar point while the planet was at a true anomaly of ~ 96°. 18 grating steps centered on the sodium D lines are sufficient to capture the signal from sodium exospheric emission while also sampling the spectrum off both sides of the sodium D lines. The tangentially integrated column density at this height has a value of $1.4*10^{11}$ Na/cm^2. The total signal corrected for grating sampling is 30337 counts/second and 17426 counts/second for the D2 and D1 lines respectively. It is important to note that count rates from each of the two sodium D lines add together for the grating steps near the center of the sodium D line region.

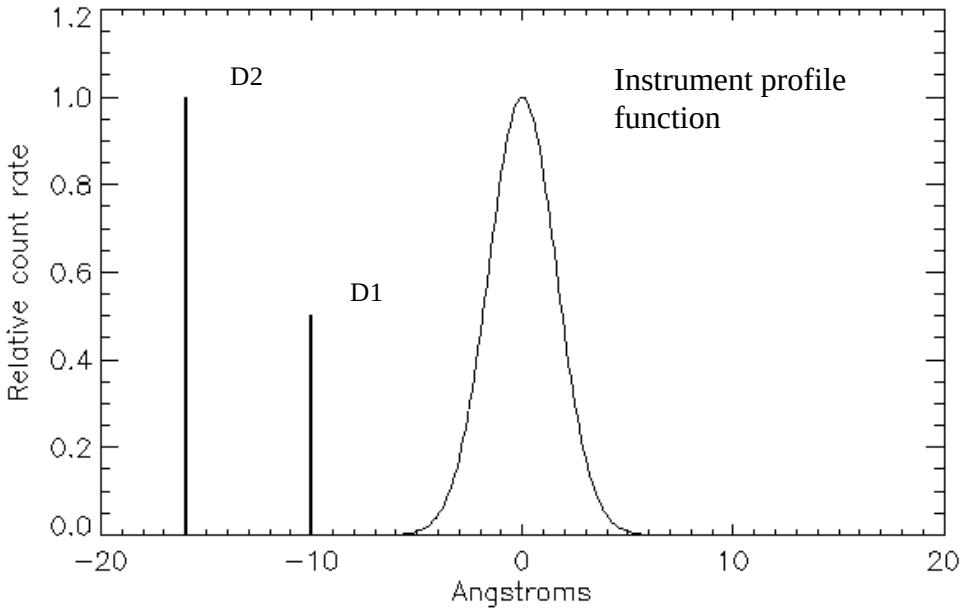

Figure 4.7. The convolution of delta functions with the instrument profile function. Since the profile is spectrally wider than the separation of the sodium D lines, the result is two lines with overlap in the central region

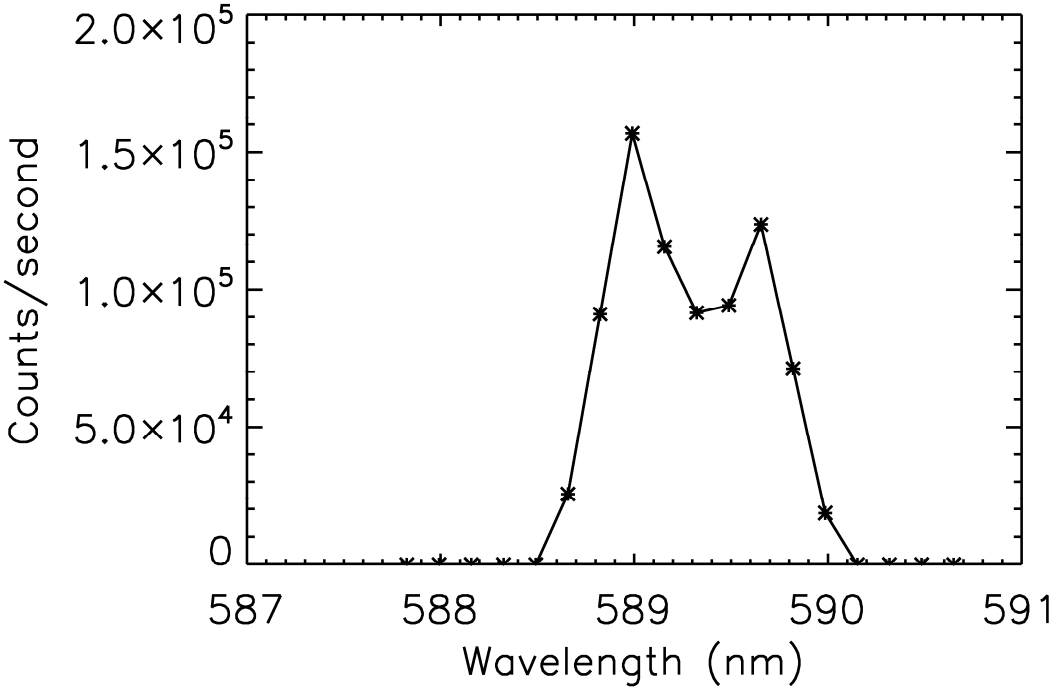

Figure 4.8. Result of the convolution of both sodium D lines with the instrument profile function for the surface slit with an observation 100 km above the limb at a planetary true anomaly angle of 97°. Although the spectral lines are modeled as delta functions, point spreading causes the lines to overlap spectrally.

4.4.2 Solar continuum background

In order to predict the off-axis component of solar radiation that enters the instrument, the solar radiation at the peak of the off-axis response curve must first be determined. The signal that would be obtained by looking directly at Mercury's surface, which corresponds to the peak of the off-axis curve, is determined by taking the solar spectrum observed at the Moon (Figure 4.9) and scaling it to the Mercury-Sun distance. Also, a correction factor of 1.8 is used to scale for differences in the reflectance of the Moon and Mercury. The average reflectance at the Moon is based on dark mare regions, whereas the average reflectance of Mercury is based on bright highland material; thus the correction factor serves to over-estimate the amount of reflected sunlight from the surface of Mercury. Furthermore, since the phase angle of the moon during the lunar observations was ~ 67°, the signal was photometrically corrected to 90°, which better suits the observing geometry above the limb of Mercury after orbit insertion. This was done by taking the incidence, emission, and phase angle for the lunar observation that produced the maximum signal (Figure 4.9) and calculating the bi-directional reflectance by use of the Hapke photometric function. The incidence, emission, and phase angles were 34°, 33°, and 67°, respectively. Then the phase and incidence angles were changed to 90° and 57°, respectively, and the bi-directional reflectance calculated again. The ratio of the reflectance for the 90 phase angle case to the 67 phase angle case was 0.625 and was used to multiply the curve of Figure 4.9. The predicted reflected solar continuum from Mercury's surface is then multiplied by the off-axis curves for the relevant off-axis angle, yielding the results shown in Figure 4.10. The curves in Figure 4.10

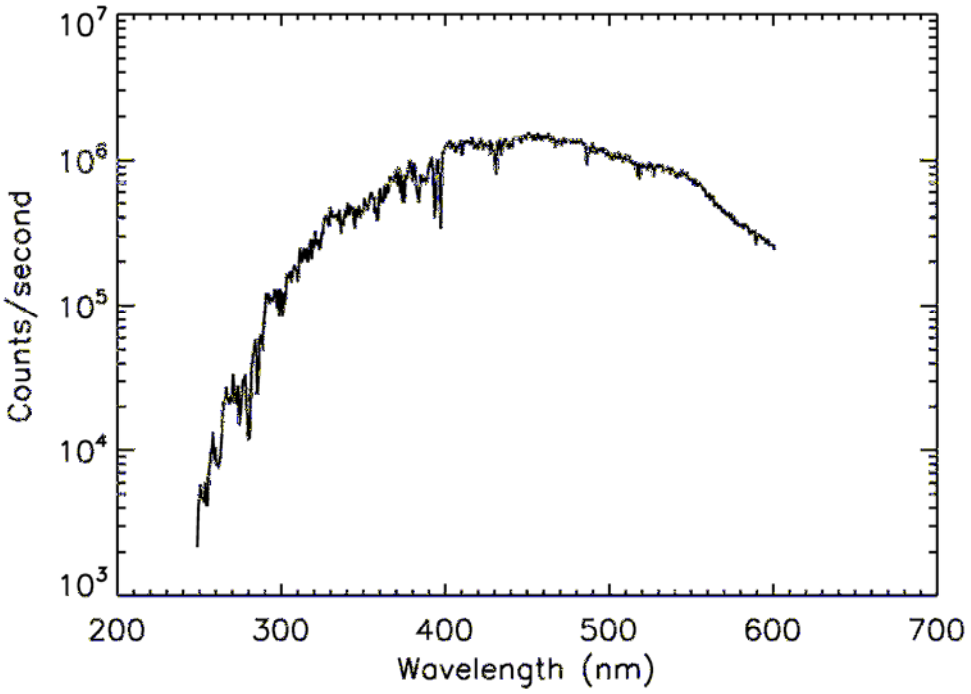

Figure 4.9. Reflected solar spectrum taken from the surface of the Moon with the UVVS surface slit. This corresponds to the grating scan with the largest count rate.

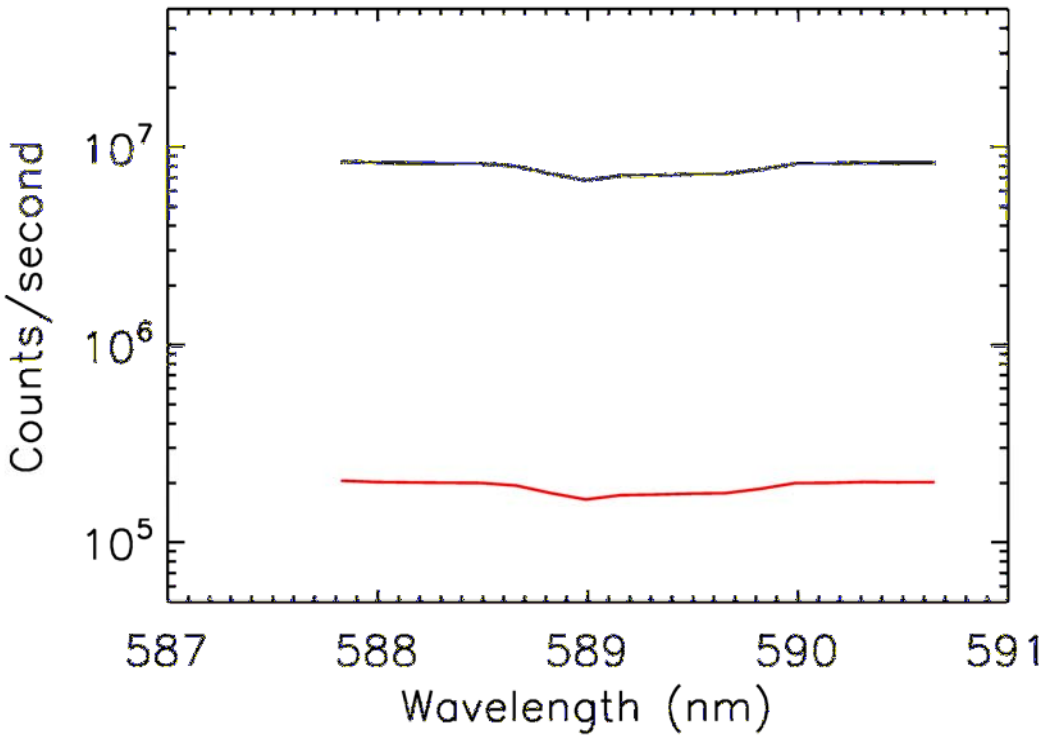

Figure 4.10. The solar continuum in the vicinity of the sodium D lines smoothed to the bandpass of the instrument. The two plots represent the off-axis solar continuum reflected from the surface of Mercury for both the surface slit (red curve) and the atmospheric slit (black curve). The observation is at a limb height of 100 km and for a planetary true anomaly of 97° and an off axis angle ~ 0.4°. The count rate from the atmospheric slit is ~ 2 orders of magnitude larger than the count rate from the surface slit due in part to differences in the off-axis response for the 2 slits and also because of the factor of 20 difference in sensitivity between the 2 slits. Note that the count rate for the atmospheric slit is larger than acceptable detector count rate upper limits. This implies the use of the surface slit for low altitude, long range observations.

are for an observation 100 km above the limb where the off-axis angle is 0.7° at a planetary true anomaly of 97° using both the atmospheric and surface slits.

4.4.3 Addition of dark counts

The dark counts from a PMT arise from thermionic emission of electrons from the photcathode and dynode and are a function of surface work function and temperature. The dark count rate was measured in the laboratory before launch and the data fit to an exponential function as described in Chapter 2.

Recent post-launch measurements of dark counts indicate that the dark count rate may be as high as 10X the value predicted by Equation 2.1 for temperatures from -10° to 10° C. No new dark count data is available for temperatures larger than 10° C. Thus the increased values for lower temperatures may consist of either an additive term or a multiplicative term to Equation 2.1. In order to take a conservative approach for including dark counts in the signal, the curve of Equation 2.1 is multiplied by 10 for all temperatures. Since the Sun-Mercury distance varies with true anomaly, the temperature of the planet also varies with true anomaly and thus causes temperature variations in the instrument. Using Equation 2.1 multiplied by 10 and the predicted temperature variations for MASCS (calibration report, unpublished) the dark count rate may be expressed as a function of planetary true anomaly as shown in Figure 4.11.

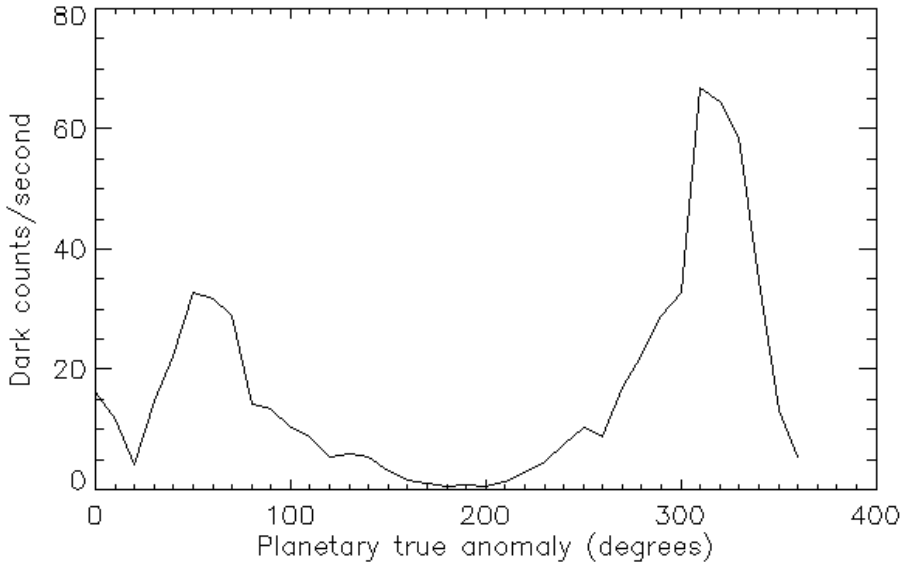

Figure 4.11. Variation of VIS channel dark count rate as a function of planetary true anomaly based on the temperature dependence determined in the laboratory multiplied by 10.

4.4.4 Addition of random noise

In order to accurately simulate real data, random noise is added to the synthetically generated data. This is achieved by using a normally distributed IDL random number generator with a mean of 0 and a standard deviation of 1 to generate a random value for each of the 18 grating steps. For each grating step, the random value is multiplied by $\sqrt{C}$ and then added back to the original value of C, which simulates 1-σ uncertainty in the data.

4.4.5 Determination of predicted signal and SNR

The 3 components of the count rates, signal, solar continuum background, and dark counts, are added together and shown in Figure 4.12 for an observation 100 km above the sub-solar region and for a planetary true anomaly = 97°. The off-axis angle for the observation is 0.42°, with data predictions are given for both slits. The red stars represent data points out in the continuum which would be used to determine the solar continuum beneath the lines for a real observation. All of the 11 black stars are data points used to determine both of the sodium D lines. Since the bandpass of the instrument is such that the sodium D lines cannot be completely resolved independently, the two lines must be considered together and separated using the instrument profile function.

The data shown in Figure 4.12 is an example of a simulated observation created by the software tool. The remainder of the software tool is used to extract the signal

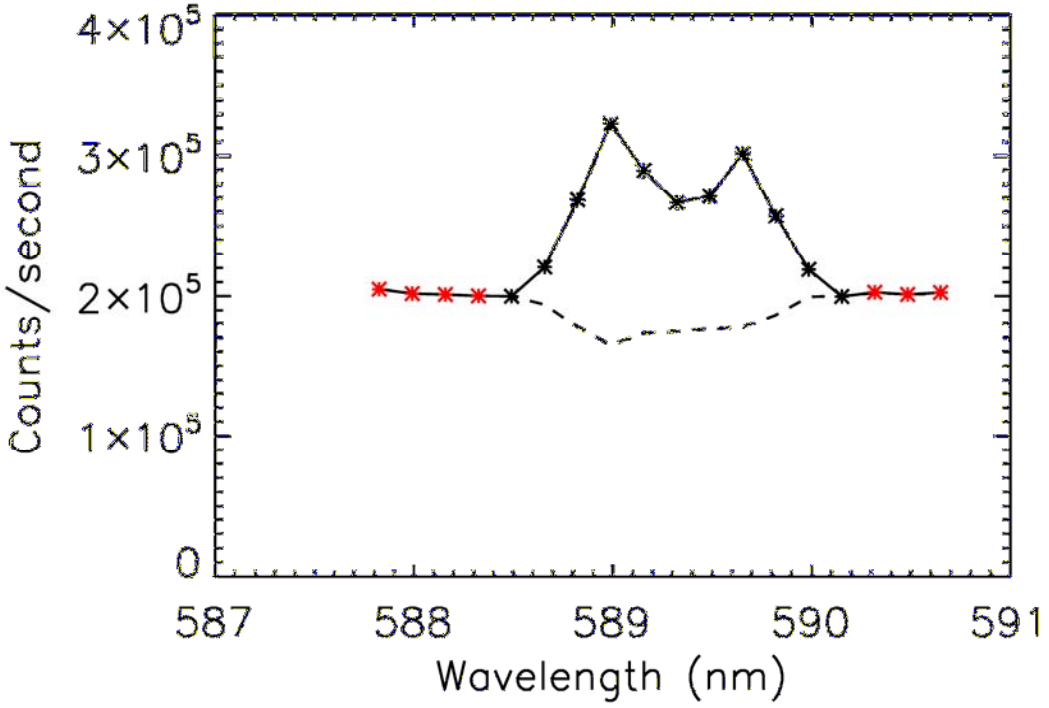

Figure 4.12. 18 grating step scan across both sodium D lines for an observation 100 km above the sub-solar region for a planetary true anomaly = 97° using the surface slit. The black stars represent the data points that capture the signal from the lines. The red stars represent data points out in the continuum that will be used to determine the solar background in the region of the lines. The black dashed line shows the reference solar continuum that has been smoothed to the bandpass of the instrument and that has been fit to the data points in the wings (red stars).

and SNR from the simulated data. The count rate at each of the 11 data points corresponding to the sodium D lines is determined by:

$$\mathrm{C_{i\_signal}} \pm \sigma_{\mathrm{C\,i\_signal}} = \mathrm{C_{i\_obs}} - \mathrm{D_i} - \mathrm{B_i} \pm \sqrt{\sigma^2_{C\_i} + \sigma^2_{D\_i} + \sigma^2_{B\_i}} \tag{4.4}$$

where $\mathrm{C_{i\_signal}}$ is the signal from exospheric sodium emission, $\sigma_{\mathrm{C\,i\_signal}}$ is the uncertainty in the signal, $\mathrm{C_{i\_obs}}$ is the count rate as shown in Figure 4.12, $\mathrm{D_i}$ is the dark count rate, $\mathrm{B_i}$ is the estimated the solar continuum background, $\sigma^2_{C\_i} = \mathrm{C_{i\_obs}}$, $\sigma^2_{D\_i} = \mathrm{D_i}$, and $\sigma^2_{B\_i}$ is the estimated uncertainty in the background; all at grating step i, with the index "i" representing the data points beneath the sodium D lines.

The inclusion of the dark counts, $\mathrm{D_i}$, in Equation 4.4 is strait-forward since the dark counts are independent of grating step; thus all dark counts are the same for a single temperature. The solar continuum background is more complicated, thus $\mathrm{B_i}$ and $\sigma^2_{B\_i}$ requires further explanation. The goal is to determine the solar continuum beneath the sodium D lines by making use of the measurements out in the wings (the 7 red star data points of Figure 4.12). This is done by first determining the average solar continuum for the 7 data points according to:

$$\mathrm{B_{avg\_obs}} = \frac{\sum_{\mathrm{k=0}}^{7} \mathrm{C_{k\_obs}} - \sum_{K=0}^{7} D_k}{7} \pm \frac{\sqrt{\sum_{\mathrm{k}}^{7} \mathrm{C_{k\_obs}} + \sum_{K=0}^{7} D_k}}{7}$$

$$\mathrm{B_{avg\_obs}} = A + \Delta A \tag{4.5}$$

where the index “k” represents the data points out in the wings. Also note that the dark counts must also be subtracted from the data points out in the wings.

The solar continuum that was used for the background has been normalized to its maximum value over the same wavelength range as the predicted data and is used as a solar continuum reference (Figure 4.13). An average of the continuum reference over the same 7 data points is given by:

$$B_{avg} = \frac{\sum_{k}^{7} b_{k\_ref}}{7} \tag{4.6}$$

A scaling factor for the average background is determined by

$$f + \Delta f = \frac{A + \Delta A}{B_{avg}} \tag{4.7}$$

The B_i data values of Equation 4.4 are now determined by multiplying the scaling factor by the normalized reference solar spectrum according to:

$$B_i = b_{i\_ref} * f \tag{4.8}$$

The estimated uncertainty in the background beneath the lines is given by

$$\sigma_{B\_i} = b_{i\_ref} * \Delta f \tag{4.9}$$

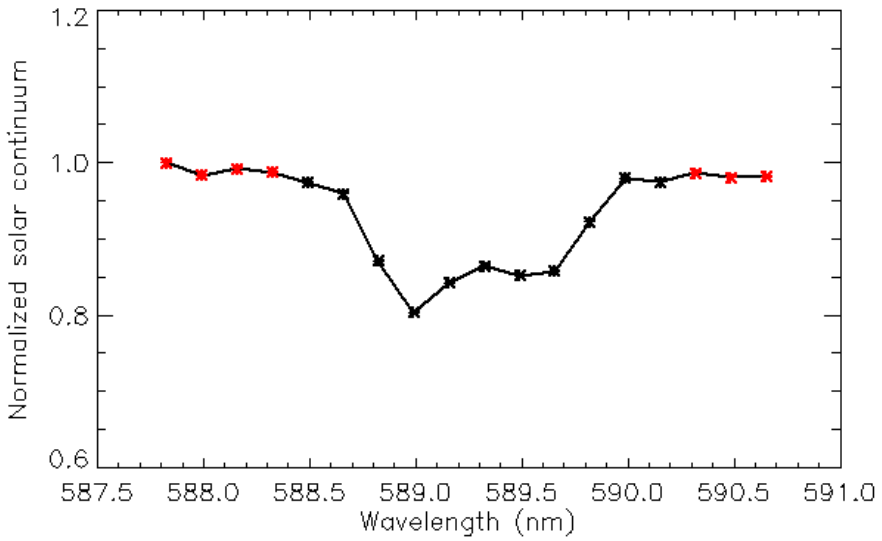

Figure 4.13. Normalized solar spectrum smoothed to the instrument bandpass that is used as the reference spectrum to be subtracted from the data.

The total uncertainty beneath the lines is given by

$$\sigma = \sqrt{\sigma_C^2 + \sigma_D^2 + \sigma_B^2} \tag{4.10}$$

where $\sigma_C = \sqrt{\sum_{i=0}^{10} \sigma_{C\_i}^2}$, $\sigma_D = \sqrt{\sum_{i=0}^{10} \sigma_{D\_i}^2}$, and $\sigma_B = \sqrt{\sum_{i=0}^{10} \sigma_{B\_i}^2}$

After subtraction of dark counts and solar continuum background, the resulting data consists of counts arising from both of the sodium D lines, similar to Figure 4.8. As previously mentioned, the count rates for data points near the centroid of the sodium D lines consists of counts from both of the sodium D lines. The data must now be separated into count rates arising from each line. This is done by an IDL curvefitting routine that fits two triangle functions centered at each of the two sodium D lines to the data. The triangle functions represent the instrument profile function with a FWHM for each determined both experimentally and theoretically. The dependent variables for both of the triangle functions are the magnitudes, center wavelength, and FWHM. The routine iterates until the minimum in the least squares of the combined triangle functions with the data points does not vary more than a preset tolerance. The result is 2 separate curves, one for each sodium D line, with count rates distributed over grating step. Figure 4.14 shows an example of the simulated count rate from Figure 4.12 after subtraction of the solar continuum background and dark counts. Also in Figure 4.14 are the fitted D1 and D2 lines from the routine, shown in blue. For each line, the magnitude is multiplied by the FWHM. This gives the effective area under each line, with the D_2/D_1 line ratio given by

$$\frac{D_2}{D_1} = \frac{M_2 * FWHM_2}{M_1 * FWHM_1} \tag{4.11}$$

where M_1 and M_2 are the magnitudes of the least square fit D_1 and D_2 lines and $FWHM_1$ and $FWHM_2$ are the full width half max of the least square fit D_1 and D_2 lines. Furthermore, the fraction of the total counts that each line contributes to the total count rate is given by

$$\begin{aligned} D_{2\_fraction} &= \frac{M_2 * FWHM_2}{M_1 * FWHM_1 + M_2 * FWHM_2} \\ D_{1\_fraction} &= \frac{M_1 * FWHM_1}{M_1 * FWHM_1 + M_2 * FWHM_2} \end{aligned} \tag{4.12}$$

The D_2 and D_1 count rates with estimated uncertainties are

$$\begin{aligned} C_{D1} &= \left[\left(\sum_{i=1}^{11} C_{i\_signal}\right)\right] * D_{1\_fraction} \\ C_{D2} &= \left[\left(\sum_{i=1}^{11} C_{i\_signal}\right)\right] * D_{2\_fraction} \\ \sigma_{D1} &= \sqrt{\left(\sigma * D_{1\_fraction}\right)^2 + \left(\sigma_{D1\_fraction} * \sum_{i=1}^{11} C_{i\_signal}\right)^2} \\ \sigma_{D2} &= \sqrt{\left(\sigma * D_{2\_fraction}\right)^2 + \left(\sigma_{D2\_fraction} * \sum_{i=1}^{11} C_{i\_signal}\right)^2} \end{aligned} \tag{4.13}$$

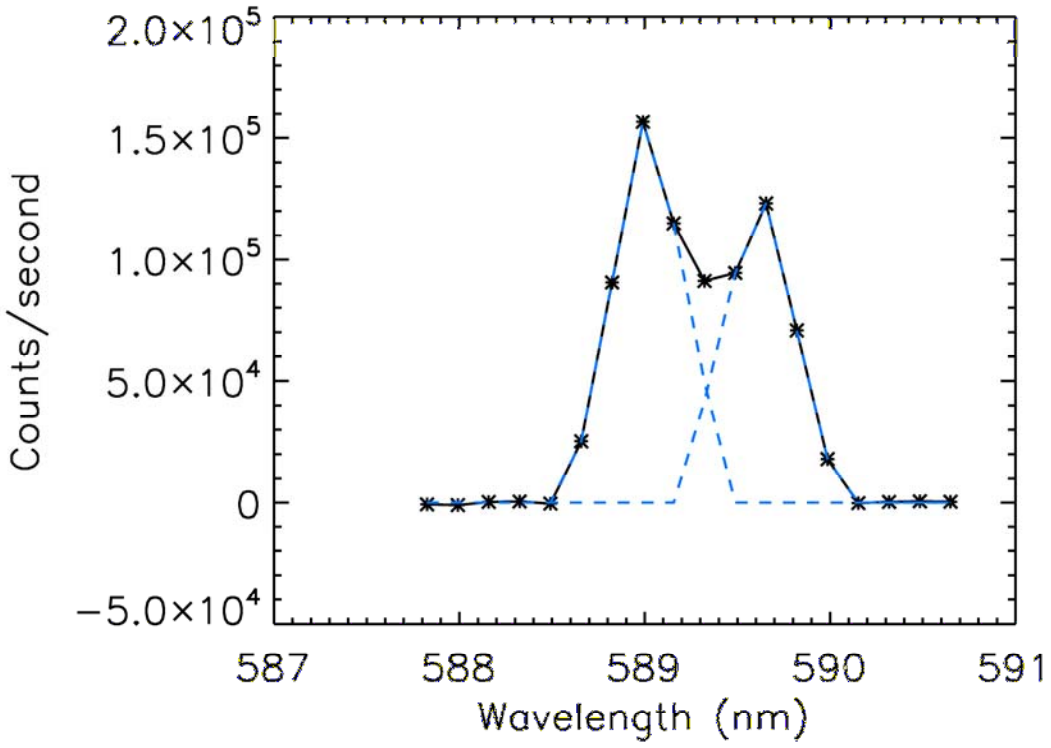

Figure 4.14. D_1 and D_2 components (blue dashed lines) for the total signal of both lines together (black line). The individual components are the result of the least squares fitting routine described above. The total of each line allows for the determination of the D_2/ D_1 line ratio as well as the fraction of each line to the total.

Equation 4.13 uses the count rates from Equation 4.4 summed over the 11 grating steps, the uncertainty, σ, from Equation 4.10, the fractions of the D_1 and D_2 lines, and the uncertainties in the D_1 and D_2 fractions ($\sigma_{D1\_fraction}$ and $\sigma_{D2\_fraction}$) to determine the fraction of the total counts and total uncertainty that are attributable to each of the D lines.

As the grating turns, the image of the entrance slit is stepped across the exit slit. The grating step size is such that the entrance slit image does not move completely across the exit slit in a single grating step, but instead is over-sampled. This in effect is what leads to the instrument profile. A correction needs to be made for grating sampling by dividing the summed counts under a spectral line by the ratio of bandpass to grating step size, as shown in Equation 4.14.

$$\frac{C_{D1} \pm \sigma_{D1}}{Bandpass / Grating\ step\ size} = C_{corr\ D1} + \sigma_{D1\,corr}$$
$$\frac{C_{D2} \pm \sigma_{D2}}{Bandpass / Grating\ step\ size} = C_{corr\ D2} + \sigma_{D2\,corr} \qquad (4.14)$$

The subscripts “corr D1” and “corr D2” correspond to the fractional totals being corrected for grating sampling.

Finally, the SNR for each line is given by

$$\begin{aligned} \mathrm{SNR}_{\mathrm{D1}} &= \frac{C_{\mathrm{corr\ D1}}}{\sigma_{\mathrm{corr}}} \\ \mathrm{SNR}_{\mathrm{D2}} &= \frac{C_{\mathrm{corr\ D2}}}{\sigma_{\mathrm{corr}}} \end{aligned} \tag{4.15}$$

Figures 4.15 and 4.16 show the steps that are taken where the counts were added together, random noise added, and then the background subtracted. These results pertain to an observation above the sub-solar region for a planetary true anomaly of 97° and for a spacecraft position approaching apoherm. Figure 4.15 is for an observation 100 km above the limb and corresponds to the same simulated observation shown in Figures 4.8-4.14. Figure 4.16 is for an observation 700 km above the sub-solar region.

For both Figures 4.15 and 4.16 panel “a” shows the count rate from the sodium D_1 and D_2 lines after having the instrument profile point spread function applied. Panel “b” shows the off-axis solar continuum that has been smoothed to the bandpass of the instrument. Panel “c” shows the dark counts which are the same for each grating step. Panel “d” shows the sum at each grating step of the counts from the D_1 and D_2 lines, the off-axis solar continuum, and the dark counts. Panel “e” shows the same sum as panel “d” but with random noise added, producing the “predicted” count rates for the simulated observation. Panel “f” shows the “predicted” count rates after the subtraction of dark counts. Panel “g” is the same as anel “f” but shows the solar continuum (dashed red curve) that has been scaled to the data in the wings of the

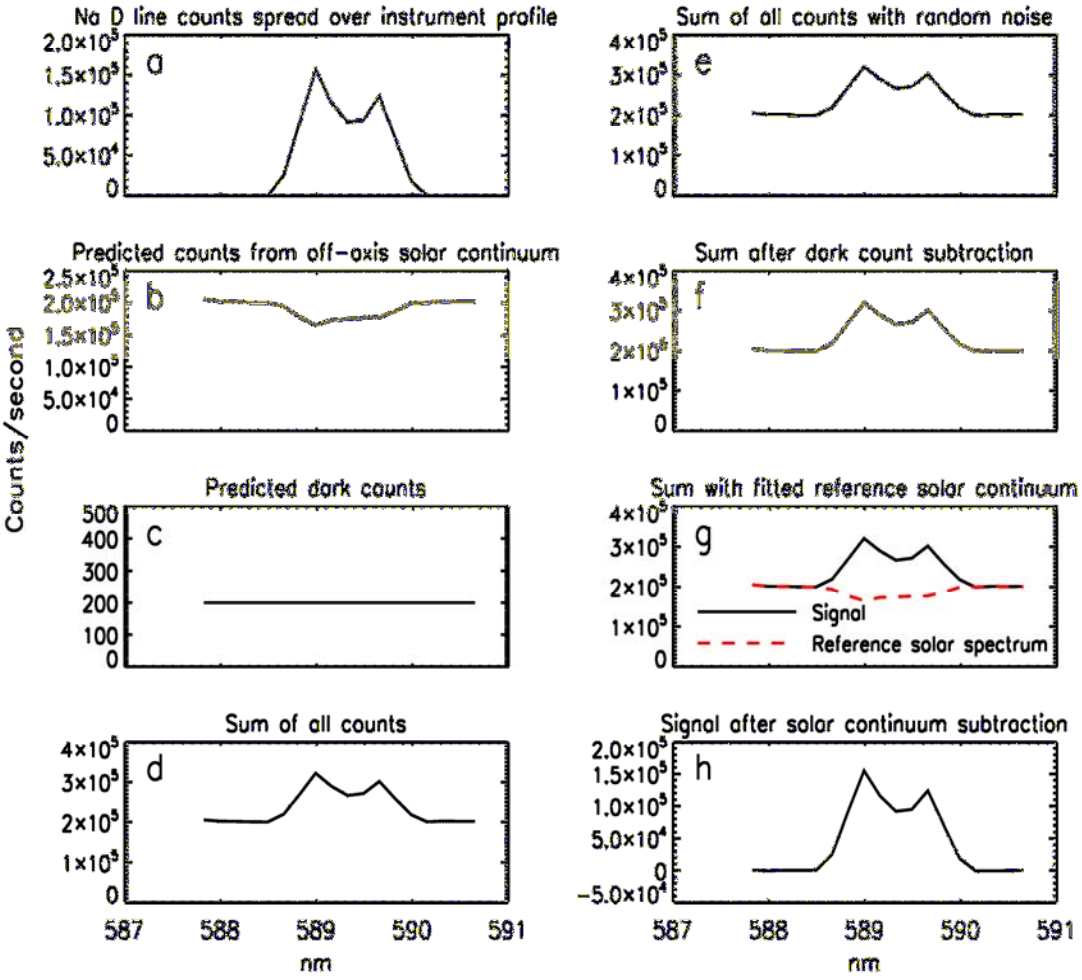

Figure 4.15. Predicted count rates for an observation 100 km above the sub-solar region and for a planetary true anomaly = 97°. A description of each panel is in the text.

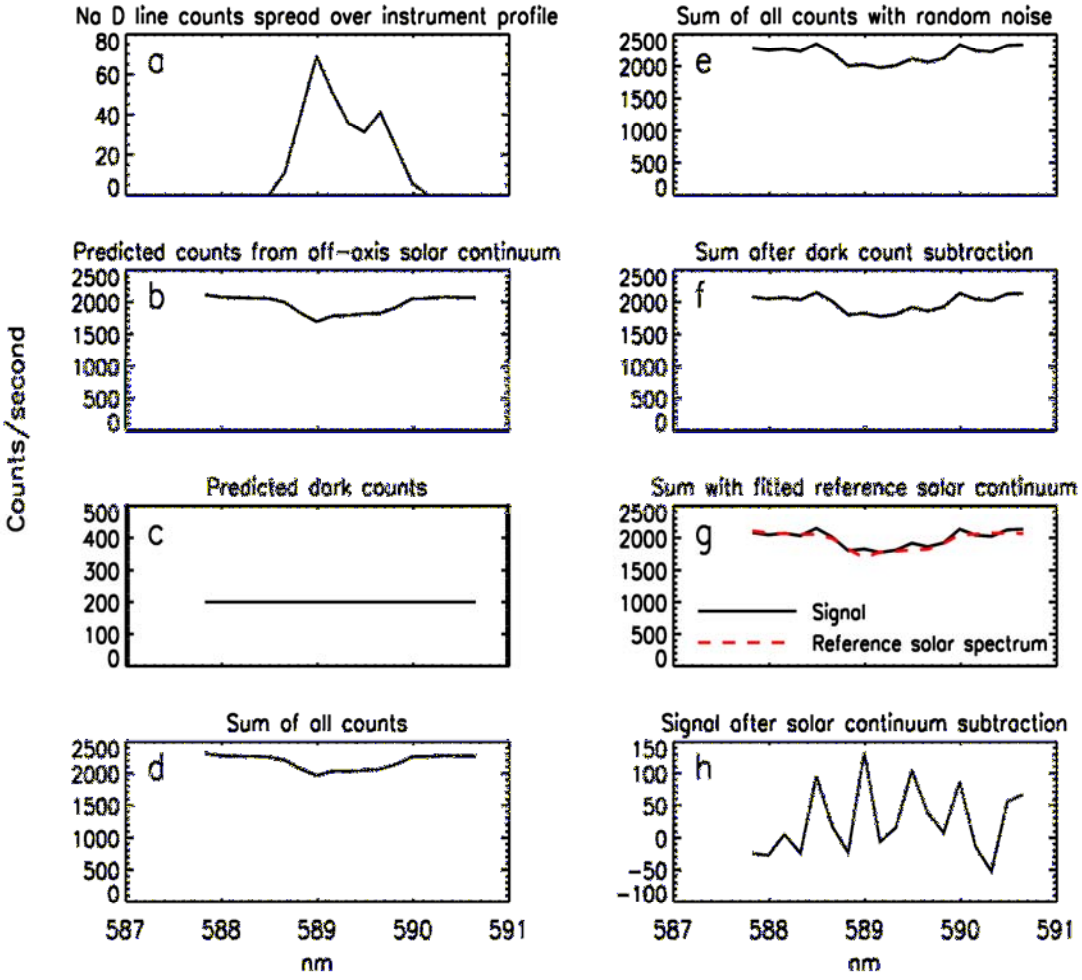

Figure 4.16. Predicted count rates for an observation 700 km above the sub-solar region and for a planetary true anomaly = 97°. A description of each panel is in the text.

"predicted" signal after dark count subtraction. Panel "h" shows the "predicted signal after the subtraction of the scaled solar continuum shown in panel "g.

The count rates from both the D_1 and D_2 lines as well as the off-axis solar continuum are much lower for the 700 km height observation than for the 100 km height observation. The 100 km height observation produces a signal that is clearly distinguishable from the background; however the 700 km height observation results in a signal that is un-distinguishable from the background.

4.5 Summary

This chapter has given the details of how to predict a signal and SNR for the sodium exosphere using the instrument performance characteristics, predicted extended source off-axis light, observational geometry, and sodium exospheric model predictions. Numerical results are plotted in Chapter 5.

The variation of density with height using a constant gravity assumption is described along with an assessment of the range of altitudes over which this assumption is valid. It has been demonstrated that the constant gravity assumption is accurate to within 70 % up to an altitude of 500 km and attention has been given to the fact that the maximum expected scale height for sodium atoms is ~ 230 km. Thus, even for these high energy atoms, an altitude of 500 km encompasses more than 2 scale heights.

The methodology for numerically integrating column abundances along the tangential line of sight has been described. A comparison with analytical predictions

has been shown for the case of an isotropic exosphere, with an error of less than 5 % over an altitude range from 50 to 1000 km.

The calculation of radiance from tangentially integrated column abundance has been shown to be based on a curve of growth model adapted to Doppler shifting phenomena at Mercury. Both the D_1 and D_2 lines are calculated.

A description of the process for determining the total count rate for both of the sodium D lines along with off-axis light and dark counts has been presented. Furthermore, the technique for subtracting the background from the signal as well as estimating the uncertainties associated with the measurements beneath the combined D_1 and D_2 lines has been described. A description of a least squares fitting routine to separate the combined signal into the individual D lines has been presented; with emphasis on estimating the uncertainties associated with each line by making use of the D_2/D_1 line ratios.

Chapter 5

Observation opportunities, Signal, and SNR Predictions

5.1 Introduction

The goal of this thesis is to develop observation strategies for MASCS that systematically map the exosphere of Mercury over local time of day, altitude, and season; resulting in a uniform data set that addresses key scientific questions (see Chapter 1). This goal is achieved by considering geometrical and temporal observational constraints and determining detection limits in order to devise a set of pre-planned observations. The planned observations are validated by testing the strategies with a sodium exospheric model and making signal and uncertainty predictions in order to characterize the ability of MASCS to distinguish between variations in exospheric processes.

Orbital geometry constrains observations by limiting the temporal and spatial coverage of observations for any given orbit. Since MESSENGER is in an orbit that is fixed in inertial space, the temporal and spatial coverage of the observations changes throughout the Mercury year. Sun-shade constraints limit pointing options and couple with the orbital geometry to form a combined set of constraints for spatial and temporal coverage of the exosphere.

Detection limits are determined by calculating the required exospheric radiance to achieve a specified SNR given predicted background signal.

Although this thesis deals with the observation and characterization of Mercury's sodium exosphere, the geometrical pointing constraints are the same for the observation of any atmospheric species. Thus the observational strategies developed in this thesis are adaptable for the observation of any exospheric species for the duration of the mission. In pursuing this goal, 3 sets of results have been produced; 1) demonstrate when and where observations are possible 2) determine detection limits based on a proposed set of systematic observations, and 3) characterize the ability of the instrument to distinguish between variations in Mercury's sodium exosphere.

5.2 MESSENGER orbital constraints

5.2.1 Geometrical pointing constraints

As discussed in Chapter 1, MESSENGER has a sunshade that protects the instrument deck from direct solar illumination. Rotation of the spacecraft around the spacecraft X and Z axes is limited to +/- 12°. The geometry of MESSENGER's orbit coupled with the sunshade constraints and the fact that the exosphere is observed by looking across the limb dictates a highly constrained observational strategy. Visualization of the pointing constraints is not intuitive, thus one thrust of this thesis is to describe spatially and temporally the pointing constraints for making observations. The problem may be formulated by posing the following question: "Imagine that the spacecraft is frozen at some position in its orbit. Where above the

planet can MASCS point at some height above the tangent point?" For such a scenario the only parameter that constrains the observational geometry is non-violation of the sun-shade constraint. Figures 5.1 and 5.2 illustrate the nature of a limb scan for the spacecraft in a fixed position in its orbit. The tangent point corresponds to the point of closest approach of the boresight to the planet, with the off-axis angle being the angle between the boresight and the vector from the spacecraft that just grazes the surface. As described in Chapter 2, off-axis light consists of contributions from all illuminated regions of the planet. Thus the point on the surface where the off-axis grazing vector intersects the planet is not the only contribution to the off-axis light, but serves as the reference point in the off-axis model that allows for the predicted off-axis light from all regions of the illuminated surface. Figure 5.2 is for the same scenario as Figure 5.1 but with a view looking down on the planetary north-pole. The projected field of view drawn to scale in the long direction is depicted above the tangent point. Notice that although the projected field of view is 1° in length, the fact that the observation is not above the sub-solar region allows for the limb scan to be closer to the surface without any portion of the planet falling within the field of view of the instrument. This is an important result that has implications for any low altitude observations; the lowest altitude observations possible are above the terminator region and must be increased as observations move towards the sub-solar region. One possible technique to circumvent this issue is to switch to the surface mode slit for low altitude observations in the sub-solar regions.

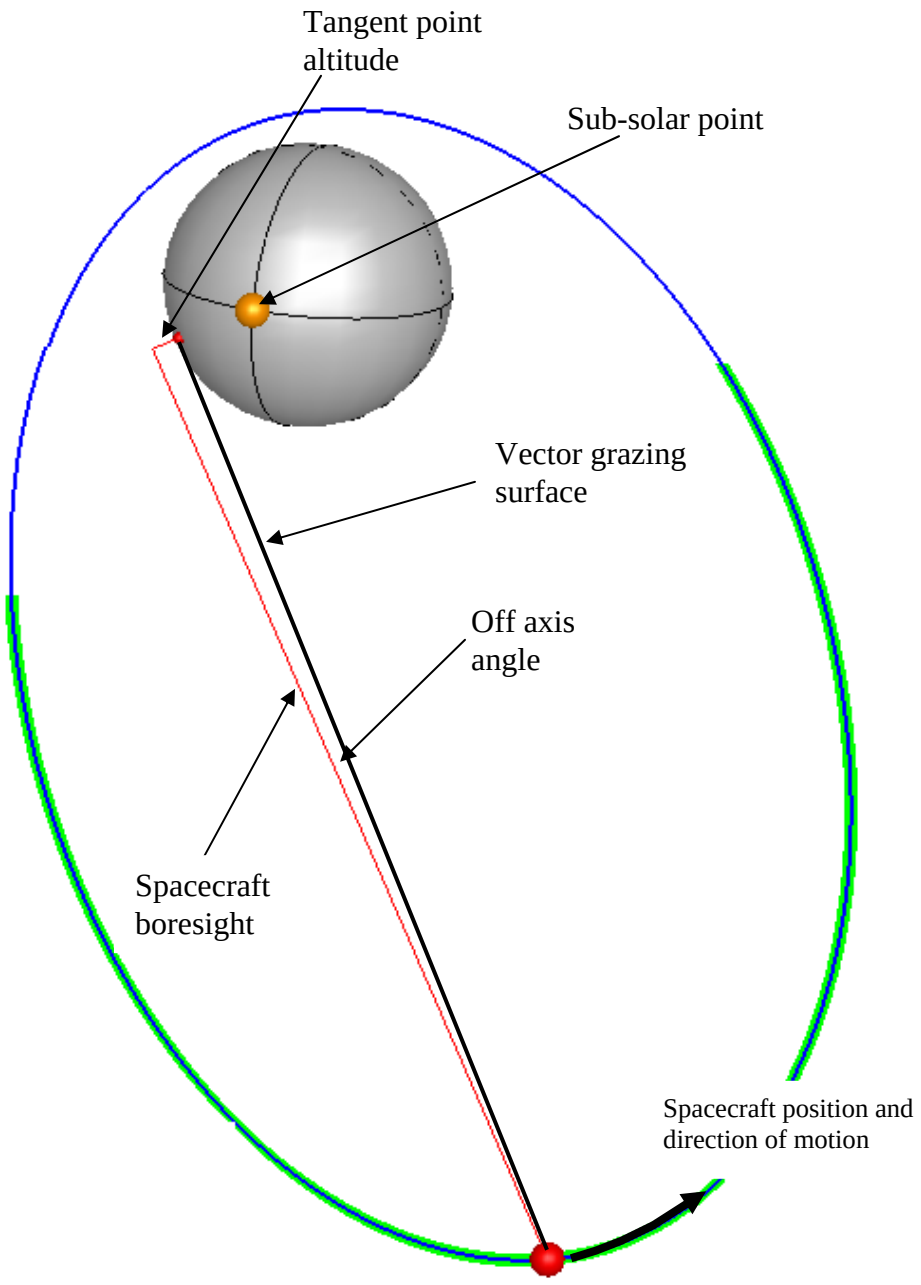

Figure 5.1. Orbit of MESSENGER showing a limb observation along with the off-axis angle.

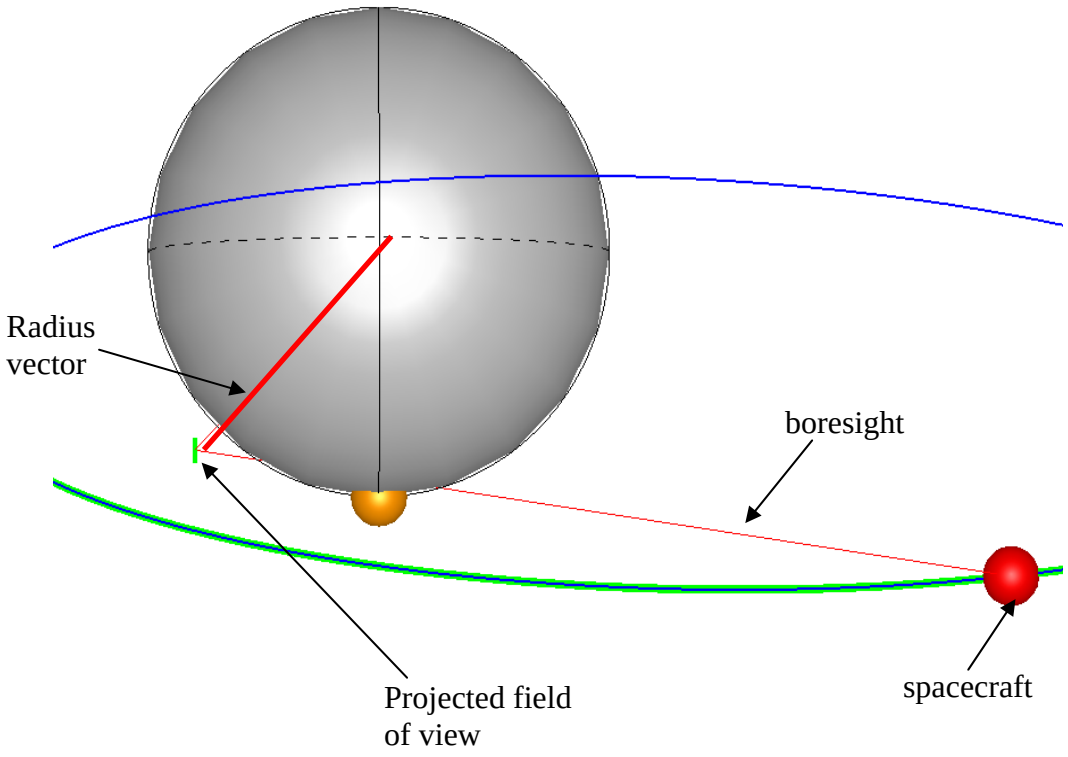

Figure 5.2. Same as Figure 5.1 but looking down on the north-pole of Mercury. This view shows the projected field of view, which is drawn to scale in the long direction.

It is instructive to plot the tangent points on the surface above which observations may be made for the spacecraft in a fixed orbital position but not fixed in attitude. Furthermore, in order to visualize how the families of tangent points vary throughout the orbit as well as throughout the Mercury year, the families of curves are plotted for every spacecraft position in increments of 10 minutes during a spacecraft orbit and for 8 planetary true anomalies throughout the Mercury year. Figure 5.3 shows the 8 planetary positions that are chosen to investigate. Important planetary positions in terms of spacecraft orbital geometry are the dawn-dusk and noon-midnight orbits, described in Chapter 1. Important planetary positions in terms of the sodium exosphere are perihelion, aphelion, and positions of maximum radiation pressure. The dawn dusk orbits are close to perihelion and aphelion. Maximum radiation pressure is at planetary true anomalies of 64°and 311°. Planetary positions of 134° and 226° are put in simply to show pointing geometries in those respective quadrants of the Mercurian year.

For a particular limb scan the key parameters that must be considered in terms of spacecraft pointing are projected field of view above the tangent point, off axis angle, and spacecraft location. For a series of limb scans within one spacecraft orbit, the velocity of the spacecraft with respect to the planet affects the duration of an observation. These two sets of parameters combine to determine the spatial and temporal constraints on exospheric limb scans. Each of these issues is discussed along with relevant figures in the following sections, with the implications of these parameters for observations summarized in section 5.2.6.

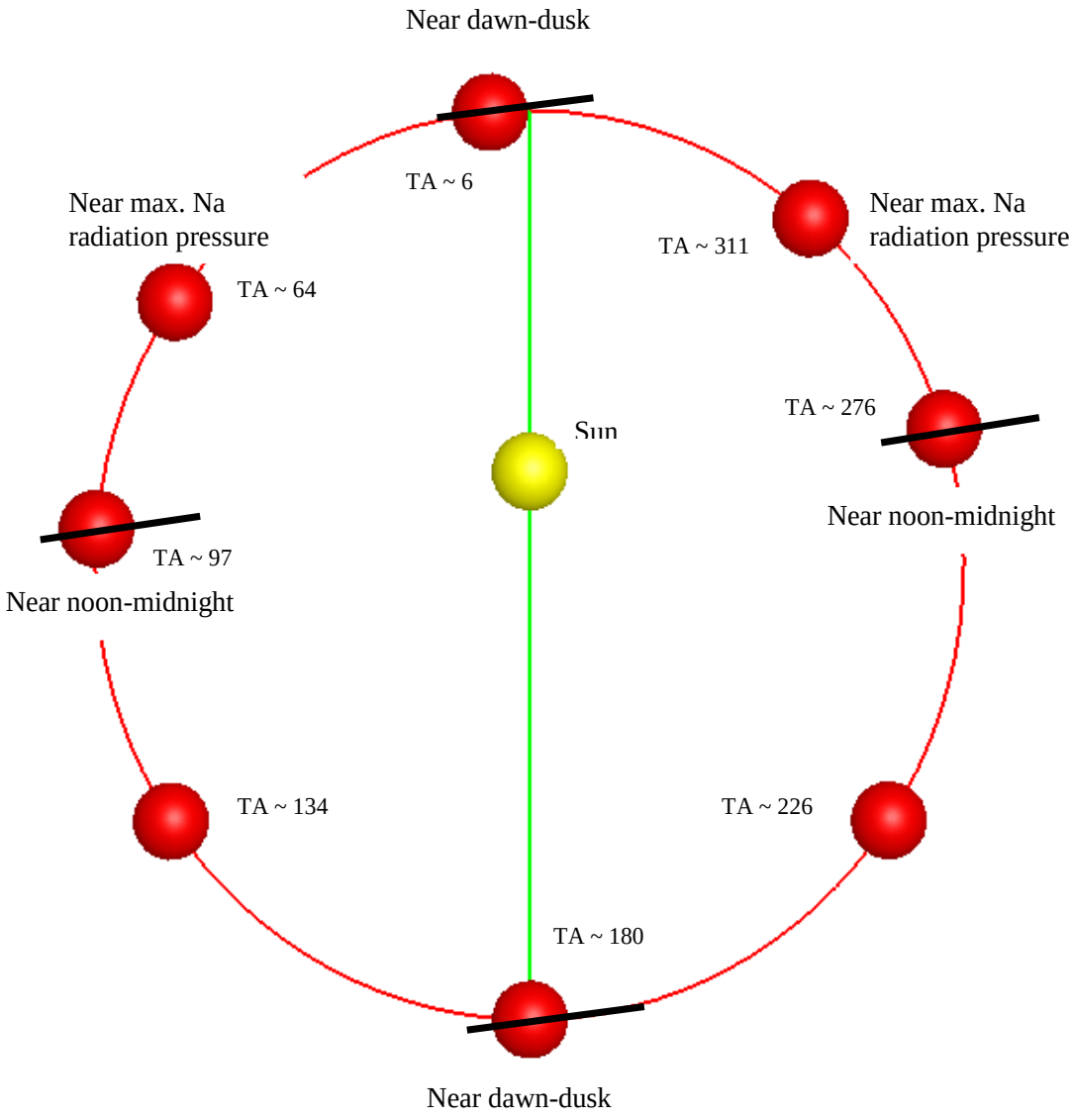

Figure 5.3. Positions of Mercury throughout the year that are considered important for observations of the sodium exosphere.

5.2.2 Projected field of view

The projected field of view is important because it is related to the spatial resolution of the observation as well as being one of the factors that determines how close to the surface limb observations can be made. Obviously, the further the spacecraft is from the tangent point the larger the projected field of view above the planetary limb; conversely the closer the spacecraft is to the tangent point the smaller the projected field of view.

Figures 5.4 and 5.5 show the family of curves associated with observing at tangent heights of 100 km and 1000 km above the surface for spacecraft positions spaced 10 minutes apart. The curves are color coded to represent the projected field of view of the atmospheric slit above the tangent point. An important issue for observing the exosphere is the spatial resolution along a radial vector extending outward from the center of the planet. Thus Figures 5.6 and 5.7 show the fraction of the slit length along the radius vector passing through the tangent point. These values are the same as multiplying the projected field of view by the cosine of the angle the field of view makes with the radius vector. Although a projected field of view may remain essentially unchanged from near the sub-solar point to the terminator, the angle it makes with the radius vector allows for a smaller projected field of view in altitude above the tangent point.

5.2.3 Off axis angle

The off-axis angle is important because of the functional dependence of reflected solar radiation from the surface that enters the instrument off axis from the telescope

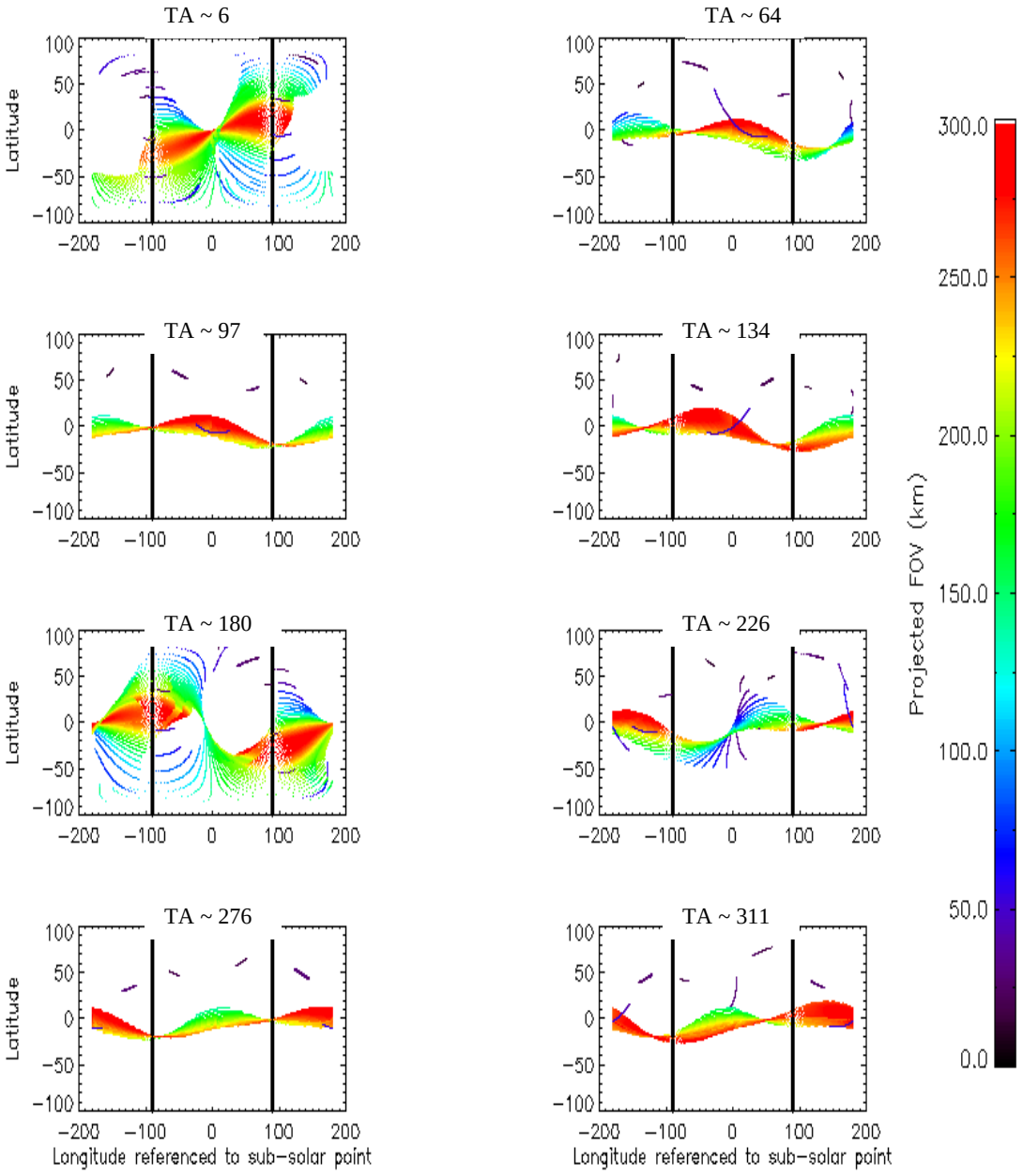

Figure 5.4. Tangent point ground tracks for spacecraft positions in 10 minute intervals. The color code represents the projected length of the atmospheric slit field of view 100 km above the tangent point. The two thick vertical black lines represent the morning and evening terminators.

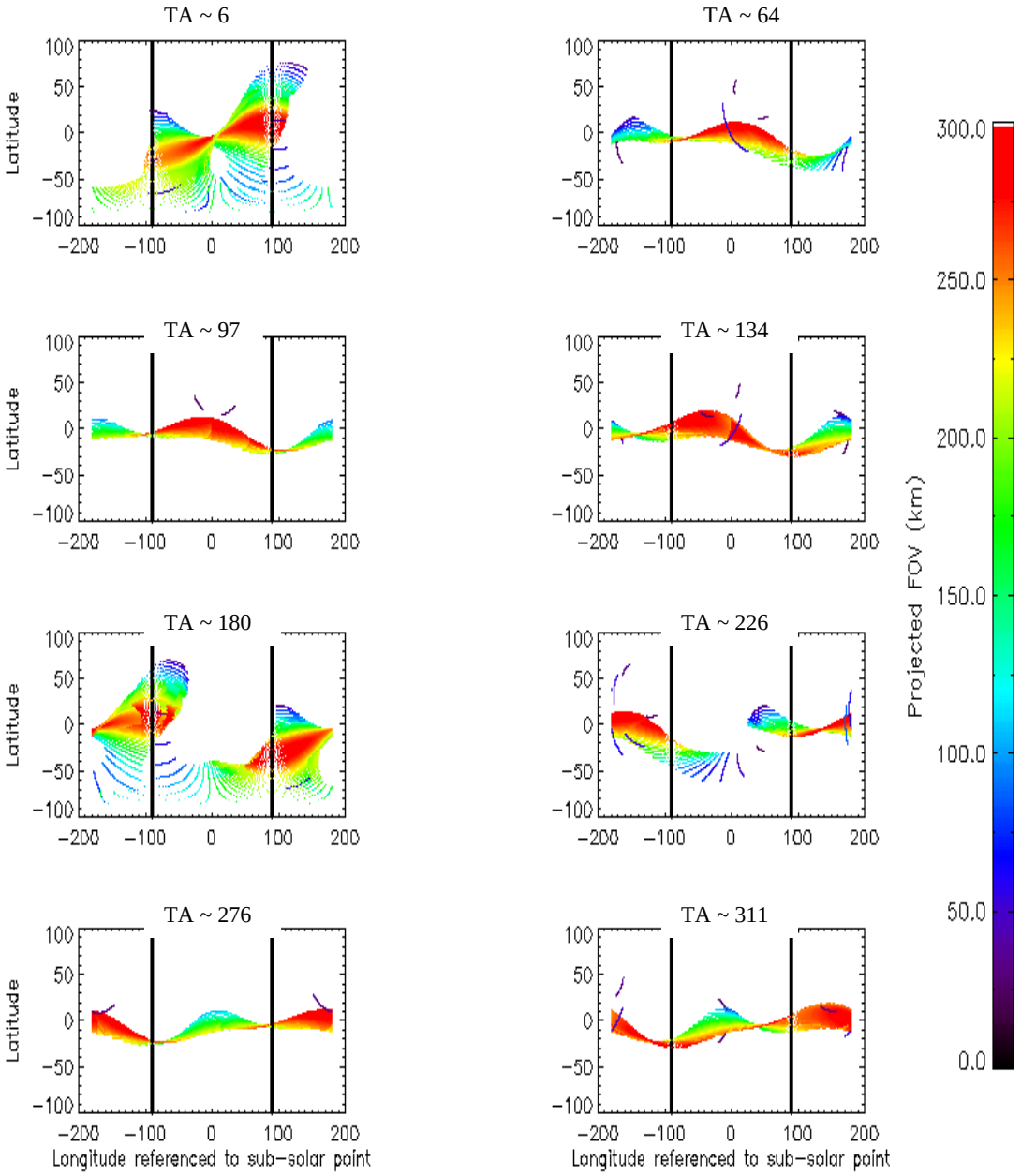

Figure 5.5. Tangent point ground tracks for spacecraft positions in 10 minute intervals. The color code represents the projected length of the atmospheric slit field of view 1000 km above the tangent point. The two thick vertical black lines represent the morning and evening terminators.

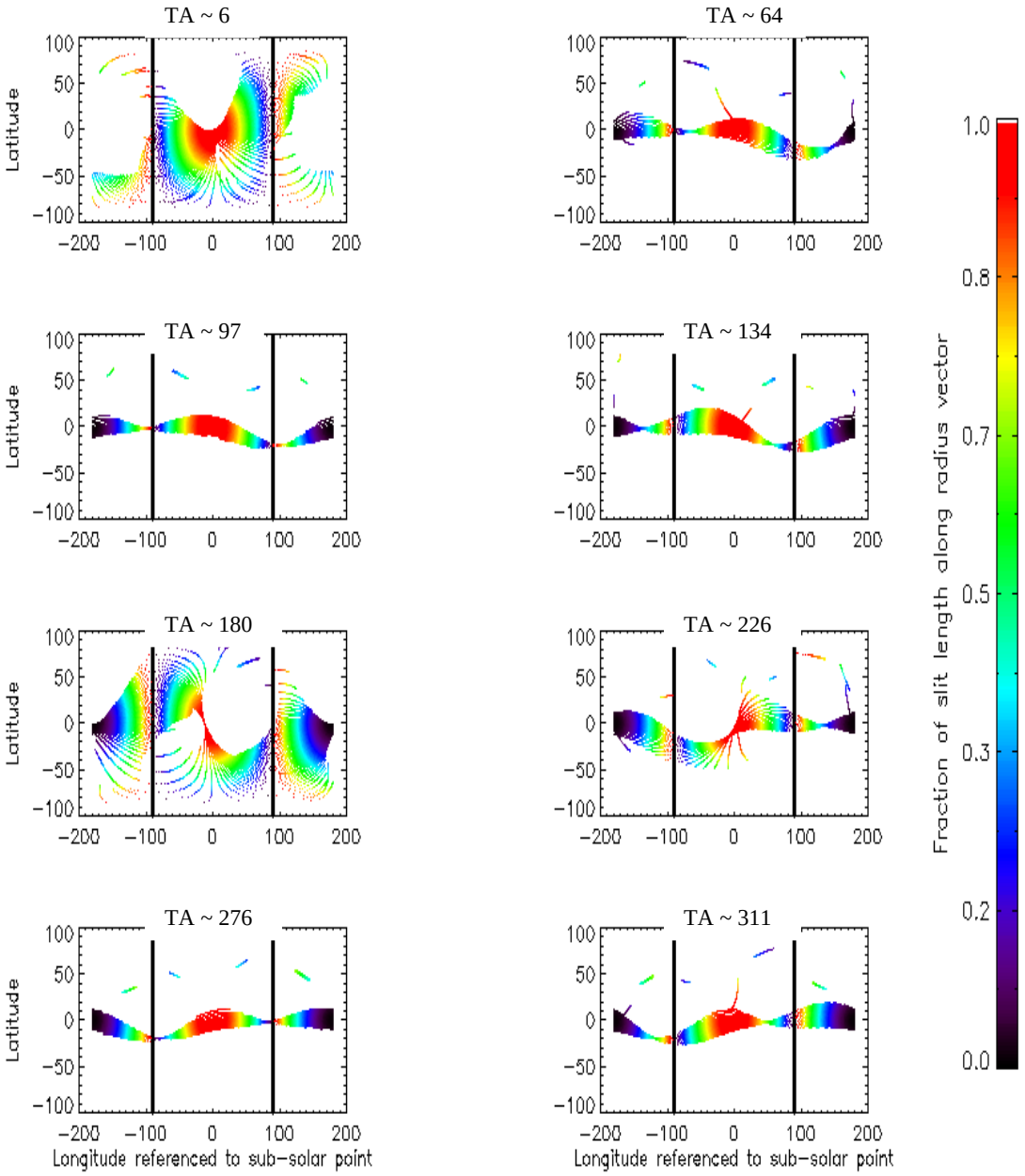

Figure 5.6. Tangent point ground tracks for spacecraft positions in 10 minute intervals. The color code represents the angle that the projected length of the slit makes with the radius vector extending through the observation line of sight at 100 km above the tangent point. The two thick vertical black lines represent the morning and evening terminators.

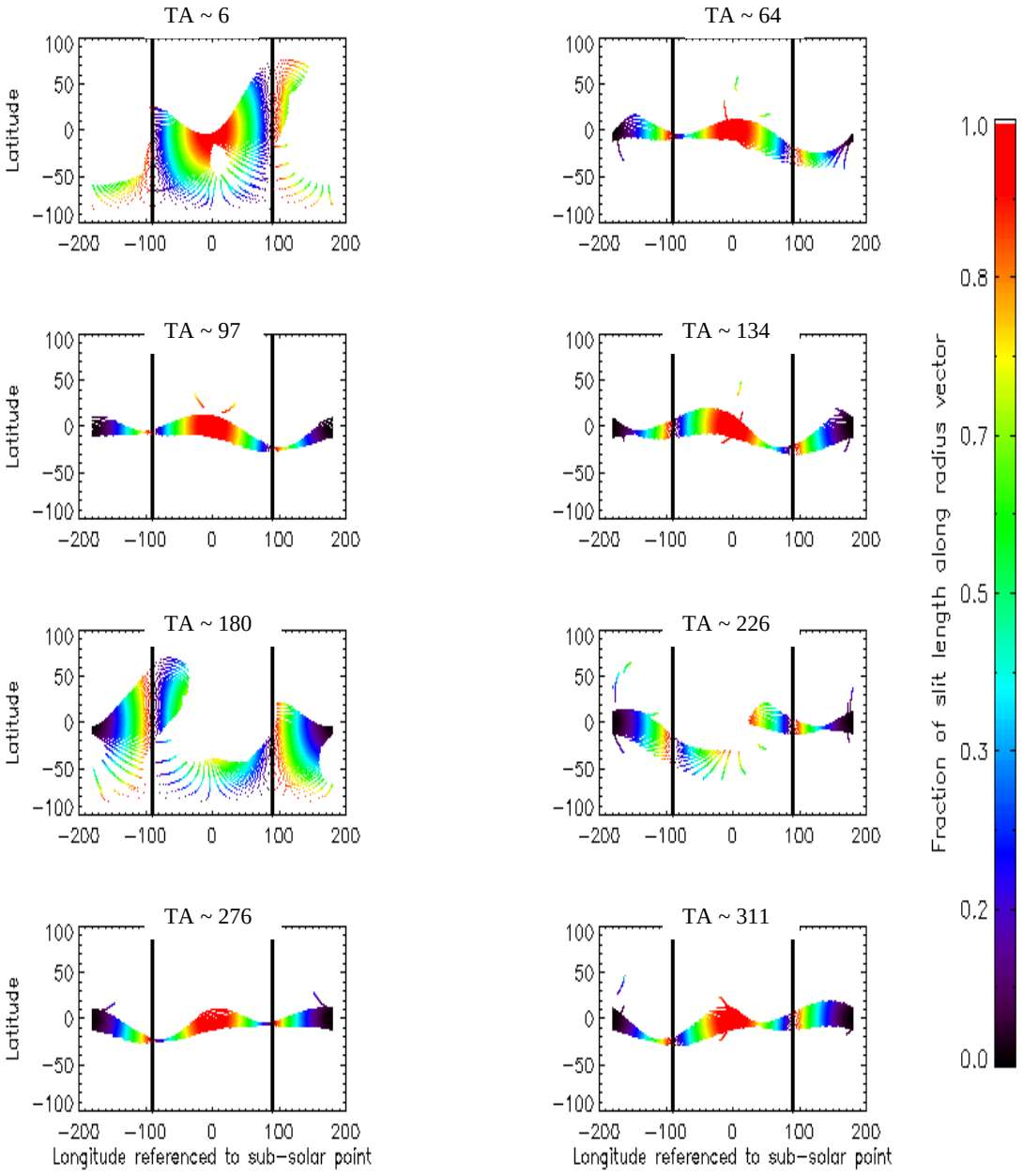

Figure 5.7. Tangent point ground tracks for spacecraft positions in 10 minute intervals. The color code represents the angle that the projected length of the slit makes with the radius vector extending through the observation line of sight at 1000 km above the tangent point. The two thick vertical black lines represent the morning and evening terminators.

boresight. The off-axis response of the telescope is described in Chapter 2. Other than dark counts, the only significant source of background signal arises from off-axis light from the surface. For limb scans that pass close to the dayside surface, the off-axis light contribution to the signal can be significant. Figures 5.8 and 5.9 show the family of curves associated with observing across tangent heights of 100 km and 200 km above the surface for spacecraft positions spaced 10 minutes apart. The curves are color coded to represent the off axis angles relative to slit center for each observation. Generally, the off-axis angles are greater for larger tangent heights, thus the off-axis angles for 100 km and 200 km are shown in order to represent the worst case for off-axis light.

5.2.4 Spacecraft velocity

Since MESSENGER is in a highly eccentric orbit the velocity of the spacecraft varies considerably from periherm to apoherm. Figure 5.10 demonstrates the variation of spacecraft velocity by showing the distance that the spacecraft moves in 2 hours as the spacecraft approaches apoherm compared to the distance the spacecraft moves in 20 minutes as it approaches periherm. This has profound implications in terms of the available time to make observations from long range or from short range and will be summarized in section 5.2.6.

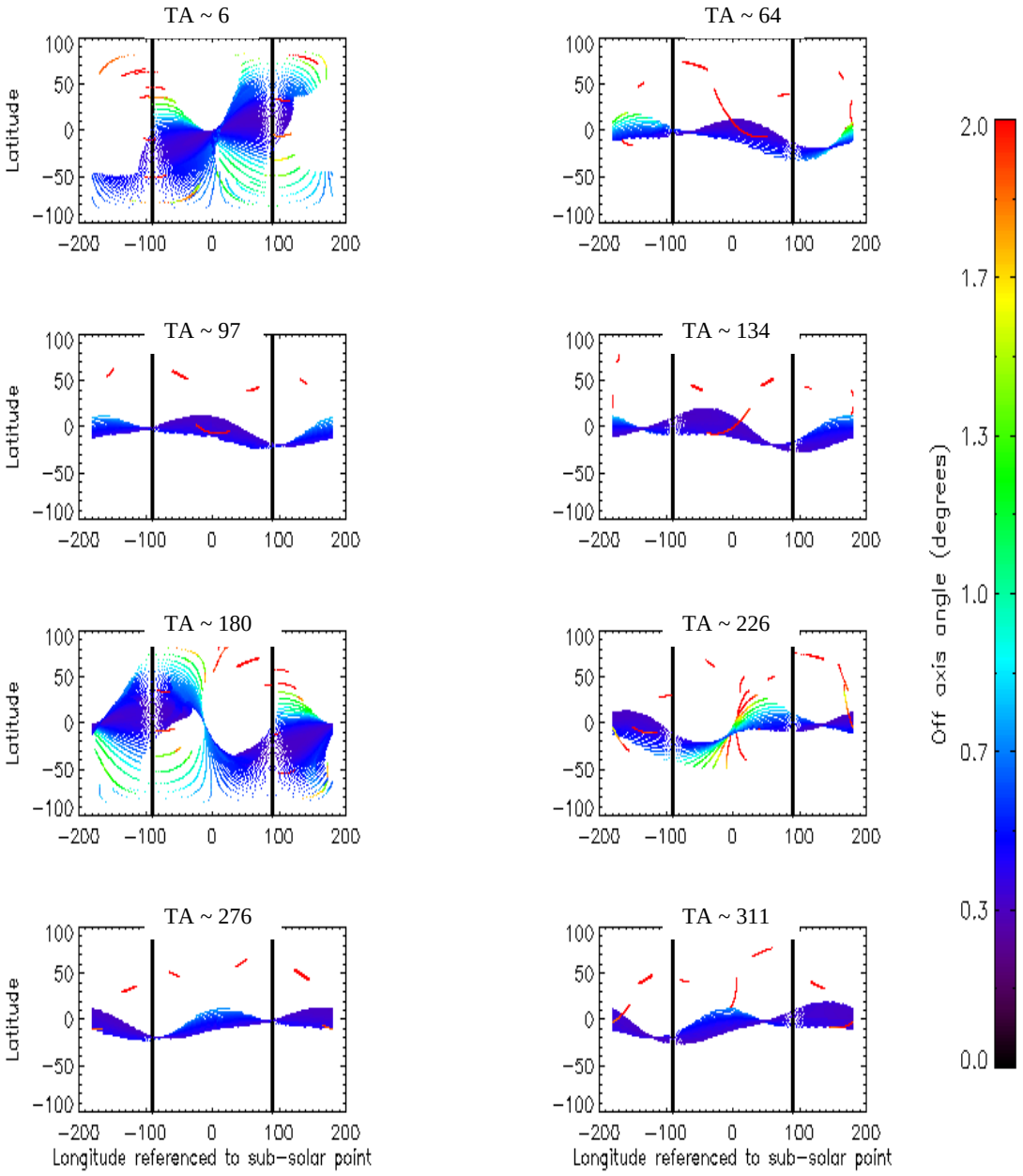

Figure 5.8. Tangent point ground tracks for spacecraft positions in 10 minute intervals. The color code represents the off-axis angle between the boresight 100 km above the tangent point and a vector from the spacecraft that just grazes the surface. The two thick vertical black lines represent the morning and evening terminators.

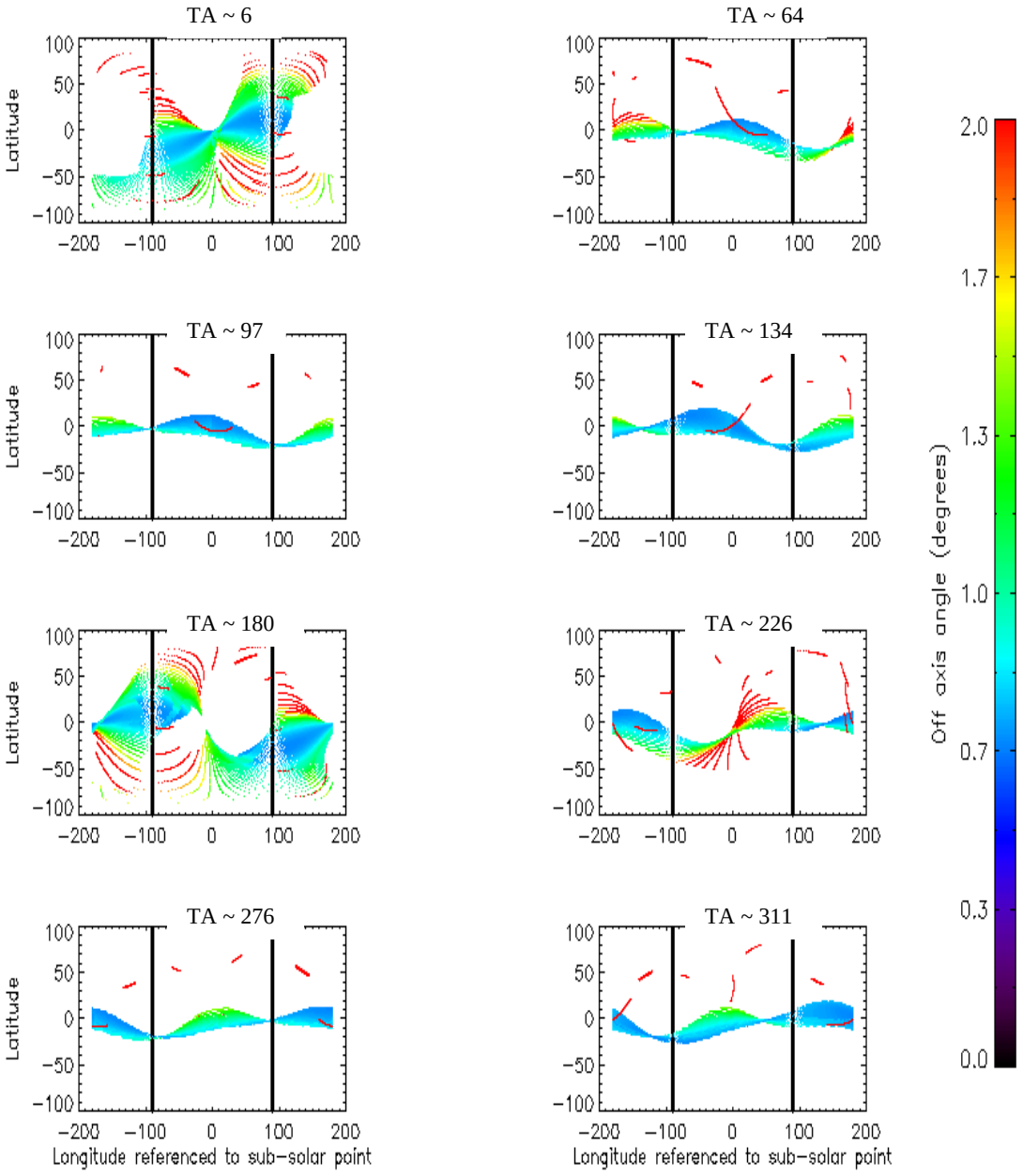

Figure 5.9. Tangent point ground tracks for spacecraft positions in 10 minute intervals. The color code represents the off axis angle between the boresight 200 km above the tangent point and a vector from the spacecraft that just grazes the surface. The two thick vertical black lines represent the morning and evening terminators.

5.2.5 Sub-spacecraft latitude

As shown in Figure 5.10, the velocity of the spacecraft varies considerably throughout a spacecraft orbit. Due to the argument of periapse being located at a high Northern latitude, the larger spacecraft velocities may be associated with Northern latitudes and the smaller spacecraft velocities may be associated with Southern latitudes. It is useful to describe the spacecraft position in terms of sub-spacecraft latitude. A plot of sub-spacecraft latitude, Figures 5.11 and 5.12, may therefore give a measure of spacecraft velocity and more importantly, gives a feel for the amount of time for an observation.

5.2.6 Summary of observation constraints

In order to quantify the most observable regions of the planet throughout the Mercury year, observational opportunities are broken up into 3 distinct regions (equatorial between +/- 30° latitude, northern hemisphere > +30° latitude, and southern hemisphere < -30° latitude) for both the dayside and nightside for a total of 6 regions. Figure 5.13 shows the percentage of observations that are possible in each region for one orbit at the designated planetary true anomaly and at 100 km and 1000 km. Given the MESSENGER orbit, observations above the equatorial region dominate the available opportunities and should allow for a systematic approach to observing the exosphere and provide a uniform data set over most of the Mercury year. Observational constraints limit the ability of MASCS to obtain the same uniform data set for high latitudes; thus high latitude dayside observations must

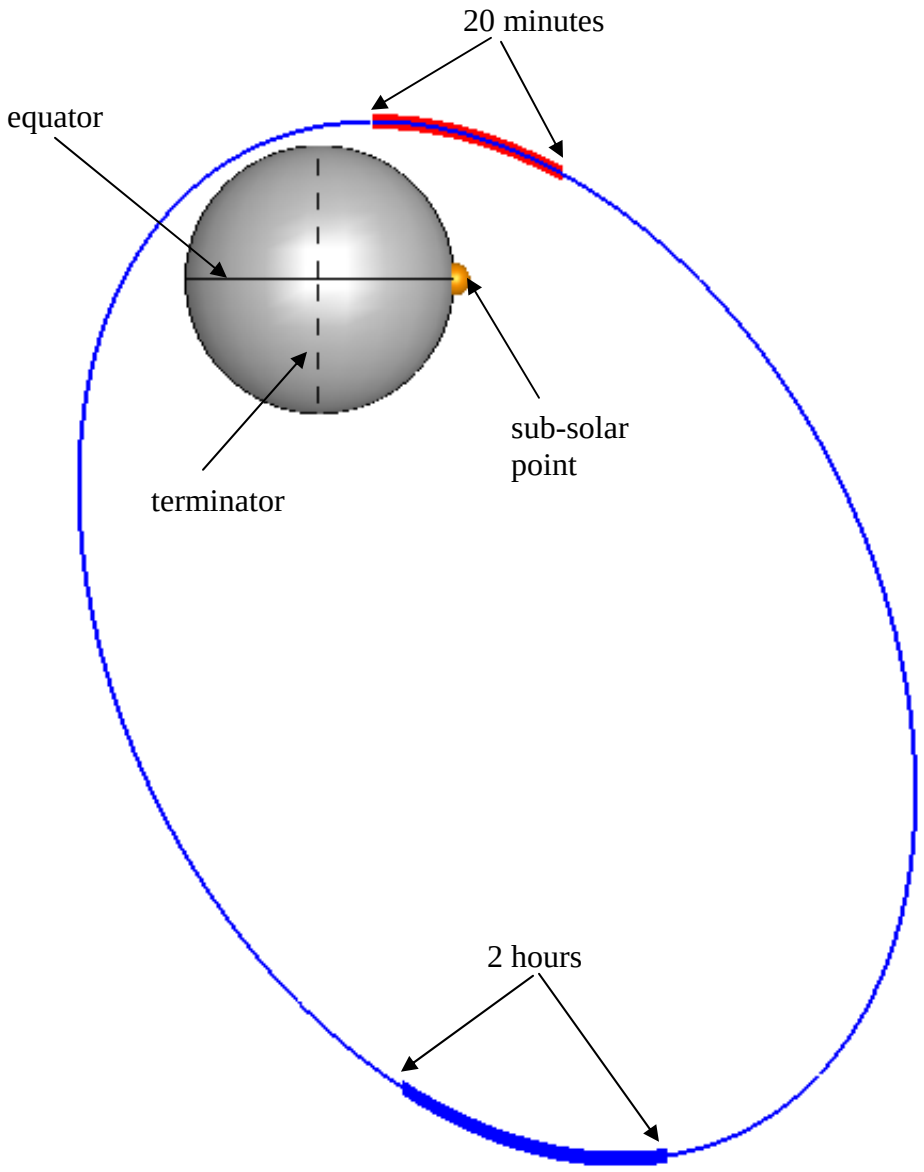

Figure 5.10. Noon midnight orbit with Mercury viewed at 90° phase. The Sun is to the right with the orange sphere representing the sub-solar point. The heavy blue portion of the orbit represents 2 hours of spacecraft travel, while the heavy red portion represents 20 minutes of spacecraft travel.

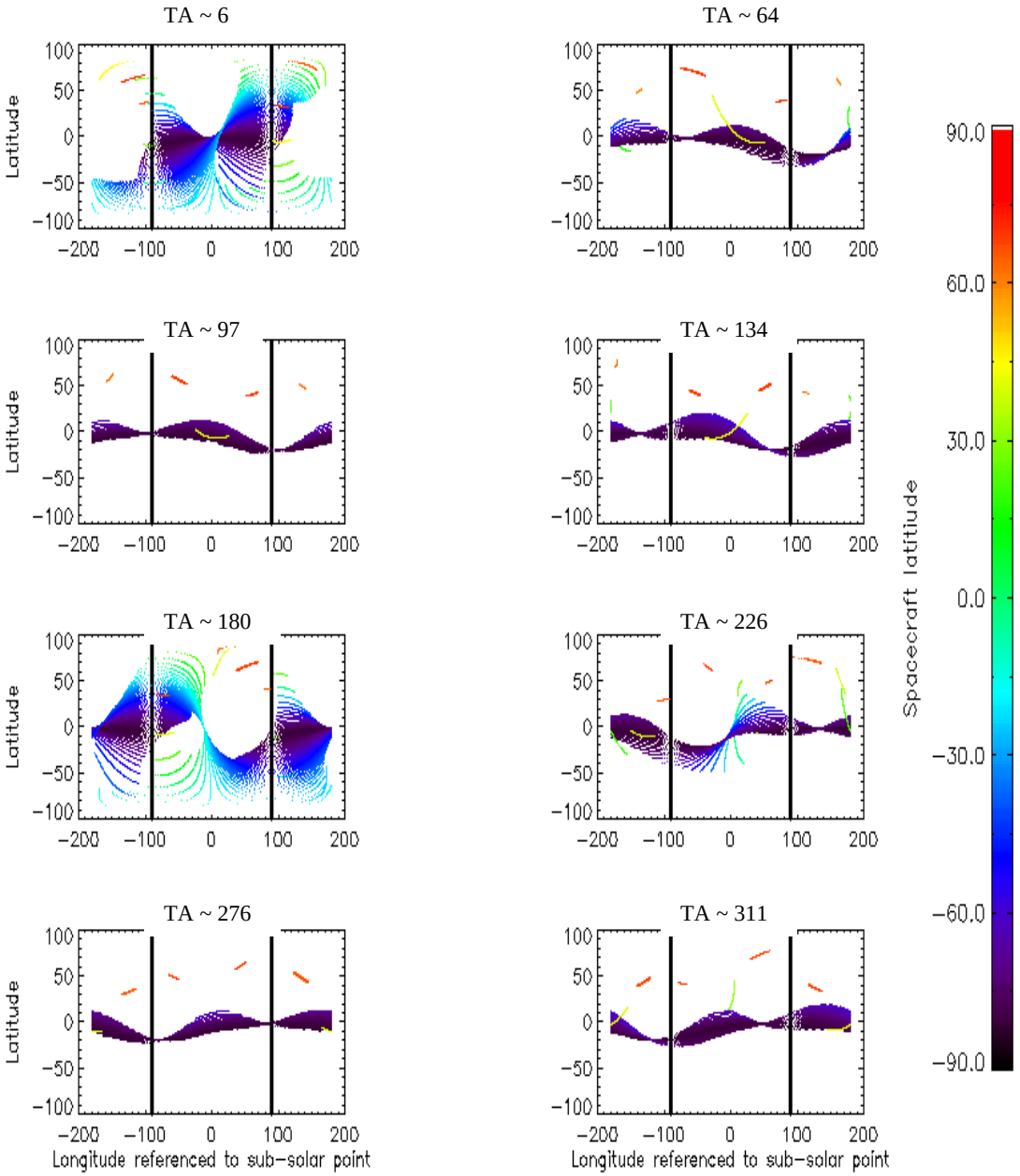

Figure 5.11. Tangent point ground tracks 100 km above the tangent point for spacecraft positions in 10 minute intervals. The color code represents the sub-spacecraft latitude. The two thick vertical black lines represent the morning and evening terminators.

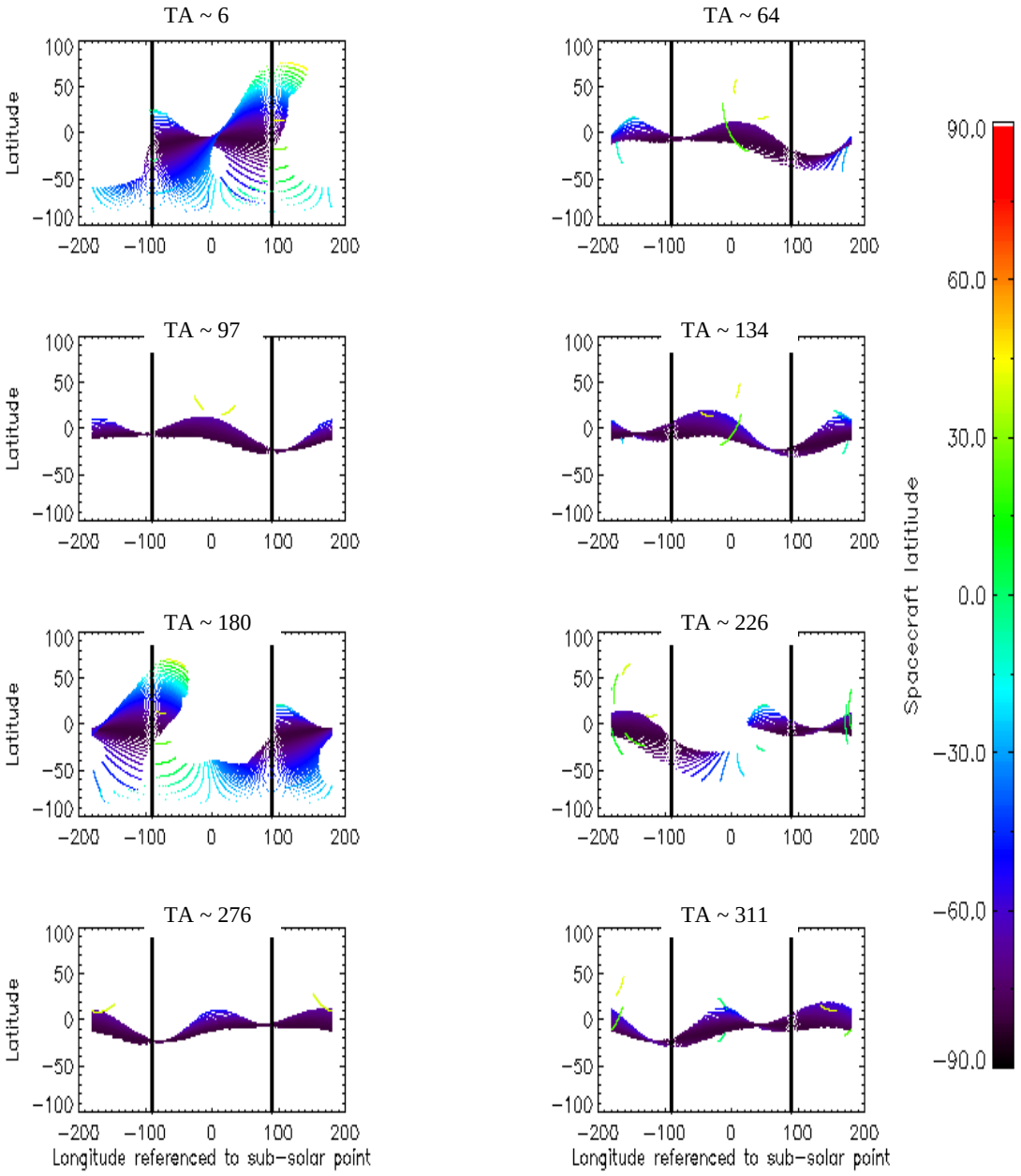

Figure 5.12. Tangent point ground tracks 1000 km above the tangent point for spacecraft positions in 10 minute intervals. The color code represents the sub spacecraft latitude. The two thick vertical black lines represent the morning and evening terminators.

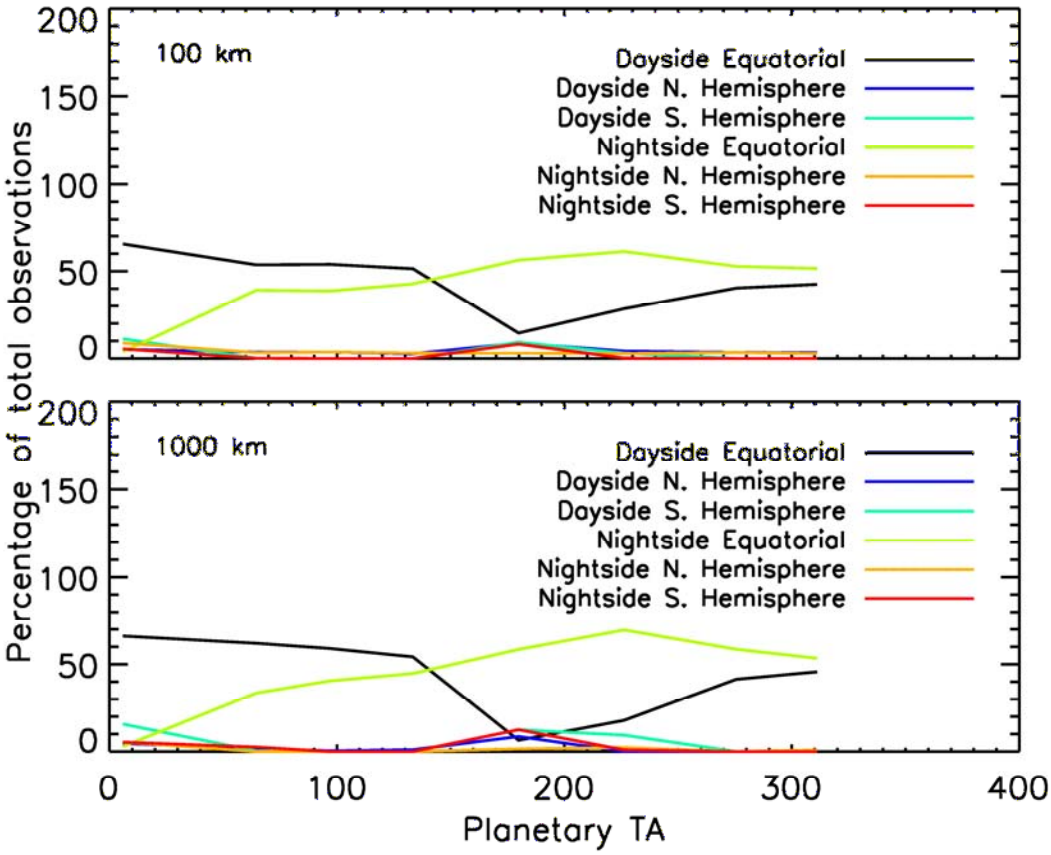

Figure 5.13. Percentage of opportunities for observations in equatorial, northern hemisphere, and southern hemisphere regions. The percentage is taken from the total number of observations possible within an orbit. The equatorial region is the range of latitude between +/- 30°, the northern hemisphere is for latitudes > 30° and the southern hemisphere is for latitudes < -30°.

consist of low altitude, short duration observations that at best are only available between true anomalies from 0° to 180°.

Table 5.1 summarizes the advantages and disadvantages for both equatorial and north-south observations. While north-south observations generally yield larger off-axis angles, and therefore better SNR for weak emissions, than equatorial observations, the low altitude range and short duration of north-south observations limit the use of these observations. Furthermore north-south observations are limited in terms of seasonal coverage. Since north-south observations yield a smaller projected field of view and larger off-axis angle, the chief advantage of north-south observations are to map low energy processes near the surface. Alternatively, equatorial observations are more conducive to long duration, 100 km and higher observations.

5.3 Observations that address science questions while obeying s/c geometrical and temporal constraints

Combining both science requirements (Chapter 1) and observational pointing constraints, 2 broad classes of dayside observations are proposed: 1) A series of radial scans that cover most of the dayside surface above the equatorial region, 2) north-south observations that will either consists of a series of radial scans or constant altitude swaths; depending on the pointing and temporal constraints for a particular planetary true anomaly. Figure 5.14 shows a series of 9 radial scans for a planetary true anomaly of 97° covering an altitude range from 100 to 1000 km. The red lines indicate the boresight of the instrument, which starts out observing at 1000 km above

Category	**Equatorial**	**North-south**
Seasonal coverage	All planetary true anomalies	Planetary true anomalies from 0° to 180°
Surface coverage	Entire dayside except for planetary true anomalies ~ 180°	Mostly northern hemisphere except for dawn-dusk orbits
Altitude coverage	100-1000 km	Low to high altitude observations at dawn-dusk orbits; 50-100 km everywhere else
Projected field of view	200 – 300 km for atmospheric slit	25 – 150 km for atmospheric slit
Off-axis angle	0.4° at 100 km altitude	> 1° at 100 km altitude
Spacecraft position	High southern latitudes	Low to high northern latitudes
Duration of observations	2 hours	~ 20 minutes with slightly more time at dawn-dusk orbits

Table 5.1. Characteristics of equatorial and north-south observations

the limb and slews down to 100 km. The initial position defines a radius vector originating at the center of the planet and terminating at the closest approach of the boresight to the planet. Subsequent observations follow along that radial vector down to 100 km altitude, at which time the spacecraft is slewed to begin another radial scan. North-south radial scans are performed in the same manner but are for a much shorter duration and typically begin at an altitude of 100 km and end at 50 km.

In order to make the most efficient use of the limited time for observations, a series of equatorial region radial scans are proposed that offer spatial coverage determined by the anticipated minimum lateral atmospheric spatial features. Ground-based radar observations of Mercury have shown bright spots that may be sources of exospheric sodium (Sprague et al., 1998). The smallest radar bright spot extends over a longitude range of ~36 degrees; and although this will only be observable by the UVVS over a limited time span, this is used to set a minimum limit of radial scan lateral spatial scale. For observations above the equatorial region of the planet, 9 radial scans spaced 20 degrees apart that extend over an altitude range from 100 km to 1000 km are proposed to achieve a compromise between limited observation time and required spatial scale. This helps answer questions about overall distribution of the exosphere along the equator. This also allows for systematic observations of dawn-dusk equatorial regions with a temporal resolution on the order of minutes. Furthermore, this strategy allows for extended altitude observations for most planetary true anomalies and allows for systematic seasonal observations in order to determine seasonal dependencies of processes.

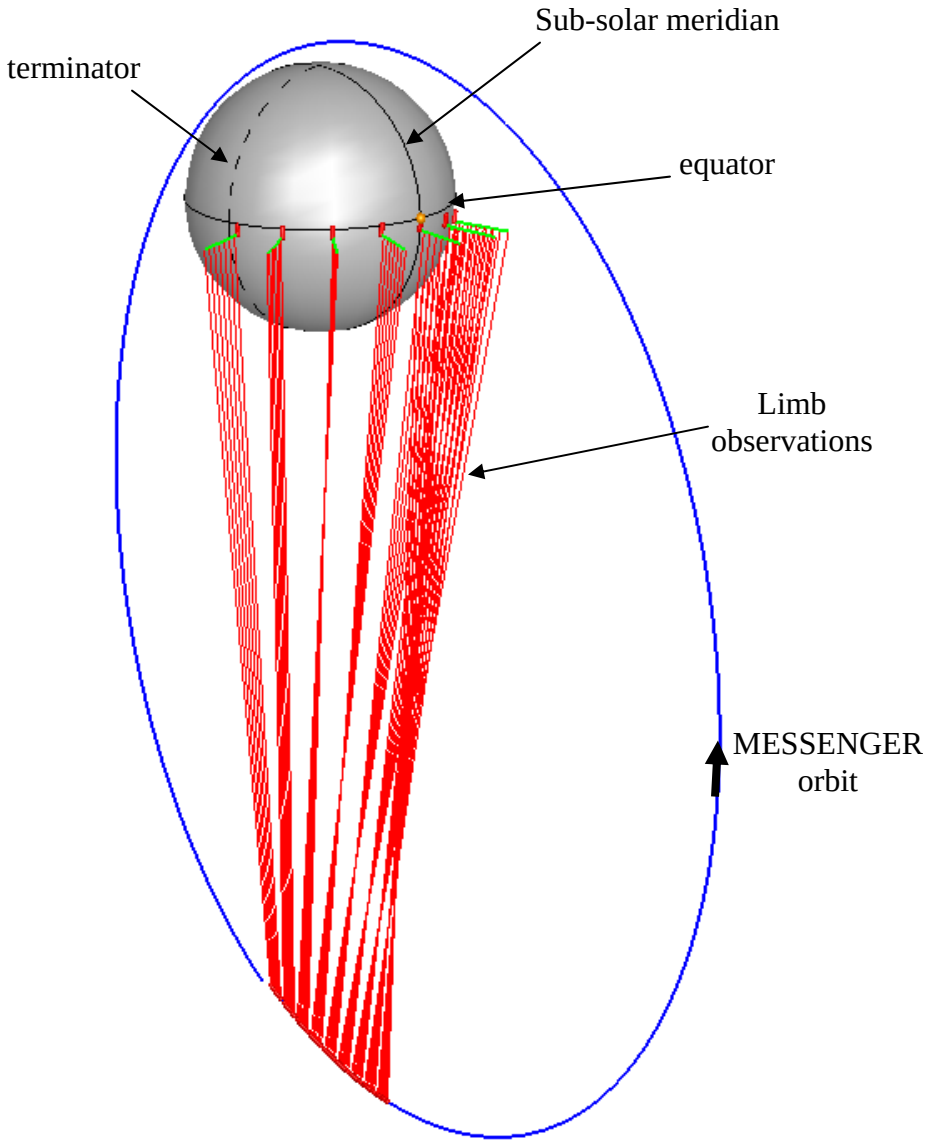

Figure 5.14. A series of 9 radial scans for a planetary true anomaly of 97°.

Since north-south observations are limited in time and altitude, but have the advantage of larger off-axis angles compared to equatorial observations, the strategy is to perform low altitude, short duration scans with coverage determined by the time of Mercury year, i.e., the coverage is not as consistent as equatorial limb scans both spatially and temporally. Similar to the case for equatorial limb scans, the latitudinal sampling of north-south limb scans is chosen to be small enough to observe radar bright spots, using radar bright spot "C" (Sprague, et. al., 1998) as a typical example of small radar bright spots. Figure 5.15 shows an example of how the north-south observations scan across radar bright spot "C", which is centered at ~ 240° W. longitude, ~15° N. latitude. This observation begins on July 19, 11:10:00 UTC and lasts for ~ 30 minutes with a planetary true anomaly of 161°. The north-south observation ziz-zags between 50 km and 100 km in altitude and offers the capability to observe directly above the center of the bright spot as well as at latitudes above and below the spot.

Figure 5.16 shows the tangent point ground track for a series of equatorial and north-south radial scans at 8 different planetary true anomaly positions throughout the Mercury year and for 4 altitude ranges. As expected the north-south observations are more conducive to low altitude, but are not as readily available as the equatorial observations. Above an altitude of 100 km, the only north-south observations available are for planetary true anomalies of 6° and 180°, corresponding to dawn-dusk orbits. Off-axis light diminishes the quality of equatorial observations below 100 km; however given the long duration of equatorial observations, altitude ranges up to 1000 km are possible.

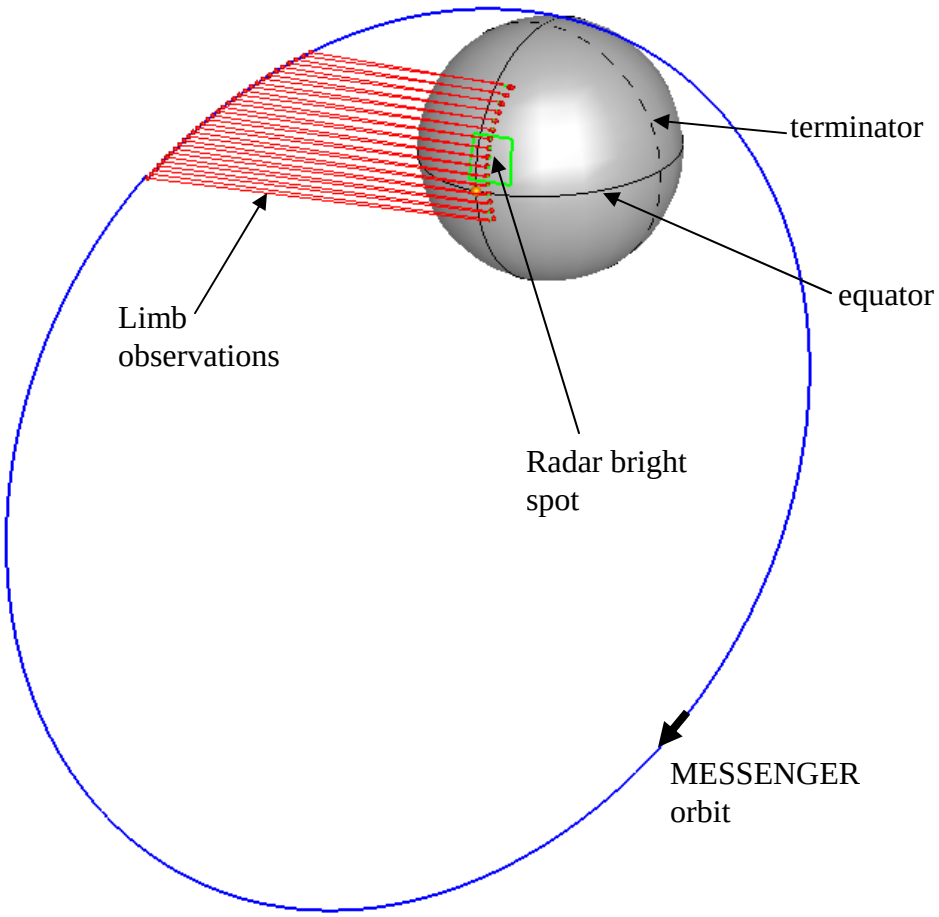

Figure 5.15. North-south observation above a radar bright spot that is observable at a planetary true anomaly of 161°. The green box represents the extent of the radar bright spot with the center at ~ 240° W. longitude and ~15° N. latitude.

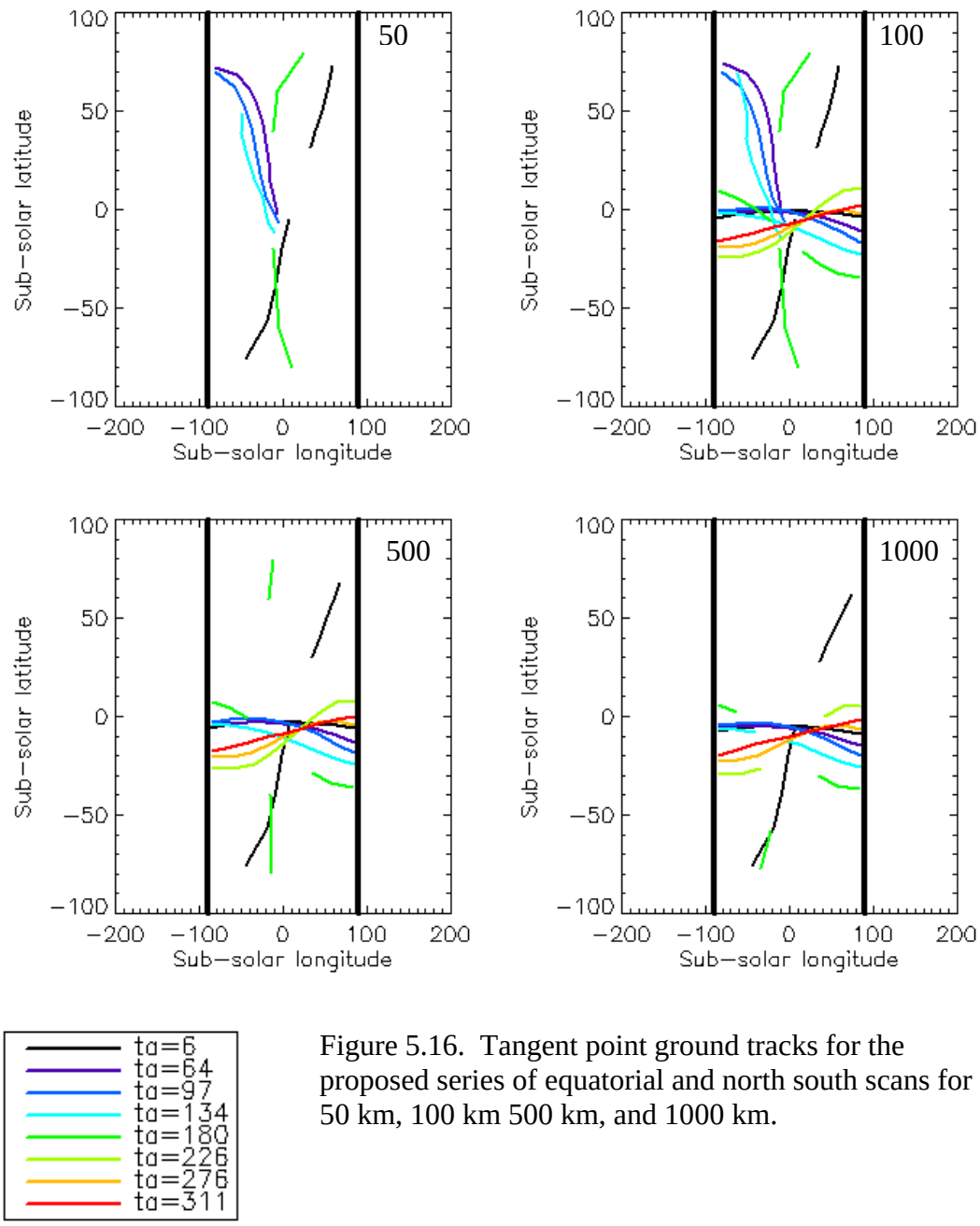

Figure 5.16. Tangent point ground tracks for the proposed series of equatorial and north south scans for 50 km, 100 km 500 km, and 1000 km.

The proposed set of equatorial and north-south observations form a systematic observing strategy that provides a uniform data set over longitude, latitude, altitude, and season. An issue that should be addressed is how well the proposed observation strategy can detect transient events where bursts of sodium have been observed at random locations with durations on the order of hours to days (Potter et al., 1999). Multiple explanations have been offered to explain these transient events. Killen et al. (2001) has proposed that IMF reconnection with Mercury's magnetic field may allow solar wind ions to sputter sodium off the surface. Mangano (2007) has proposed that the observed transient events could be due to large meteoritic impact. Sprague et al. (1998) has argued that transient events could be due to sodium associated with radar bright spots that must reach a minimum local time of day before the surface temperature has reached a level to begin evaporating the sodium from the surface. Other than the radar bright spot explanation, none of the other explanations can be explicitly planned for; thus the observation of these transient events will depend on the systematic spatial and temporal mapping strategy that has already been outlined. Sarantos (private communication, 2005), indicated that modeling suggests solar wind sputtering spot sizes on the surface with a solid angle as small as 40°. This size is within the spatial resolution of the proposed set of radial scans, but will only be detected if they fall within the observed regions of the planet.

5.4 Detection limits

As described in Chapter 4, the count rate for any observation consists of counts from exospheric emissions, counts from off-axis light, and dark counts. Each of these

3 count rate sources contribute to the total count rate in varying degrees depending on the time and location of the observation. The off-axis light and dark counts collectively determine the background, thus it is advantageous to set detection limits based on the predicted background for an observation.

The detection limit is based on specifying a desired SNR and computing the required radiance based on the SNR and expected background. The detection limit is derived in the following equations.

$$SNR = \frac{Signal}{\sigma} = \frac{Signal}{\sqrt{\sigma_{signal}^2 + \sigma_{cont\,1}^2 + \sigma_{cont\,2}^2 + 2*\sigma_{dark}^2}} \tag{5.1}$$

$$SNR^2 = \frac{Signal^2}{Signal + \sigma_{cont\,1}^2 + \sigma_{cont\,2}^2 + 2*\sigma_{dark}^2} \tag{5.2}$$

$$\begin{aligned} &SNR^2\left(Signal + 2*\sigma_{dark}^2 + \sigma_{cont\,1}^2 + \sigma_{cont\,2}^2\right) = Signal^2 \\ &Signal^2 - SNR^2 * Signal - SNR^2 * \left(2*\sigma_{dark}^2 + \sigma_{cont\,1}^2 + \sigma_{cont\,2}^2\right) = 0 \end{aligned} \tag{5.3}$$

Solving for the signal gives

$$Signal = \frac{(SNR)^2 + \sqrt{(SNR)^4 + 4 * SNR^2 * \left(\sigma_{cont1}^2 + \sigma_{cont2}^2 + 2 * \sigma_{dark}^2\right)}}{2} \tag{5.4}$$

where σ_{cont1}^2 is the uncertainty squared in the determination of the solar continuum beneath the sodium D lines using counts from spectra out in the wings, σ_{cont2}^2 is the uncertainty squared in the actual solar continuum counts beneath the sodium D lines that contributed to the summed total counts, and σ_{dark}^2 is the uncertainty squared in the dark counts.

The signal is readily converted to a radiance by

$$L = \frac{Signal}{Sensitivity} \tag{5.5}$$

Off-axis modeling as well as dark count estimations allow for the determination of the background uncertainties for any simulated observation. This allows for the determination of the required signal in order to achieve a specified SNR. Figures 5.17-5.19 show 1 second integration detection limits for SNR values of 10 and 20. Figure 5.17 is for 100 km altitude taken from the series of equatorial radial scans over the Mercury year proposed in Section 5.3. Results for both surface and atmospheric slits are shown. For all test cases the results show that the detection limit peaks around the sub-solar point and typically drops by greater than a factor of 5 for terminator observations. This dependence is due to a combination of 1) the fact that for a fixed off-axis angle, the off- axis light varies inversely with solar incidence

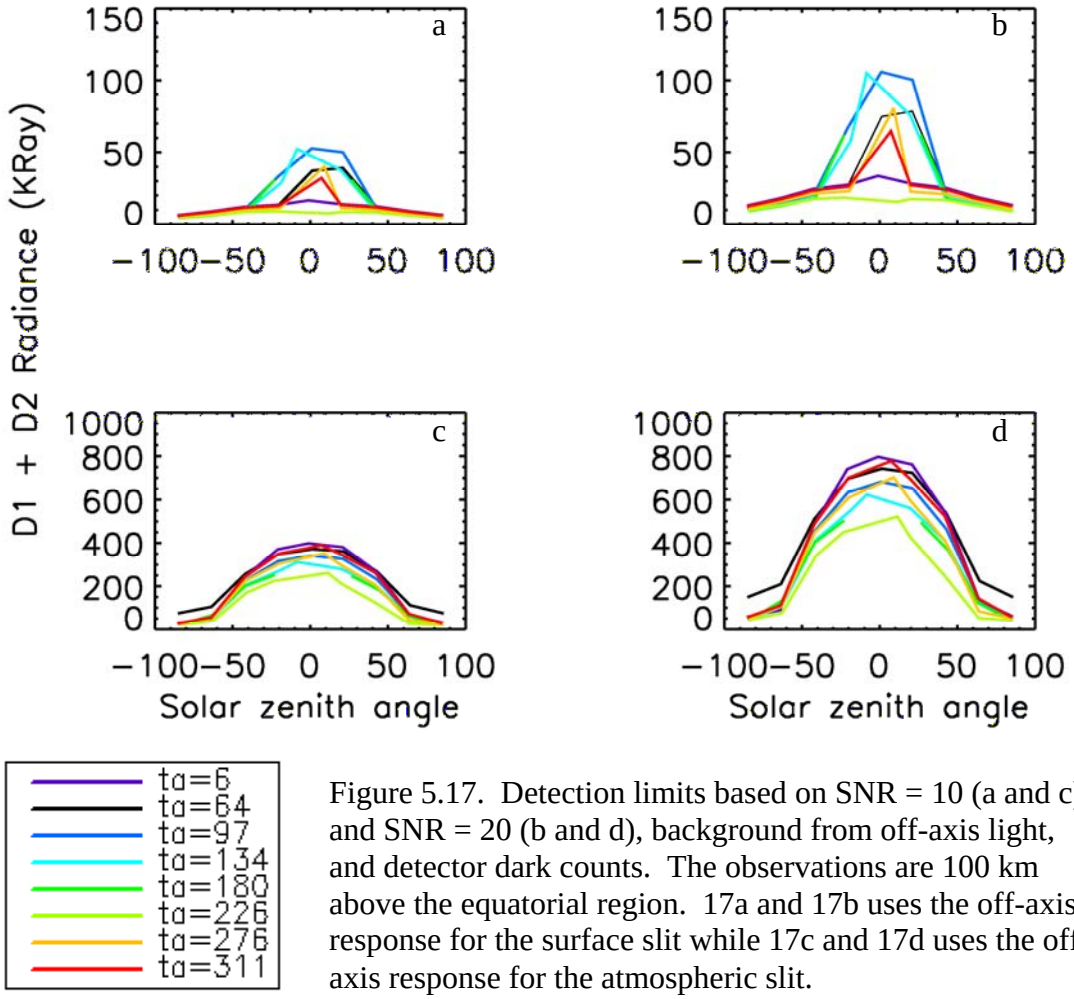

Figure 5.17. Detection limits based on SNR = 10 (a and c) and SNR = 20 (b and d), background from off-axis light, and detector dark counts. The observations are 100 km above the equatorial region. 17a and 17b uses the off-axis response for the surface slit while 17c and 17d uses the off-axis response for the atmospheric slit.

angle for light reflecting from the surface (see Chapter 2), and 2) for the atmospheric slit, the orientation of the slit is such that the long direction of the slit is along a radius extending from the planet center to the tangent point for observations above the sub-solar point and the narrow direction of the slit is along a radius extending from the planet center to the tangent point for observations above the terminator, as shown in Figures 5.6 and 5.7. The tangent altitudes presented are for the center of the projected field of view; thus for observations above the sub-solar region that employ the atmospheric slit, the lower altitude edge of the projected field of view is 0.5° lower in altitude than the center. This allows for more off-axis light to enter the instrument than if the slit were oriented 90°, as is the case for observations above the terminator. There is a dependence on planetary true anomaly of a factor of ~ 2-3. For low altitudes, the detection limit is dominated by off-axis solar continuum reflected from the surface of the planet. The magnitude of the off-axis light is a function of both the off-axis angle as well as the amount of the reflected solar continuum. The peak off-axis light for the surface slit and for 100 km above the limb occurs at planetary true anomalies from 97° to 134°. The off-axis angle for a planetary true anomaly of 180° is actually smaller than for from 97° and 134°, but since the solar continuum varies according to $1/r^2$, the combined effect of off-axis light is not as great for a planetary true anomaly of 180°. The situation is somewhat different for the atmospheric slit at 100 km limb height because the lower edge of the slit is much closer to the planet, causing the maximum amount of off-axis light to occur for planetary true anomalies where the planet is closer to the Sun. Figure 5.18 shows the detection limits as a function of altitude. An equatorial radial scan occurring near a solar zenith angle

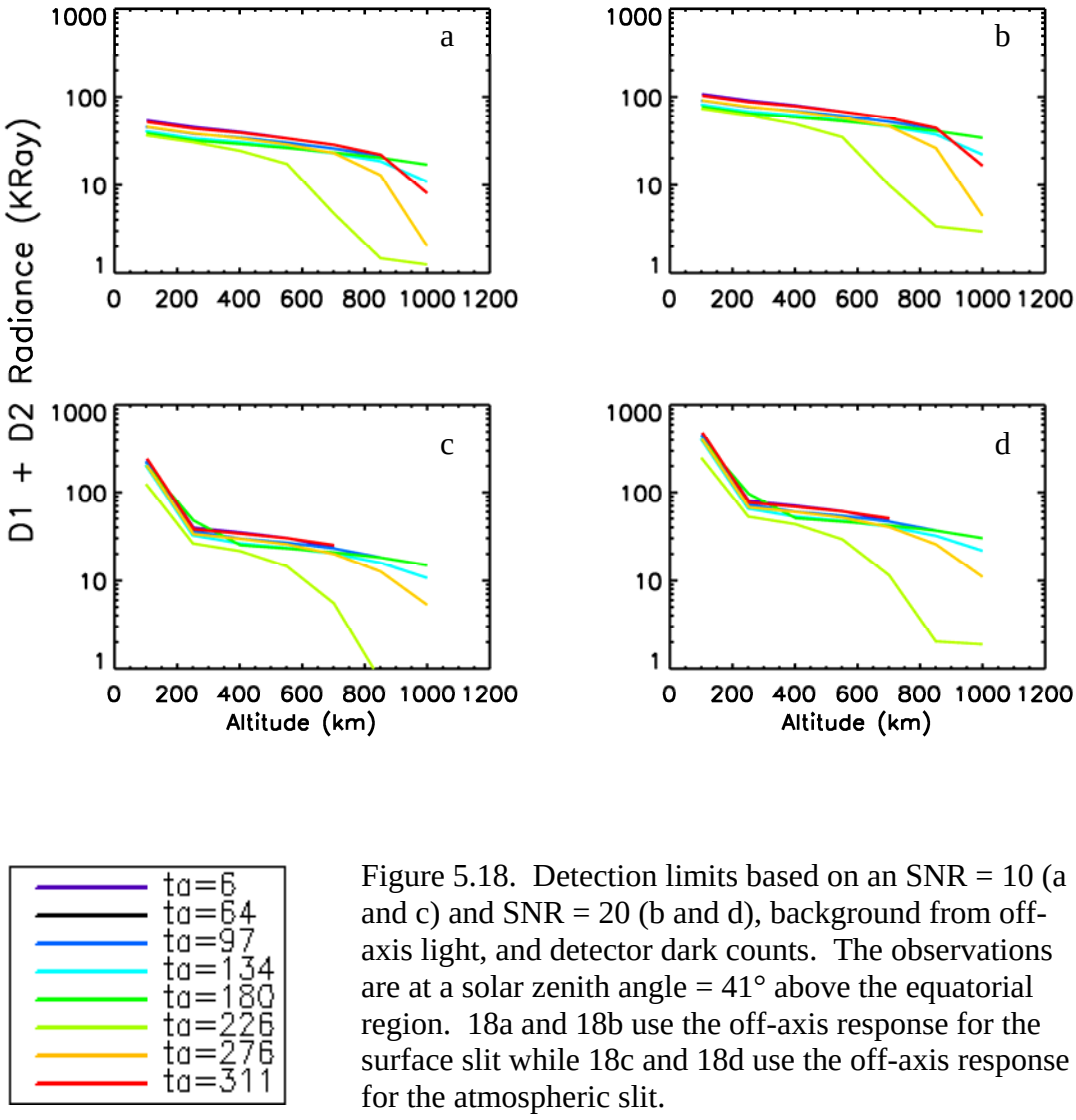

Figure 5.18. Detection limits based on an SNR = 10 (a and c) and SNR = 20 (b and d), background from off-axis light, and detector dark counts. The observations are at a solar zenith angle = 41° above the equatorial region. 18a and 18b use the off-axis response for the surface slit while 18c and 18d use the off-axis response for the atmospheric slit.

of 41° is used over its full range of altitude. The signal detection limit decreases for increasing altitude due to the fact that off-axis light decreases for higher altitudes, leaving the background to be dominated by detector dark counts. The atmospheric slit shows a large decrease from altitude close to the surface up to ~ 250 km, and then decreases in a similar fashion to the surface slit. This is due to the fact that even for a solar zenith angle of 41° the lower edge of the long dimension of the slit is still relatively close to the planet compared to the center of the boresight. This allows off-axis light from a smaller off-axis angle to enter the instrument. The signal detection limit is at a minimum for a planetary true anomaly of 226°. This is because the off-axis angle is relatively large compared to those for other planetary true anomalies, as shown in Figures 5.8 and 5.9.

Figure 5.19 shows the detection limits for the proposed series of north-south observations at 100 km above the surface. The majority of the detection limits are smaller than for the equatorial scans at the same altitude due to larger off-axis angles (see Figures 5.8 and 5.9) and consequently smaller background counts from the solar continuum. The only exception is for the surface slit at a planetary true anomaly of 6°, where the off-axis angle is much smaller. As with the case for the equatorial observations, the detection limits peak near the sub-solar point and decrease above the terminator. For the atmospheric slit, the variation in detection limit over solar zenith angle is greater than an order of magnitude for most planetary true anomalies. The reason for the solar zenith angle dependence as well as the planetary true anomaly dependence is the same as for the equatorial scans; the orientation of the slit, the incidence angle dependence of reflected solar radiation, and the $1/r^2$ dependence

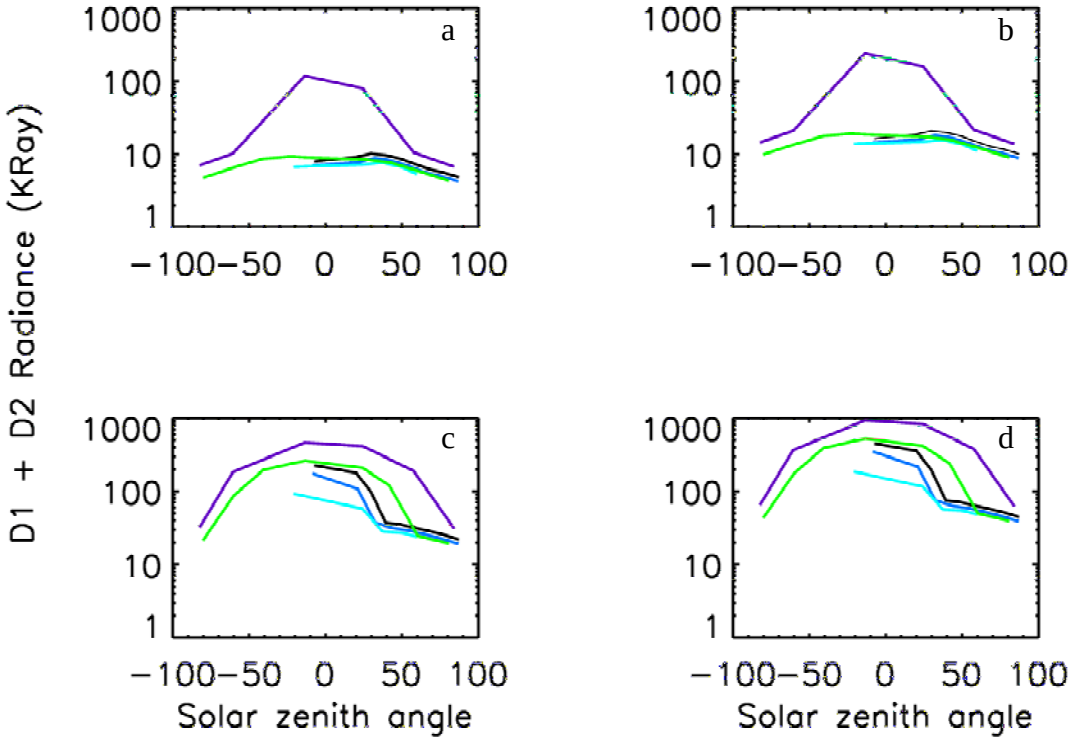

Figure 5.19. Detection limits based on an SNR = 10 (a and c) and SNR = 20 (b and d), background from off-axis light, and detector dark counts. The observations are 100 km above the surface for the north-south observations. 19a and 19b use the off-axis response for the surface slit while 19c and 19d uses the off-axis response for the atmospheric slit.

of solar photons. Altitude variations are not presented for north-south scans because dayside coverage in the north-south direction at high altitudes is only possible for orbits near dawn-dusk orbits. Detection limits for high altitude, dayside, north-south observations at dawn-dusk orbits are similar to those observations at the same height above the equatorial region.

5.5 Test cases that address physical processes associated with the exosphere

Considerable debate exists over the abundance of sodium in Mercury's exosphere. Killen et al. (2004b) states an increase by approximately a factor of 2 in measured abundance from perihelion to aphelion. Furthermore, Killen proposes that gardening of sodium from beneath the extreme surface layer may provide adequate amounts of sodium to be observed over the entire dayside surface. Alternatively, Leblanc and Johnson (2003) predicted an abundance variation of ~ 1 order of magnitude over the same seasonal variation. In addition, Leblanc concluded that sodium is depleted from the surface over large areas surrounding the sub-solar region. In order to determine the trends of source processes, a constant surface concentration is assumed because large voids of sodium over the dayside surface would simply produce a trivial result. Furthermore, given the disagreement in absolute sodium abundances, normalized tangential column abundances are initially shown with the idea that the trends for a given process behave similarly over a wide range of absolute values of abundance.

Thermal desorption is modeled in two different manners in this investigation. Since the characteristic energy of thermally vaporized atoms is the energy associated with the surface temperature, it is not unreasonable to propose that upon the first

bounce the atoms stick to the surface. This is because there the atoms do not have to lose energy before accommodating to the surface temperature. This implies that the surface sticking has a value of unity (or 100 %). Alternatively, one may propose that even though the atoms are already accommodated to the surface temperature, the porosity of the surface could be such that upon hitting the surface, the atom continues to bounce. Therefore, in this investigation, thermal desorption is first modeled with sticking set to 1, which corresponds to the atoms being ejected and sticking to the surface at the first encounter with the surface after being ejected. Second, thermal desorption is modeled with sticking set to the same coefficient recommended by Killen, (private communication, 2006) for photon stimulated desorption and meteoritic vaporization which corresponds to thermally vaporized atoms becoming a part of the ambient exosphere, i.e., atoms that survive for more than one bounce. In this case, the sticking coefficient has an inverse dependence on surface temperature. So for the sub-solar region where temperatures are highest, the sticking coefficient is much lower than for the colder, terminator regions.

After the behavior of each process has been established, test cases that incorporate absolute abundances are performed in order to make signal and uncertainty predictions. The absolute abundances predicted by the model reflect observations performed by Potter et al. (1999) with the average abundance varying by a factor of ~ 2 throughout the Mercury year. Furthermore, given the disagreement in sodium surface concentration, simulated observations that test for variations in the surface concentration are also performed. Trends in the source processes and test cases for a variety of exospheric conditions using actual signal and uncertainty predictions form

the basis for characterizing the ability of MASCS to distinguish between source processes as well as variations within source process for variable sodium surface concentration.

5.5.1 Trends for each source process

The sodium exosphere may consist of atoms from 3 source process: photon stimulated desorption, meteoritic vaporization, and thermal desorption. The dominant process should be a function of local time of day, height above the planet, and time of the year. Thus measured exospheric abundances may have components from each of the three processes in varying degree. In order to distinguish one process from the other, it is necessary to determine the trends that are characteristic of each process separately. Figures 5.20 and 5.21 show the normalized model predicted tangentially integrated column abundances for each process using the equatorial observation schemes described in section 5.3. The column abundances are normalized for each planetary true anomaly in order to see the behavior of the processes over solar zenith angle as well as over altitude. Furthermore, variations over solar zenith angle and over altitude may also be seen as a function of planetary true anomaly. Signal predictions based on non-normalized column abundances will be dealt with in Sections 5.5.3 – 5.5.5.

Figure 5.20 shows the variation of tangentially integrated column abundance over solar zenith angle for planetary true anomalies covering 1 Mercury year. The abundances are for equatorial limb observations at 100 km altitude. Photon

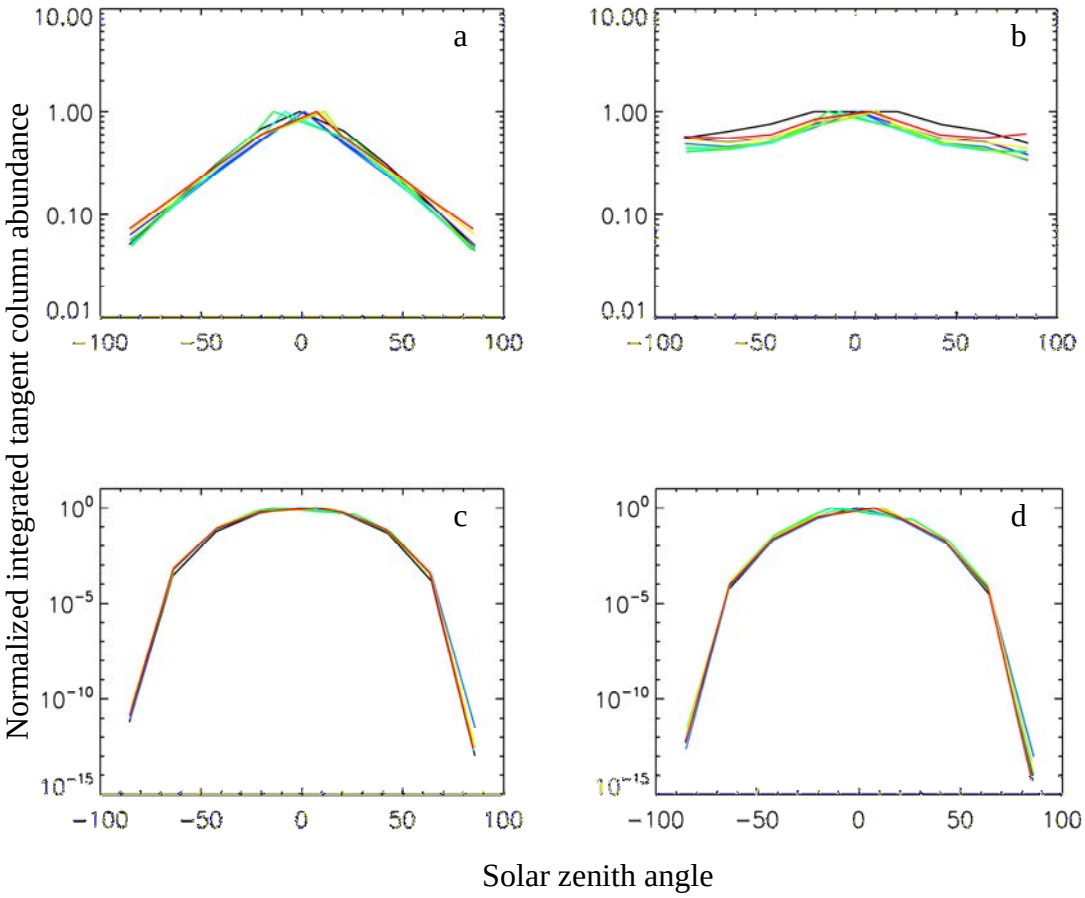

Figure 5.20. Normalized integrated tangential column abundance for sodium at 100 km above the limb of the equatorial region of the planet over 8 different true anomaly values. Photon stimulated desorption is shown in (a), meteoritic vaporization is shown in (b), thermal vaporization with surface sticking = 1 is shown in (c), and thermal vaporization with surface sticking < 1 is shown in (d).

stimulated desorption, meteoritic vaporization, and thermal vaporization (both with sticking = 1 and with sticking < 1) are shown. Photon stimulated desorption varies by ~ 1 order of magnitude from terminator to the sub-solar region, while meteoritic vaporization varies by less that 1 order of magnitude over the same angular range. Thermal vaporization varies by more than 10 orders of magnitude for both test cases of sticking. These dependencies on solar zenith angle for each process are expected from the physics that governs each process. Photon stimulated desorption is largely dependent on the number of photons available; which is dependent on the cosine of the solar zenith angle and thus implies a peak at the sub-solar point. Meteoritic vaporization is modeled as an isotropic source process. The small peak that occurs near the sub-solar point is due to the fact that the sticking coefficient, and consequently the loss rate, is temperature dependent. This causes the lifetime of exospheric atoms to be longer for sub-solar regions and leads to an increase in column abundance. Thermal vaporization is exponentially dependent on surface temperature, which is responsible for the large variations in column abundance from thermal vaporization as a function of solar zenith angle (see Chapter 1 for a discussion of the variation in surface temperature over solar zenith angle).

The solar-angle-dependent curves for each process show a small variation over planetary true anomaly. Section 5.5.3 will demonstrate this variation by means of fitting cosine power law functions to the curves over multiple true anomalies. There is also an asymmetry in the curves at extreme solar zenith angles; the most prevalent of which is for thermal vaporization. This is due to the fact that the limb observations were not made symmetrically, i.e., a limb observation at a solar zenith angle of -85°

cuts through the exosphere at a different angle than a limb observation at a solar zenith angle of +85°. Therefore abundances were integrated through slightly different regions of the exosphere.

Figure 5.21 shows the variation of tangentially integrated column abundance over altitude for a range of planetary true anomalies extending over the entire year. Photon stimulated desorption decreases by approximately 2 orders of magnitude from 100 km above the surface to 500 km above the surface while meteoritic vaporization decreases by less than 1 order of magnitude over the same altitude range. Thermal vaporization (both cases of sticking) varies by ~ 4 orders of magnitude over this altitude range. These results are expected from the respective scale heights of each process; as discussed in Chapter 3.

Also note that there is ~ 3 orders of magnitude difference between the column abundance for a planetary true anomaly of 6° and the other planetary true anomalies for thermal vaporization at 1000 km altitude. This is due to the variation in scale height, where the scale height above the sub-solar point for thermal vaporization is 63 km and 41 km for planetary true anomalies of 6° and 64°, respectively. The scale heights vary because of the variation in surface temperature and due to the variation of solar radiation pressure that acts as a downward force on atoms above the sub-solar region, both of which vary with planetary true anomaly. Although this effect is also seen in the other source processes, it is not as prevalent because the scale heights do not vary by as much. The predicted data is associated with a series of 9 radial scans above the equatorial region and the trends in each process are summarized in Table 5.2.

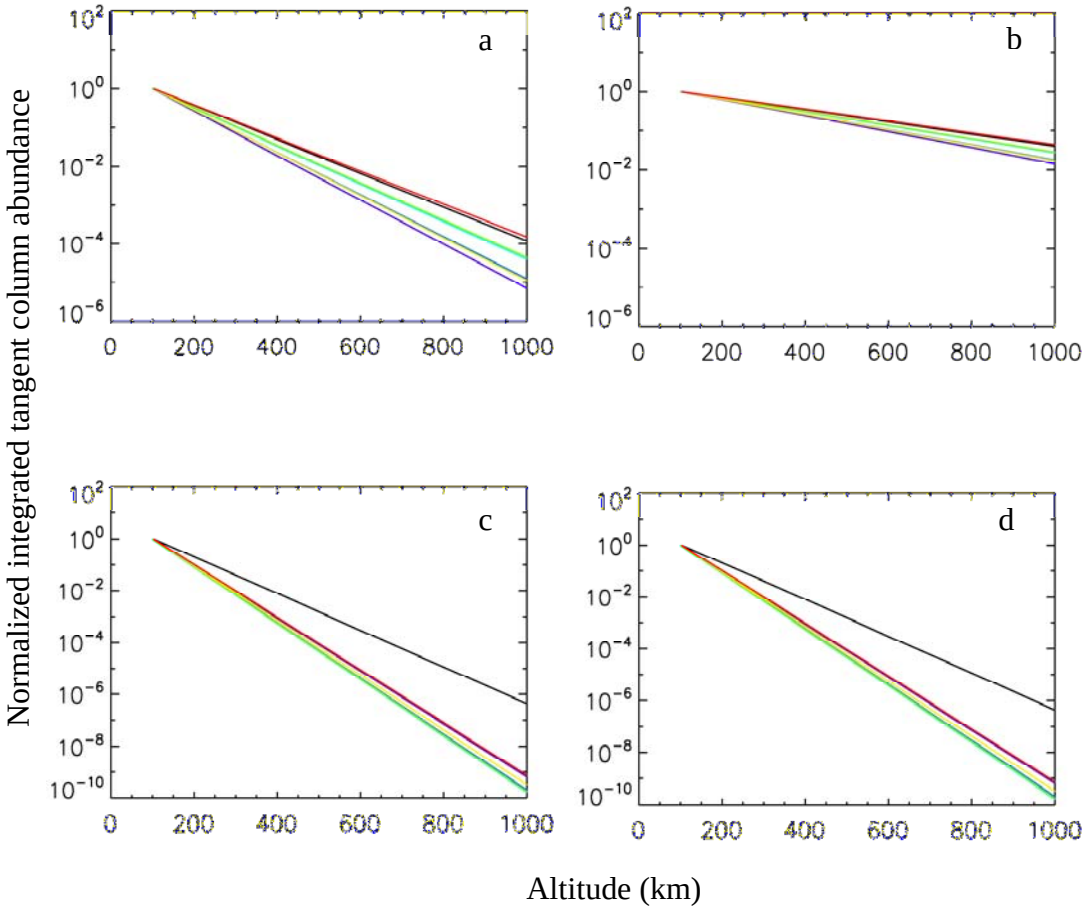

Figure 5.21. Normalized integrated tangential column abundance for sodium from 100 km to 1000 km above the limb of the equatorial region of the planet over 8 different true anomaly values. Photon stimulated desorption is shown in (a), meteoritic vaporization is shown in (b), thermal vaporization with surface sticking = 1 is shown in (c), and thermal vaporization with surface sticking < 1 is shown in (d).

Source process	Photon Stimulated Desorption	Meteoritic Vaporization	Thermal Vaporization (sticking = 1)	Thermal Vaporization (sticking < 1)
Solar zenith angle dependence	Column varies by ~ 1 order of magnitude from maximum value near sub-solar point to minimum value at terminator	Column varies by < 1 order of magnitude from maximum value near sub-solar point to minimum value at terminator	Column varies by greater than 10 orders of magnitude from maximum near sub-solar point to minimum at terminator	Column varies by greater than 10 orders of magnitude from maximum near sub-solar point to minimum at terminator. ~ 1 order of magnitude more variation than for the sticking = 1 case
Altitude variation	Column varies by ~ 2 orders of magnitude over altitude range.	Column varies by < 1 order of magnitude over altitude range.	Column varies by ~ 4 orders of magnitude over altitude range.	Column varies by ~ 4 orders of magnitude over altitude range.
Key observations	Complete dayside coverage is important at low to mid altitudes	Observe at altitudes > 300 km over entire dayside. May possibly be only component at terminator regions, thus may be distinguishable at lower altitudes in these regions	Complete dayside coverage and seasonal coverage at low altitudes	Complete dayside coverage and seasonal coverage at low altitudes

Table 5.2. Summary and defining characteristics of each source process. Most probable ejection speeds and scale heights for each process are given in table 3.2.

5.5.2 Observation strategies to test physical processes

Having determined pointing constraints, temporal constraints, and detection limits for proposed equatorial and north-south radial scans, observation strategies are devised for certain test cases that characterize the ability of MASCS to address some of the more fundamental science questions concerning Mercury's sodium exosphere. The observation strategies build on the observational constraints, strategies, and detection limits of Sections 5.2 – 5.4. The goal is to demonstrate that the proposed set of radial limb scans builds up a systematic data set that results in answering key scientific questions concerning the exosphere. The test cases include 1) the determination of MASCS's ability to distinguish between temperatures for high energy micro-meteoritic driven processes, 2) the determination of MASCS's ability to distinguish between solar zenith angle dependencies for photon stimulated desorption, meteoritic vaporization, and thermal desorption, and 3) the determination of MASCS's ability to measure latitudinal variations in sodium surface density concentration. For each test case, the model developed by Killen is used to make exospheric abundance predictions with model parameters set to values that result in the desired test cases. The exospheric abundances are converted to signal along with associated uncertainties as described in Chapter 4.

5.5.3 Distinguishing between temperatures for high energy processes

Figure 5.20 shows that meteoritic vaporization depends weakly on local time of day. This makes physical sense with the assumptions that meteoritic impact is modeled as being isotropic around the surface of the planet and that the meteoritic

vaporization column abundance is mostly independent of surface temperature. Conversely, the column abundance for photon stimulated desorption varies by ~ 1 order of magnitude and the column abundance for thermal vaporization varies by several orders of magnitude from the sub-solar region to the terminator. Figure 5.21 shows that the column abundance from meteoritic vaporization varies by less than an order of magnitude over an altitude range from 0 to 500 km, whereas the column abundances from photon stimulated desorption and thermal vaporization vary by 2 and 4 orders of magnitude, respectively, over the same altitude range. This is because typical scale heights for thermal desorption, photon stimulated desorption, and meteoritic vaporization are ~ 50 km, 100 km, and 240 km respectively.

The component of meteoritic vaporization may best be distinguished from the other processes by looking at high altitudes, with the best opportunities being above the terminator regions where the other processes have decreased to minimal contribution to the total column. The 2 upper panels of Figure 5.22 shows the predicted sodium D_2 signal values for meteoritic vaporization over a range of temperatures for observations above the dawn side terminator at planetary true anomalies of 64° and 180°.

For a planetary true anomaly of 64° meteoritic vaporization produces a tangentially integrated column abundance of $1.0*10^{10}$ Na/cm^2 at 100 km above the terminator region. For the same set of model parameters, the tangentially integrated column abundance produced by meteoritic vaporization at 100 km above the limb for a planetary true anomaly of 180° is $5.7*10^{9}$ Na/cm^2. This decrease was due primarily

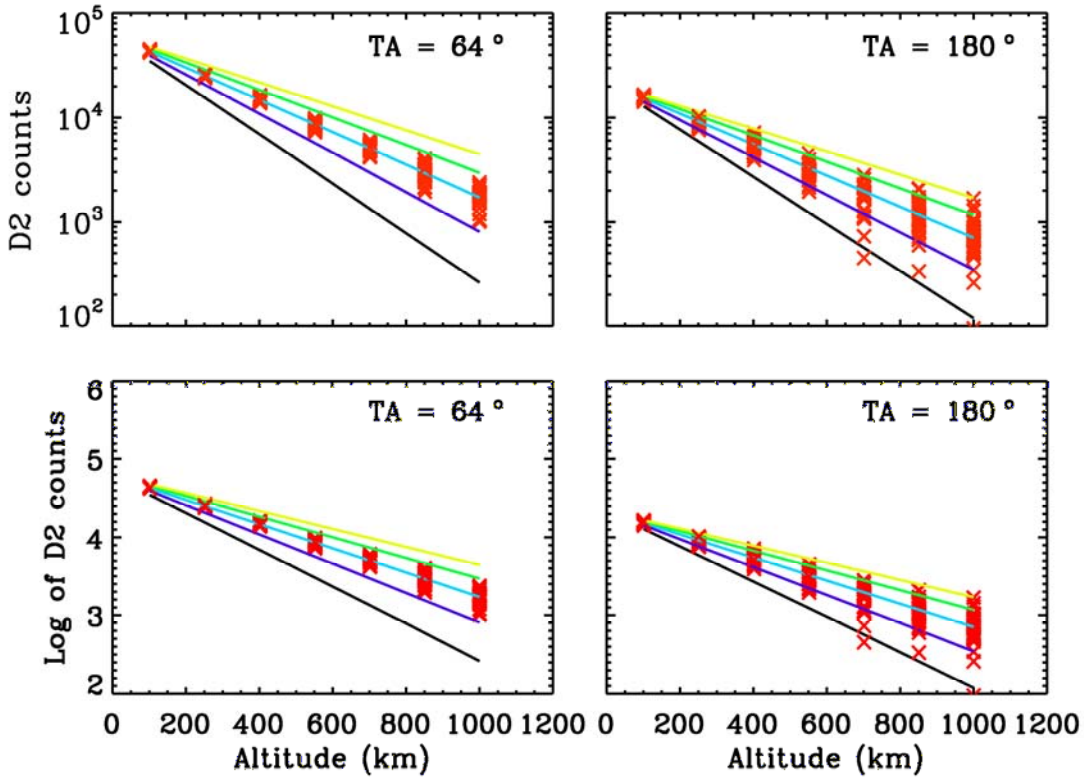

Figure 5.22. The model predicted D_2 counts in the top 2 panels and the log of the model predicted D_2 counts in the lower 2 panels for meteoritic vaporization for 5 different temperatures and for 2 planetary true anomalies (solid lines). Also shown are signal predictions (red crosses) for 30 different sets of signal predictions at 3000 K. The spread in the 180° data is greater than the spread in the 64 data because of lower signal and corresponding smaller SNR. The peak tangential column abundances corresponding to the lowest altitude are $1.0*10^{10}$ Na/cm^2 and $5.7*10^{10}$ Na/cm^2 for planetary true anomalies of 64° and 180°, respectively. These values are discussed in the text.

to the temperature dependence of surface sticking. Furthermore, the g-value is a factor of ~16 lower at 180° compared to 64°. The combined effects of lower column abundance and lower g-value causes the signal at 180° to be ~ a factor of 30 lower than at 64°. SNR values were computed and found that none exceeded an SNR of 3, leading to the conclusion that meteoritic vaporization cannot be observed at a planetary true anomaly of 180° if the same parameters are used that produced a reasonable signal at a true anomaly of 64°. Instead of presenting a "null" result, the source rate for meteoritic vaporization was increased by a factor of 10 for the true anomaly = 180° test case. This is justified since the micro-meteorite density and velocity dispersion as well as the production rate of sodium from meteoritic impact are poorly constrained and could vary by an order of magnitude. Using the larger value for meteoritic vaporization, the tangentially integrated column abundance 100 km above the terminator region at a planetary true anomaly of 180° was $5.7*10^{10}$ Na/cm^2. The signal is still more noisy than for the true anomaly = 64° case due to the decrease in the g-value.

The red crosses of Figure 5.22 represent 30 simulations of data from meteoritic vaporization at a temperature of 3000 K where background counts have been added, then random noise added, and then the background has been subtracted off with the sodium D_2 signal recovered according to the methods outlined in Chapter 4. The integration time was 1 second and the atmospheric slit was used for all observations. The solid lines represent model predicted count rates at 5 different temperatures without the addition of background counts or random noise. The lower panels of Figure 5.22 are the same as the upper panels but with the log of all data taken in order

to plot on a liner scale. The log of the simulated data closely follows a strait line, and thus motivates a method to characterize how well temperatures can be measured by fitting a strait line to the simulated data points. The absolute magnitudes of the signal could vary by either varying the instrument sensitivity or varying source rates. However, the slope of each line varies with temperature and thus represents a more viable method to discriminate between different temperatures.

The SNR of the predicted signal for meteoritic vaporization over the range of altitudes from Figure 5.22 is shown in Figure 5.23. The SNR decreases with altitude; which is due chiefly to the fact that the signal from exospheric emissions decreases with altitude. The off-axis light also decreases with altitude, but within most of this altitude regime does not decrease as much as the exospheric emissions (see Chapter 2 for off-axis curves with angle). The detector dark counts have no dependence on altitude within this regime. These factors combine to reduce the SNR for higher altitudes. Also, the SNR for a planetary true anomaly of 180° is less than for 64° due mainly to the g-value being reduced by ~ 16. Solar irradiance, and consequently off-axis light, only decreases by a factor of ~ 2 from a true anomaly of 64° to 180°. The spread in the SNR data is consistent with the signal predictions shown in Figure 5.22.

A least squares strait line was fit to the log of each of the 30 sets of data points following the techniques outlined by Bevington, 1992. The data were weighted by the predicted uncertainties obtained from the signal recovery method outlined in Chapter 4.

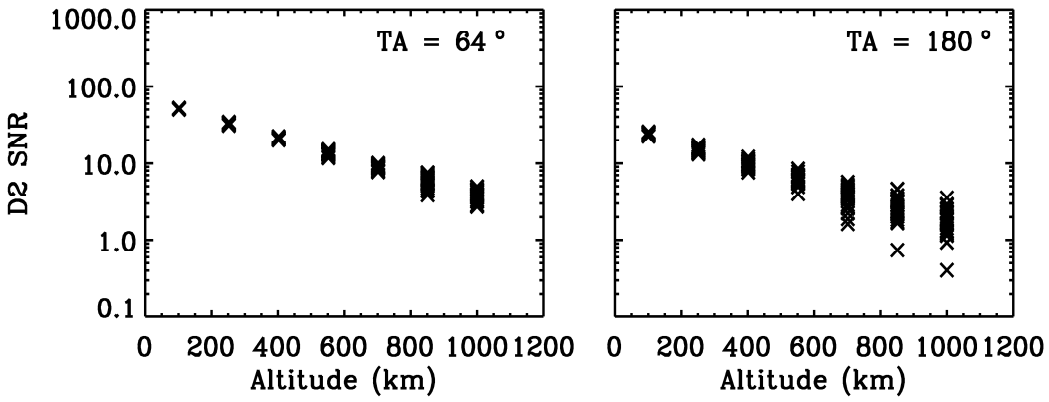

Figure 5.23. SNR for 30 different sets of simulations. The SNR decreases with altitude because the exospheric emissions decrease with increasing altitude. The off-axis continuum also decreases, but for off-axis angles associated with high altitudes the off-axis light does not decrease as quickly with altitude as the exospheric emissions. Furthermore, the detector dark counts do not decrease with altitude.

The equation was

$$y = A + B * x \tag{5.6}$$

where A is the constant for the y intercept, B is the slope, and x is the altitude. The uncertainties in the constants A and B were also calculated. Since the calculations were weighted with the uncertainties of the retrieved data points, the uncertainties associated with the data retrieval algorithm outlined in Chapter 4 propagated through to the uncertainties associated with A and B.

Figure 5.24 shows the slope of the log of the model predicted counts rates at the 5 different temperatures from Figure 5.22 plotted as a function of temperature. The recovered "B" values from Equation 5.6 for all 30 simulations were interpolated to the temperature-slope curve and also plotted. Also shown are the 1 σ uncertainties in the "B" values. The lower panels in Figure 5.24 shows the mean of the "B" values from the 30 simulated observations along with the standard deviation of the 30 data points projected over onto the slope verses temperature plot. This indicates that for the predictions of meteoritic vaporization in this particular sodium exospheric model, the observation strategy proposed, and the present knowledge of instrument performance, a temperature of 3000 K can be distinguished to between 2934 K and 3088 K with a mean of 2999 K for a planetary true anomaly of 64° and between 2807 K and 3187 K with a mean of 2970 K for a planetary true anomaly of 180° within 1 σ uncertainty. The explanation for the uncertainty in recovered temperature for a

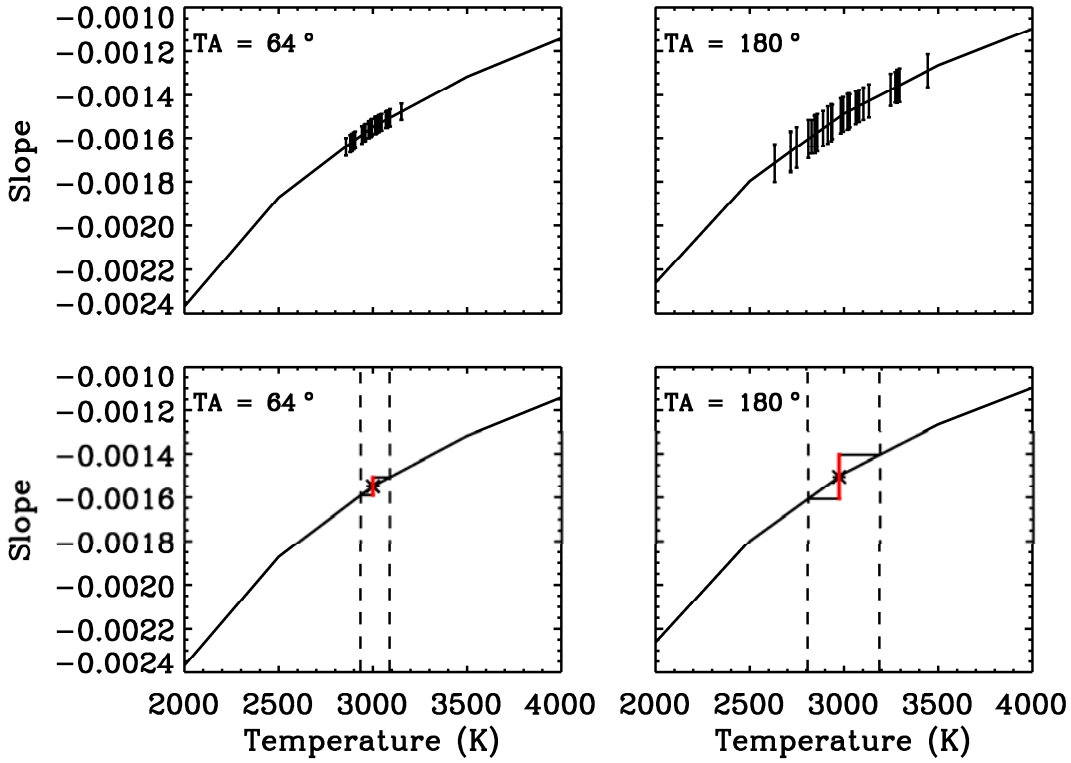

Figure 5.24. For each of the 5 model predicted temperature curves shown in the 2 lower panels of Figure 5.22, the slope of the log of each curve is plotted as a function of temperature. Recovered "B" values from Equation 5.6 are shown in figures (a) and (b) for the 30 simulated observations that have been interpolated to the temperature-slope curve. The lower 2 panels show the mean of the values from the upper 2 panels with the error bar representing the standard deviation of the 30 "B" values. The dashed lines are the projection of the error bars over onto the temperature-slope curve. The mean retrieved temperature for a planetary true anomaly of 64° is 2999 K with a 1 σ upper temperature of 3088 K and a 1 σ lower temperature of 2934 K. The mean retrieved temperature for a planetary true anomaly of 180° is 2970 K with a 1 σ upper temperature of 3187 K and a 1 σ lower temperature of 2807 K.

planetary true anomaly of 180° being larger than for the other case is due to the decreased g-value at this planetary position. Only a further increase in that absolute tangential column abundance corresponding to an increase in radiance would lead to SNR values large enough that the spread in individual measurements would become smaller. Thus an increase of a factor of 10 in source rate at a true anomaly of 180° was not enough to produce the same precision in temperature recovery as at a true anomaly of 64°. Also, note that the difference between the mean temperature and the lower limit is not as great as the difference between the upper limit and the mean temperature. This is due to the fact that the temperature-slope curve of Figure 5.24 is not a strait line. The slope of the curve decreases with increasing temperature; implying that for a 1 σ variation in the "B" parameter, the lower limit corresponds to a smaller change in temperature than the upper limit for the same variation in the "B" parameter.

5.5.4 Distinguishing between dominant source processes

Figures 5.20 and 5.21 show the different trends for photon stimulated desorption, meteoritic vaporization, and thermal vaporization. Each of the processes shows different behavior over local time of day as well as seasonal variations. The goal of the investigation presented in this section is to characterize the ability of the instrument to distinguish between solar zenith angle dependencies of the 3 major source processes. Simulated observations over a full range of solar zenith angles are performed that make use of 9 equatorial radial scans (see Section 5.3 and Figure 5.14 as an example) at a specific planetary true anomaly. Ten simulated observations for

each source process are performed for 4 different planetary true anomalies from perihelion to aphelion.

The atmospheric model developed by Killen is used to generate column abundances and ultimately signal predictions for the proposed set of observations. Distinguishing between source processes as predicted by the model ultimately results in using the observations strategies developed earlier in the chapter to test the model. The model predicts variations in sodium exospheric abundance of a factor of ~ 2 from perihelion to aphelion, with the abundance at aphelion being greatest. This was modeled after observational results by Potter et al. (1999). Furthermore the dominant process in the model is photon stimulated desorption with meteoritic vaporization as a background source that is from 1 – 2 orders of magnitude less than photon stimulated desorption. Debate exists in the Mercury exospheric community concerning the dominance of photon stimulated desorption or thermal vaporization (see Chapter 3). To that end the thermal vaporization was also investigated as an alternate dominant source process to photon stimulated desorption, with both cases of sticking considered (see Section 5.5). In order to give thermal vaporization the same abundance as photon stimulated desorption, the binding energy for thermal vaporization was adjusted at each planetary true anomaly tested to give a maximum zenith column abundance nearly equal to the maximum zenith column abundance of photon stimulated desorption. Binding energies ranged from ~ 2.5 eV at a planetary true anomaly of 6° to ~1.6 eV at a planetary true anomaly of 180°. Maximum zenith column abundances for photon stimulated desorption as well as for thermal vaporization were ~ 4.4 X 10^{11} Na/cm^2 at a planetary true anomaly of 6° and ~ 7.2 X

10^{11} Na/cm^2 at a planetary true anomaly of 180°. The maximum zenith column abundance for meteoritic vaporization was nearly constant over planetary true anomaly with a value of ~ 1.9 X 10^{10} Na/cm^2.

For each planetary true anomaly, 10 separate data sets were generated for the 9 observations at an altitude of ~100 km above the limb for each of the source processes. Given the random noise that was included in each data prediction (see Chapter 4), the 10 data sets represented normally distributed signals around model predicted signal values for each source process and for each observation. Since thermal vaporization has such a strong dependence on surface temperature, the signal for thermal vaporization for extreme solar zenith angles was typically too low to be detected above the noise level. Therefore, for thermal vaporization, only 5 of the 9 observations centered on the sub-solar point were able to be used, which corresponded to a range of solar zenith angles of +/- 50°, with SNR values in the extreme observations of ~ 3.

Figure 5.25 shows the D_2 line model results for the 3 processes over 4 different planetary true anomaly angles with the solid lines representing the count rate without the addition of random noise, detector dark counts, or off-axis light background. The crosses, diamonds, stars, and triangles represent the 10 sets of simulated data for each of the source processes after the addition of random noise and the subtraction of dark counts and off-axis light background as described in Chapter 4. The integration time was 1 second and the surface slit was used for all but the 180° planetary true anomaly observations. The signal varies by over an order of magnitude from a true anomaly of 6° to a true anomaly of 64° despite the fact that the column abundance varies very

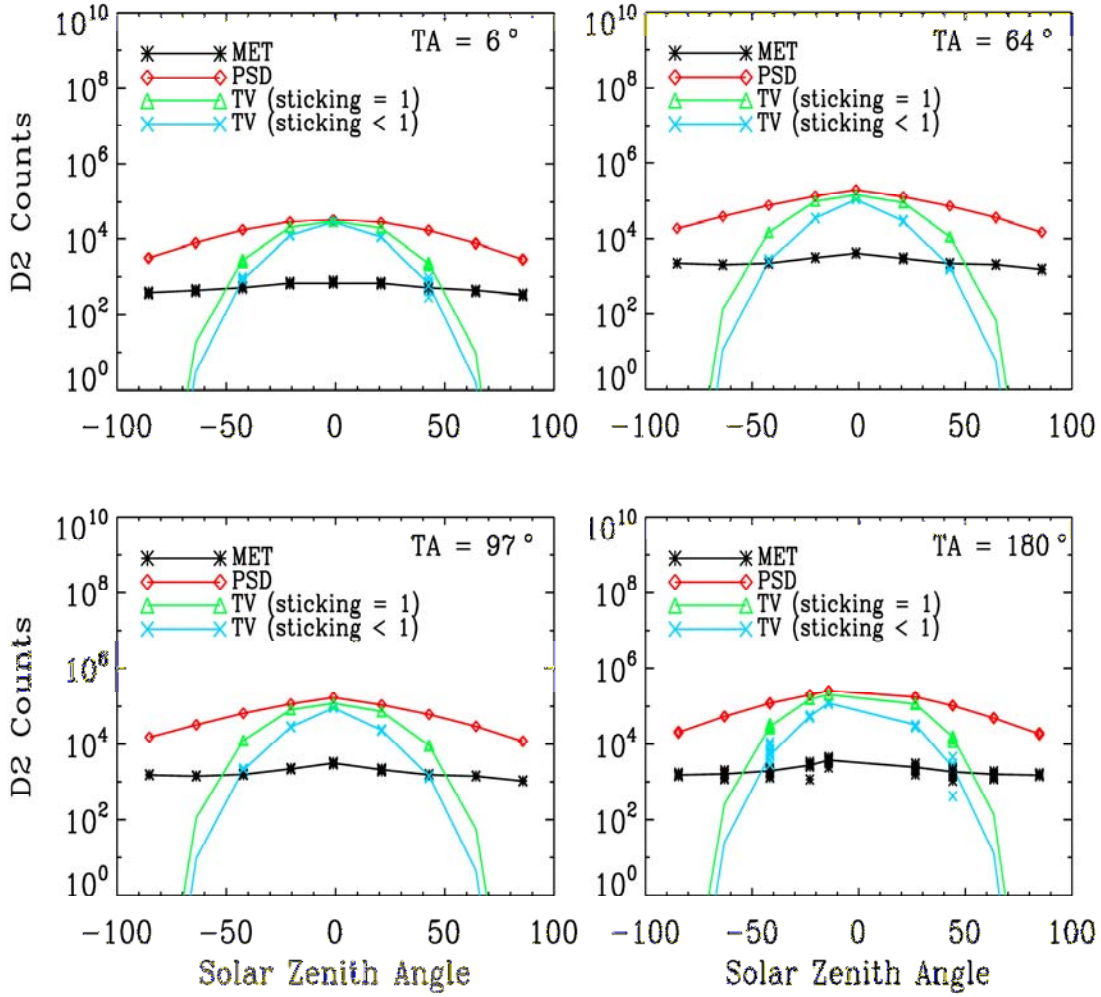

Figure 5.25. The D_2 model counts for all source processes and for 4 different planetary true anomalies shown as solid color coded lines. Also shown are signal predictions (crosses, diamonds, stars and trianlges) for 10 different sets of predictions for each source process. The surface slit was used for planetary true anomalies of 6°, 64°, and 97°. The atmospheric slit had to be used for the observations at a planetary true anomaly of 180° because the SNR was too small with the surface slit in place.

little. This illustrates the effect of the variation in the g-value with planetary true anomaly. Figure 1.8 shows that the g-value varies by almost an order of magnitude between these 2 planetary true anomalies and thus is responsible for the majority of the variation in signal. The signal at a true anomaly of 180° is a factor of ~ 20 greater due to the use of the atmospheric slit.

For a signal prediction, the uncertainties arise from statistical uncertainties in photoncounting of the signal and background. The background, which for low altitudes is dominated by off-axis light, as well as the signal from exospheric emissions, varies with both altitude as well as solar zenith angle. However, these two sources of photons that enter the instrument do not necessarily vary in the same manner with altitude and solar zenith angle and therefore the SNR may have unexpected variations. Figure 5.26 shows the SNR for equatorial observations 100 km above the limb at planetary true anomalies of 6°, 64°, 97°, and 180°. The SNR is cutoff if it falls below a value a 3, which explains the incomplete curves for thermal vaporization. For a planetary true anomaly of 6° photon stimulated desorption and thermal vaporization behave in a relatively uncomplicated manner, where the signal decreases with solar zenith angle at a rate faster than the off-axis light and produces SNR values that peak at the sub-solar point. Alternatively, the signal from meteoritic vaporization does not decrease significantly with solar zenith angle, as discussed in Section 5.5.1. The off-axis light component decreases by a factor of ~ 5 from the sub-solar point to the terminator and leads to an increase in the SNR for meteoritic vaporization from the sub-solar point to the terminator. For the remainder of the planetary true anomalies, the behavior of the SNR for meteoritic vaporization and

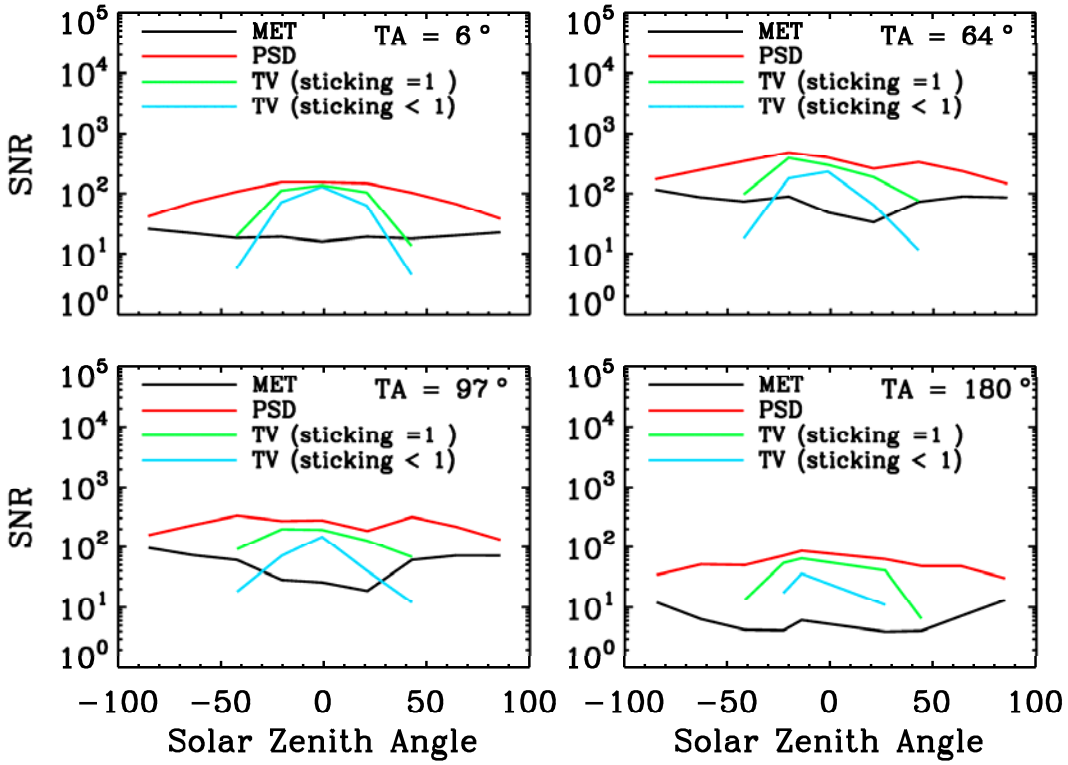

Figure 5.26. SNR curves corresponding to 1 simulation from each of the data points in Figure 5.25. As expected, meteoritic vaporization has the lowest SNR since its abundance is 1-2 orders of magnitude less than for the other processes. Since there is little variation of the column abundance for meteoritic vaporization with solar zenith angle, the SNR tends to increase near the terminator since the off-axis light decreases for this region of the planet. Only values of SNR > 3 are plotted, which explains the incomplete curves for thermal vaporization.

thermal vaporization is similar to that for a planetary true anomaly of 6°. For a planetary true anomaly of 97° the SNR for photon stimulated desorption experiences an increase for solar zenith angles of +/- 40°, which is due to the off-axis light having decreased from the value it had above the sub-solar region at a greater rate than the corresponding decrease in exospheric emission. All SNR curves show a strong asymmetry with solar zenith angle for a planetary true anomaly of 64°. This is due to the fact that the off-axis angle ranges from 0.4° to 0.37° from a solar zenith angle of 0° to +20°. This falls in the steep variation regime for the off-axis response of the instrument where a small change in angle results in a large change in off-axis response (see Chapter 2).

The SNR curves also illustrate the variation of g-value effect as was previously shown for the D_2 signals of Figure 5.25. The SNR was largest at a planetary true anomaly of 64°, coincident with the peak of the g-value. Since the atmospheric slit was used for a planetary true anomaly of 180° the SNR was not as small as it would have been using the surface slit. This illustrates that successful observations must consist of using both the surface slit or the atmospheric slit, depending on the planetary true anomaly.

In order to characterize the ability of the instrument (as well as the proposed observation strategy) to distinguish between the source process variations with solar zenith angle, a cosine power law of the form

$$y = A\cos(\theta)^B + C \tag{5.7}$$

was fit to the data for each of the processes; where θ is the solar zenith angle of the tangent point of the observation and A, B, and C are parameters that were determined by an IDL least squares minimization procedure. The uncertainties for each signal prediction were calculated by the method explained in Chapter 4 and were used as weighting values for the recovery of their respective A, B, and C parameters in the IDL routine. The parameter that was most useful in distinguishing between the processes was the power term "B".

Figure 5.27 shows the retrieved "B" parameter for each of the 10 simulated observations and for each source process. Table 5.3 summarizes the mean and standard deviation for the "B" terms for all of the source processes and for the 4 planetary true anomaly angles tested. Since the SNR for thermal vaporization was below 3 for the 4 outermost solar zenith angles, only the 5 data points nearest the sub-solar region were used in the curvefitting routine. This caused the noise for thermal vaporization with sticking < 1 to be worst at a planetary true anomaly of 180° and made the recovery of the "B" parameter difficult. Also, this particular source process showed large variations in the "B" parameter from a planetary true anomaly of 6° to planetary true anomalies of 64° and 97°. This is because the temperature gradient across the surface near perihelion is smaller than for other planetary true anomalies (see Figure 1.2) and results in the curve not being as steep near perihelion.

Meteoritic vaporization was noisy for most of the year and reached its most noisy state for a planetary true anomaly of 180°; which was expected given the low SNR from this process. The behavior of meteoritic vaporization requires some explanation. At a planetary true anomaly of 6°, the shape of the signal from

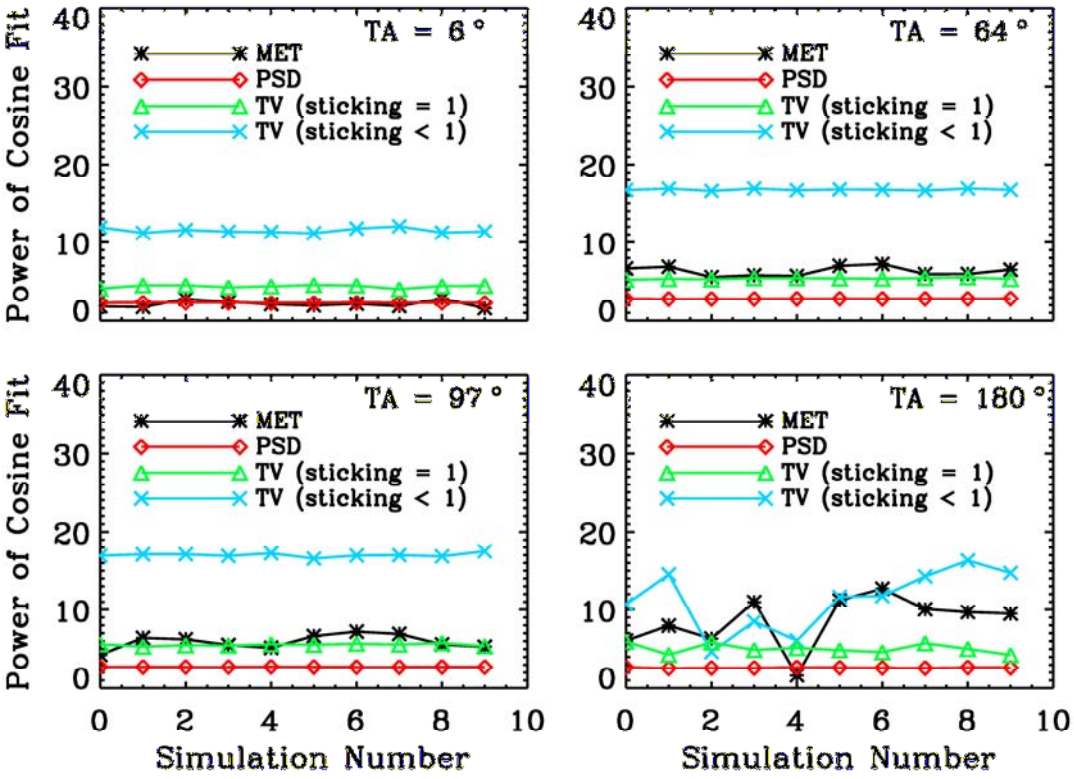

Figure 5.27. Results of the recovered "B" parameter power term from Equation 5.7 for all test cases. The "B" parameter was retrieved easily for photon stimulated desorption since that signal was relatively large. Since meteoritic vaporization was treated as a background source with column abundances 1-2 orders of magnitude less than for photon stimulated desorption, the data had a much lower SNR and made retrieval of the "B" parameter difficult. For a planetary true anomaly of 6° the "B" parameter is indistinguishable between photon stimulated desorption and meteoritic vaporization due to the low SNR for the meteoritic vaporization signal. The large jump in the "B" parameter for thermal vaporization with temperature dependent sticking (blue curve) from a planetary true anomaly of 6° to 64° is because the curve becomes more "peaked" at the sub-solar region due to colder temperatures in regions away from the sub-solar point. At 180° the SNR from thermal vaporization with temperature dependent sticking and meteoritic vaporization becomes so low that recovery of the "B" parameter is difficult.

Planetary true anomaly	Photon stimulated desorption Mean Std Deviation	Meteoritic vaporization Mean Std Deviation	Thermal desorption (sticking = 1) Mean Std Deviation	Thermal desorption (sticking < 1) Mean Std Deviation
6°	2.31 0.0214	2.14 0.427	4.40 0.183	12.8 0.349
64°	2.82 0.0152	6.33 0.601	5.38 0.0901	18.6 0.122
97°	2.72 0.0120	5.92 0.912	5.53 0.137	18.9 0.279
180°	2.63 0.0416	8.61 3.23	5.53 0.612	12.6 4.33

Table 5.3. Summary of the retrieved “B” parameters from the cosine power law. The “B” parameter at a planetary true anomaly of 6° is indistinguishable between photon stimulated desorption and meteoritic vaporization. This is expected because the SNR for meteoritic vaporization is relatively low at 6° and thus the recovered “B” parameter has a larger standard deviation. For all other true anomalies stimulated desorption is clearly distinguishable from the other processes.

meteoritic vaporization follows a fairly smooth curve where the signal peaks near the sub-solar point and decreases with increasing solar zenith angle. This is because radiation pressure is very low (~ 7% of surface gravity) and a relatively small number of atoms get blown towards the terminator. Hence the fitting of the data to the cosine power law returns a very low "B" value as would be expected. For all other planetary true anomalies, the signal from the observations above the terminator begins to increase. For planetary true anomalies of 64° and 97° this is due to radiation pressure pushing the atoms back towards the terminator and thereby increasing the column abundance. For a planetary true anomaly of 180°, the radiation pressure is only 3% of surface gravity, but there is still a slight upturn in the column abundance at the terminator. The explanation for this is that unlike conditions at a planetary true anomaly of 6°, the temperature near the sub-solar point has decreased substantially. This causes the column abundance to decrease in the regions surrounding the sub-solar region relative to the terminator, thereby allowing the small amount of atoms pushed back by radiation pressure to have more of an effect by comparison. This causes the curve-fitting routine for planetary true anomalies of 64°, 97°, and 180° to fit a larger "B" value for meteoritic vaporization, which seems counterintuitive since the curve for meteoritic vaporization is obviously shallower than the other curves. However, with the increased signal above the terminator, the curvefitting routine returns a larger "C" parameter from Equation 5.7. This explains why the "B" parameter makes a noticeable jump from a true anomaly of 6° to the other true anomalies. This implies that the "B" parameter alone may not be adequate for distinguishing meteoritic vaporization from the other processes.

Based on the recovered “B” parameter, photon stimulated desorption and thermal vaporization with surface sticking = 1 are clearly distinguishable from each other at all planetary true anomalies. However, since the SNR for meteoritic vaporization is relatively small and since the “B” parameter alone is not adequate for distinguishing meteoritic vaporization from the other processes (as discussed in the previous paragraph), meteoritic vaporization is not clearly distinguished from the other processes based on this technique. Also the “B” parameter for thermal vaporization with temperature dependent surface sticking is noisy at a planetary true anomaly = 180°. This is because the of the low temperatures associated with the surface at 180° which causes the signal to be very low for all but the sub-solar regions.

Figure 5.28 shows the 10 sets of simulated observations for each source process with curves plotted that used Equation 5.7 along with the mean of the retrieved values for A, B, and C. The curves for thermal vaporization are only plotted over the range of solar zenith angles where the SNR > 3.

5.5.5 North-south asymmetries

The surface concentration of sodium is presently an unconstrained parameter. Killen proposes that because of gardening coupled with diffusion of Na through surface grains, energetic processes may bring adequate amounts of sodium to the surface resulting in near constant reservoirs of sodium from beneath the surface (private communication, 2006). This does not imply that external processes could not deliver sodium at localized regions of the surface resulting in sodium enhancements; but instead that there should be an underlying constant supply of sodium even in the

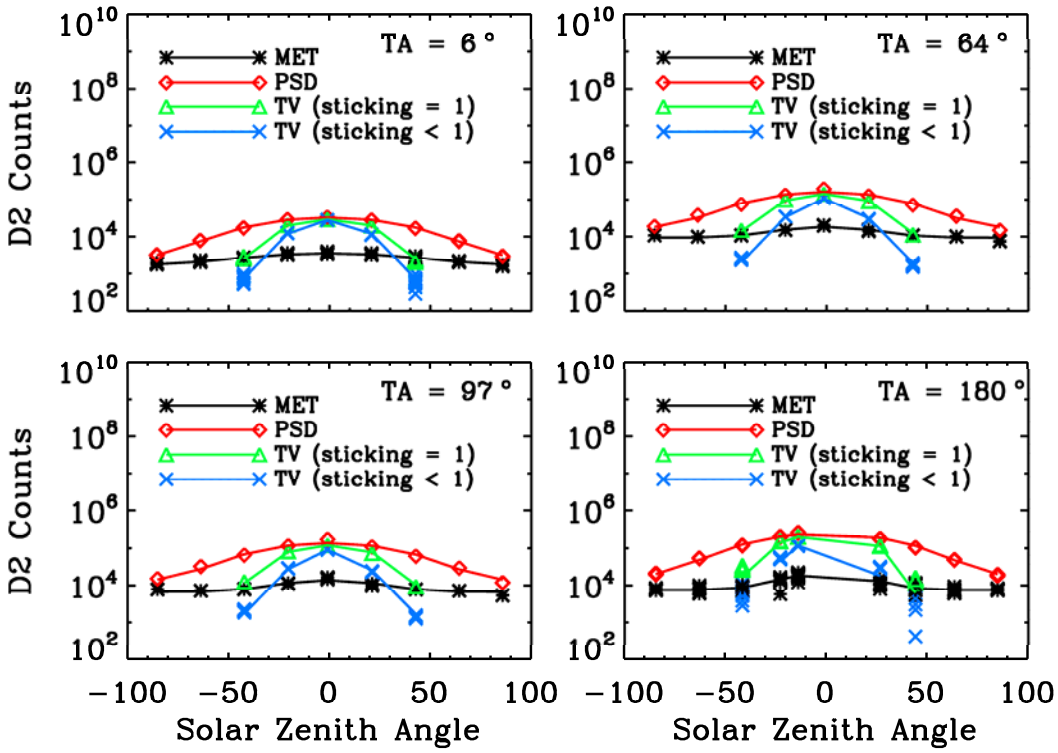

Figure 5.28. Curves calculated by using the retrieved parameters A, B, and C (solid curves). Also shown are the signal values from Figure 5.25 (crosses)

absence of localized enhancements. Others (Leblanc and Johnson, 2003; Strom and Sprague, 2003) suggest that the dayside surface surrounding the sub-solar point may be devoid of sodium. Due to temperature dependent sticking, sodium could possibly become cold trapped at high latitudes, forming concentrations of sodium much larger than in the equatorial regions. It is not unreasonable to postulate a latitudinal dependence on surface concentration given that high latitude regions have never received as much solar insolation as equatorial and mid-latitude regions. Mapping latitudinal variations in sodium surface concentration will give important clues as to processes at work on the surface as well as surface characteristics such as thermal annealing of surface grains, rate of gardening, and migration patterns of sodium. It should be mentioned that the only way for MASCS to detect sodium is for the sodium to be airborne, which implies that cold trapped sodium at high latitudes may be undetectable unless liberated by some source process.

The goal of this section is to determine how well variations in sodium surface concentration can be distinguished for a given source process by means of low altitude (50 km tangent height) north-south observations. Since this deals with low altitude observations, photon stimulated desorption and thermal vaporization (with both cases of surface sticking) are investigated since these processes have scale heights on the order of 50 km to 100 km

In regards to this hypothesis, observations have been designed to test latitudinal dependencies of sodium surface concentration with the goal of quantifying the ability of MASCS to measure the variation in surface concentration. Figure 5.16 indicates that a range of north-south observations exist between planetary true anomalies of ~

0° and 180°, with the tangent points being on the dusk side for planetary true anomalies in the 0° region and then crossing over to the dawn side for true anomalies > 64°. The software planning tool was used to determine that a planetary true anomaly of 31° is where the tangent points closely follow the sub-solar meridian from -50° latitude up to the north- polar region; thus this represents the best opportunity to observe latitudinal variations. Since solar insolation is zenith angle dependent, it is reasonable to assume a sine angle dependent surface concentration with latitude of the form

$$\sigma_{surf} = \sigma_{nominal}\left[1 + f * \sin(lat)\right] \tag{5.8}$$

where σ_{surf} is the surface concentration of sodium in units of Na/cm^2, $\sigma_{nominal}$ is the nominal value of sodium surface concentration in the absence of latitude enhancements, "f" is a scaling factor, and lat is the latitude that ranges from -90° to + 90° from south pole to north pole, respectively. Since time and sunshade constraints limit north-south observations to low altitude short duration limb scans, altitudes of 50 km and 100 km were observed as shown in Figure 5.29, with results presented for the 50 km limb observations.

The model was run without the addition of random noise for 5 values of "f" from Equation 5.8 with peak zenith column abundances that ranged from $4.5*10^{11}$ Na/cm^2 to $6.4*10^{11}$ Na/cm^2, depending on the "f" value. The binding energies for thermal vaporization for sticking <1 and sticking = 1 were 2.5 eVand 2.3 eV, respectively in order to give maximum tangential column abundances similar to those for photon

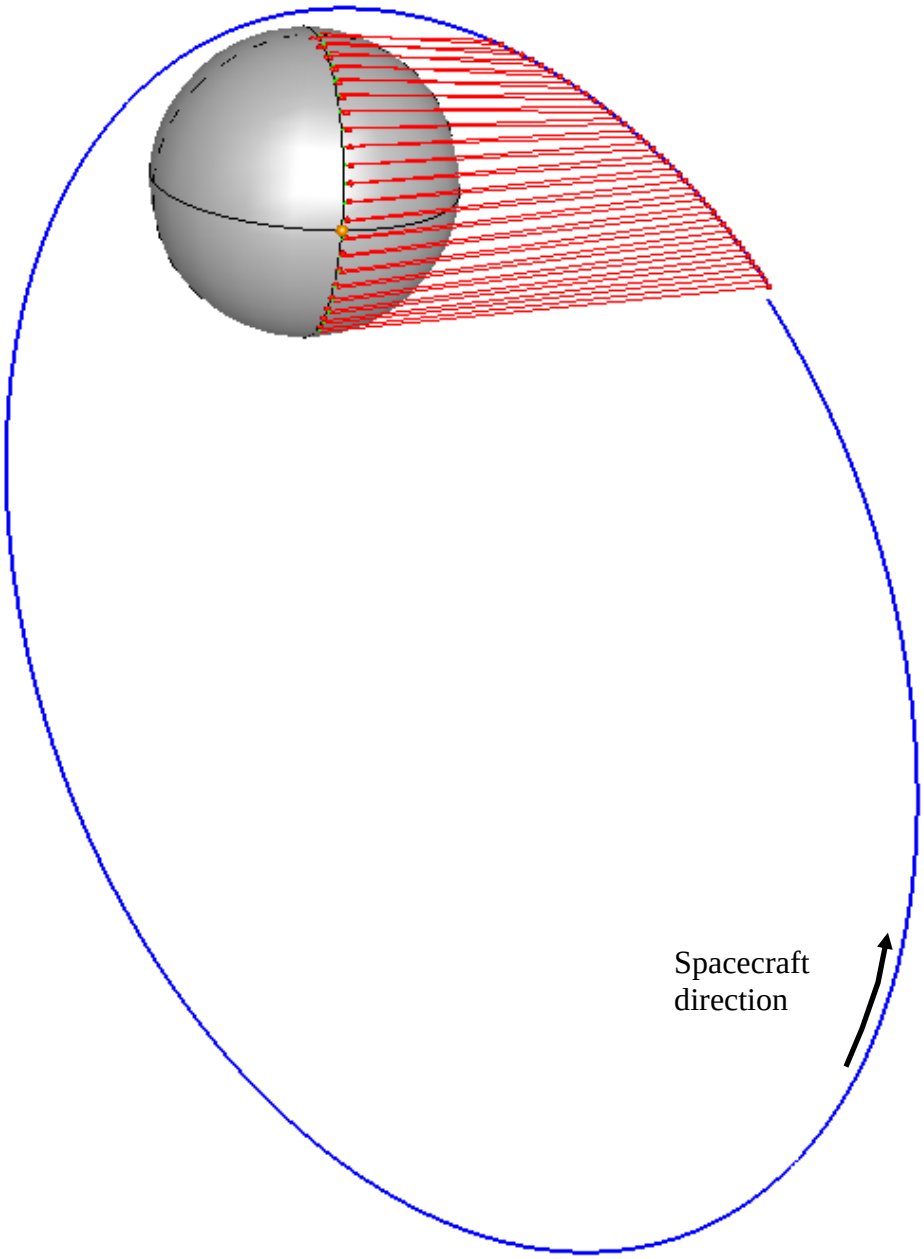

Figure 5.29. North-south observations at a planetary true anomaly = 31°. This represents the best opportunity to cover the sub-solar meridian from southern latitudes up to the north polar region.

stimulated desorption. Figures 5.30 – 5.32 show the D_2 and SNR predictions for each of the source processes tested. The solid curves represent model predictions for values of "f" = 0, 1, 2, 3, and 4 without the addition of random noise. The stars represent 10 observation simulations for each "f" value that were run where background counts were added, then random noise added, then the background subtracted off and the D_2 line recovered by the method outlined in Chapter 4. The integration time was 1 second and the surface slit was used for all observations.

The SNR for photon stimulated desorption remained relatively large even for high latitudes. However, due to the strong surface temperature dependence of thermal vaporization, the SNR dropped below 3 at latitudes in the range from 50° to 60°. The signal as well as SNR dropped off more quickly with latitude for thermal vaporization with temperature dependent surface sticking < 1 than for thermal vaporization with surface sticking = 1. This was expected since surface sticking is temperature dependent and causes more atoms to stick to the surface at the colder surface temperatures associated with higher latitudes than for the case where surface sticking is constant over the surface.

Each curve is a convolution of the surface concentration dependence (Equation 5.8) and processes that affect the distribution of exosphere over latitude such as surface sticking, radiation pressure, and surface temperature. Each source process is affected uniquely by these processes, thus it is impractical to retrieve the "f" parameter based solely on Equation 5.8. Therefore, in order to determine how well variations in sodium surface concentration could be distinguished from one another

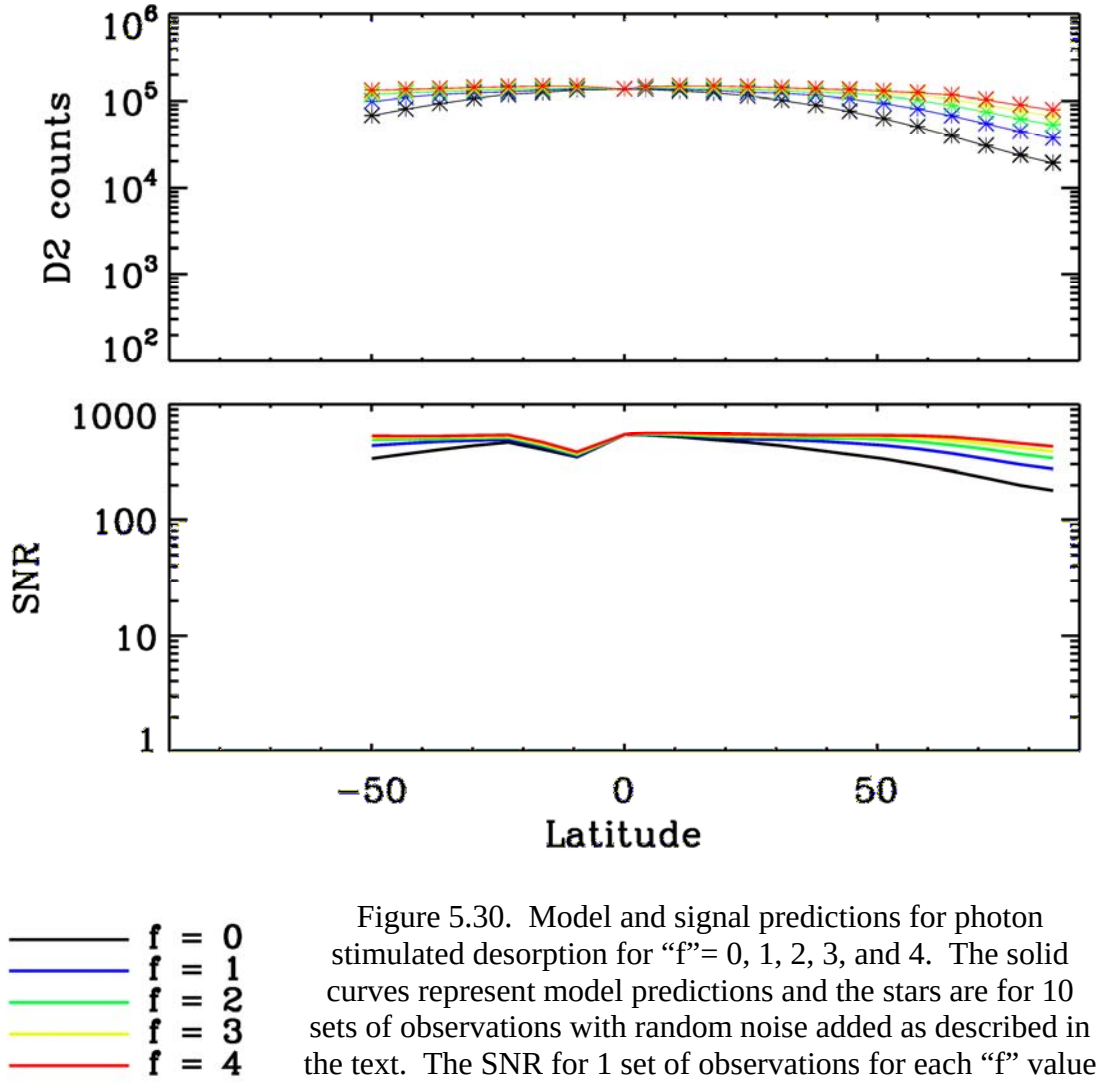

Figure 5.30. Model and signal predictions for photon stimulated desorption for "f"= 0, 1, 2, 3, and 4. The solid curves represent model predictions and the stars are for 10 sets of observations with random noise added as described in the text. The SNR for 1 set of observations for each "f" value is plotted.

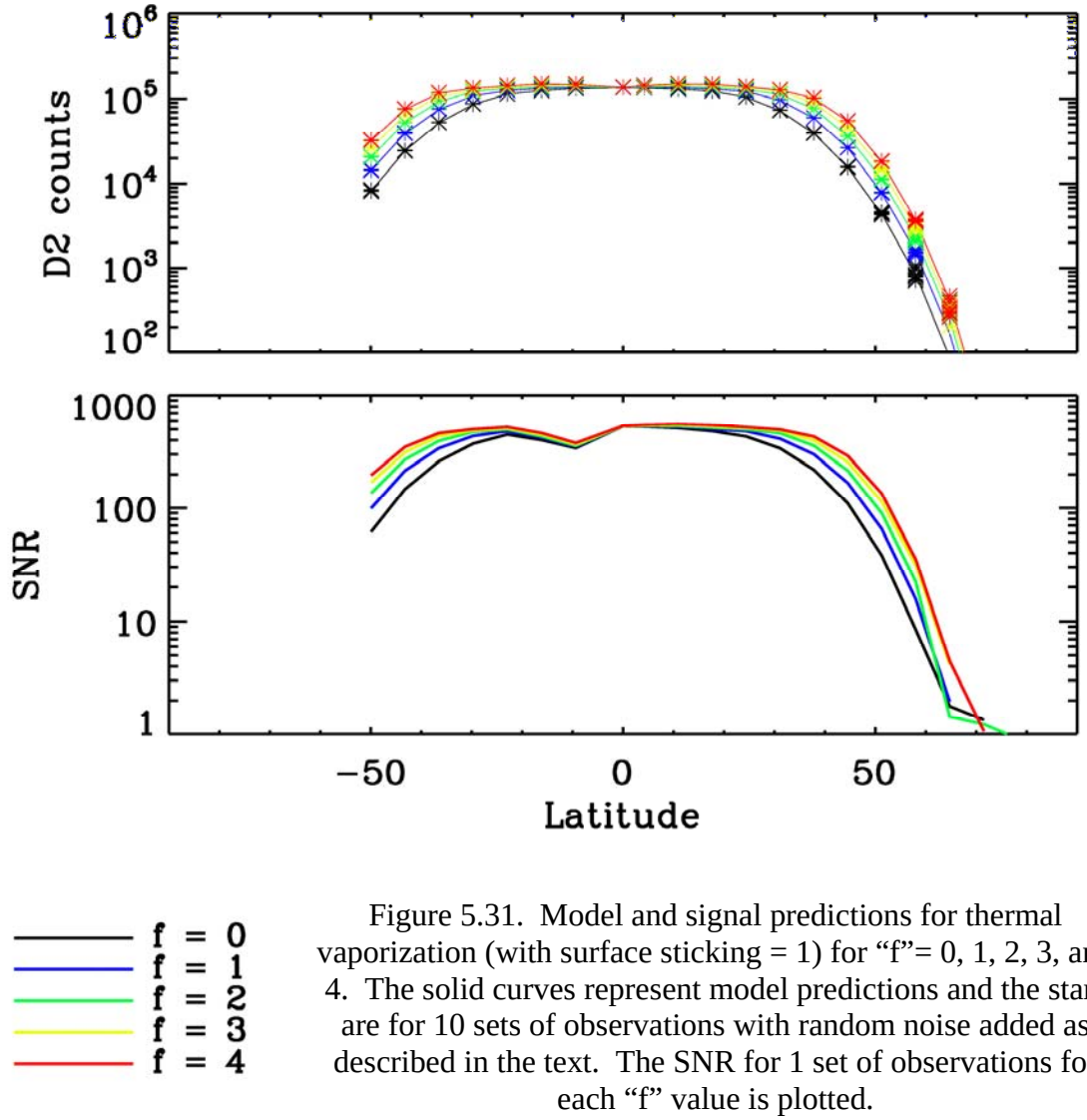

Figure 5.31. Model and signal predictions for thermal vaporization (with surface sticking = 1) for "f"= 0, 1, 2, 3, and 4. The solid curves represent model predictions and the stars are for 10 sets of observations with random noise added as described in the text. The SNR for 1 set of observations for each "f" value is plotted.

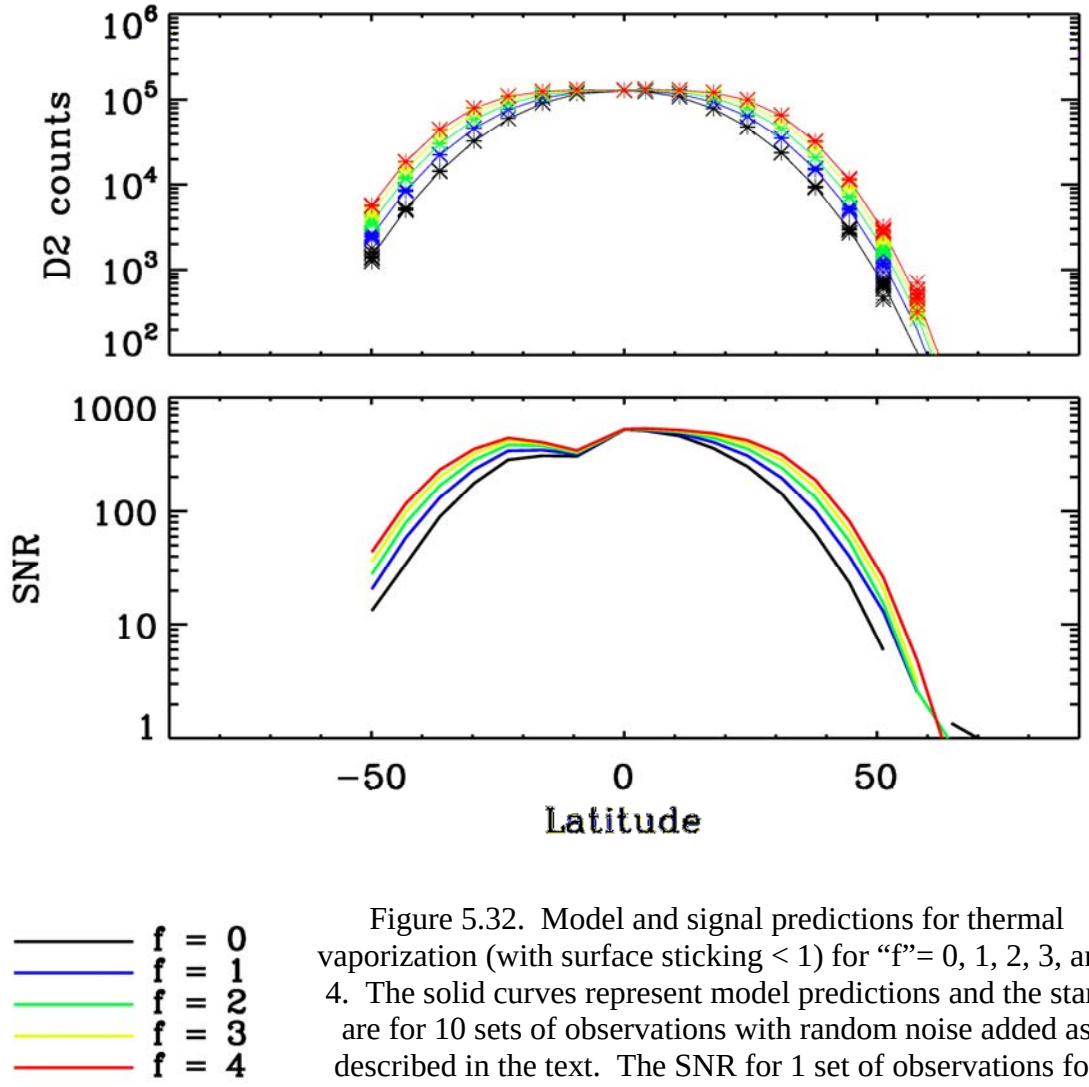

Figure 5.32. Model and signal predictions for thermal vaporization (with surface sticking < 1) for "f"= 0, 1, 2, 3, and 4. The solid curves represent model predictions and the stars are for 10 sets of observations with random noise added as described in the text. The SNR for 1 set of observations for each "f" value is plotted.

for a given source process, a cosine power law of the form

$$y = A\cos(\theta)^B + C \tag{5.9}$$

is used to fit to the data. Similar to the investigation of Section 5.5.3, the goal is to retrieve the "B" parameter for the 10 sets of data associated with each value of "f". Only data points with and SNR greater than 3 are used in the IDL curvefitting routine. Since the SNR drops to such low values at high latitudes for thermal vaporization, data points for this source process were only used for latitudes less than ~ 60°.

The results of the recovered "B" parameter are shown in Figure 5.33 and summarized in Table 5.4. Given the large SNR for photon stimulated desorption, the "B" term was clearly distinguishable within the standard deviation for all "f" values. For thermal vaporization, the case for "f" = 0 was clearly distinguishable from all other "f" value test cases. However, for "f" > 0, the "B" term was not distinguishable. This is due to the fact that the SNR drops to such low values at high latitudes and prevents using data points that cover the full range of latitudes. As can be seen in Figures 5.31 and 5.32, the model predictions for different "f" values are typically separated more for larger latitudes than for smaller latitudes. Since data at high latitudes were discarded due to low SNR values, the remainder of the data points at lower latitudes did not differ greatly from one another for different "f" values. Thus it is difficult to detect latitudinal variations in sodium surface concentration based on the detection of thermally vaporized sodium due to the steep decrease in signal with high latitudes. Alternatively, according to the predictions of this model,

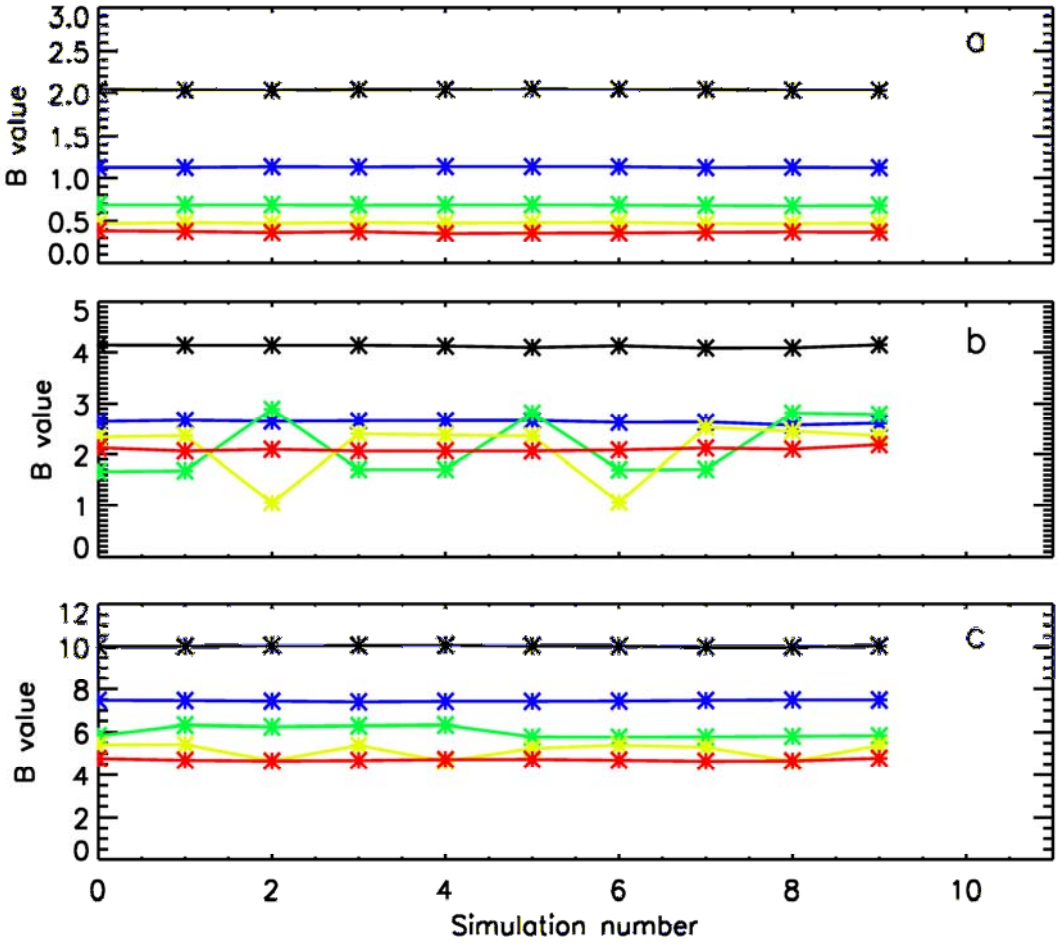

Figure 5.33. Plot of retrieved "f" values for each source process for 10 simulations. Panel (a) is for photon stimulated desorption, panel (b) is for thermal vaporization with surface sticking = 1, and panel (c) is for thermal vaporization with sticking < 1.

F value	Psd Mean Standard deviation	Tv (sticking = 1) Mean Standard deviation	Tv (sticking < 1) Mean Standard deviation
0	2.04 0.0065	4.12 0.024	10.0 0.025
1	1.13 0.0053	2.64 0.030	7.44 0.031
2	0.685 0.0039	2.15 0.586	6.00 0.255
3	0.475 0.0058	2.13 0.570	5.15 0.352
4	0.367 0.0098	2.10 0.039	4.70 0.049

Table 5.4. Summary of the mean "B" values with standard deviation for each of the source processes. The variations in surface density concentration are easily distinguishable within 1 σ uncertainty for photon stimulated desorption. This is because the signal remains relatively large at high latitudes. For both cases of thermal vaporization, the latitudinal variations in surface density concentration are difficult to distinguish. This is because the signal for thermal vaporization decreases to non-detectable levels for latitudes > 50°. Since it is at high latitudes that the curves from variations in surface density concentrations have maximum divergence, data points from high latitudes are essential for distinguishing between surface density variations where the density increases with latitude.

latitudinal variations in sodium surface concentration were easily distinguishable for an exosphere dominated by photon stimulated desorption. The differences in the mean of the “B” terms for different “f” values are outside the standard deviation in the spread of the “B” term.

5.5.6 Summary of test cases

Table 5.5 summarizes the observations required to perform the test case experiments. Opportunities, spatial sampling, and seasonal sampling are given. Each of the test cases is unique in the information it provides concerning the physics of Mercury’s exosphere. However, the observations required for the test cases may all be conducted by the systematic observation strategy proposed in section 5.3. The test cases chosen gives an overview of the capabilities of the instrument to make measurements over the entire dayside along the equatorial region, observations in the north-south direction, and observations that cover a large range of altitudes extending outward from the dayside surface.

5.6 Optimum altitudes for observations

For a given source process the density of the exosphere decreases with altitude with a corresponding decrease in radiance. Since observations at increasing altitudes are generally associated with increasing off-axis angles, the off-axis light entering the instrument typically decreases as observations are performed at increasing heights above the limb of the planet. The SNR of the signal decreases with decreasing radiance but increases with decreasing off-axis light; thus these 2 contributions to the

Observational experiment	**Opportunities**	**Spatial sampling**	**Seasonal sampling**
Discrimination between 3 major source processes	Throughout the entire Mercury year	North-south or equatorial observations at low altitudes for the sake of low scale height processes	Only small variation in solar zenith angle dependence throughout the year
Latitudinal variations of surface density concentration	Planetary true anomalies from 0° to 180°. 20 to 30 minutes each	North-south scans from 50 to 100 km	Best opportunity is for planetary true anomaly ~ 34°
Determination of temperature of meteoritic vaporization component	Throughout the entire Mercury year	Equatorial high altitude observations, especially above the terminator regions	Best opportunity at 64° planetary true anomaly, but possible all year

Table 5.5. Description of observations needed to achieve the experimental goals of the test cases chosen. Equatorial observations covering the dayside surface, north-south observations, and altitude variable observations have been tested and shown to meet the requirements to characterize physical processes in the exosphere.

SNR vary inversely with variations in altitude of limb observations. This implies that there may be locations above the limb where the SNR is optimized. This phenomenon is investigated for observations that range in altitude from the surface to 1000 km above the sub-solar region for planetary true anomalies of 6° and 64°. The exosphere source rate is isotropic and decreases exponentially with height. Surface dependent processes, i.e., surface sticking, surface temperature effects on source rates, etc., are excluded in order to make these simulations model independent. Several source rates that result in radiances at 0 km altitude ranging from 100 to 10,000 kilo-Rayliegh are tested. Furthermore, 6 different temperatures of the source rate are tested that result in 6 different scale heights. Radiation pressure is present since this effect applies to Mercury's sodium exosphere independent of model processes.

The results for observations with both the surface and atmospheric slits for a planetary true anomaly of 6° are shown in Figure 5.34 where contours of SNR are plotted as a function of radiance at 0 km altitude and height above the limb. The typical maximum tangentially integrated column abundances corresponding to a radiance of 10,000 kilo-Rayleighs are $> 10^{13}$ Na/cm^2, implying that these abundances fall in the non-linear regime of the curve of growth. Results for the surface slit show that for a given surface radiance above the sub-solar region, the SNR is maximum at heights of ~ 100 km and 200 km for scale heights of 50 km and 300 km, respectively. This is because the off-axis light decreases more rapidly for increasing heights above the surface up to 100 – 200 km. Above that, the radiance decreases more rapidly than the off-axis light and therefore the SNR begins to decrease with height. Low scale

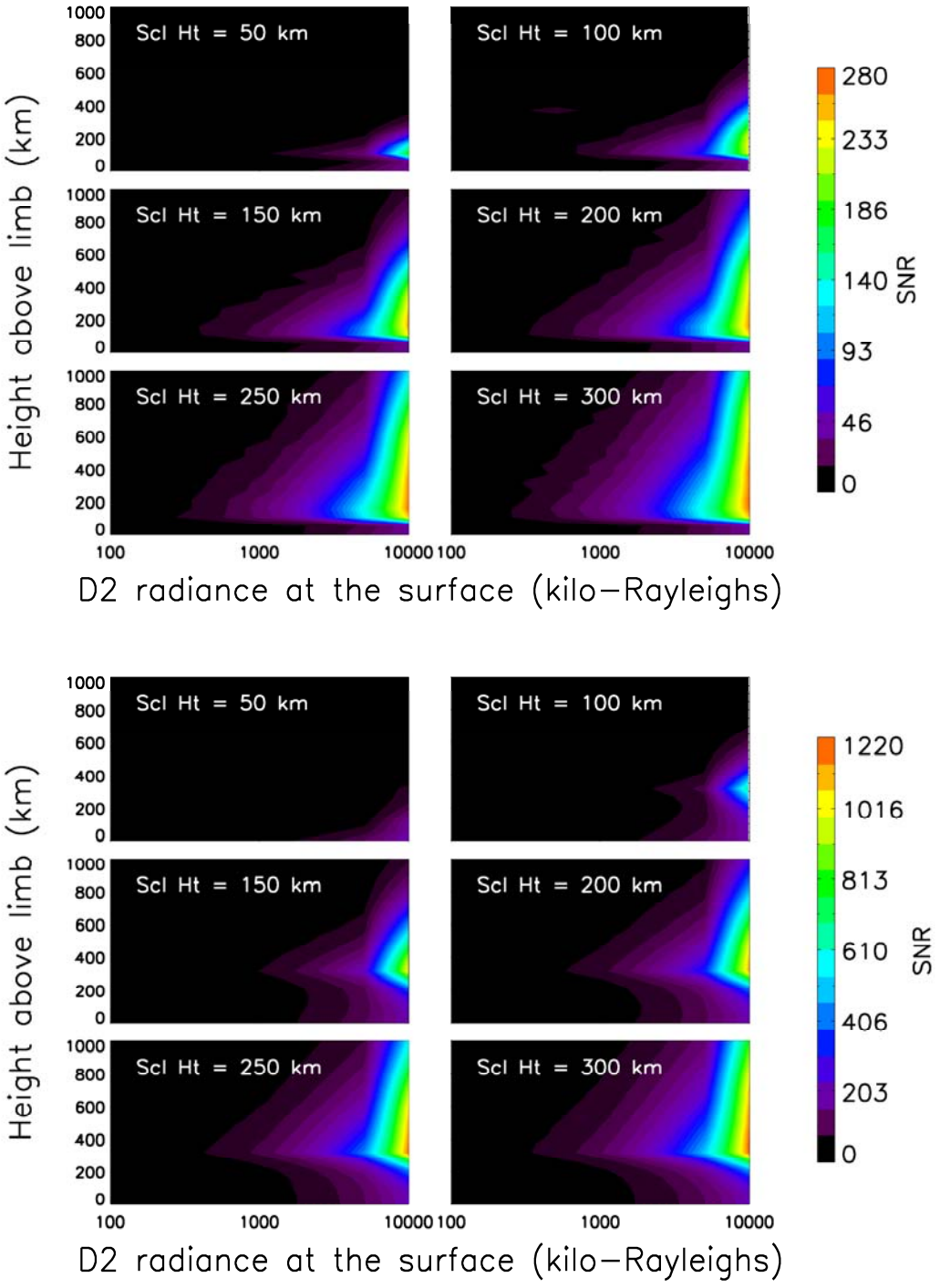

Figure 5.34. Contours of SNR for both the surface slit (upper panel) and atmospheric slit (lower panel) for a planetary true anomaly of 6°.

height simulations do not achieve as high of an SNR as large scale height processes for a specific radiance since the abundance for lower scale heights is closer to the surface and observations at low altitudes contain more off-axis light from the planet's surface. For the atmospheric slit, a similar result is obtained but with the maximum SNR between 300km and 400 km. The only exception is for the 50 km scale height case which has a maximum SNR near the surface. The reason for the peak SNR being at typically being at higher altitudes for the atmospheric slit than for the surface slit is because of the more rounded roll-off of the off-axis light as described in Section 2.11.

At altitudes below the peak SNR level the SNR decreases to much lower values and then begins to either remain constant or increase slightly with decreasing altitude. This is because close to the surface the off-axis light begins to reach its maximum value and changes very little while the exosphere continues to increase with decreasing altitude. Thus the SNR becomes insensitive to variations in height for low altitudes.

For both slits and for the larger scale heights and radiances the SNR shows little dependence on altitude once above the altitude of maximum SNR. This is because the abundances are optically thick and are therefore in the non-linear regime of the curve-of-growth. A decrease in the density with height results in a smaller associated decrease in radiance than for cases where the column abundance is optically thin and is on the linear portion of the curve-of-growth.

Figure 5.35 shows contours of tangential column abundance plotted against radiance at 0 km altitude and scale height. Also on each sub-plot is the $\tau = 1$ curve

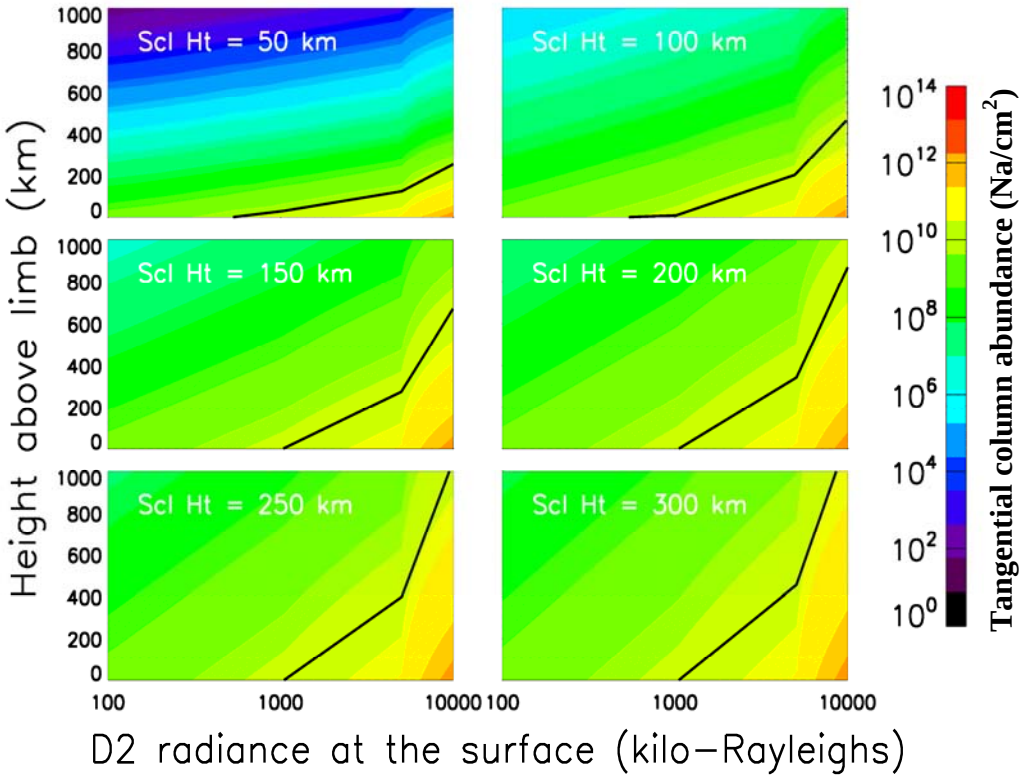

Figure 5.35. Contours of tangentially integrated column abundance above the sub-solar region at a planetary true anomaly of 6°. The black curves denote $\tau = 1$ where the abundance below the curve is optically thick.

below which the abundances are optically thick. As scale heights increase, the column abundance remains optically thick over a larger range of altitude, which is consistent with the conclusion based on the results presented in Figure 5.34. This can be explained as follows. The scale height is increased by increasing the characteristic temperature of the source, leading to 2 different phenomena. First, as the temperature increases, the exosphere spreads out in height requiring larger column abundances to achieve a specified radiance. Second, as temperature increases, the non-linear portion of the curve-of-growth moves to larger column abundances. The first phenomenon results in shifting the $\tau = 1$ curve to larger heights for increasing scale heights. The second phenomenon results in shifting the $\tau = 1$ curve to lower heights for increasing scale height. For a planetary true anomaly of 6°, the g-value is low enough that the first phenomenon dominates and the tau = 1 curve shifts to higher altitudes for increasing scale heights.

Results are similar for a planetary true anomaly 64° (Figure 5.36) for both the atmospheric and surface slits with the exception that the exosphere is predominantly optically thin. This causes the radiance to decrease linearly with column abundance and thus does not produce the nearly constant SNR with increasing height as was the case for a true anomaly of 6°. Figure 5.37 shows the contour of the tangential column abundance as a function of radiance at 0 km altitude verses height above the limb. A curve denoting an optical depth of 1 is shown where the exosphere is optically thick below the curve. The larger temperatures responsible for the larger scale heights shift the linear portion of the curve of growth to higher column abundances. Unlike the case for a planetary true anomaly of 6°, this phenomenon dominates over the fact that

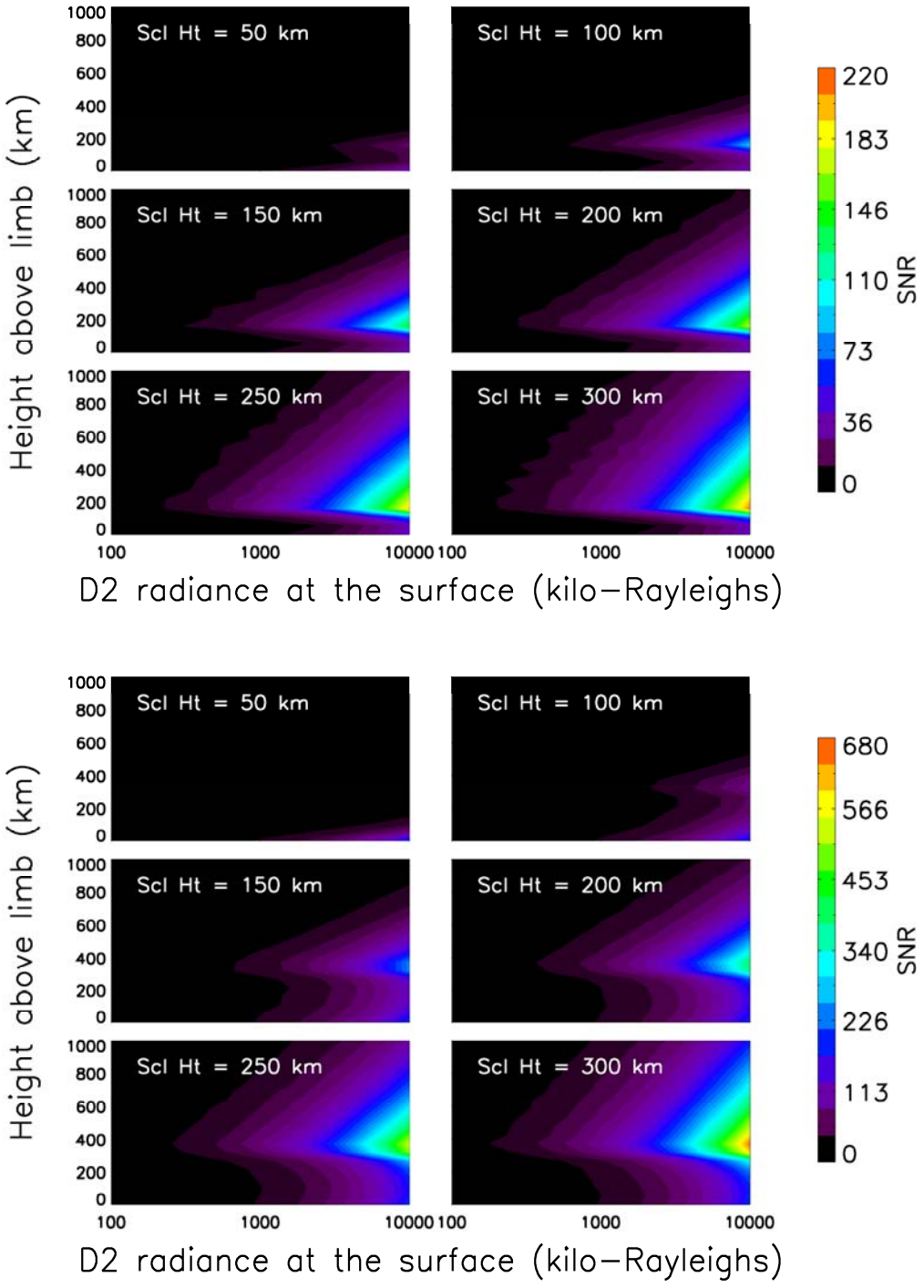

Figure 5.36. Contours of SNR for both the surface slit (upper panel) and atmospheric slit (lower panel) for a planetary true anomaly of 64°.

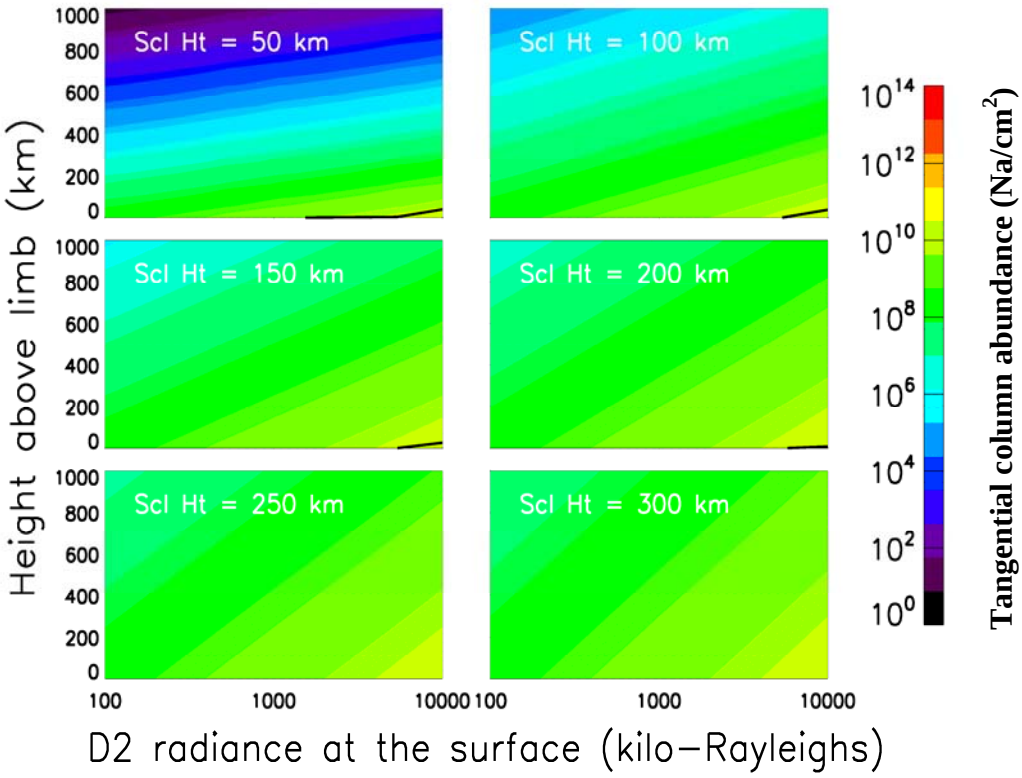

Figure 5.37. Contours of tangentially integrated column abundance above the sub-solar region at a planetary true anomaly of 64°. The black curves denote $\tau = 1$ where the abundance below the curve is optically thick.

larger radiances require larger column abundances and tend to approach an optically thick atmosphere. This is because the g-value is ~ 7 times larger at a true anomaly of 64° than at 6° and thus a smaller abundance is needed to achieve the same radiance. Therefore the $\tau = 1$ curve decreases for larger scale heights.

5.7 Error analysis

One source of possible error is that the absolute tangential column abundances may be different from those used to make signal and uncertainty predictions. Smaller column abundances would generally imply lower signals and consequently larger uncertainties. Thus the ability of MASCS to discriminate between different exospheric processes as demonstrated in the preceding test cases may be compromised by much larger uncertainties. The column abundances in this investigation were predicted from the atmospheric model developed by Killen (unpublished) and could vary if another model were employed.

Another source of error is in the constant gravity assumption of this model. As shown in Chapter 4, the assumption of constant gravity is ~ 30% in error at 500 km above the planetary surface. However, it is possible that the velocity distributions of some of the processes may not be purely Maxwellian. If they lack a high energy tail, as proposed by Madey et al. (1998) for photon stimulated desorption, then a rapid fall-off of atoms at large altitudes may counteract the error associated with the constant gravity assumption.

Once in orbit, spacecraft pointing uncertainties may also affect the ability of MASCS to retrieve parameters for exospheric processes. The calculated 1 σ

spacecraft pointing control and pointing knowledge are 500 μrad and 250 μrad, respectively (Santo, et. al., 2001). This does not account for the effects of uncertainties in spacecraft orbital position. However, using the published pointing knowledge as a guide, an observation 15000 km from the limb would result in a 1-σ uncertainty of 3.75 km, which is well below the
minimum expected scale height for sodium. A larger error in tangent height arises from not considering the projected size of the instrument field of view above the tangent point for an observation. For an observation 15,000 km from the sub-solar limb, the 1° field of view along the length of the slit amounts to a 262 km projected field of view. This is close to the maximum expected scale height of sodium. One possible means of circumventing this problem is to use the surface slit for long range observations above the sub-solar region. For the 0.05° field of view, a 15,000 km observation would give a projected field of view of 13 km. However, care must be maintained since the use of the surface slit reduces instrument sensitivity by a factor of 20. Long range observations above the terminator have the advantage that the slit is oriented with the narrow (0.04°) perpendicular to a radial vector extending outward from the planet. Recall that the tests cases of section 5.5.3 utilized the surface slit for all but observations at a planetary true anomaly of 180°. This is because the observations were long range and had to scan across the sub-solar region.

5.8 Summary

To this date Mercury's exosphere has been observed with ground-based telescopes and by Mariner 10. Ground-based observations have resulted in the discovery of sodium (Potter and Morgan, 1985), potassium (Potter and Morgan, 1986), and calcium (Bida, et. al., 2000). Limitations to ground-based observations are due to the small angular size of Mercury from the earth, the proximity of Mercury to the Sun, and the earth's atmosphere. Even with adaptive optics, ground based observations typically achieve 0.5" to 1.6" spatial resolution (Killen, et. al., 2005a; Leblanc, et. al., 2006) with the disk of Mercury on the order of 5" to 6", which implies spatial resolutions of ~ 400 km at best. Furthermore, if Mercury is to be observed with the Sun below the horizon, observations are limited to ~ 1 hour or less and also require that observations be made through multiple airmasses. Mariner 10 did not go into orbit but made 3 flybys of Mercury, and instruments on board were not designed to measure sodium.

This chapter has shown that opportunities for observations of the day-side exosphere are greater for planetary true anomalies from 0° to 180° and opportunities for observations of the night-side exosphere are greater for planetary true anomalies from 180° to 360°. Within these constraints, a series of equatorial radial scans that map the dayside surface with a surface resolution of 20° and for altitudes from 100 km to greater than 1000 km year within a reasonable time within an orbit may be conducted throughout the Mercury year. The opportunities for north-south observations have been shown to be much less than for equatorial observations. A method for obtaining north-south observations has been proposed with coverage from

low southern latitudes up to high northern latitudes over an altitude range from 50 km to 100 km for planetary true anomalies from 0° to 180°. Observations at higher altitudes are possible, but time does not permit both high altitude and low altitude observations. The low altitude observations for north-south observations have been opted for since low altitude observations, i.e., 50 km, equatorial observations inherently have lower SNR values due to small off-axis angles and consequently larger solar continuum background.

The detection limits for equatorial observations show a peak around the sub-solar point and decrease by a factor of ~ 5 for terminator observations. Peak required D_1 + D_2 radiance for SNR's of 10 and 20 are ~ 50 and 100 KRay for the surface slit and ~ 400 and 800 KRay for the atmospheric slit. The detection limit as a function of altitude for SNR's of 10 and 20 are typically less than 100 KRay for the surface slit for altitudes above 100 km and less than 100 KRay for the atmospheric slit for altitudes greater than ~ 250 km. The detection limits for north-south observations are generally lower than for the equatorial observations with the exception of those for a planetary true anomaly of 6°. This is because the observational geometry at this true anomaly is such that the off-axis angle is much smaller than for the other planetary true anomalies and leads to larger off-axis light contributions to the total count rate.

It has been shown that the temperature for meteoritic vaporization modeled at 3000 K may be determined to within a range of 154 K and 380 K for planetary true anomalies of 64° and 180°, respectively. The abundance of sodium from meteoritic vaporization was increased by 1 order of magnitude from 60° to 180°; otherwise the emissions from meteoritic vaporization were not detectable at 180°. The signal was

still noisier at 180° due to a decrease in the g-value of 16 from a true anomaly of 64°. It was shown that the best opportunity for isolating emissions arising from atoms ejected by meteoritic vaporization from the other source processes is to observe at high altitudes, with optimum observations being above the terminator. This is due to meteoritic vaporization being modeled as an isotropic process so that the column abundance does not vary by as much from sub-solar point to terminator as it does for the other source processes.

For a constant surface concentration of sodium, the 3 major source processes (photon stimulated desorption, meteoritic vaporization, and thermal vaporization) were compared in order to determine how well solar zenith angle dependencies could be distinguished given the proposed observation strategies as well as predicted signal and SNR values. Thermal vaporization was modeled with surface sticking = 1 for the entire surface as well as modeled with a temperature dependent sticking coefficient < 1. The sticking coefficient is minimal at the sub-solar point where surface temperatures are highest and maximum near the terminator where temperatures are lowest. A cosine power law was fit to the predicted signal for multiple simulations at an altitude of 100 km. The determination of how distinguishable the processes were was based on comparing the mean and standard deviation of the exponent in the power law. Photon stimulated desorption and thermal vaporization were distinguishable to greater than 1 standard deviation of the power (B) term in the cosine power law; although thermal vaporization with temperature dependent surface sticking < 1 was difficult to parameterize for a planetary true anomaly of 180°. Since meteoritic vaporization was modeled as a background source and had a much lower

SNR, it was more difficult to distinguish the “B” term associated with it from the same term from the other processes. Both the atmospheric and surface slits were utilized, with the surface slit being used for planetary true anomalies of 6°, 64°, and 97° and the atmospheric slit used for a planetary true anomaly of 180°. The atmospheric slit was used at 180° in order to give larger signal and SNR values.

The best opportunity for making north-south observations that follow along the sub-solar meridian are for a planetary true anomaly of 34°. However, north-south observations are possible for planetary true anomalies from 0° to 180° but do not follow along the sub-solar meridian (see Figure 5.16). Latitudinal variations of sodium surface concentration are difficult to distinguish for thermal vaporization being the dominant source process. This is due to the fact that thermal vaporization is strongly dependent on surface temperature. At high latitudes, the surface temperature is too low to give appreciable signal from thermal vaporization. However, it is at high latitudes where differences in sodium surface concentration are most prevalent in model predicted column abundances. Therefore measurements at high latitudes are needed to distinguish between latitudinal surface concentrations; making it difficult if thermal vaporization is the dominant process. Alternatively, latitudinal variations are more easily distinguished if photon stimulated desorption is the dominant source process since the signal and SNR levels remain relatively large over a greater range of latitudes than for thermal vaporization.

Both the atmospheric and surface slits must be utilized depending on the type of observation as well as the time during the Mercury year. The surface slit may be used to reduce off-axis light when the signal levels are large enough to compensate for the

factor of 20 reduction in sensitivity. Alternatively, the atmospheric slit should be used when off-axis angles are large enough that off-axis light does not compromise a reasonable SNR.

The investigations presented in this chapter have led to systematic observational strategies, the determination of detection limits for the sodium D lines, and the characterization of the ability of the instrument to distinguish between variations in exospheric source processes. The wealth of data that will be obtained by MASCS through the systematic mapping of the exosphere both spatially and temporally will provide a uniform data set that will help to identify processes that maintain the exosphere.

Chapter 6

Lunar Flyby

6.1 Introduction

MESSENGER flew by the Earth-moon system with a closest approach on August 2, 2005 after a 1 year parking orbit around the Earth. The flyby marked the end of the parking orbit and the beginning of MESSENGER's trajectory towards Mercury. During the flyby, multiple instruments on MESSENGER had the opportunity to make measurements of the moon. Both the UVVS and VIRS channels of MASCS were used to make lunar surface measurements over the full disk as well as observations focused on Orientale. Furthermore, the UVVS was used to make limb scans of the lunar exosphere with the goal of searching for lunar hydrogen and sodium. This chapter describes the geometry of the observations that were made, the data reduction, the analysis of the surface data in terms of the radiance values, and the analysis of the sodium limb scans with a comparison to predicted signal-to-noise levels and other data sets.

6.2 Observations

6.2.1 Full disk observations

The spacecraft made a series of raster scans across the disk of the moon for the FUV, MUV, and VIS channels when the Moon was ~ 0.2° in diameter. Figure 6.1 (upper panel) shows the geometry associated with the raster scan. The observations extended over a 0.5° X 0.5° box with a step size between rows of ~0.015°. The spacecraft motion along the horizontal direction was 0.0076° per second. The integration time for the FUV and MUV channels was 0.012 seconds and the integration time for the VIS channel was 0.006 seconds. Using the surface slit, this resulted in an instantaneous projected field of view for each grating step of ~ 0.04° X 0.05°, as shown by the small box in the lower left hand corner of Figure 6.1 (upper panel). The FUV/MUV grating scans cover 325 grating steps, while the VIS channel grating scans cover 590 grating steps. The combination of the time it takes to complete a grating scan along with the spacecraft motion along a row causes the projected field of view to be elongated in the horizontal direction, as shown by the larger box in the lower left corner of Figure 6.1.

The spacecraft then made a series of raster scans targeting the Orientale impact basin for the FUV, MUV, and VIS channels when the Moon was ~ 0.22° in diameter. Figure 6.1 (lower panel) shows the geometry associated with the raster scan. The observations extended over a 0.08° X 0.08° box with a step size between rows of ~0.0077°. The spacecraft motion along the horizontal direction was ~0.006° per second. The integration time for the FUV and MUV channels was 0.012 seconds and the integration time for the VIS channel was 0.006 seconds. Since the scan rate and

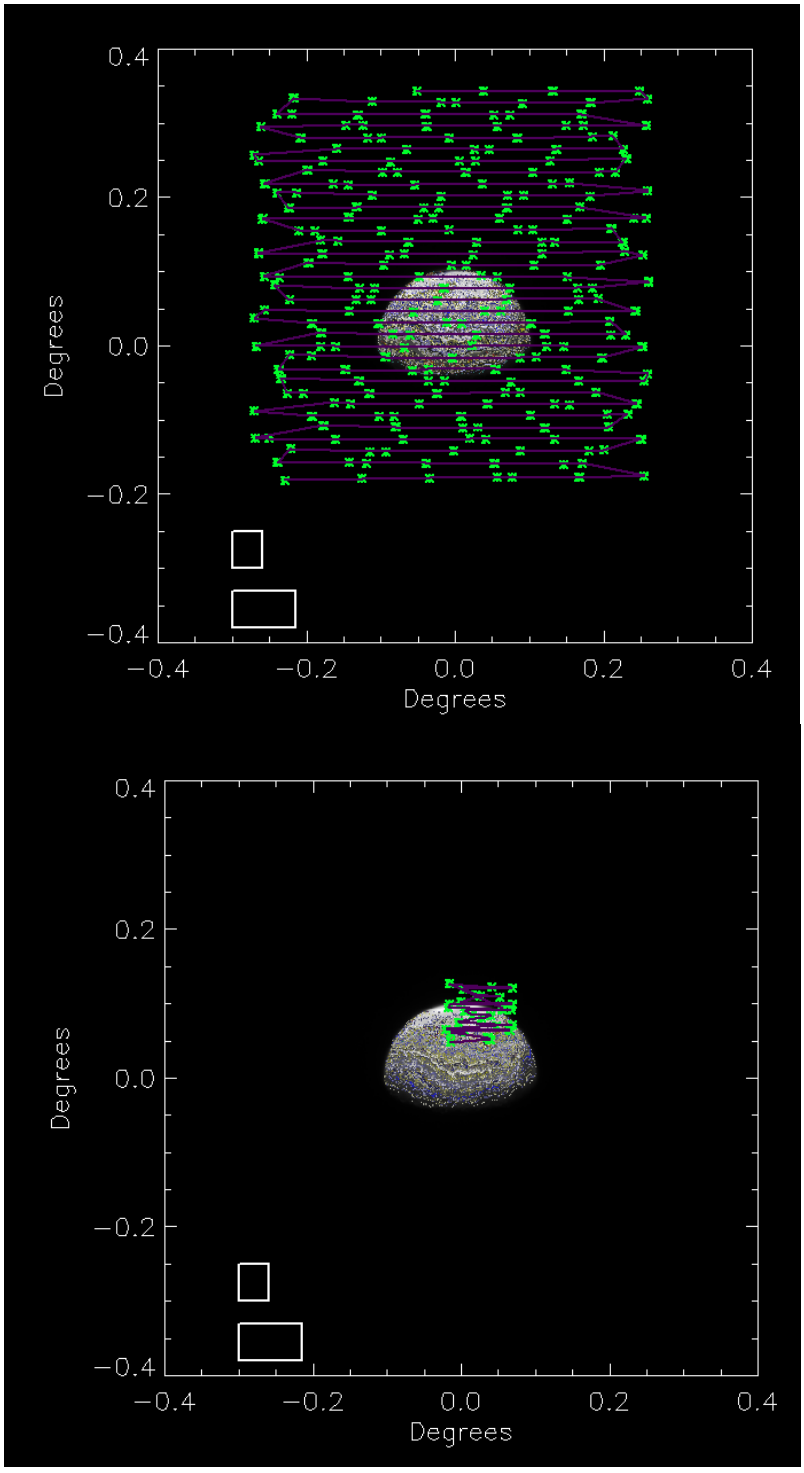

Figure 6.1. Geometry of lunar surface observations. Each star represents the center of the field of view footprint on the surface. The upper panel is for the raster scan that covered the entire lunar disk whereas the lower panel is for the observations that targeted Orientale.

integration times are similar to those for the full disk observation, the projected field of view for both a single grating step and a full grating scan are similar as shown in the bottom left corner of Figure 6.1 (lower panel).

6.2.2 Limb scans

The FUV and VIS channels where used with the slit in atmospheric mode to make off-limb scans of the lunar exosphere. Figure 6.2 shows the geometry associated with the limb observations. The observations extended over 5° in the horizontal direction and 5° in the vertical direction with the observations centered on the moon. The spacecraft scan rate along each limb observation was 0.0085° per second. The integration time for the FUV and VIS channels was 0.25 seconds. Using the atmospheric slit, this resulted in an instantaneous projected field of view for each grating step of ~ 0.04° X 1.0°, as shown by the white box in the lower left hand corner of Figure 6.2. The FUV and VIS grating scans cover 16 grating steps each and were interleaved between the two channels. The projected field of view over all 16 grating steps was 0.074° X 1.0° for the horizontal limb observations and 0.04° X 1.034° for the vertical limb observations.

6.3 Data reduction

6.3.1 Extra grating step removal

There were additional data values in some of the data packets associated with the surface observations that were random in number and location within the packet. All 3 channels had additional data values with the VIS channel having the largest number

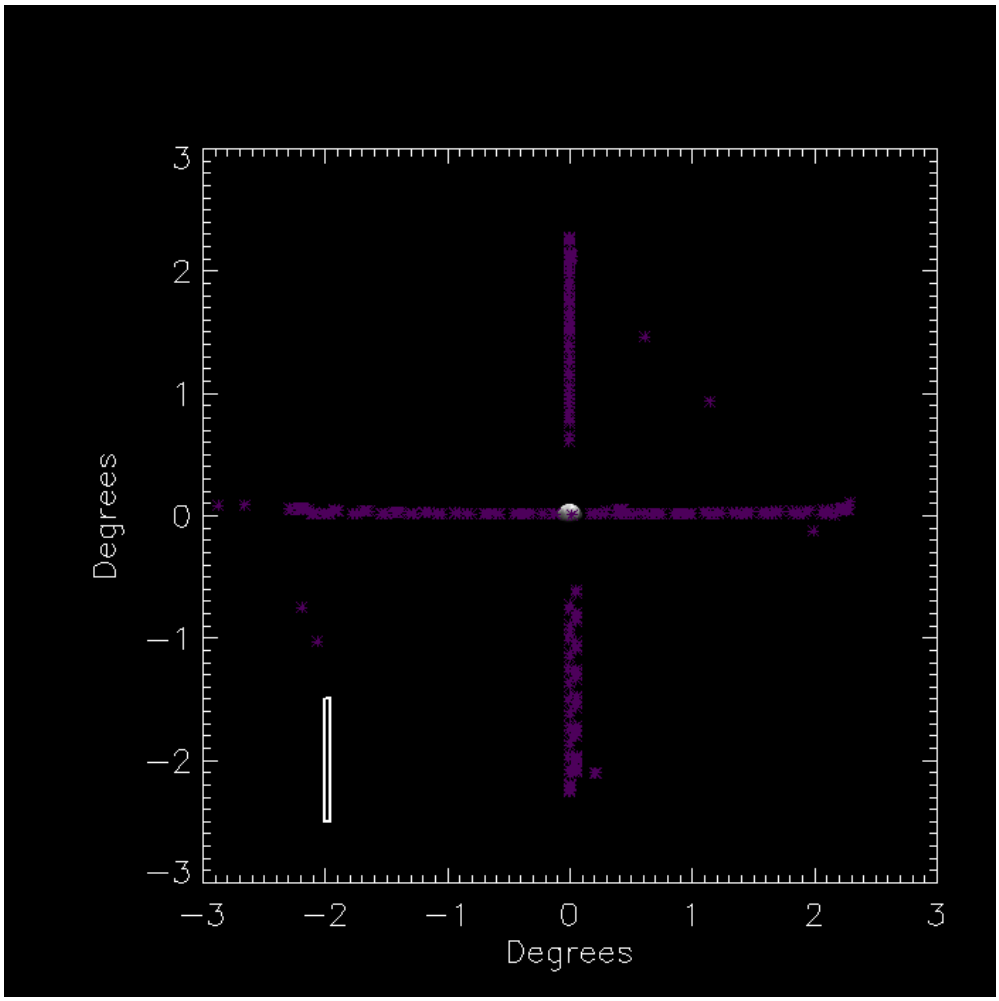

Figure 6.2. Geometry of lunar limb observations. The Sun is towards the top so that the horizontal observation are mostly above the terminator and the vertical observations are closely along the Moon-Sun line. The upper vertical observation is above the sub-solar point. The projected size of the atmospheric slit is shown in the bottom left corner.

of extra data points. Close examination showed that the grating drive seemed to pause at some random step position and data was taken multiple times. Figure 6.3 shows an example of the calcium K lines from the solar continuum reflected from the lunar surface. The data consists of grating scans 164 and 197 from the VIS channel for the full disk observations. Within the packet that contained grating scan 197, 19 additional data points were acquired, causing the spectra to be shifted with respect to grating scan 164, which came from a packet with no additional data points.

Figure 6.1 shows that the projected field of view coincided with the lunar surface for only a small fraction of the total number of grating scans. The grating scans that contained lunar surface data and that also came from packets that contained extra data points were scrutinized to determine which data points to disregard. This was done by registering the spectra from each grating scan with spectral features such as the Ca K lines as well as other prominent solar features seen in reflection from the lunar surface.

6.3.2 Dark count and spectrometer scattered light removal

Dark count rates were determined as a function of temperature during ground calibration (described in Chapter 2). However, since launch, stellar calibrations have been used to determined dark count rates that do not agree with pre-launch dark count rates. It has been found that for grating scans that cover spectral regions outside the spectral sensitivity of the channel, the dark counts may be determined by averaging the count rates in these regions. In addition to the dark counts, there are also counts arising from spectrometer stray light. Subtraction of the average of the combined

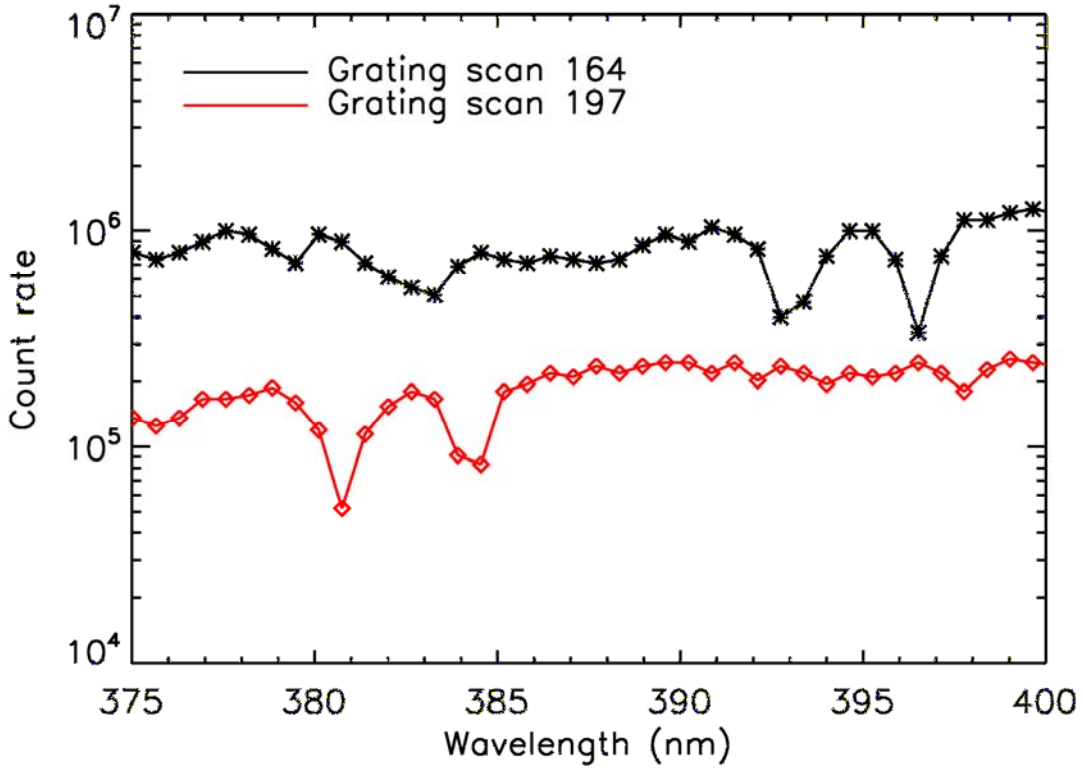

Figure 6.3. Example of 2 different grating scans taken during the lunar surface observations that demonstrate the effect of extra data points. The two prominent dips in each spectra are the Ca K lines. The spectral location for gratin scan 164 is correct, but the location of the Ca K lines for grating scan 197 need to be shifted by 19 grating steps to be in the correct spectral position. This was caused by that packet containing extra data points that then caused the spectra to be shifted.

counts in the non-sensitive spectral regime has proven to be a reasonable approach to dealing with both dark counts and spectrometer stray light counts. This method has been implemented for both the MUV and VIS channels. The FUV channel contained insufficient count rates to justify the use of this method.

6.3.3 Integration time and non-linearity correction

The raw data counts from each channel were divided by the respective integration time. The non-linearity correction was applied to the data for each channel as described in Chapter 2. The non-linearity correction for the VIS channel resulted in a 95 % increase for the peak count rates; however, negligible change resulted in the correction for the FUV and MUV channels.

6.3.4 Pointing correction

Since the lunar flyby in 2005, the boresight of the instrument with respect to spacecraft axes for both the surface and atmospheric slits have been determined to within 0.02° by means of stellar calibrations. The location of the moon in the spacecraft body frame was returned every second during the lunar observations. Knowledge of the location of the moon in the spacecraft frame in conjunction with instrument boresight knowledge allowed for the calculation of the location of the moon with respect to the instrument boresight. This correction has been applied to all lunar pointing data.

6.3.5 Removal of off-axis light

The off-axis light that enters the instrument is described in Chapters 2 and 4. The techniques described in Chapter 4 for dealing with off-axis light were applied to the lunar sodium limb scans with the exception that the example from Chapter 4 deals with 18 grating steps while the lunar sodium limb scans consist of 16 grating steps.

6.3.6 Removal of grating scans with noise spikes

Some of the grating scans had noise spikes that were much greater than typical detector dark counts and needed to be eliminated. Figure 6.4 shows an example from a grating scan from the lunar limb observations. An IDL routine was written that compared the maximum raw count from each grating scan to the median value of the same grating scan. All grating scans that had a maximum raw count greater than 2X the median value for that particular grating scan were eliminated.

6.3.7 Disk integrated radiance and reflectance

The lunar surface scans were used to determine the disk integrated radiance and reflectance. Observations were used where the center of the boresight was within 0.08° of the edge of the lunar disk. This insured that the projected field of view was completely on the surface of the moon. In order to improve signal-to-noise, the data were binnned into 4 nm bandwidths over the grating scan range from ~ 260 nm to ~ 580 nm.

As the spacecraft slewed, the projected field of view moved across the surface. At the same time, the grating was scanning, producing data that was coupled both

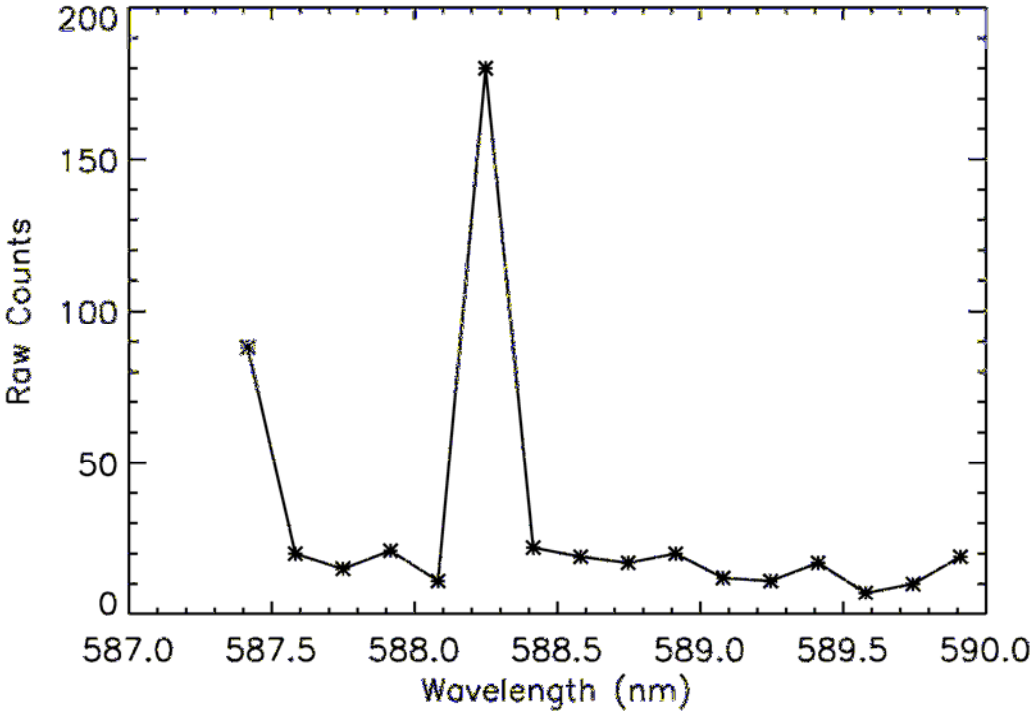

Figure 6.4. A grating scan from the lunar limb observations that contained a large noise spike. These grating scans were eliminated by an IDL routine discussed in the text.

spectrally and spatially. The binning of the data into 4 nm bandwidths consisted of summing 6 consecutive grating steps. With an integration time of 6 msecs and a grating step time of 4 msecs, a 4 nm bandwidth represented 60 msecs during which the spacecraft was slewing. With the spacecraft slew rate of 0.0076°/second, the spacecraft slewed 4.6 mili-degrees. Since the field of view of the surface slit is 0.04°, this represented a movement of only 1% of the projected field of view and is thus negligible. It should be mentioned binning over a larger bandwidth could lead to significant variations in the location of the projected field over view on the surface.

Figure 6.5 shows the disk integrated radiance and I/F reflectance. A detailed comparison to the VIRS data as well as to other datasets was mostly done by Holsclaw, (Ph.D. thesis, 2006) and the data of Figure 6.5 was provided for that analysis. The analysis is not repeated here.

6.3.8 Determination of background for limb observations

The background is considered to consist of 2 sources: reflected solar radiation from the surface of the moon that enters the instrument off-axis from the boresight and detector dark counts. The off-axis solar continuum has a spectral shape while the dark counts do not. Therefore, in order to set detection limits, the background is modeled in two regimes that depend on the value of the counts out in the wings compared to the mean detector dark counts for the temperatures associated with the lunar limb scans. The mean detector dark counts have been determined from other measurements to be ~ 10 counts/integration time/grating step, where the integration time is 0.25 seconds. Furthermore, the detector dark counts have been shown to be

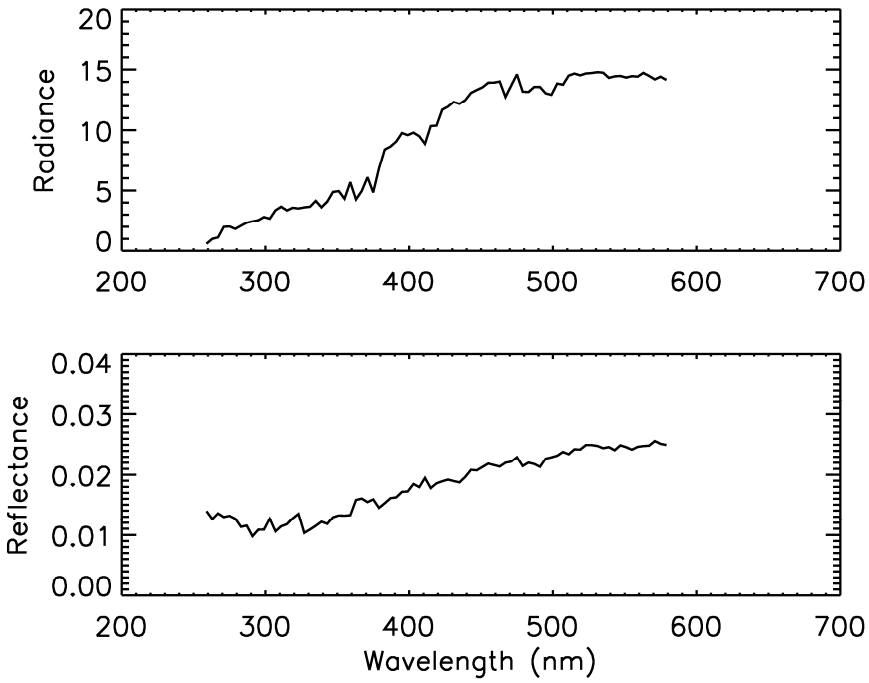

Figure 6.5. The lunar disk integrated radiance (top panel) and the lunar disk integrated reflectance (I/F) in the bottom panel measured by the UVVS during the full disk surface observations. An in-depth analysis of these results along with similar results from MASCS/VIRS is given in Holsclaw (Ph.D. thesis, 2006)

distributed according to a poisson distribution. Thus it is possible that in one regime the solar continuum off-axis light could be well above the detector dark counts; in which case the background consists of the solar continuum that is offset by the detector dark counts. The other regime consists of the solar continuum being less than the detector dark counts, in which case the solar continuum would be lost in the noise of the detector dark counts. These two regimes must be distinguished in order to characterize the shape of the background beneath the sodium D lines. If the background is dominated by the solar continuum off-axis light then the spectral region beneath the sodium D lines will consist of the solar continuum smoothed to the bandpass of the instrument, which contains spectral structure that includes the sodium fraunhofer lines. If the background is dominated by detector dark counts, then there is no spectral structure to the background beneath the sodium D lines.

The criteria adopted to distinguish between the two background regimes is to require the mean of the counts out in the wings to be larger than the square root of the detector dark counts times an SNR value added to the detector counts in order to be dominated by the solar continuum. Equation 6.1 shows this as

$$\overline{B} > D^{1/2} * SNR + D \qquad (6.1)$$

with $\overline{B}$ the mean of the background counts in the wings of a grating scan, D the detector dark counts, which is ~ 10 counts/0.25 seconds for temperatures associated with the lunar observations, and SNR is any value that is chosen as a detection limit.

Any $\overline{B}$ less than this will be considered as dominated by detector dark counts. An example of this is shown in figure 6.6.

6.4 Analysis of lunar limb observations

Figure 6.2 shows the geometry of the lunar limb observations with the projected size of the entrance slit at the limb of the moon. This section deals with the analysis of the data acquired from the horizontal limb observations where the slit moved perpendicular to the length. The data acquired in the other direction were examined and found to be of poorer quality than for the horizontal observations and are not presented here.

6.4.1 Comparison of lunar data off-axis light with the off-axis model

One use made of the lunar limb scans was to validate the software planning tool. This was achieved by making off-axis light predictions using the model and comparing to off-axis counts derived from the wings of the limb scan spectra. The off-axis light model described in Chapter 2 was used to predict the solar continuum contribution to the background count rate for the lunar limb scans. As was the case for the Mercury off-axis light predictions, the off-axis model produces a normalized response whose peak must be scaled to the value that would be measured if the instrument were pointed directly at the lunar surface. None of the measurements from the lunar limb scans were made while pointing directly at the surface. However, the lunar surface scans contained many spectra in the spectral vicinity of the sodium D lines while the instrument was pointed at the surface. Figure 6.7 shows a sample

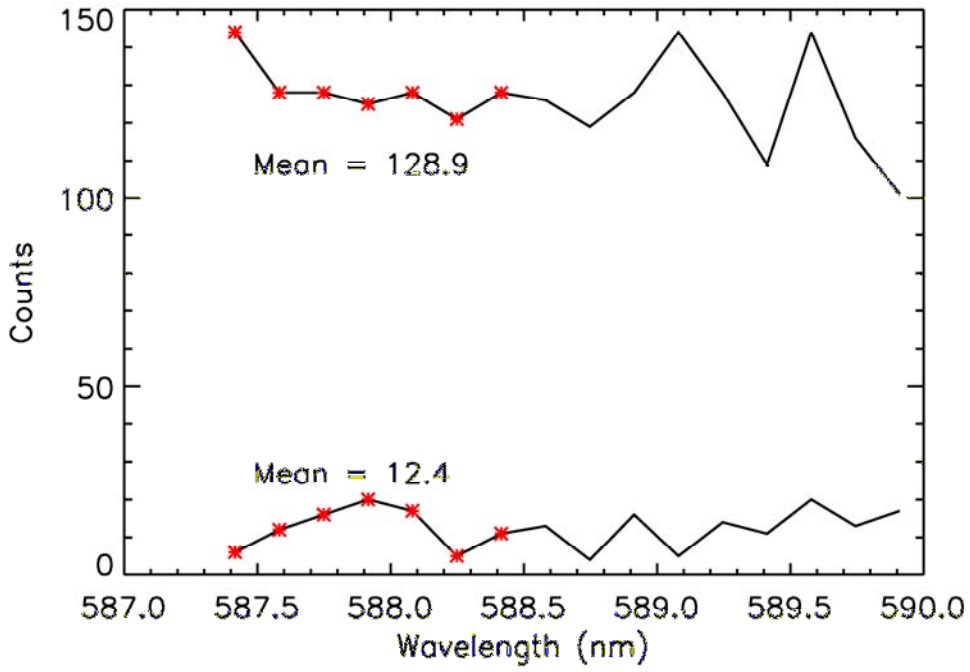

Figure 6.6. Spectra from 2 different grating scans showing the 2 regimes of background. The red stars represent the grating steps from which the mean of the background is computed. The upper spectra is well above the mean detector dark counts and thus falls in the solar continuum background regime. The mean of the lower spectra is less than the criteria established in Equation 6.1 and thus falls in the dark count regime.

solar continuum taken by MASCS using the surface slit pointed directly at the surface. This particular grating scan contained the largest count rate of all the lunar spectra taken. The peak surface scan was used to scale the off-axis curve.

In order to scale the peak of the off-axis response to the lunar radiance, the measured values from one of the larger count rate grating scans from the lunar surface scans were used. The counts from the surface scan was divided by the integration time, corrected for non-linearity, and then the mean taken in the spectral region that corresponds to the wings of the sodium D lines, i.e., 586 - 588 nm. The mean value was 323,017 counts/second, which was multiplied by 20 to convert from the surface slit (used for the surface observations) to the atmospheric slit (used for the limb scans). This resulted in a value of 6,460,340 counts/second; that was then divided by 10 since the lunar disk size was ~ 0.2° across and the length of the atmospheric slit is 1°, with roughly half of the lunar disk illuminated as seen from the spacecraft. This resulted in a value of 646,034 counts/second that were used for the peak value of the off-axis response.

The resulting off-axis model curve for observations made above the terminator is shown in Figure 6.8. Note that this is simply the “clean” off-axis model in the sense that no statistical fluctuations or dark counts have been added to the model. Also shown are the averages of counts from the spectral wings of the grating scans above the lunar terminator. Grating scans with mean count rates less than 3-σ of the detector dark counts were eliminated as a means of selecting only the real data that has a significant off-axis light component. After selection of these data points,

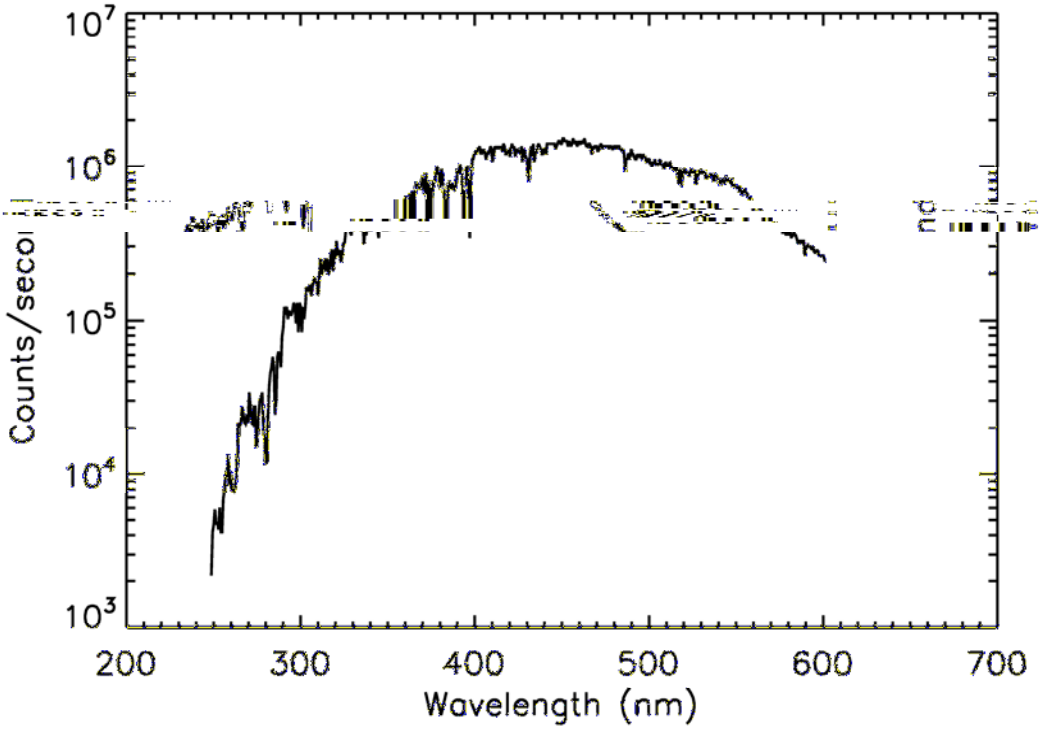

Figure 6.7. Spectrum obtained from the lunar surface observations using the surface slit. This is the grating scan with the peak measured counts. The integration time was 6 msecs and has been divided out to give counts per second. The count rate in the spectral vicinity of the sodium D lines was used to scale the off axis curve for the sodium limb observations.

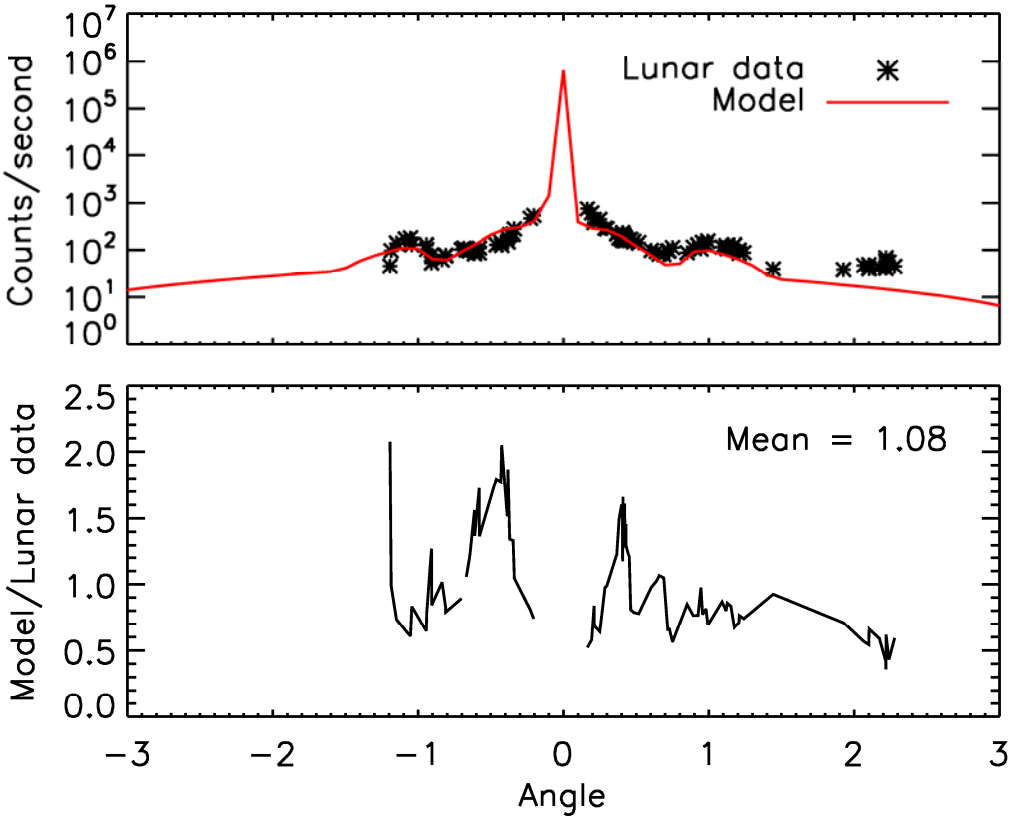

Figure 6.8. Comparison of the off-axis light model with actual data from the limb observations. With the exception of one large spike, the ratio in the lower panel is reasonably close to unity with a mean of 1.08.

detector dark counts were subtracted from the real counts in order to leave only the off-axis component to the background. The lower window in Figure 6.8 shows the ratio of the off-axis model to the lunar data. With the exception of one large spike, the ratio is close to unity with a mean of 1.08. Ideally the mean of the ratio would be 1, so a mean of 1.08 is considered an acceptable validation of the off-axis model to the real data.

6.4.2 Comparison of lunar data detection limits with model predicted detection limits

The solar continuum predicted from the off-axis model of Figure 6.8 along with predicted dark counts were used to make predicted detection limits for the lunar limb scans. The detection limits were determined by the method outlined in Chapter 5 where statistical noise and dark counts were added to the model off-axis signal, with the solar continuum determined by the method described in Chapter 4. Detection limits were also calculated by using the measured data in the continuum wings from the limb scans. As with the comparison of Section 6.4.1, grating scans with a mean count rate less than 3-σ of the detector dark counts were eliminated in order to set a baseline for data points considered. However, in this case, the detector dark counts were not subtracted off from the selected grating scans used in the comparison. The detection limit was based on a SNR = 3, with the detection limit defined for the combined $D_1 + D_2$ counts.

The comparison of the two methods of determining detection limits are shown in Figure 6.9. Both the required $D_1 + D_2$ counts for the model and from the data as well

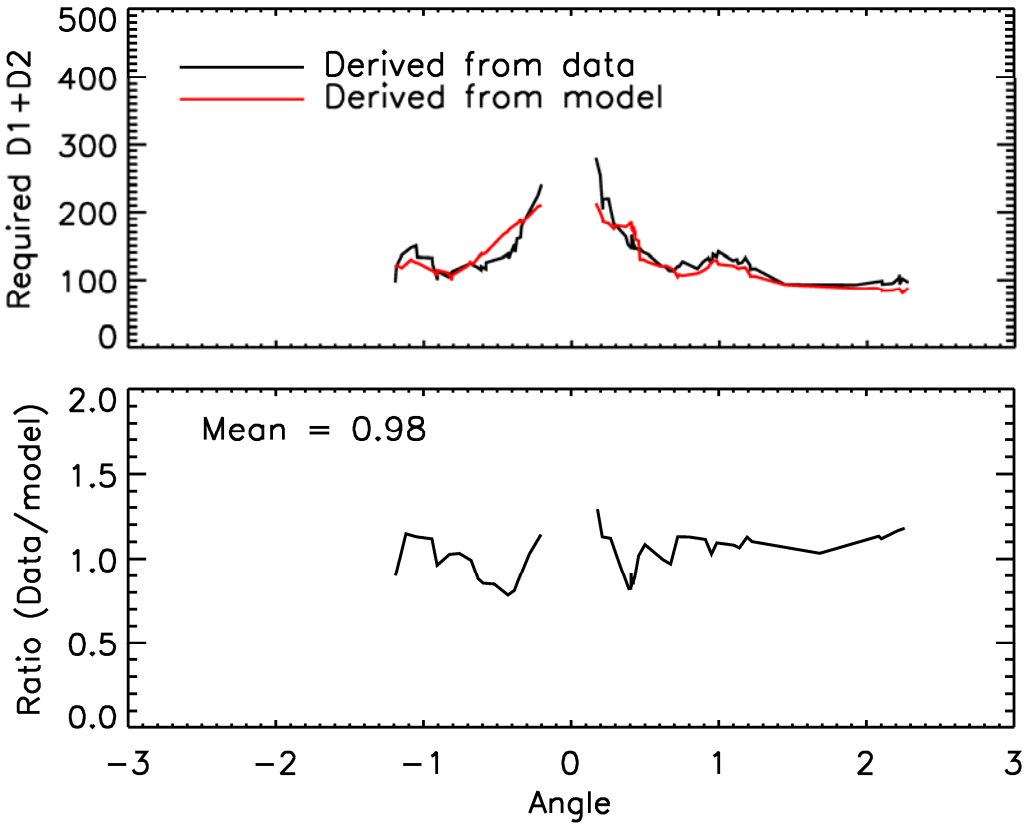

Figure 6.9. Comparison of detection limits determined from the model and from real data for an SNR of 3. The detection limits are defined as the corrected $D_1 + D_2$ counts/second required to produce an SNR = 3 in the presence of detector dark counts and off-axis light.

as the ratio are shown. The $D_1 + D_2$ counts represent the corrected total of the counts in the spectral vicinity of the D_1 and D_2 lines. The correction is made by dividing the total by the bandpass/grating step size ratio (discussed in Chapter 4). Reasonable agreement exists between the model predicted detection limits and those derived from measured values with a mean of 0.98 in the ratio, as shown in the lower panel of Figure 6.9. This comparison serves to further validate the model, software, and technique used to predict the detection limits. Since the same components go into making detection limit predictions for Mercury in Chapter 5, this comparison with real data serves to validate those results as well.

6.4.3 Variation of off-axis light during a grating scan

One phenomenon concerning off-axis light deals with the spacecraft motion, and therefore a variation in the off-axis angle, during a grating scan. For the off-axis curve in Figure 6.8, the off-axis light count rate from the data is derived from the solar continuum in the wings, which consists of only 6 grating steps. The entire grating scan is 16 grating steps with an integration time of 0.25 seconds per step. For the total time to make one grating scan (4 seconds) the spacecraft slews in angle 0.034°. This can make a significant difference depending on the off-axis angle of the boresight. Figure 6.10 illustrates this effect for a reference solar continuum that has been smoothed to the bandpass of the instrument. The grating was scanning from short wavelengths to long wavelengths as the spacecraft slewed closer to the planet. The off-axis angle at the short wavelength side of the grating scan is 0.21°. The solid black curve shows the non-modified solar continuum where the spectrum has been

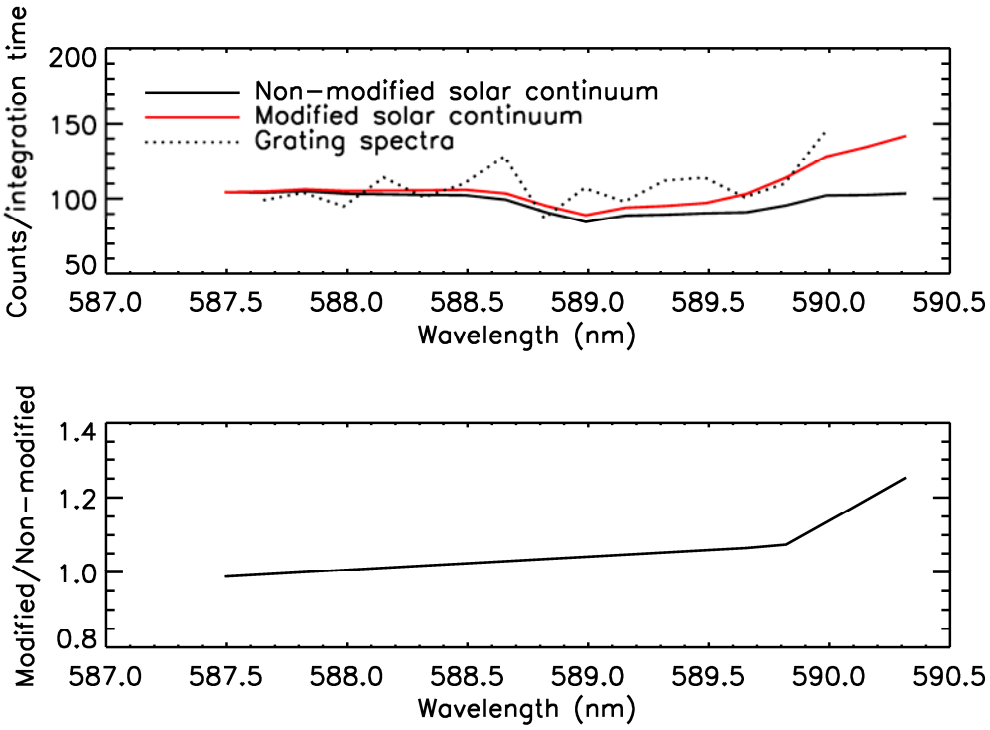

Figure 6.10. Upper panel shows the non-modified solar continuum that has been smoothed to the bandpass of the instrument (black). The red curve shows the smoothed solar continuum that has been modified to account for variations in the off-axis angle during a single 4 second grating scan. The dotted line is the actual spectra from the corresponding grating scan that appears to follow the modified solar continuum more closely than the non-modified solar continuum. The lower panel shows the ratio of the modified to non-modified solar continuum, implying at least a factor of 10% larger count rate in the spectral region of the sodium D lines. Other grating scans will differ depending of the mean off-axis angle as well as the direction of the grating scan with respect to the direction of the slewing spacecraft.

scaled to the off-axis model for an angle of 0.21°. The red curve represents the same solar continuum where the short wavelength side has been scaled to the off-axis curve for 0.21° and the long wavelength side has scaled to the off-axis response for an angle of 0.21° - 0.034°. All the points in between have been interpolated accordingly between these extreme values. The grating scan for this particular example is shown as the dotted line and follows the modified solar continuum more closely than the non-modified continuum. The result is that the region where the sodium doublet is located contains more off-axis light than would have been calculated if the varying off-axis light effect were not taken into account. The lower panel of Figure 6.10 shows the ratio of the modified solar continuum to the non-modified solar continuum, illustrating as much as 10 % more solar continuum photons in the region of the sodium D lines. In light of this phenomenon, an IDL routine was written that determined the direction of grating scan as well as the direction of spacecraft motion. Any solar continuum that is subtracted from the data is modified accordingly.

6.4.4 Comparison of detection limits with $D_1 + D_2$ counts

The detection limits for an SNR of 3 that were determined from the lunar limb scan data presented in Section 6.4.2 were compared with the $D_1 + D_2$ counts from the same grating scans. The $D_1 + D_2$ counts were determined by subtracting the background from the grating steps that contained the D lines. The background was determined by scaling a reference solar continuum out in the spectral wings to the actual data from a grating scan in the same spectral region. The solar continuum was modified to take into account the variation of the off-axis angle during the 4 seconds

for a grating scan as described in Section 6.4.3. The results are shown in Figure 6.11 and indicate that none of the observations are above the detection limit established by the technique described above. The ratio of the $D_1 + D_2$ counts to the detection limit is also shown with a line drawn at a value of 1. There are 2 data points that are "border-line", but after looking at those grating scans, the data was ruled out based on excess noise.

The two grating scans that were made closest to the lunar surface are shown in Figure 6.12. The scans were adjacent in time and the limb observation was approaching the closest position to the moon for the grating scan in the top panel and moving back away from the limb during the grating scan in the lower panel. Furthermore, since the instrument was in ziz-zag mode, time proceeds from short to long wavelengths in the grating scan shown in the upper panel and from long to short wavelengths in the grating scan shown in the lower panel. During the 4 seconds of each grating scan the off-axis angle changed by ~ .015° from the beginning to the end of the grating scan, with the boresight at the middle of the grating scan being 0.137° and 0.125° from the lunar center for the grating scans in the upper and lower panels, respectively. The angular change during each grating scan is less than the normal spacecraft slew rate because the limb observation was coming to an end in the upper grating scan from the upper panel, reversing direction, and starting to move away from the limb for the grating scan in the lower panel.

The angular position of the boresight for both of the grating scans in Figure 6.12 was recorded in telemetry every second. Since each grating scan lasts 4 seconds, 5

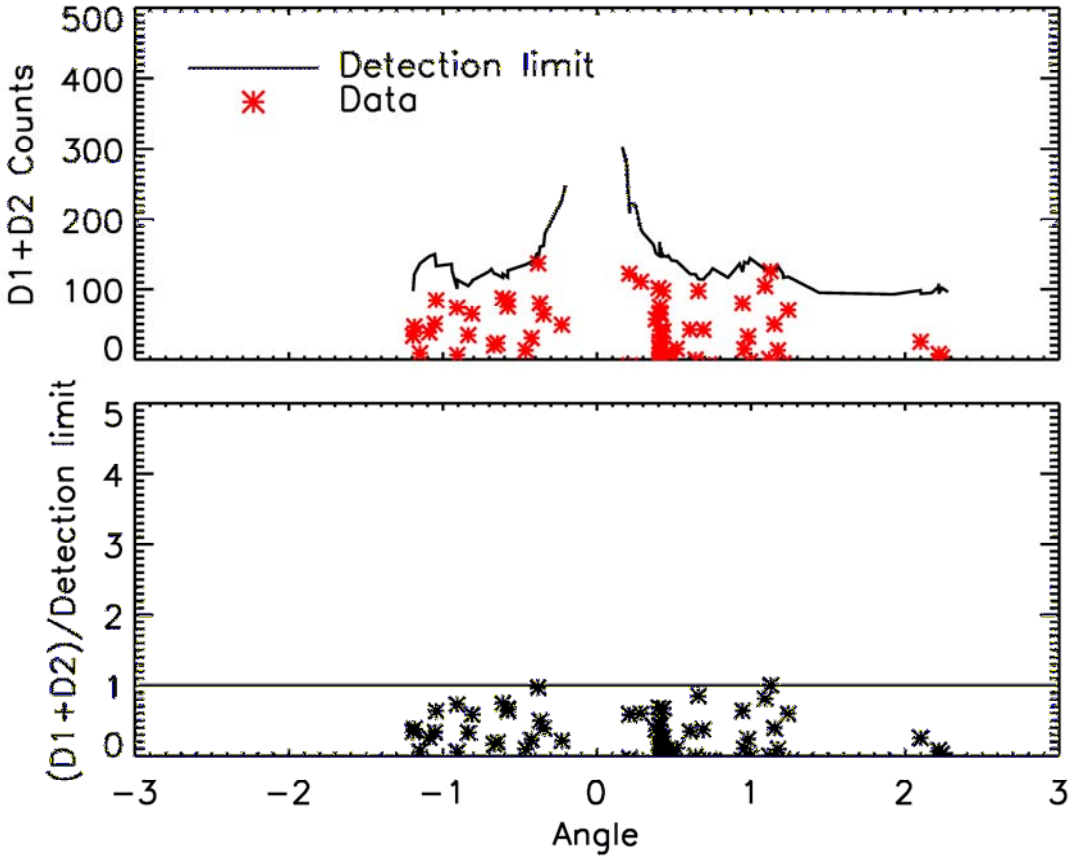

Figure 6.11. Comparison between the detection limit determined by using the measured radiance from the spectral wings of the limb observations and the actual corrected $D_1 + D_2$ total counts/second. The correction was made by dividing the $D_1 + D_2$ total by the ratio of the bandpass to grating step size. The lower panel shows the ratio and gives an indication of the grating scans that may possibly be considered to contain detections of sodium above an SNR of 3.

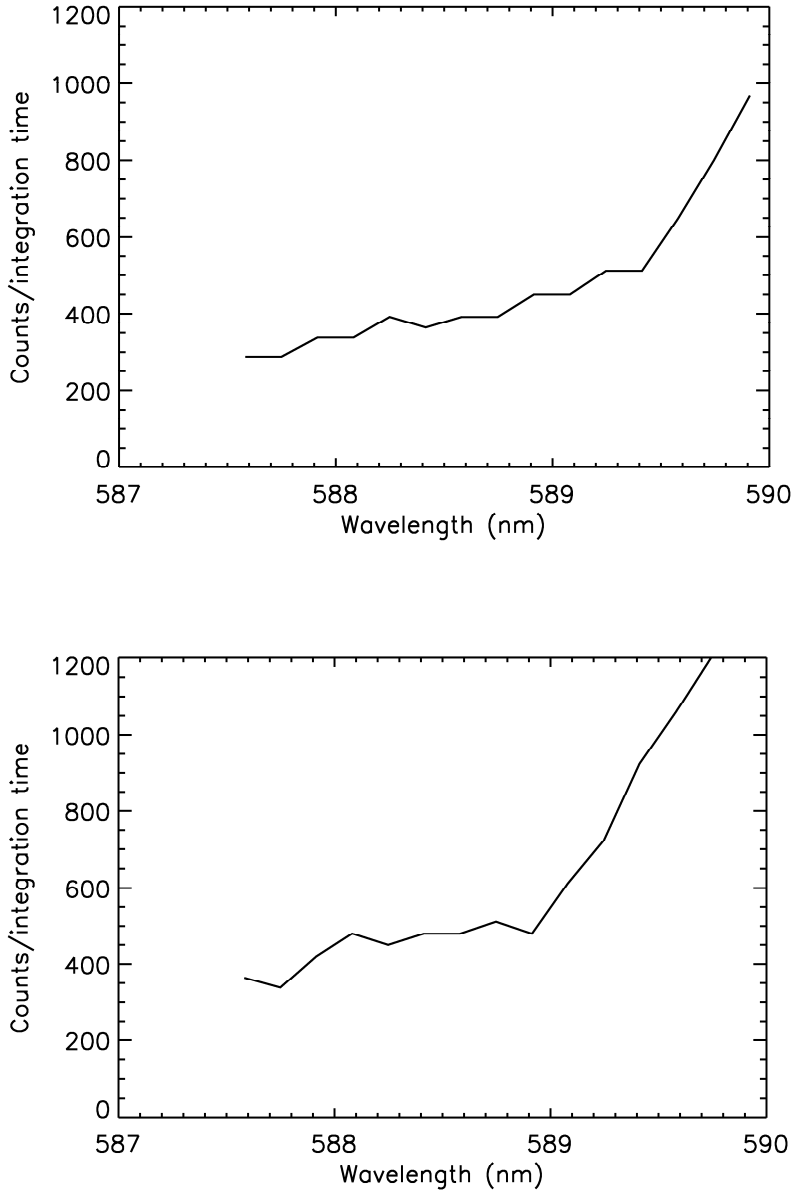

Figure 6.12. Spectra from the 2 closest lunar limb observations. The top panel was taken when the center of the field of view was 0.137° from lunar center at the middle of the grating scan. The lower panel was taken when the center of the field of view was 0.125° from lunar center. Each grating scan took 4 seconds to complete in which time the boresight moved ~ 0.015°. There is no apparent sodium D line spectra present in these 2 grating scans.

angular positions were recorded from the beginning of a grating scan to the end. The angular range corresponding to the 2 grating scans was compared to the off-axis response and found to fall within the portion of the curve where the counts begin to increase steeply with angle. This explains the large increase in the off-axis light that is obvious in both grating scans. Furthermore, no apparent sodium D line spectra is present in these two grating scans, which is in agreement with the conclusion from the detection limits shown in Figure 6.11.

6.4.5 Comparison with other datasets

A forward model prediction of the signal and SNR that would be produced in the instrument has been produced making use of data taken from Mendillo et al. (1991); who presented data taken by the authors as well as from Potter and Morgan (1988). Figure 6.13 shows plots of the data as a function of distance from the lunar center in lunar radii and in angle (upper and lower panels, respectively). The data presented as a function of angle uses the angular diameter of the Moon (0.212°) during the MASCS observations. Six data points were chosen that spanned an angular range from 0.12° to 0.9°. The data was read off of Figure 3 from Mendillo et al. (1991). The data were from above the sub-solar region of the Moon. The goal is to convert the data to counts spread over the instrument profile function, add a solar continuum background, add dark counts, and then add random noise; which is the same procedure described in Chapter 4. The data was converted to an integration time of 0.25 seconds in order to compare with the observations that were made by MASCS. The solar continuum background was modified to account for variation in the off-axis

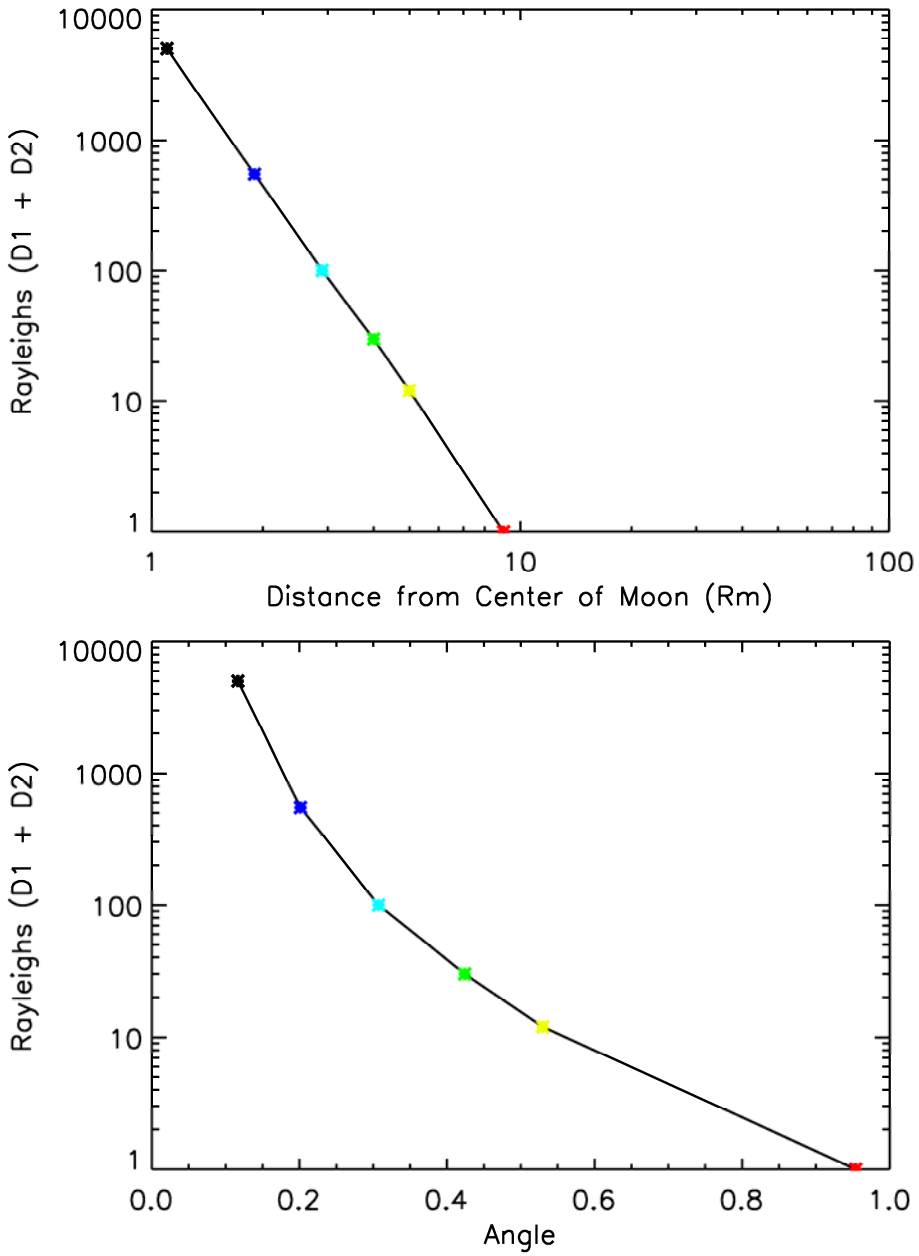

Figure 6.13. Curve showing the 6 data points chosen from Mendillo et al. (1991). The data was read off of a plot. The color coding is arbitrary and serves only to distinguish between the different data points. The plot in the upper panel shows the distribution of data as a function of distance from the center of the Moon in units of lunar radius. The lower panel presents the same data plotted as a function of angular distance from the center of the Moon. The angular diameter used for the Moon was 0.212°, which was the angular size as seen by MASCS during the MESSENGER flyby in 2005.

response during a 4 second grating scan assuming a spacecraft raster rate of 0.034° during a 4 second interval. This was also done to compare with MASCS observations, as discussed in Section 6.4.3.

The predicted the $D_1 + D_2$ counts for a 0.25 second integration time were analytically computed in order to compare with retrieved total counts. In order to convert the $D_1 + D_2$ radiance to a signal prediction for the UVVS, the sensitivity equation for a spectral line is given in Equation 6.2

$$L_{line} = \frac{\dot{C}_{corr}}{S_{line}} \tag{6.2}$$

where L_{line} is the radiance in a spectral line in Kilo-Rayleighs, $\dot{C}_{corr}$ is the corrected counts/second, and S_{line} is the sensitivity for a spectral line. For this case, L_{line} is the sum of the radiance from both sodium D lines. $\dot{C}_{corr}$ is obtained by

$$\dot{C}_{corr} = \frac{\sum_i C_i}{B.P./S.S} = \frac{C_{total}}{B.P./S.S} \tag{6.3}$$

where C is in counts/second, the summation is over the data points in the region of the spectral line, and B.P./S.S. is the ratio of bandpass to grating step size. For the spectral region at the sodium D lines, B.P./S.S. ~ 2.58 and the sensitivity of a spectral line is 104.5 counts/second/Kilo-Rayleigh Combining Equations 6.2 and 6.3 and rearranging gives

$$C_{total} = S_{line} * L_{line} * 2.58 * 0.25 \quad (6.4)$$

where 0.25 accounts for the fact that the integration time of the MASCS observations was 0.25 seconds. The sensitivity does not vary considerably over the spectral range of the sodium D lines, so the value of 104.5 is sufficient. Also, L_{line}, which is the sum of the radiances from both of the sodium D lines) is the data read from Figure 6.13 and given in column 3 of Table 6.1. Equation 6.4 gives the predicted total counts that would be obtained by MASCS if the radiances given by Mendillo were observed and completely filled the slit. This does not account for offsets due to dark counts or off-axis light. The predicted C_{total} values calculated from Equation 6.4 are given in column 4 of Table 6.1.

Five hundred simulations of simulated data were run for each of the 6 data points using the techniques of Chapter 4. An example of simulated spectra from each of the 6 data points is given in Figure 6.14. The spectra shown consists of the instrument profile function for both of the sodium D lines added to both the predicted solar continuum from the off-axis model as well as predicted detector dark counts. The counts from the instrument profile for the sodium D lines were generated from radiances from column 3 of Table 6.1, with an assumed value of 1.6 for the ratio of the D_2/D_1 line. The off-axis solar continuum has been modified to account for spacecraft slewing over a 4 second grating scan period (see Section 6.4.3). The detector dark counts are ~10 counts for each grating step per 0.25 second integration time. The dashed lines are the solar continuum that have been scaled to the mean

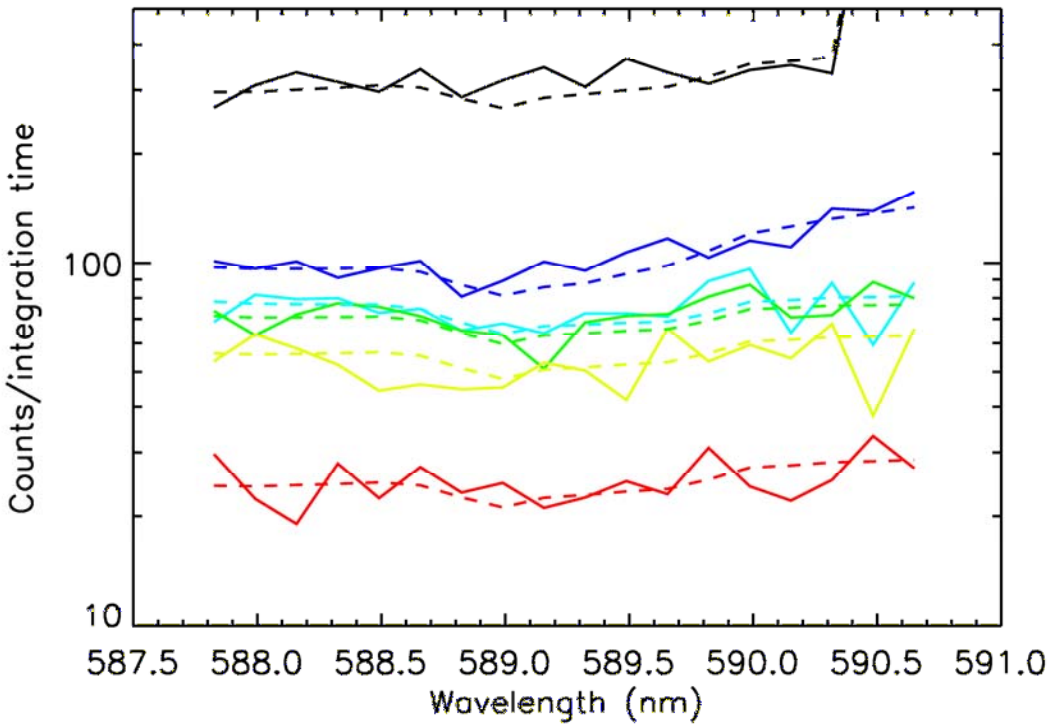

Figure 6.14. Examples of spectra obtained from the simulated observations. The color coding of the spectra corresponds the color coded data points of Figure 6.13. The dashed lines are the solar continuum that have been smoothed to the bandpass of the instrument and scaled to the mean of the values of the data points in the short wavelength region of the wings.

of the values in the spectral wings. The color code follows the data points of Figure 6.13.

After subtraction of the solar continuum from each spectrum, the counts beneath the sodium D lines were summed and the results plotted in Figure 6.15 (upper panel). The red stars represent the analytically predicted total count values from Equation 6.4. The spread in the simulated data is consistent with normally distributed noise. The mean and standard deviation of the data points for a given angle were computed and used to calculate the SNR. The mean and SNR are given in columns 5 and 6 in Table 6.1. The SNR is also plotted in Figure 6.15 (lower panel). According to these results, if the sodium radiance during the MASCS lunar observations was similar to the observations presented by Mendillo, then MASCS was unable to detect the emissions. This is consistent with the results presented in Figure 6.11 that shows no data points above a detection limit for an SNR of 3. Since the total $D_1 + D_2$ counts did not produce an SNR > 3, it was not necessary to try and separate the two lines.

6.5 Uncertainty analysis

The pointing of the boresight has 3 sources of possible error. The boresight is only known to within ½ of a slit width, or 0.02°. For the angular diameter of the moon to be 0.212°, this uncertainty translates to an altitude uncertainty of 327 km. The pointing knowledge of the spacecraft is 250 μ radians, which translates to 234 km. The pointing angle associated with each grating scan is taken at the center of the grating scan as the spacecraft slewed at a rate of ~ 0.0085°/second. Each grating scan consists of 16 grating steps with 0.25 second integration times. So the spacecraft

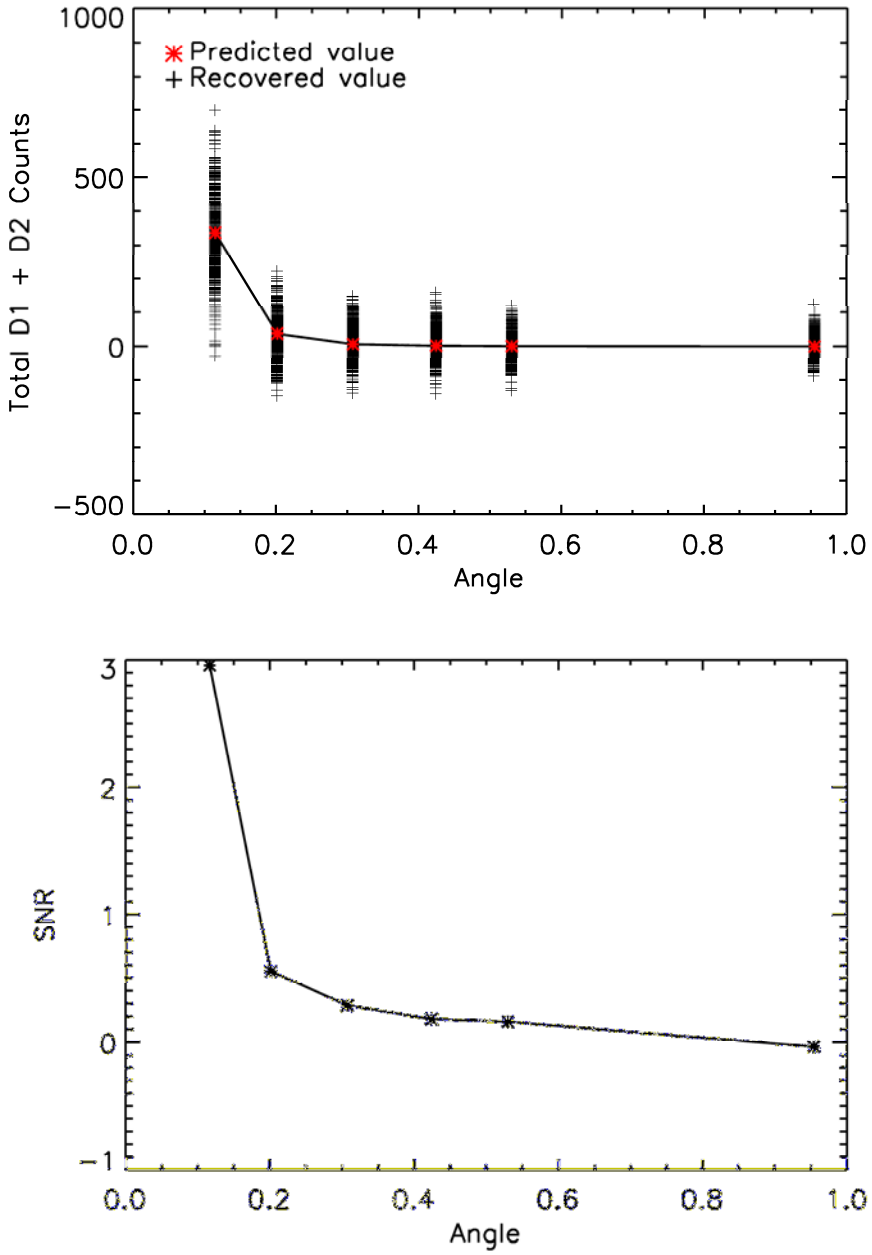

Figure 6.15. The upper panel shows the analytically predicted $D_1 + D_2$ UVVS counts as the red stars. The black stars represent 500 simulations of $D_1 + D_2$ UVVS counts that were generated and recovered by the techniques discussed in Chapter 4. The lower panel shows the SNR that was calculated by taking the ratio of the mean to standard deviation of the 500 data points. The low SNR values imply that detections with MASCS under the observing conditions for the lunar limb scans were not possible.

Distance from center of moon (lunar radius)	Distance from center of moon (angle)	Mendillo et al. (1991) $D_1 + D_2$ data Kilo-Rayleighs	Predicted total counts beneath the $D_1 + D_2$ lines	Mean of retrieved total counts beneath the $D_1 + D_2$ lines	SNR
1.1	0.117	5.0	337	334	2.96
1.9	0.201	0.55	37.1	30.2	0.551
2.9	0.307	0.10	6.74	16.0	0.286
4.0	0.424	0.030	2.02	9.00	0.180
5.0	0.530	0.0120	0.809	3.79	0.161
9.0	0.954	0.0010	0.067	2.22	_____

Table 6.1. Column 1 is the distance from the center of the Moon in units of lunar radius for the data points that follow the data from Mendillo et al. (1991). Column 2 is the distance in units of angle from the Moon, where the angular diameter of the lunar disk was 0.212° during MASCS limb observations. Column 3 is the $D_1 + D_2$ radiance from Mendillo corresponding to the chosen locations. Column 4 is the analytically predicted total counts beneath the sodium D lines that would be produced if the UVVS observed the radiances of column 3. Column 5 is the mean of the retrieved signal beneath the sodium D lines from the 500 simulated observations. After the addition of background counts and random noise the retrieval algorithm was applied, as discussed in Chapter 4. Column 6 is the SNR, computed from the mean of the retrieved counts divided by the standard deviation of the retrieved data.

slews 0.034° during one grating scan. From the center grating step, the spacecraft slews ½ of this, or 0.017°.ccTherefore the grating steps at one of the extreme edges of the grating scan are as much as 278 km. All 3 of these errors are independent and when added together could account for as much as 840 km in error in the pointing.

The difference in the model off-axis response and the actual off-axis data shown in Figure 6.8 is possibly due to incorrect scaling. With a mean of 1.08, the scaling of the off-axis curve to the peak measured surface scan may be better dealt with in several surface grating scans were averaged.

6.6 Summary

The Earth-Moon flyby allowed for lunar observations on July 31 and August 1, 2005. The angular diameter of the Moon was ~ 0.2° and the phase angle as seen from the spacecraft was ~ 67°. The UVVS was used to make both lunar surface observations as well as lunar limb observations; with the surface observations consisting of full disk raster observations and a smaller raster observation that targeted the Orientale impact basin.

Some of the grating scans for the surface observations were noticed to have extra data points that caused the spectra to appear shifted in wavelength. This occurred for all 3 channels, but was most prevalent in the VIS channel. The phenomena was random and thus required that each grating scan be looked at for known spectral lines, Ca K lines, in order to determine how much to shift the data. This technique only worked when observations were made of the surface since off limb observations did not contain suitable spectra.

Some of the grating scans contained noise spikes that were much larger than typical detector dark counts. The cause for this is still unknown; however and IDL routine was written that searched for and eliminated those grating scans. The technique was to take the median value over a wavelength range where the spectra were not expected to vary considerably. The maximum count value from that range was compared to the median from the same set of counts and if the maximum were greater than 2X the median value, then that data was discarded.

The full disk surface observations were used to determine the disk integrated radiance and reflectance (I/F). In order to keep from portions of the projected field of view from not intersected the surface, only the grating scans where the telescope boresight was pointed to less than 0.08° of the lunar center were used. The data were binned into 4 nm bandwidths in order to improve signal to noise. These results were provided to Holsclaw (Ph.D thesis, 2006) where a detailed analysis was done comparing to similar MASCS/VIRS results as well as other data sets.

The off-axis limb observations that were designed to look for sodium were placed into 2 categories depending on the background. If the data points in the spectral wings away from the sodium D lines were larger than a preset SNR times the square root of the detector dark counts that were then added to the detector dark count level, then the spectra was deemed to contain sufficient off-axis light to be above the detector dark count limit and thus for the background to be dominated by the solar continuum. If on the other hand this criterion was not met for a grating scan, then the background was deemed to be dominated by the detector dark counts. Distinguishing between these two cases is important since a solar continuum dominated background

requires that a model solar continuum smoothed to the bandpass of the instrument be subtracted from the spectra. Alternatively, a detector dark count dominated background requires that a random background whose mean is that of the detector dark count for the temperatures associated with these observations be subtracted off from the data.

Since the off-axis light model was used extensively in Chapter 5 to make signal and SNR predictions at Mercury, it was necessary to test the off-axis light model against the off-axis solar continuum background obtained from the limb scans. The limb observations where the observations moved up and down in altitude above the terminator, which had the long direction of the slit oriented perpendicular to the direction of motion, were used. The peak of the normalized off-axis response from the model was determined by scaling the peak count rate surface observation (taken with the surface slit in place) to the value that would be measured if the atmospheric slit were in place. The off-axis model was then compared to the off-axis data taken from the spectral wings of the grating scans. Reasonable agreement to within a few percent was obtained and thus served to validate the use of the off-axis model for making signal predictions.

The off-axis model as well as signal prediction techniques was further validated by comparing predicted detection limits to detection limits derived from the lunar limb data. Dark counts and random noise were added to the off-axis model predicted count rate. A detection limit based on an SNR of 3 was determined for both the model as well as the actual data. The 2 techniques agreed to within a few percent

across the angular range of the limb scans. This and the off-axis model comparison serve to help validate the prediction techniques for Mercury limb observations.

Before a solar continuum could be subtracted from grating scans, a modification to the solar continuum had to be made due to the varying off-axis angle associated with the spacecraft slewing during the 4 second grating scan time. The off-axis model was used to produce a modified solar continuum by considering the off-axis angle for each of the 16 grating steps. An IDL routine was written that kept track of the direction of the grating scan as well as the spacecraft slewing direction in order to know which side of the grating was nearest to the lunar limb. All solar continuum spectra were modified accordingly before being subtracted off from the corresponding grating scan data.

Detection limits determined from the real data for the limb observations were compared to the corrected $D_1 + D_2$ counts within each grating scan. None of the corrected $D_1 + D_2$ counts were above the detection limit with an SNR = 3. Spectra from the 2 closest limb scans showed no visible signs of sodium D lines. Furthermore, the spectra, which were taken from two consecutive grating scans that were in zig-zag mode, showed variations by a factor of ~ 3 in off-axis light over the 16 steps of each grating scan. The angular position at the center of each grating scan was 0.125° and 0.137°, which falls on the region of the off-axis light curve where values increase sharply for a small change in angle.

The lack of detection of sodium was validated by using previous datasets from Mendillo et al. (1991) and Potter and Morgan (1988) and making signal and SNR predictions for the UVVS based on this data. Five hundred simulations were

performed where the radiances were converted to counts distributed according to the instrument profile function, background counts from both off-axis light and detector dark counts were added, random noise applied, and then the total $D_1 + D_2$ counts retrieved. The results showed a maximum SNR value of less than 3, implying that based on the radiances measured by Mendillo et al. and Potter and Morgan, detections by MASCS were not possible. Sodium emissions at the Moon are well documented; therefore it is reasonable to assume that there were sodium emissions during the MASCS limb observations. The cause of the MASCS non-detection was most likely due to large off-axis light background compared to the counts from sodium exospheric emissions.

Chapter 7

Conclusions

MASCS was subjected to a rigorous laboratory calibration procedure in order to characterize the performance of the instrument. After launch in 2004, stellar observations have been performed in order to further calibrate the instrument. The direction cosines of the mean boresight of the atmospheric and surface slits in the spacecraft body frame were determined to be [0.00102281, 0.0024908088, 0.999984] and [0.000932230, 0.0023419775, 0.999997], respectively. The dark counts show an exponential dependence with increasing temperature as predicted from the data sheets of the photomultiplier tubes. Post-launch calibrations indicate that detector dark counts may be ~ 10X the value determined in the laboratory for lower temperatures and motivates the need to make further detector dark count measurements at higher temperatures. The wavelength scale was determined by observing spectral lines at discrete locations that cover the full spectral operational range. Results are consistent with calculated values to within ~ 0.05 nm. All three channels show nearly the same dependence of wavelength scale on temperature, with a maximum deviation < 0.4 grating steps for the highest temperatures. Spectral resolution of MASCS varies as a function of wavelength. At 121 nm the FUV channel spectral resolution is 0.33 nm while at 589 nm the VIS channel spectral resolution is 0.47 nm. The field of view

and telescope off-axis response were determined by rotating the instrument while observing a point source, thus mapping out the edges of the field of view and measuring the decrease in count rates as the point source image moved outside the instrument field of view. The field of view for the atmospheric slit is 0.04° X 1° while the field of view for the surface slit is 0.04° X 0.05° in the spectral and spatial directions, respectively. The field of view is similar for all 3 spectral channels. The off-axis response of the telescope was measured in the laboratory for a point source in the across slit and along slit directions. The off-axis light drops by 10^{-5} at 1° off axis from the boresight for a point source. An off axis model was created in order to make predictions for an extended source. A detailed explanation as well as assumptions made in creating the model are given in Chapter 2. Off-axis light predictions are comparable to a single measurement performed by VIRS of the off-axis light from Venus during the flyby of 2007. Spectrometer scattered light drops by several orders of magnitude over a small grating step range. A large lobe exists at ~ 50 grating steps shortward of the central grating step position. Spectrometer stray light is ~ 0.1% of the peak value for observing a broad spectrum such as the reflected solar spectrum from the lunar surface. The absolute value of the polarization ranges from 0% at short wavelengths to 80% at long wavelengths. The window transmission was typical for the transmission properties of MgFl. However, since the contamination cover is now open and will remain open for the duration of the mission, the window transmission does not need to be factored into the data. The radiometric sensitivity of all 3 channels was determined by measuring count rates from known lamp sources in the laboratory and from known stellar sources in flight. Laboratory lamp sources

consisted of calibrated deuterium and FEL lamps. For count rates exceeding 10^5 counts per second, the non-linearity correction results in a factor of ~ 2 greater counts for the VIS channel.

An observation software planning tool has been developed that combines observational geometry, instrument performance characteristics, and a sodium exospheric model in order to 1) determine observation pointing strategies and 2) characterize the ability of the UVVS to distinguish between source processes as well as variations within a single process. Using the software planning tool, observation strategies called radial scans were devised that start at 1000 km and follow a radial vector down to 100 km. Nine equatorial radial scans that last 7 minutes each and with 1 minute spacecraft slew time between successive radial scans were shown to be possible throughout the Mercury year. For the Mercury year from perihelion to close to aphelion, 1-2 hours for dayside observations from the periherm region of the MESSENGER orbit is possible if more time for spacecraft slewing is required. In addition, north-south limb observations were proposed but are more limited in terms of the amount of time to perform them, altitude coverage, and seasonal coverage. The north-south observations of the dayside were generally found to be associated with planetary true anomalies between 0° and 180° and the portion of the MESSENGER orbit with the sub-spacecraft point at northern latitudes. The spacecraft velocity approaches its maximum during this time and typically only 20 minutes are available for observations.

Using the proposed set of equatorial and north-south radial scans, detection limits were determined for the required $D_1 + D_2$ radiance to achieve SNR values of 10 and

20. The detection limits for equatorial observations show a peak around the sub-solar point and decrease by a factor of ~ 5 for terminator observations. Peak required D_1 + D_2 radiance for SNR's of 10 and 20 are ~ 50 and 100 KRay for the surface slit and ~ 400 and 800 KRay for the atmospheric slit. The detection limit as a function of altitude for SNR's of 10 and 20 are typically less than 100 KRay for the surface slit for altitudes above 100 km and less than 100 KRay for the atmospheric slit for altitudes greater than ~ 250 km. The detection limits for north-south observations are generally lower than for the equatorial observations

Meteoritic vaporization was tested at 3000 K to determine how well the temperature could be measured. Observations above the terminator region were simulated in order to reduce the effects of other solar driven source production processes. The log of data over a range of altitudes from 100 km to 1000 km and above the terminator region was used to fit a strait line to. Thirty simulations were performed using the atmospheric slit in order to build up statistics and determine the mean and standard deviation of the slope of the line. Curves without the addition of random noise at temperatures of 2000, 2500, 3000, 3500, and 4000 K were produced in order to build up a temperature-slope curve. Retrieved slopes from the 30 simulations were mapped onto the temperature-slope curve to determine the range of temperatures over which the meteoritic vaporization could be known. Results showed that the temperature of a 3000 K process could be retrieved to within a range of 154 K and 380 K for planetary true anomalies of 64° and 180°, respectively. The source for meteoritic vaporization used at a planetary true anomaly of 64° did not produce an SNR value above 3 for a planetary true anomaly = 180°. Instead of

presenting a null result, the source rate was increased by a factor of 10 for a true anomaly of 180°. The reason for the large difference in signal values for the same source rate is a demonstration of the strong dependence of signal values on the g-value; which decreases by ~ 16 from a true anomaly of 64° to a true anomaly of 180°.

Test cases were devised that characterized the ability of the UVVS to distinguish between major source processes as a function of solar zenith angle. The dominant source process was either photon stimulated desorption or thermal vaporization with typical maximum zenith column abundance ~ 4.4 X 10^{11} Na/cm^2 for a planetary true anomaly = 64°. Meteoritic vaporization was modeled with global abundances that were 1-2 orders of magnitude less than the other 2 processes. A cosine power law was used to distinguish between different source processes. Ten simulations were performed with results showing that photon stimulated desorption and thermal vaporization were typically distinguishable from each other at all planetary true anomalies. However, since the signal and SNR for meteoritic vaporization was relatively small and because meteoritic vaporization does not follow a cosine power law, meteoritic vaporization was not clearly distinguished from the other processes using this technique. Signal and SNR levels also demonstrated the effects of varying g-values over planetary true anomaly. In most cases, this had the dominant effect on the signal instead of varying sodium exospheric abundances with planetary true anomaly. In order to overcome low g-values at a planetary true anomaly of 180°, the atmospheric slit had to be used to collect more photons, whereas for the other planetary true anomalies testes, the surface slit was used.

A test case was performed that characterized the ability of MASCS to determine sodium surface concentration variations. The surface abundance was given a latitudinal variation following a sine of latitude dependence. The software planning tool was used to determine that the best observing geometry was a series of north-south radial scans between 100 km to 50 km for a planetary true anomaly of 31°. Simulated data from the 50 km altitude was presented. Based of the shape of the resulting curves, a cosine power law was fit to the data in order to determine how well the power law parameter could be distinguished for variations in the surface density distribution for a given source process. Photon stimulated desorption and thermal were tested. Ten simulations were performed using the surface slit with results showing that over the range of latitudinal surface density variations tested, the power law parameter was easily distinguishable for different sodium surface concentration variations when photon stimulated desorption was the dominant source process. However, due to the strong temperature dependence of thermal vaporization and the need to have data points at high latitudes to distinguish between variations in sodium surface concentrations, it was difficult to distinguish the power law parameter for different sodium surface concentrations for a thermal vaporization dominated exosphere.

MESSENGER flew by the Earth-Moon system in 2005 and made observations of the Moon. Observations of the lunar surface and limb were performed. Using data acquired in the spectral wings during the sodium limb observations, off-axis light was compared to off-axis model predictions. Results between the model and observations showed agreement to within 10 %. A correction to the predicted solar continuum that

enters the instrument from off-axis angles had to be made to account for the variation in the off-axis angle during the time for a single grating scan, which was 4 seconds. In this time, the spacecraft slewed ~ 0.034° and affected the off-axis solar continuum from the beginning of a grating scan to the end. Spectra were shown for the 2 closest limb observations and illustrated that over the 4 seconds of a grating scan, the off-axis light can vary by ~ a factor of 3 from one end of the grating scan to the other. This effect may vary depending on the off-axis angle; where observations at smaller off-axis angles are associated with a larger variation in off-axis light than for observations at larger off-axis angles for the same variation in off-axis angle during a grating scan.

Detection limits were made for an SNR = 3 by using the counts from grating steps in the spectral wings of the sodium D lines. It was found that none of the data in the spectral line region exceeded the detection limit, implying that MASCS did not detect sodium in the lunar exosphere. Spectra from the 2 closest limb observations showed no visible signs of sodium D line profiles.

Data taken from Mendillo et al. (1991) and Potter and Morgan (1988) of the lunar sodium corona was forward modeled to make signal and SNR predictions for the MASCS observations. The data was corrected to the integration time for MASCS (0.25 seconds) and then added to an off-axis solar continuum predicted from the off-axis model. The solar continuum was modified in order to account for spacecraft motion as discussed above. Random noise was added to the signal and then the total $D_1 + D_2$ counts were retrieved by the methods described in Chapter 4. Five hundred simulations were performed and the mean and standard deviation of the results

computed. The SNR was computed by taking the ratio of the mean to the standard deviation of the 500 simulations and found to be < 3, which is consistent with the earlier prediction that no detection was made.

Bibliography

Barbieri, C., Verani, S., Cremonese, G., Sprageue, Mendillo, M., Cosentino, R., Hunten, D., 2004. First observations of the Na exosphere of Mercury with the high-resolution spectrograph of the 3.5M Telescopio Nazionale Galileo. *Planetary and Space Science, 52*, Issue 13, 1169-1175.

Bida, T. A., Killen, R. M., Morgan, T. H., 2000. Discovery of calcium in Mercury's atmosphere. *Nature, 404*, 159-161.

Broadfoot, A. L., Shemansky, D. E., Kumar, S., 1976. Mariner 10 – Mercury atmosphere. *Geophysical Research Letters, 3*, 577-580.

Brown, R. A., Yung, Y. L., 1976. Io, Its Atmosphere and Optical Emissions. *Jupiter*, The University of Arizona Press, Tucson.

Cameron, A. G. W., 1985. The partial volatilization of Mercury. *Icarus 64*, 285-294

Chamberlain, J. W., 1978. *Theory of planetary atmospheres: an introduction to their physics and chemistry*. Academic press, New York.

Chamberlain, J. W., Hunten, D. M., 1987. *Theory of planetary atmospheres: an introduction to their physics and chemistry, second edition*. Academic press, inc, Orlando.

Chamberlain, J. W., 1961. *Physics of the Aurora and Airglow*. International Geophysics Series. Academic Press, New York.

Chang, J-J., Kelly, H. P., 1975. Photoabsorptioin of the neutral sodium atom: A many-body calculation. *Physical Rev. A, 12*, no. 1, 92-98.

Cintala, M. J., 1992. Impact-induced thermal effects in the lunar and mercurian regoliths. *J. Geophys. Res., 97*, 947-973.

Eichhorn, G., 1977a. Heating and vaporization during hypervelocity particle impact. *Planet. Space Sci., 26*, 463-467.

Eichhorn, G., 1977b. Primary velocity dependence of impact ejecta parameters. *Planet. Space Sci., 26*, 469-471.

Flavill, R. P., Carey, W. C., McDonnell, J. A. M., Ashworth, D. G., Allison, R. J., 1980. Progress in defining the solar wind sputter rate on protoplanets and interplanetary matter. *Planet. Space Sci., 28*, 511-524.

Goettel, K. A., 1988. Present bound on the bulk composition of Mercury: implications for planetary formation processes. *Mercury*. The University of Arizona Press, Tucson.

Hamamatsu Photonics, 1994. *Photomultiplier Tube: Principle to Application*. Hamamatsu Photonics, Electron Tube Center.

Holsclaw, G. M., 2006. *The MESSENGER Visible and Infrared Spectrograph: Design, Calibration, and Analysis of Lunar Observations*. Ph.D. thesis, University of Colorado.

Hord, C. W., McClintock, W. E., Stewart, A. I. F., Barth, C. A., Esposito, L. W., Thomas, G. E., Sandel, B. R., Hunten, D., M., Broadfoot, A. L., Shemansky, D. E., 1992. Galileo Ultraviolet Spectrometer experiment. *Space Science Reviews, 60*, no. 1-4, 503-530.

Hudson, R. D., Carter, V. L., 1967. *J. Optical Society of America, 57*, 651.

Huebner, W. F., Keady, J. J., Lyon, S. P., 1992. Solar photo rates for planetary atmospheres and atmospheric pollutants. *Astrophysics and Space Science, 195*, 1-294.

Hunten, D. M., Morgan, T. H., Shemansky, D. E., 1988. The Mercury Atmosphere. *Mercury*. Univ. of Arizona Press, Tucson.

Hunten, D. M., Sprague, A. L., 2002. Diurnal variation of Na and K at Mercury. *Meteoritics & Planetary Science, 37*, no. 9, 1191-1195.

Ip, W.-H., 1986. The sodium exosphere and magnetosphere of Mercury. *Geophysical Research Letters, 13*, no. 5, 423-426.

Ip, W.-H., 1990. On solar radiation-driven surface transport of sodium atoms at Mercury.
Astrophysical Journal, Part 1, 356, 675-681.

Ip, W.-H., 1993. On the surface sputtering effects of magnetospheric charged particles at Mercury. *The Astrophysical Journal, 418*, 451-456.

Killen, R. M., Potter, A. E., Morgan, T. H., 1990. Spatial distribution of sodium vapor in the atmosphere of Mercury. *Icarus, 85*, 145-167.

Killen, R. M., Morgan, T. H., 1993. Maintaining the Na atmosphere of Mercury. *Icarus 101*, Issue 2, 293-312.

Killen, R. M., Potter, A., Fitzsimmons, A., Morgan, T. H., 1999. Sodium D2 line profiles: clues to the temperature structure of Mercury's exosphere. *Planetary and Space Science, 47*, Issue 12, 1449-1458.

Killen, R. M., Potter, A. E., Sarantos, M., Jackson, B. V., Hick, P., Giles, B., 2001. Evidence for space weather at Mercury. *Journal of Geophysical Res., 106*, no. E9, 20509-20525.

Killen, R. M., 2003. Private communication.

Killen, R. M. Sarantos, M., Reiff, P., 2004a. Space weather at Mercury. *Advances in Space Research, 33*, 1899-1904.

Killen, R. M., Sarantos, M., Potter, A. E., Reiff, P., 2004b. Source rates and ion recycling rates for Na and K in Mercury's atmosphere. *Icarus, 171*, 1-19.

Killen, R. M., Bida, T. A., Morgan, T. M., 2005a. The calcium exosphere of Mercury. *Icarus, 173*, Issue 2, 300-311.

Killen, R. M., 2005b. Private communication.

Killen, R. M., 2006. Private communication.

Koehn, P. L., Sprague, A. L., 2007. Solar oxygen and calcium in Mercury's exosphere. *Planetary and Space Science, 55*, Issue 11, 1530-1540.

Lange, M. A., Ahrens, T. J., 1982. The evolution of an impact generated atmosphere. *Icarus, 51*, 96-120

Leblanc, F., Johnson, R. E., 2003. Mercury's sodium exosphere. *Icarus, 164*, 261-281.

Leblanc, F., Barbieri, C., Cremonese, G., Verani, S., Cosentino, R.., Mendillo, M., Sprague, A., Hunten, D., 2006. Observations of Mercury's exosphere: spatial distributions and variations of its Na component during August 8, 9, and 10, 2003. Icarus, 185, Issue 2, 395-402.

Madey, T. E., Yakshinskiy, N. V., Ageev, V. N., Johnson, R. E., 1998. Desorption of alkali atoms and ions from oxide surfaces: relevance to origins of Na and K in atmospheres of Mercury and the Moon. *Journal of Geophysical Res., 103,* no. E3, 5873-5887.

Mangonao, V., Milillo, A., Mura, A., Orsini, S., de Angelis, E., di Lellis, A. M., Wurz, P., 2007. The contribution of impulsive meteoritic vapourization to the Hermean exosphere. *Planetary and Space Science, 55,* Issue 11, 1541-1556.

McClintock, W. E., Lankton, M., 2007. The Mercury Atmospheric and Surface Composition Spectrometer for the MESSENGER Mission. *Space Science Reviews*. In Press.

McClintock, W. E., 2007. Private communication.

McDonnell, J. A. M., Flavill, R. P., 1974. Solar wind sputtering on the lunar surface: equilibrium crater densities related to past and present microparticle influx rates. *Proceeding of the fifth lunar conference, ,* 2441-2449.

Melosh, H. J., 1989. Impact Cratering: A Geologic Process. Oxford Univ. Pres, New York.

Mihalas, D., (1978). *Stellar Atmospheres*. W. H. Freeman and Company, San Francisco.

Morgan, T. H., Killen, R. M., 1998. Production mechanisms for faint but possibly detectable coronae about asteroids. *Planetary and Space Science, 46,* no. 8, 843-850.

Potter, A., Morgan, T., 1985. Discovery of sodium in the atmosphere of Mercury. *Science, 229,* 651-653.

Potter, A. E., Morgan, T. H., 1986. Potassium in the atmosphere of Mercury. *Icaurs, 67,* 336-340.

Potter, A. E., Morgan, T. H., 1988. Extended sodium exosphere of the moon. *Geophysical Research Letters, 15,* 1515-1518.

Potter, A. E., Killen, R. M., Morgan, T. H., 1999. Rapid changes in the sodium exosphere of Mercury. *Planetary and Space Science, 47,* Issue 12, 1441-1448.

Potter, A. E., Killen, R. M., Morgan, T. H., 2000. Variation of lunar sodium during passage of the Moon through the Earth's magnetotail. *Journal of Geophysical Research, 105,* 15,073-15,084.

Potter, A. E., Killen, R. M., Morgan, T. H., 2001. The distant sodium tail of Mercury. *Proc. Mercury: Space environment, Surface, and Interior*.

Potter, A. E., Killen, R. M., Morgan, T. H., 2002. The sodium tail of Mercury. *Meteoritics & Planetary Science, 37*, no. 9, 1165-1172.

Potter, A. E., Killen, R. M., Sarantos, M., 2006. Spatial distribution of sodium on Mercury. *Icarus, 181*, issue 1, 1-12.

Rietmeijer, F. J. M., 2004. Mesospheric metal abundances and meteoritic dust: analysis of surviving meteoroids. *Advances in Space Research, 33*, Issue 9, 1475-1480.

Riner, M. A., Bina, C. R., Robinson, M. S., 2007. Compressible Mercury – insights into its composition and interior structure. *38th Lunar and Planetary Science Conferenc*e, no. 1338, 2391.

Rybicki, G. B., Lightman, A. P., 1979. *Radiative processes in astrophysics*. John Wiley & Sons, New York.

Santo, A. G., et al., 2001. The MESSENGER mission to Mercury: spacecraft and mission design. *Planetary and Space Science, 49*, Issue 14-15, 1481-1500.

Sarantos, M., Reiff, P. H., Hill, T. W., Killen, R. M., Andrew, L.U., 2001. A Bx-interconnected magnetosphere model for Mercury. *Planetary and Space Science, 49*, 1629-1635.

Sarantos, M., 2005. Private communication.

Sigmund, P., 1981. Sputtering by ion bombardment: theoretical concepts. *Topics in Applied Physics, sputtering by particle bombardment I, 47*, 9-71.

Smyth, W. H., Marconi, M. L., 1995. Theoretical overview and modeling of sodium and potassium atmospheres of Mercury. *The Astrophysical Journal, 441*, 839-864.

Solomon, S. C., et al., 2001. The MESSENGER mission to Mercury: Scientific objectives and implamentation. *Planetary and Space Science, 49*, Issues 14 and 15, 1445-1465.

Sprague, A. L., Kozlowski, R. W. H., Hunten, D. M., Wells, W. K., Grosse, F. A., 1992. The sodium and potassium atmosphere of the moon and its interaction with the surface. *Icarus, 96*, 27-42.

Sprague, A. L., Kozlowski, R. W. H., Hunten, D. M., Schneider, N. M., Domingue, D. L., Well, W. K., Schmitt, W., Fink, U. 1997. Distribution and abundance of sodium in Mercury's atmosphere, 1895-1988. *Icarus, 129*, issue 2, 506-527.

Sprague, A. L., Schmitt, W. J., Hill, R. E., 1998. Mercury: Sodium atmospheric enhancements, radar-bright spots, and visible surface features. *Icarus, 136*, Issue 1, 60-68.

Sprague, A. L., 2007. Private communication.

Strom, R. G., 1997. Mercury: An overview. *Advances in Space Research, 19*, no. 10, 1471-1485.

Strom, R. G., Sprague, A. L., 2003. *Exploring Mercury: The Iron Planet*. Springer-Praxis Books in Astronomy and Space Sciences, London (UK).

Taylor, G. J., Scott, E. R. D., 2005. Meteorites, Comets and Planets: Treatise on Geochemistry, Vol. 1. Elsevier B. V., Amsterdam, The Netherlands, 477.

Urey, H. C., 1952. *The Planets: Their Origin and Development*. New Haven: Yale University Press.

Wetherill, G. W., 1988. Accumulation of Mercury from planetesimals. *Mercury*, The University of Arizona Press, Tucson.

Weins, R. C., Burnett, D. S., Calaway, W. F., Hansen, C. S., Lykke, D. R., Pellin, M. J., 1997. Sputtering products of sodium sulfate: implications for Io's surface and for sodium-bearing molecules in the Io torus. *Icarus, 128*, 386-397.

Wurtz, P., Lammer, H., 2003. Monte-Carlo simulation of Mercury's exosphere. *Icarus, 164*, 1-13.

Yakshinskiy, B. V., Madey, T. E., 1999. Photon-stimulated desorption as a substantial source of sodium in the lunar atmosphere. *Nature, 400*, August 12, 642-64.

Yakshinskiy, B. V., Madey, T. E., Ageev, V. N., 2000. Thermal desorption of sodium atoms from thin SiO2 films. *Surface Review and Letters, 7*, nos. 1 & 2, 75-87.

Yakshinskiy, B. V., Madey, T. E., 2001. Electron- and photon-stimulated desorption of K from ice surfaces. *Journal of Geophysical Research, 106*, no. E12, 33303-33307.

Yakshinskiy, B. V., Madey, T. E., 2004. Photon-stimulated desorption of Na from a lunar sample: temperature-dependent effects. *Icarus, 168*, 53-59.

Yen, C.-W., 1989. Ballistic Mercury orbiter mission via Venus and Mercury gravity assists. *Journal of the Astronautical Sciences, 37*, 417-432.